A Beam Tracing Model for Electromagnetic Scattering by Atmospheric Ice Crystals

Submitted to the University of Hertfordshire in partial fulfilment of the requirements of the degree of PhD

Laurence Charles Taylor

July 2016

Abstract

While exact methods, such as DDA or T-matrix, can be applied to particles with sizes comparable to the wavelength, computational demands mean that they are size limited. For particles much larger than the wavelength, the Geometric Optics approximation can be employed, but in doing so wave effects, such as interference and diffraction, are ignored. In between these two size extremes there exists a need for computational techniques which are capable of handling the wide array of ice crystal shapes and sizes that are observed in cirrus clouds. The Beam Tracing model developed within this project meets these criteria. It combines aspects of geometric optics and physical optics. Beam propagation is handled by Snell's law and the law of reflection. A beam is divided into reflected and transmitted components each time a crystal facet is illuminated. If the incident beam illuminates multiple facets it is split, with a new beam being formed for each illuminated facet. The phase-dependent electric field amplitude of the beams is known from their amplitude (Jones) matrices. These are modified by transmission and reflection matrices, whose elements are Fresnel amplitude coefficients, each time a beam intersects a crystal facet. Phase tracing is carried out for each beam by considering the path that its 'centre ray' would have taken. The local near-field is then mapped, via a surface integral formulation of a vector Kirchhoff diffraction approximation, to the far-field. Once in the far-field the four elements of the amplitude matrix are transformed into the sixteen elements of the scattering matrix via known relations.

The model is discussed in depth, with details given on its implementation. The physical basis of the model is given through a discussion of Ray Tracing and how this leads to the notion of Beam Tracing. The beam splitting algorithm is described for convex particles followed by the necessary adaptations for concave and/or absorbing particles. Once geometric aspects have been established details are given as to how physical properties of beams are traced including: amplitude, phase and power. How diffraction is implemented in the model is given along with a review of existing diffraction implementations.

Comparisons are given, first against a modified Ray Tracing code to validate the geometric optics aspects of the model. Then, specific examples are given for the cases of transparent, pristine, smooth hexagonal columns of four different sizes and orientations; a highly absorbing, pristine, smooth hexagonal column and a highly absorbing, indented, smooth hexagonal column. Analysis of two-dimensional and one-dimensional intensity distributions and degree of linear polarisation results are given for each case and compared with results acquired through use of the Amsterdam Discrete-Dipole Approximation (ADDA) code; with good agreement observed.

To the author's best knowledge, the Beam Tracer developed here is unique in its ability to handle concave particles; particles with complex structures and the manner in which beams are divided into sub-beams of quasi-constant intensity when propagating in an absorbing medium.

One of the model's potential applications is to create a database of known particle scattering patterns, for use in aiding particle classification from images taken by the Small Ice Detector (SID) *in-situ* probe. An example of creating such a database for hexagonal columns is given.

Acknowledgements

This thesis represents the culmination of the best part of four year's work, over which time I have benefitted from the good counsel of many friends, family and colleagues. I should therefore like to thank, first and foremost, my supervisor, Dr. Evelyn Hesse; who throughout my PhD, and a good part of my undergraduate degree, has been unwavering in her support. Her advice, both friendly and technical, has helped me get to this stage and I doubt I would have come close without it. My thanks is extended to my other supervisors, Professor. Zbigniew Ulanowski and Professor. Paul Kaye.

To my friends Jenna Thornton, Chris Stopford and Helen Smith within the Centre for Atmospheric and Instrumentation Research I give thanks for their (un)willingness to listen to me talk about beams and polarisation. I hope they will carry with them always the many happy times that we have shared. A special thank you is given to Jennifer Kyan who, not only kindly proof read this thesis, has been a great friend of mine for more years than I care count. To Ben Holland, Cameron Stewart, Holly Batchelor, James Bower and William Oliver I hope you know that your friendship has been a great comfort and that you have all played your part in making this happen.

There are of course numerous people within the Physics, Astronomy and Mathematics department who have helped me throughout my time at the University. In particular, I owe a great deal to Dr. Jim Collett and all the other members of the ever infamous *check-in* crowd.

Finally, but by no means least, I thank my family, whose patience and support has not gone unnoticed. I will always be grateful for all they have done to help me.

Contents

List of Figures

List of Tables

List of Acronyms

The following acronyms are used throughout the report:

ADDA	Amsterdam Discrete Dipole Approximation.
AIITS	Aerosol Ice Interface Transition Spectrometer.
BEM	Boundary Element Method.
BT	Beam Tracing.
CAST	Coordinated Airborne Studies in the Tropics.
CCD	Charged Coupled Device.
CPI	Cloud Particle Imager.
DDA	Discrete Dipole Approximation.
DLP	Degree of Linear Polarisation.
EM	Electromagnetic.
FAAM	Facility for Airborne Atmospheric Measurements.
FDTD	Finite Difference Time Domain.
GO	Geometric Optics.
IGOM	Improved Geometric Optics Method.
IN	Ice Nuclei.
IPCC	Intergovernmental Panel on Climate Change.
LIDAR	LIght Detection And Ranging.
MKA	Modified Kirchhoff Approximation.
PGOH	Physical Geometric Optics Hybrid.
PHIPPS	Particle Habit Imaging and Polar Scattering.
RADAR	RAdio Detection and Ranging.
RTDF	Ray Tracing with Diffraction on Facets.
SEM	Scanning Electron Microscope.
SID	Small Ice Detector.
SVM	Separation of Variables Method.
VSHF	Vector Spherical Harmonic Function.
VSWF	Vector Spherical Wave Function.

List of Symbols

Unless stated otherwise, the symbols used throughout this report are defined below.

Symbol	Description
$\vartheta_i, \vartheta_r, \vartheta_t$	Angles of incidence, reflection and transmission.
$\hat{\mathbf{k}}^i, \hat{\mathbf{k}}^r, \hat{\mathbf{k}}^t$	Unit vectors in the direction of incidence, reflection and transmission.
$\mathbf{k}$	Wave vector.
k_0, k	Free space and media wavenumbers.
p	Beam recursion index.
I, Q, U, V	Stokes parameters.
g	Asymmetry parameter.
C_{sca}, C_{abs}, C_{ext}, C_{Π}	Scattering, absorption, extinction and backscatter cross sections.
Q_{sca}, Q_{abs}, Q_{ext}	Scattering, absorption and extinction efficiencies.
G	Projected cross section.
$\bar{\omega}$	Single scattering albedo.
$\bar{k}$	Lidar ratio.
$\mathbf{E}$, $\mathbf{E}_{\parallel}$, $\mathbf{E}_{\perp}$	Electric field amplitude; electric field amplitudes parallel and perpendicular to the plane.
$\mathbf{B}$	Magnetic flux density.
$\mathbf{H}$	Magnetic field.
ϵ, μ	Permittivity and permeability.
ρ	Charge density; ray density.
$\mathbf{J}$	Current density.
c	Speed of light in vacuum.
∇	Del operator.
ω	Angular frequency.
λ	Wavelength.
t	Time.
m, $\hat{m}, \widetilde{m}$	Refractive index, complex refractive index, variant of complex refractive index.
$\hat{\tau}$	Surface normal.
$\hat{\mathbf{e}}_{\parallel}$, $\hat{\mathbf{e}}_{\perp}$	Unit vectors parallel and perpendicular to the plane.
i	Imaginary unit.
$\mathbf{r}$	Position vector of intersection between a line and a plane.
$\mathbf{x}$	A general position vector.
ζ, μ, ν	A general scalar multiple.
B	The set of beam vertices.

$\mathbf{b}$	The position vector of a beam vertex.
$\mathbf{v}$	The position vector of a crystal vertex.
$\mathbf{m}$	The position vector of a beam's mid point on a facet.
θ, ϕ	Scattering (zenith) angle and azimuthal angle.
I	Irradiance.
P	Power.
d	Distance travelled between two facets in an absorbing crystal.
A	Area of a beam.
$\mathbf{L}$	Rotation matrix.
Θ	A general rotation angle.
$r_\parallel,\ r_\perp,\ t_\parallel,\ t_\perp$	Fresnel amplitude coefficients.
$\mathbf{R},\ \mathbf{T}$	Fresnel Reflection and Transmission matrices.
F	Diffraction surface integral.
α, β, γ	Euler rotation angles.
$\mathbf{D}$	Diffraction amplitude matrix; electric displacement vector.
$\mathbf{M}$	Beam amplitude matrix; magnetisation field vector.
$\mathbf{S}$	Scattering amplitude matrix.
$\mathbf{P}$	Phase matrix; polarisation field vector.
x	Size parameter.

Chapter 1

Introduction

> Go on till you come to the end;
> then stop.
>
> Lewis Carroll,
> in Alice's Adventures in
> Wonderland

The actions of humans on the Earth's climate has almost certainly had a warming effect since the industrial revolution. The increased use of fossil-fuels, in conjunction with deforestation, has led to an increase in greenhouse gases and particulate matter in the atmosphere. This disruption to the Earth's radiation budget is still poorly understood and attempts to quantify it have come with the caveat of large uncertainties.

The role of clouds in the Earth's radiation balance has been the focus of intense research over the past few decades. A rich variety of clouds exist in nature, from the towering cumulonimbus to the saucer like lenticular, but for our purposes we restrict our attention to cirrus. Despite their somewhat innocuous appearance, due to their large global coverage (which is, on average, 70% in the tropics [1] and 30% at mid-latitudes [2]) their potential to alter the net radiative forcing could be significant. Indeed, the 2013 meeting of the Intergovernmental Panel on Climate Change (IPCC) [3] highlighted that "*the role of thin cirrus clouds for cloud feedback is not known and remains a source of possible systematic bias*". Therefore, if we are to better understand the Earth's climate system, we need to work to reduce these uncertainties.

Cirrus, see Figure 1.1, are high altitude clouds forming at altitudes above 6km. Due to their high altitude, water vapour freezes forming ice crystals which are in general nonspherical. While ice crystals can adopt complex structures their basic shapes are polyhedral, e.g. hexagonal prisms. The ambient environment in cirrus has a dominating effect on the type of ice crystal formed. The shape, size and orientation of ice crystals all affect their interaction with electromagnetic radiation, a process known as *scattering*. At some wavelengths, electromagnetic energy can be converted into heat in a process known as *absorption*. The combined effects of scattering and absorption is called *extinction*. The nonsphericity of ice crystals makes modelling their scattering properties problematic as exact solutions to Maxwell's

equations can either not be found, or are restricted to certain shapes and sizes. This has led to the development of numerical methods which seek to find approximate solutions.

Figure 1.1: Cirrus clouds over the Bay of Gibraltar

Investigatory methods into ice crystal habit have included: ground based capture of snow-flakes; ground based radar [4] and space based Lidar [5]; laboratory studies of ice crystal growth under a Scanning Electron Microscope [6, 7] and in cloud chambers; and ice analogue growth [8, 9] as well as *in-situ* measurements via direct [10] and indirect imaging [11]. Each of these methods has associated advantages and disadvantages, but combined they help to develop a somewhat comprehensive picture of ice crystal habits. Possible shapes include the simple hexagonal plate/ column and more complicated structures such as aggregates and rosettes. To further complicate matters, recent observations [11] have suggested that pristine structures are often distorted through surface roughness or deviations from their regular form. Despite this, on days where there is plentiful cirrus coverage we can often be treated to optical displays such as the 22° halo (Figure 1.2) or sun-dogs which are indicative of ice clouds comprised of effectively pristine hexagonal columns and plates.

Figure 1.2: A section of a 22° halo taken in Albufeira, Portugal

The Small Ice Detector (SID) *in-situ* probes employ an indirect technique, capturing the two-dimensional light scattering distribution over the angular range $6° - 25°$. This removes issues such as constrained depth of field which restrict the use of direct imaging probes to particles with sizes greater than 100μm. However they introduce the inverse scattering problem, i.e. the need to identify the particle through analysis of its scattering pattern. For this to be achieved, the use of large scattering pattern databases derived from known particle geometries and properties is required. In order for such databases to be made, versatile computational models are required which can determine the intensity of scattered light from a given particle over a given angular range. Unfortunately, the most accurate numerical methods are size-restricted to small particle sizes due to computational demands. The Ray-Tracing with Diffraction on Facets (RTDF) [12] model developed at the University of Hertfordshire has been used to generate such a database. The RTDF model marked a significant improvement on conventional ray tracing giving very good results when the particles modelled are in random orientation. However the rays used only have their intensity tracked, not their amplitude and phase, meaning that interference is neglected. It has been the endeavour of this project to develop a Beam Tracing model, where plane parallel beams and not rays will be traced. These beams will have their amplitude and phase traced allowing for interference to be modelled. This report will outline the theoretical aspects of Beam Tracing and how it is implemented within a hybrid light scattering model.

Chapter 2

Fundamentals of Electromagnetism and Light Scattering

> And God said, "Let there be light," and there was light.
>
> Genesis 1:3, The Bible

Modelling electromagnetic (EM) scattering requires an understanding of the underlying principles of electromagnetic theory. In this section we will briefly discuss all the necessary prerequisites, starting with Maxwell's equations and how these lead to the notion of a propagating, transverse wave; this naturally leads to polarisation. We finish the discussion on electromagnetism by examining the behaviour of an electromagnetic wave at a boundary.

Once the electromagnetic principles have been outlined we turn our attention to the topic of electromagnetic scattering. An overview is given and key concepts such as the amplitude scattering matrix, Stokes parameters and optical cross sections are defined. A short review of computational methods is also given with emphasis on Ray Tracing and we close the discussion by introducing Beam Tracing.

2.1 Maxwell's Equations

Classical electromagnetism is described by the four Maxwell equations and the Lorentz force. The Maxwell equations in differential form describe the nature of the electric field $\mathbf{E}$ and the magnetic flux density $\mathbf{B}$ in terms of spatial and temporal derivatives along with two fundamental constants. These constants ϵ_0 and μ_0 are called the *permittivity* and *permeability* of free space respectively. In the presence of charges one also needs to define the charge density ρ and the current density $\mathbf{J}$. While the Maxwell equations can also be described in integral form, this restricts their use to localised regions (i.e. regions bound by a surface). The microscopic Maxwell equations in differential form are:

$$\nabla \cdot \mathbf{E} = \frac{\rho}{\epsilon_0}, \tag{2.1a}$$

$$\nabla \cdot \mathbf{B} = 0, \tag{2.1b}$$

$$\nabla \times \mathbf{E} = -\frac{\partial \mathbf{B}}{\partial t}, \tag{2.1c}$$

$$\nabla \times \mathbf{B} = \mu_0 \mathbf{J} + \epsilon_0 \mu_0 \frac{\partial \mathbf{E}}{\partial t}. \tag{2.1d}$$

These four equations are commonly known as Gauss's law for the electric field; Gauss's law for the magnetic field; Faraday's law and the Ampère-Maxwell law. An electromagnetic field will induce an effect in the medium with which it is interacting. The electric displacement $\mathbf{D}$ and magnetic field $\mathbf{H}$ are defined as:

$$\mathbf{D} = \epsilon_0 \mathbf{E} + \mathbf{P}, \tag{2.2a}$$

$$\mathbf{H} = \frac{1}{\mu_0} \mathbf{B} - \mathbf{M}, \tag{2.2b}$$

where $\mathbf{P}$ and $\mathbf{M}$ are the electric and magnetic polarisation fields, i.e. the sum of all the microscopic induced moments within the medium. The macroscopic fields $\mathbf{D}$ and $\mathbf{H}$ include induced effects and allow one to write the Maxwell equations in macroscopic form:

$$\nabla \cdot \mathbf{D} = \rho_f, \tag{2.3a}$$

$$\nabla \cdot \mathbf{B} = 0, \tag{2.3b}$$

$$\nabla \times \mathbf{E} + \frac{\partial \mathbf{B}}{\partial t} = 0, \tag{2.3c}$$

$$\nabla \times \mathbf{H} - \frac{\partial \mathbf{D}}{\partial t} = \mathbf{J}_f. \tag{2.3d}$$

Here the subscript f denotes the current and charge densities that are not bound by the medium. Ice crystals are electrically neutral ($\rho_f = 0$) and non-conducting ($\mathbf{J}_f = 0$) and as such the macroscopic Maxwell equations reduce to four linear, homogeneous partial differential equations. Solving the reduced equations is possible through numerical methods such as the Finite Difference Time Domain (FDTD) and the Discrete Dipole Approximation (DDA), which are discussed in Section 2.7.

Taking the curl of Equation 2.1c, making use of the vector identity $\nabla \times (\nabla \times \mathbf{E}) = \nabla(\nabla \cdot \mathbf{E}) - \nabla^2 \mathbf{E}$ and invoking the free space approximation ($\nabla \cdot \mathbf{E} = 0$) yields the following vector wave equation:

$$\nabla^2 \mathbf{E} = \epsilon_0 \mu_0 \frac{\partial^2 \mathbf{E}}{\partial t^2}. \tag{2.4}$$

This wave equation pertains to a transverse propagating wave with velocity

$$c = \frac{1}{\sqrt{\epsilon_0 \mu_0}} = 2.998 \times 10^8 \text{ ms}^{-1}, \tag{2.5}$$

known as the *speed of light*. The electric and magnetic fields are perpendicular to each other and both are perpendicular to the direction of propagation. Furthermore, the magnitude of the $\mathbf{E}$ field is proportional to the magnitude of the $\mathbf{B}$ field with the proportionality constant being c. We note the following relation for plane waves:

$$\mathbf{B} = \frac{1}{c} \mathbf{k} \times \mathbf{E}, \tag{2.6}$$

where $\mathbf{k}$ is the *wave-vector*, which points in the direction of propagation for homogeneous waves. Equation 2.6 allows us to model only the electric or magnetic field. It is customary to choose the electric field and this convention is maintained in this piece of work.

2.2 The Electric Field and Polarisation

Assuming a time harmonic incident electromagnetic wave, the amplitude of the electric field at some point $\mathbf{x}$ at a time t is given by

$$\mathbf{E}(\mathbf{x}, t) = \mathrm{Re}\{\mathbf{E}_0 \exp[\mathrm{i}(\mathbf{k} \cdot \mathbf{x} - \omega t)]\}, \tag{2.7}$$

where $\mathrm{i} = \sqrt{-1}$ is the imaginary unit, $\mathbf{E}_0$ is the complex electric field amplitude and $\mathrm{Re}\{\cdot\}$ denotes the real part of the bracketed quantity. The angular frequency in time is given by ω and the angular frequency in space is given by the *wave-number* $|\mathbf{k}| = k = 2\pi/\lambda$ with λ being the wavelength. As the wave is transverse, the wave vector is not a sufficient means of describing the wave. Since the electric field oscillates in time we can describe an additional property of the wave known as *polarisation* by the locus of the tip drawn out over time by the electric vector on an arbitrary fixed plane, known as the *polarisation plane*. Decomposing the electric field into components parallel and perpendicular to the incidence plane provides the mechanism for determining the polarisation state. Consider the case where the two components are in phase, but their amplitudes vary in time. The resulting electric field vector would sweep out a straight line of varying length, hence yielding *linearly* (or plane) polarised light. Alternatively, if the two components are out of phase by $\pi/2$ but have equal amplitude then the electric field vector will trace out a circle thus giving rise to *circular* polarisation. Such situations are special cases and in general the two components have different amplitudes and phases resulting in *elliptical* polarisation. Natural light from the sun is *unpolarised* which means that there is no preference in the polarisation state of the wave.

A detector recording the properties of incident radiation may detect both circularly and linearly polarised light within a majority of unpolarised light. This leads to the idea of *partially polarised* light which, when quantified, can be thought of as being the proportion of the detected light which is polarised in a particular way. The amount, or degree, of polarisation is an important quantity that can be calculated in some light scattering models. A property of dielectrics is that they can alter the polarisation state of a wave through scattering and as such the scattering process undergone by light with an ice crystal can be considered a polarising mechanism. The fact that scattering by ice crystals can affect the polarisation state of an incident wave means that measuring the change in polarisation can be used as a technique for identifying ice crystals, see e.g. [13].

To close this discussion we note that within electromagnetic scattering the time dependence is suppressed by removing the time harmonic factor $\exp(-\mathrm{i}\omega t)$. The negative in the exponential ensures that the imaginary part of the refractive index is positive. With the time dependence removed we have an expression for the amplitude of the electric field:

$$\mathbf{E}(\mathbf{x}) = \mathrm{Re}\{\mathbf{E}_0 \exp(\mathrm{i}\mathbf{k} \cdot \mathbf{x})\}, \tag{2.8}$$

which is assumed throughout this report.

2.3 Electromagnetic Waves at a Boundary

When an electromagnetic wave encounters a boundary between two media it is split (assuming no total reflection) into reflected and transmitted components. Denoting the wave vectors of these components as $\mathbf{k}^i$, $\mathbf{k}^r$ and $\mathbf{k}^t$ respectively and the outward surface normal as $\hat{\tau}$, we can construct a diagram such as the one shown in Figure 2.1. The angles ϑ_i, ϑ_r and ϑ_t are called the angles of incidence, reflection and transmission. The laws of reflection and refraction can both be derived from Fermat's principle of least time and can be found in most optics texts, e.g. [14]. The law of reflection states that the angle of reflection is equal to the angle of incidence, that is $\vartheta_i = \vartheta_r$. For transmission one uses Snell's law,

$$m_1 \sin\vartheta_i = m_2 \sin\vartheta_t, \tag{2.9}$$

with m_1 and m_2 being the refractive indices, which for now are considered real. Complex refractive indices, which describe an absorbing medium, are discussed later. For cases where $m_1 > m_2$ such as light travelling from ice into air one can encounter the phenomenon of *total internal reflection* where no transmitted component arises. This occurs when the angle of incidence is greater than the so-called *critical angle*, which for the ice-air situation discussed so far is:

$$\vartheta_c = \arcsin\left(\frac{m_2}{m_1}\right) \rightarrow \vartheta_{c,\text{ice}} \simeq 49.8^\circ. \tag{2.10}$$

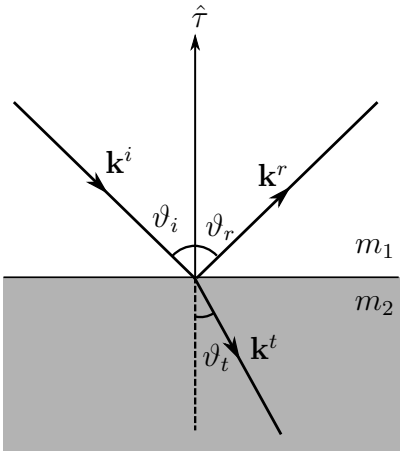

Figure 2.1: The direction vectors associated with incidence, reflection and transmission at a boundary.

At the interface there are certain boundary conditions which have to be satisfied, given in Equations 2.11a - 2.11d for the case where there are no surface charges or currents. These pertain to the continuity of the tangential component of $\mathbf{E}$ and $\mathbf{H}$ as well as the normal component of $\mathbf{D}$ and $\mathbf{B}$ to the surface [15]:

$$\hat{\tau} \times (\mathbf{E}_1 - \mathbf{E}_2) = 0, \tag{2.11a}$$
$$\hat{\tau} \times (\mathbf{H}_1 - \mathbf{H}_2) = 0, \tag{2.11b}$$

$$\hat{\tau} \cdot (\mathbf{D}_1 - \mathbf{D}_2) = 0, \tag{2.11c}$$
$$\hat{\tau} \cdot (\mathbf{B}_1 - \mathbf{B}_2) = 0, \tag{2.11d}$$

where the subscripts denote the amplitude of the field in the first and second medium. We define the *plane of incidence* as the plane containing the three wave vectors and the boundary surface normal. Polarised light can be split into components parallel and perpendicular to the incidence plane. Considering the two cases where the electric field is entirely polarised parallel and perpendicular to it while invoking the above boundary conditions one arrives at the four *Fresnel equations* [14].

$$r_\perp = \left(\frac{E_r}{E_i}\right)_\perp = \frac{m_1 \cos\vartheta_i - m_2 \cos\vartheta_t}{m_1 \cos\vartheta_i + m_2 \cos\vartheta_t}, \tag{2.12a}$$
$$r_\parallel = \left(\frac{E_r}{E_i}\right)_\parallel = \frac{m_2 \cos\vartheta_i - m_1 \cos\vartheta_t}{m_2 \cos\vartheta_i + m_1 \cos\vartheta_t}, \tag{2.12b}$$
$$t_\perp = \left(\frac{E_t}{E_i}\right)_\perp = \frac{2m_1 \cos\vartheta_i}{m_1 \cos\vartheta_i + m_2 \cos\vartheta_t}, \tag{2.12c}$$
$$t_\parallel = \left(\frac{E_t}{E_i}\right)_\parallel = \frac{2m_1 \cos\vartheta_i}{m_2 \cos\vartheta_i + m_1 \cos\vartheta_t}. \tag{2.12d}$$

The two reflection terms, $r_\parallel$ and $r_\perp$ are known as the *reflection amplitude coefficients* and describe the ratio of the reflected field polarised parallel and perpendicular to the incident field respectively. Likewise, the two transmission terms, $t_\parallel$ and $t_\perp$ are called the *transmission amplitude coefficients* and quantify the ratio of the transmitted field to the incident field. A plot of the four amplitude coefficients for an air-ice interface with refractive indices of $m_1 = 1$ and $m_2 = 1.31$ is given in Figure 2.2.

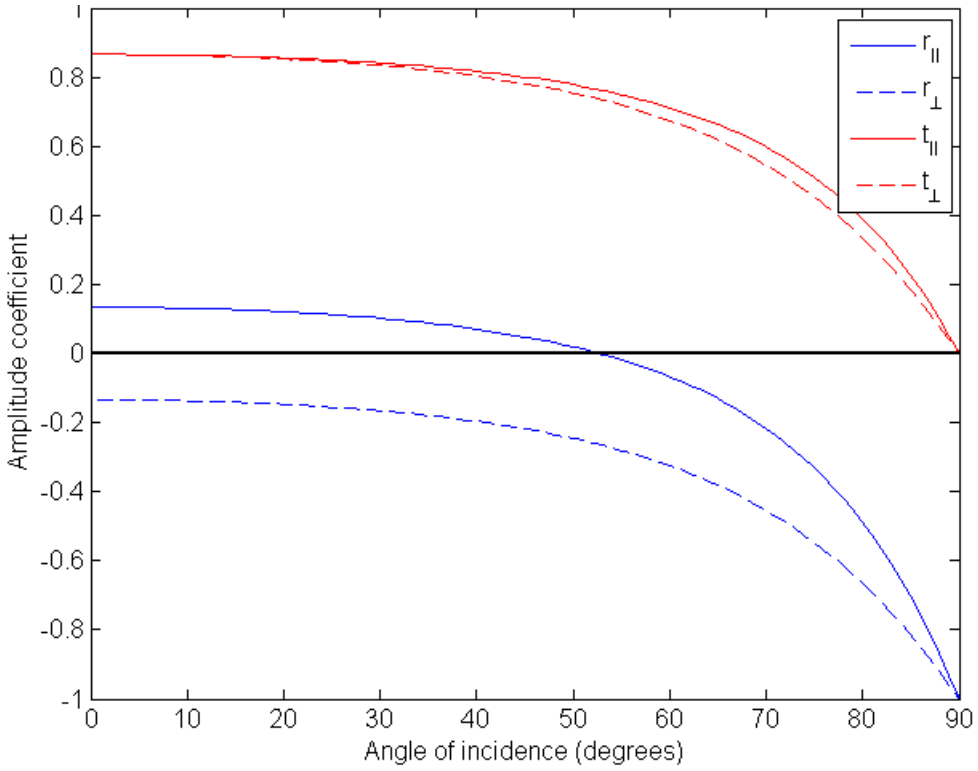

Figure 2.2: Amplitude coefficients for light incident on an air-ice interface. The incident light has a wavelength of $\lambda = 0.532\mu m$ leading to refractive indices of $m_1 = 1$ and $m_2 = 1.31 + 0.0\text{i}$ (the imaginary part has been ignored here).

2.4 Electromagnetic Scattering

Electromagnetic scattering and absorption, is the umbrella term covering the modification of an electromagnetic wave by an obstacle. That obstacle may be a single particle, an aggregate or a collection of particles. Electromagnetic scattering as a technique has been utilised in several fields including medicine, astronomy and atmospheric science among many others.

When considering electromagnetic scattering, it is sufficient to only consider the modification of the electric field, since the magnetic field follows directly from it, see Equation 2.6. It has become tradition almost to view scattering as a three stage process. A wave is incident on an obstacle, this wave then interacts with the particle and is changed in some way. The emerging wave (formed through excitation and reradiation) is then viewed as the *scattered wave*. This interpretation of scattering is shown in Figure 2.3.

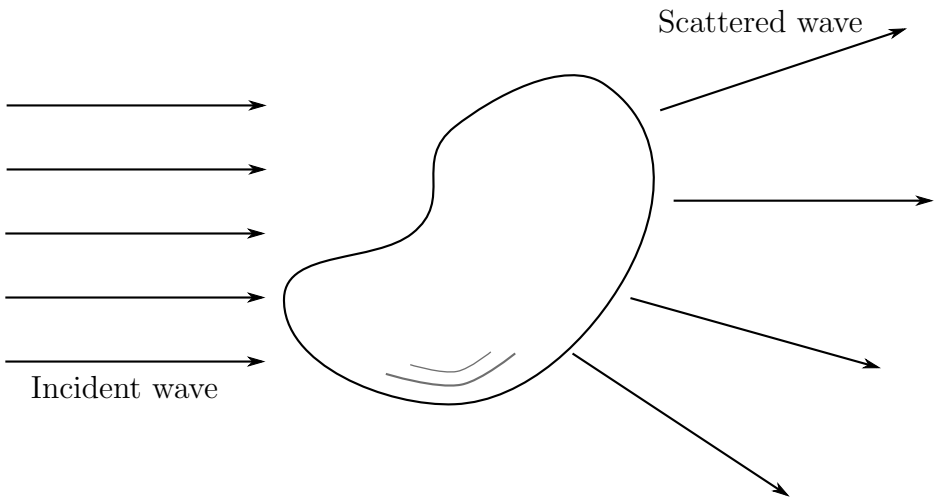

Figure 2.3: The 'traditional' view of electromagnetic scattering, the incident wave is changed by the presence of an obstacle into the scattered wave.

This view of scattering is somewhat artificial and in actuality one measures a modification of the field. In other words, one first takes a recording without the scattering particle being present ($\mathbf{E}^{\text{inc}}$) and then a measurement with it present ($\mathbf{E}^{\text{tot}}$). The difference between the measurements gives an indication of the scattered field ($\mathbf{E}^{\text{sca}}$) and we write:

$$\mathbf{E}^{\text{sca}} = \mathbf{E}^{\text{tot}} - \mathbf{E}^{\text{inc}}. \tag{2.13}$$

Note how this differs from the 'traditional' view of scattering where there was a propagating scattered wave. In this version the scattered field only exists as a modification of the entire electric field, rather than a separate entity. The merits of this view are discussed in the literature, see [16].

2.5 Amplitude Scattering Matrices

Maxwell's equations imply a linearity between the incident and scattered fields allowing the use of matrices in describing the transformation. The use of amplitude matrices to describe the change in electric field amplitude can be attributed to Jones [17]. If the waves under consideration are completely polarised with coherent orthogonal components then one can use the so-called *Jones calculus* [18]. It is therefore necessary to decompose the fields parallel and perpendicular to the *scattering plane* which contains the direction vectors corresponding to incidence and scattering.

$$\mathbf{E}^i = E^i_{\parallel}\hat{\mathbf{e}}^i_{\parallel} + E^i_{\perp}\hat{\mathbf{e}}^i_{\perp}, \tag{2.14}$$

where $\hat{\mathbf{e}}^i_{\parallel}$, $\hat{\mathbf{e}}^i_{\perp}$ are orthogonal unit vectors parallel and perpendicular to the scattering plane; $E^i_{\parallel}$, $E^i_{\perp}$ are the amplitudes of the incident electric field in these directions. An analogous expression for the wave which emerges is:

$$\mathbf{E}^s = E^s_{\parallel}\hat{\mathbf{e}}^s_{\parallel} + E^s_{\perp}\hat{\mathbf{e}}^s_{\perp}. \tag{2.15}$$

The two unit vectors $\hat{\mathbf{e}}_{\parallel}$ and $\hat{\mathbf{e}}_{\perp}$ are related to the direction of propagation via:

$$\hat{\mathbf{k}} = \frac{\hat{\mathbf{e}}_{\perp} \times \hat{\mathbf{e}}_{\parallel}}{||\hat{\mathbf{e}}_{\perp} \times \hat{\mathbf{e}}_{\parallel}||^2}, \tag{2.16}$$

where $||\cdot||$ denotes the inner product. For a fixed plane of observation it follows that a matrix relating Equations 2.14 and 2.15 is given by:

$$\begin{pmatrix} E^s_{\parallel} \\ E^s_{\perp} \end{pmatrix} = \begin{pmatrix} S_{11} & S_{12} \\ S_{21} & S_{22} \end{pmatrix} \begin{pmatrix} E^i_{\parallel} \\ E^i_{\perp} \end{pmatrix}, \tag{2.17}$$

where the elements in the matrix are in general non-zero and complex. In its original form described by Jones the matrix would be the product of several matrices relating to polarisers and retarders within an optical system. For applications in atmospheric scattering we pre-multiply the above matrix by a factor pertaining to an outgoing spherical wave since this is the form of the scattered wave. The *amplitude scattering matrix* is given by [19]:

$$\begin{pmatrix} E^s_{\parallel} \\ E^s_{\perp} \end{pmatrix} = \frac{\exp(\mathrm{i}kR)}{-\mathrm{i}kR} \begin{pmatrix} S_2(\theta,\phi) & S_3(\theta,\phi) \\ S_4(\theta,\phi) & S_1(\theta,\phi) \end{pmatrix} \begin{pmatrix} E^i_{\parallel} \\ E^i_{\perp} \end{pmatrix}, \tag{2.18}$$

where R is the distance from the centre of the scattering object to the point of observation, θ and ϕ are the scattering (zenith) angle and azimuthal angle respectively. The division by the wavenumber serves to make the transformation matrix dimensionless. Equation 2.18 relates the incident electric field amplitudes parallel and perpendicular to the scattering plane to the corresponding field amplitudes of the scattered wave. In this work the direction of external incidence is fixed as $\hat{\mathbf{k}}^i_0 = [0, 0, -1]^T$ and as such the scattering plane is only determined by the azimuthal angle ϕ.

An advantage of using the scattering plane is that there exist relationships between the elements of the amplitude scattering matrix and the phase matrix which provides an analogous transformation for the Stokes parameters.

2.6 Stokes Parameters, the Scattering Matrix and Scattering Cross Sections.

The 4×4 *phase matrix*, $\mathbf{P}(\theta, \phi)$ transforms the incident Stokes parameters to those associated with the scattered field. The advantage of using this approach is that unpolarised light can be modelled but at a cost of losing phase information. The Stokes parameters I, Q, U, V are usually written as a column vector $\mathbf{I}$. The phase matrix is therefore the Mueller matrix that transforms the incident Stokes vector to the scattered Stokes vector [19]:

$$\begin{pmatrix} I^s \\ Q^s \\ U^s \\ V^s \end{pmatrix} = \frac{1}{k^2 R^2} \begin{pmatrix} P_{11} & P_{12} & P_{13} & P_{14} \\ P_{21} & P_{22} & P_{23} & P_{24} \\ P_{31} & P_{32} & P_{33} & P_{34} \\ P_{41} & P_{42} & P_{43} & P_{44} \end{pmatrix} \begin{pmatrix} I^i \\ Q^i \\ U^i \\ V^i \end{pmatrix}. \tag{2.19}$$

The first Stokes parameter I gives the intensity of the light and the remaining three all contain information regarding the polarisation state. Each parameter can be related to the time averaged electric field amplitude given with respect to the scattering plane [19]:

$$I = \langle E_\parallel E_\parallel^* + E_\perp E_\perp^* \rangle, \tag{2.20a}$$
$$Q = \langle E_\parallel E_\parallel^* - E_\perp E_\perp^* \rangle, \tag{2.20b}$$
$$U = \langle E_\parallel E_\perp^* + E_\perp E_\parallel^* \rangle, \tag{2.20c}$$
$$V = \mathrm{i}\langle E_\parallel E_\perp^* - E_\perp E_\parallel^* \rangle. \tag{2.20d}$$

Unpolarised light of unit intensity has the form $(1, 0, 0, 0)^T$ corresponding to $Q = U = V = 0$. The degree of elliptical polarisation is given by:

$$p = \frac{(Q^2 + U^2 + V^2)^{\frac{1}{2}}}{I} \tag{2.21}$$

which by definition must be less than or equal to one (corresponding to light which is fully polarised). For natural light, $p = 0$.

The elements of the phase matrix can be calculated from the amplitude scattering matrix through sixteen equations, two of which are given in Equations 2.22a and 2.22b. The full list is given in Appendix B.2.

$$P_{11} = \frac{1}{2}(|S_2|^2 + |S_3|^2 + |S_4|^2 + |S_1|^2), \tag{2.22a}$$
$$P_{12} = \frac{1}{2}(|S_2|^2 - |S_3|^2 + |S_4|^2 - |S_1|^2), \tag{2.22b}$$

where the product $|S_i|^2 = S_i \cdot S_i^*$ with the asterisk denoting the complex conjugate. The P_{11} element will be discussed frequently in this work as it describes the angular intensity distribution of the scattered light. It is normalised so that the integral over all solid angles is unity, that is:

$$\frac{1}{4\pi} \int_{\phi=0}^{\phi=2\pi} \int_{\theta=0}^{\theta=\pi} P_{11}(\theta, \phi) \sin\theta \mathrm{d}\theta \mathrm{d}\phi = 1. \tag{2.23}$$

This normalisation permits the interpretation of P_{11} as a probability distribution describing the probability of light being scattered into a given direction. When a large number of different, fixed orientations are used P_{11} is orientationally averaged to model scattering by a randomly oriented particle. This removes the ϕ dependency leaving only a dependency on the scattering angle θ. This distribution is known as the *phase function*.

Due to the large number of variables which are inputted into climate models, it is necessary to use parameterisations. For example, it would be computationally demanding to give the phase function for a range of ice crystal shapes found in cirrus. Instead one uses the *asymmetry parameter* g which is the weighted average of the P_{11} element:

$$g = \int_{\theta=0}^{\theta=\pi} P_{11}(\theta) \cos\theta \mathrm{d}\theta. \tag{2.24}$$

The asymmetry parameter takes values in the range $-1 \leq g \leq 1$ and describes whether more light is scattered in the forward ($g > 0$) than in the backward ($g < 0$) direction. For atmospheric ice crystals their transparency combined with the effects of external diffraction mean that the asymmetry parameter is always positive.

The degree of linear polarisation (dlp) is a special case of Equation 2.21 with $V = 0$. It describes how the scattered light is polarised with respect to the scattering plane and is given by:

$$\text{dlp} = -\frac{P_{12}}{P_{11}}. \tag{2.25}$$

It has values in the range $[-1, 1]$ with negative values implying horizontal polarisation and positive values implying vertical polarisation.

There are three cross sections corresponding to absorption, scattering and extinction, each with units of area. They are imaginary areas such that if multiplied by the incident wave's irradiance one would retrieve the power absorbed, scattered and the combined effect. The relation,

$$C_{\text{ext}} = C_{\text{sca}} + C_{\text{abs}} \tag{2.26}$$

is therefore an expression of energy conservation. For non absorbing particles $C_{\text{sca}} = C_{\text{ext}}$ and Equation 2.26 becomes

$$C_{\text{ext}} = C_{\text{sca}}. \tag{2.27}$$

Dividing the scattering cross sections by the particle's projected area G yields the scattering efficiencies $Q_{\text{abs}},\ Q_{\text{sca}},\ Q_{\text{ext}}$. As in Equation 2.26 we have:

$$Q_{\text{ext}} = Q_{\text{sca}} + Q_{\text{abs}} \tag{2.28}$$

which has the interesting property that:

$$\lim_{x \to \infty} Q_{\text{ext}} = 2, \tag{2.29}$$

where x is the size parameter (see Appendix B.2). This result is known as the *extinction paradox* and is usually written in terms of the extinction cross section,

$$\lim_{x \to \infty} C_{\text{ext}} = 2G. \tag{2.30}$$

Physically this states that as the particle size becomes sufficiently large, twice as much energy is removed by the particle as is incident upon it [20]. From the physical optics point of view we interpret this as external diffraction removing an amount G from the incoming wave and an additional amount G being removed by transmission/ reflection.

The extinction cross section can be found through direct application of the optical theorem which states that the particle extinction cross section is related to the imaginary part of the scattering amplitude f in the forward direction [21],

$$C_{\text{ext}} = \frac{4\pi}{k}\text{Im}\{f(0)\}. \tag{2.31}$$

While this is the traditional form of the optical theorem, it assumes that the scattering amplitude function has units of $[\mathrm{L}^{-1}]$ which is not the case for the scattering amplitude matrix. We therefore note the following form of the optical theorem [22]

$$C_{\text{ext}} = \frac{4\pi}{k^2}\text{Re}\{S_2(0)\}, \tag{2.32}$$

where $S_2(0)$ is the upper left element of the amplitude scattering matrix given in Equation 2.18 in the direction $\theta = 0°$. Note that for direct forward and backward scattering there is no azimuthal angle ϕ.

The ratio between the scattering cross section and the extinction cross section defines the *single scattering albedo*:

$$\bar{\omega} = \frac{C_{\text{sca}}}{C_{\text{ext}}}. \tag{2.33}$$

By definition $\bar{\omega} \leq 1$. In essence it is a statistical measurement of the probability that a given interaction will lead to scattering rather than absorption. Much like the asymmetry parameter it is of great interest in radiative transfer investigations. Calculation of the single scattering albedo is not the only use of the optical cross sections, in their own right they are of much use in remote sensing observations. As lidar records backscattered light, an additional cross section is used known as the backscatter cross section C_{Π} which has units of area per solid angle. It can be used to determine the backscattered power per steradian. Defining the backscattered efficiency as Q_{Π}, in the same way as with the other efficiencies, we can define the *backscatter-to-extinction ratio* as:

$$\bar{k} = \frac{Q_{\Pi}}{Q_{\text{ext}}}. \tag{2.34}$$

The reciprocal of $\bar{k}$ is commonly found in the literature and is known as the *lidar ratio*. By taking measurements of $\bar{k}$ at different wavelengths one is able to estimate the particle size distribution within the volume of atmosphere being investigated [23].

2.7 An Overview of Computational Techniques

The nonsphericity of atmospheric ice crystals has led to the development of various computational techniques to evaluate their light scattering properties. No single method is capable of being applied across the entire range of particle sizes and shapes observed in cirrus, and it is likely that this will always be the case. In this section we briefly review some methods available to the community such as T-Matrix and the Discrete Dipole Approximation.

2.7.1 Separation of Variables Method and Lorenz-Mie Theory

The Separation of Variables Method (SVM) is a general method of solving partial differential equations. Specifically applied to light scattering it provides exact analytical solutions for particles where the surfaces can be made to coincide with coordinate surfaces. The need to match coordinate surfaces with crystal surfaces

limits the applicability to spheroidal particles, which have been used as proxies for non-spherical particles, but have been shown to be an inaccurate approximation [24–26]. The electric and magnetic fields are represented by Vector Spheroidal Wave Functions (VSWFs) which are given by infinite series. In order to be applied computationally these series must be truncated meaning that accuracy is dependent on the number of terms used. Parameters such as size, frequency and the refractive index of the medium being investigated must all be considered when determining the summation cut off index.

The method can be applied to multiple scattering systems. Each particle is assigned its own local coordinate system and rotation and translation addition theorems for VSWFs are applied. Note that due to SVM giving exact analytical solutions it is ideal for benchmarking.

Scattering by a dielectric sphere was solved independently by Mie [27] and Lorenz. The solution has become known as *Lorenz-Mie Theory*. In effect it is a special case of the SVM where the particle is spherical, rather than spheroidal. Vector Spherical Harmonic Functions (VSHFs) are used instead of their spheroidal counterparts. The relative simplicity of implementing the Lorenz-Mie solution computationally has led to it being applied across a wide range of applications from biological [28] to astronomical [29].

2.7.2 T-Matrix

Waterman [30] devised the *T-matrix* method, which is in essence an extension of the SVM to non-spherical particles. Much like in SVM, the incident and scattered waves are expressed as VSHFs and the relationship between them is the T-matrix. Because of the expression of fields as infinite series, one can encounter truncation errors if not enough terms are used, which is complicated further by each term in the T-matrix requiring a different number of terms in order to achieve good accuracy. The T-matrix method can be considered numerically exact, its accuracy being affected only by computational factors and not because of inherent assumptions. It is the summations which consume most of the CPU time and therefore limit its applicability.

The T-matrix method depends only on the physical and geometric properties of the particle, e.g. its shape, orientation, refractive index and size. It is completely independent of the incident and scattered fields. As such, a particle's T-matrix need only be calculated once and then it can be used for any polarisation and incidence direction. This property means that it has been used in the creation of extensive databases of non-spherical particles in random orientation [31, 32]. However, the T-matrix method does suffer from poor numerical stability when the particle is much larger than the wavelength, if the particle has extreme geometries (such as for spheroids) or if the particle has a large real or imaginary part of the refractive index.

Recently, the *invariant imbedding T-matrix* [33] method was used by Bi et al. [34,35] to model light scattering by non-spherical particles and aggregates of columns. This method discretizes the scattering volume as a series of inhomogeneous spherical lay-

ers, in the sense that a given layer has regions of differing refractive index. The total T-matrix for the system is derived from the individual layers' T-matrices.

2.7.3 Discrete Dipole Approximation

The Discrete Dipole Approximation (DDA) was devised by Purcell and Pennypacker [36] and developed by Draine [37] who applied it to non-spherical astronomical dust grains using the DDSCAT code. The particle volume is discretised as a grid of polarisable dipoles, each of which has an associated complex polarisability tensor. An incident harmonic wave drives these dipoles and the field at each grid point is evaluated, taking into consideration the radiated field from all the other dipoles. This leads to a system of linear equations that are solved numerically to find the value of the dipole moment at each grid point. Once known, further parameters can be derived from other relations. Convergence is not always guaranteed and the technique is notoriously computationally demanding, becoming more demanding as the number of dipoles is increased. A rule of thumb for choosing the number of dipoles is ten per wavelength [38]. As with T-matrix, the DDA method is size limited.

The Amsterdam-DDA (ADDA) code developed by Hoekstra and Sloot [39] and improved by Yurkin et al. [40] is a modernised DDA implementation. It has been widely applied by researchers in the atmospheric community, see e.g. [40–42]. Comparisons between DDSCAT and ADDA (among others) were performed by Penttilä et al. [43] where it was found that while DDSCAT is slightly more accurate, it offers far less versatility than ADDA. Reviews of DDA and ADDA can be found in [38,40].

2.7.4 Finite Difference Time Domain

The discretisation in the Finite Difference Time Domain (FDTD) method is a grid mesh, as opposed to a dipole discretisation used in DDA. At each grid point material properties are assigned. The solutions to the scattering problem are given in the time domain, these are then transformed into the frequency domain before being mapped to the far-field via either a surface integral or a volume integral. By working in the time domain, rather than the frequency domain, the problem is transformed from a boundary value problem to an initial value problem. The method was pioneered by Yee [44] and sees the Maxwell curl equations discretised using a finite difference scheme. A time marching iteration is used and a convergent scattered field is achieved when a steady state field is established at each grid point (assuming a sinusoidal incident field).

Like in the DDA method the accuracy of FDTD is affected by the mesh resolution. Errors of less than 3% (compared to exact solutions for spheres) have been achieved when the grid spacing was $(1/20)\lambda$; this reduces to less than 1% when the spacing is reduced by a factor of two [45, 46]. These errors are partly due to a stair-casing effect which stems from modelling a sphere with a rectangular mesh (an issue which also arises in DDA computations). Further errors in FDTD implementations arise from incorrect artificial boundary conditions which serve to truncate the scattered wave at the edge of the computational domain. This absorbing boundary condition

must not reflect the scattered wave as this reflected wave would then interfere with the scattered near field leading to errors.

2.7.5 Boundary Element Method

The Boundary Element Method (BEM) reformulates the electromagnetic transmission problems into a set of Boundary Integral Equations [47, 48]. The technique is most easily applied to scattering problems where the surrounding medium is homogeneous as this leads to a finite computational domain, i.e. the interface between the two regions. To formulate the problem two domains are defined, one within the scatterer, and one outside of it. Then, the incident and scattered fields are written in terms of their unknown values on the boundary by means of a single-layer potential operator and the Dirichlet and Neumann traces are applied leading to four boundary integral equations. Solutions to these equations can in turn be used to derive an amplitude scattering matrix [49]. Common techniques for solving such equations include *the collocation method* and *Galerkin's* method.

Direct application of BEM to electromagnetic scattering has been largely overlooked, and where it has been applied it has been to small particle size parameters of the order $x \leq 15$, this is due to its high computational demand. Groth et al. [22] used a particular formulation of BEM called BEM++ on a range of small particle shapes including spheres, hexagonal columns and rosettes.

2.8 Geometric Optics Approximation and Hybrid Methods

The Geometric Optics approximation (GO) represents wave propagation using rays, mathematical constructs perpendicular to the wavefront which point in the direction of propagation. It can be applied to objects which are much larger than the wavelength of the incident light (a 'rule of thumb' is that GO can only really be applied to particles with size parameters of $x \geq 100$). The basic idea is that rays encounter the interface between two media such as air and ice. At this boundary surface, the rays are reflected and refracted according to the law of reflection and Snell's law; the change in amplitude being determined by Fresnel's equations, see Section 2.3. One then assumes that the total field at a point is equal to the sum of the electric fields linked to all rays which have passed through that point.

In this section the key principles behind geometric optics will be outlined along with some nomenclature. We will also discuss certain hybrid methods that have been developed, before finishing with a brief introduction to the idea of Beam Tracing.

2.8.1 Ray Tracing

Ray Tracing's strength lies in its simplicity. In a ray tracing program like [50], a user defined number of parallel rays, simulating a plane wave, are 'launched' at a particle from a pre-defined plane at random coordinates within this plane. Each

ray is assigned a pair of polarisation direction vectors, a propagation direction and its initial physical properties using either a Stokes or amplitude vector. The change in these properties, due to the particle, as the ray propagates is described by either the Mueller or Jones matrix (see Equations 2.19 and 2.18 respectively). The matrix describing the effect the particle has on the incident light is therefore found by calculating the respective reflection and refraction matrices for each ray-surface interaction event. For each interaction (assuming no total internal reflection) two new rays are spawned, one for the transmitted ray and one for the reflected ray. Externally reflected rays and outward refracted rays are removed from the process. Their respective amplitude or phase matrices are rotated into the scattering plane and added to the existing matrix for the scattering angle. This process of division is repeated until a pre-determined cut-off is reached, which can take the form of an energy cut-off or a maximum ray-recursion cut-off. In keeping with Van de Hulst [51] the number of ray-recursions is denoted by p, where $p = 1$ would correspond to external reflection only; $p = 2$ would be allowing for one transmission and $p = 3$ would include a single internal reflection etc., see Figure 2.4.

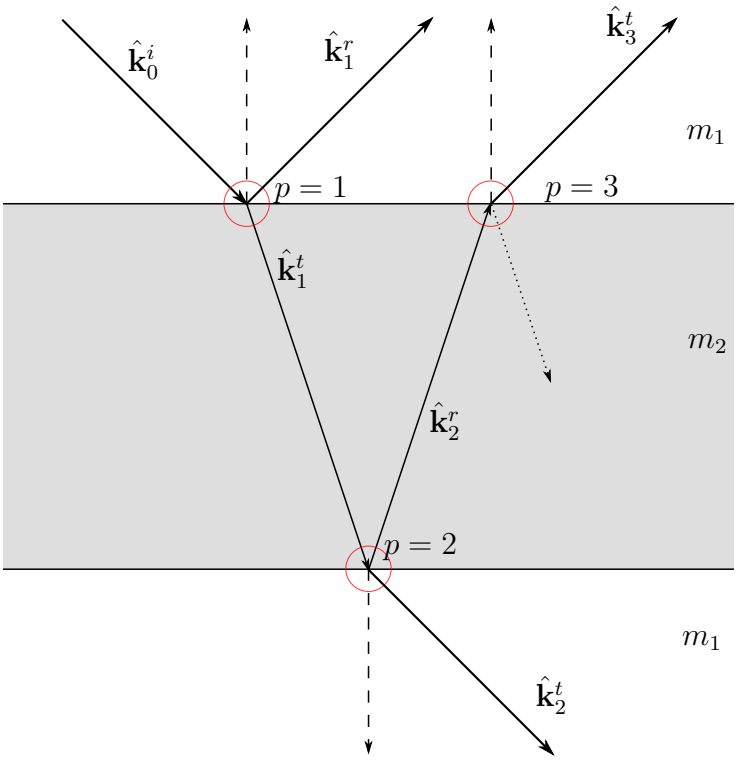

Figure 2.4: Rays at a boundary between two media with real refractive indexes m_1 and m_2 with $m_2 > m_1$. At each reflection / refraction event, two rays are spawned, those rays which leave the medium carry energy away with them. The dashed lines represent the local, outward facing surface normals.

A typical ray-surface interaction is shown in Figure 2.1. In accordance with the law of reflection the angle of incidence ϑ_i is the same as the angle of reflection ϑ_r. As

such, the unit vector in the direction of the reflected ray is [52]:

$$\hat{\mathbf{k}}^r = \hat{\mathbf{k}}^i - 2(\hat{\mathbf{k}}^i \cdot \hat{\tau})\hat{\tau}. \tag{2.35}$$

The transmitted ray is bent towards the surface normal due to the change in medium (here, $m_2 > m_1$). The direction of transmission is given by [52]:

$$\mathbf{k}^t = \frac{m_1}{m_2}(\hat{\mathbf{k}}^i - \cos\theta_i\hat{\tau}) \pm \cos\theta_t\hat{\tau}. \tag{2.36}$$

The plus-minus ensures that the equation holds when the transmitted ray is going from the crystal back into the surrounding medium. In cases of total internal reflection no transmitted ray is formed.

The main advantage of Ray Tracing is that it is computationally cheap and can be readily applied to complex particle shapes. However, it neglects phase and so interference effects are ignored.

2.8.2 Hybrid Geometric Optics Methods

Using Ray Tracing alone will lead to a series of discrete scattering directions instead of a continuous intensity distribution for a given orientation. Often, an additional modification of the incident wave takes place due to external diffraction, by which we mean diffraction around the crystal. It has become common to use diffraction at the projected cross section, i.e. over an aperture with dimensions equal to the particle shadow.

By incorporating diffraction a Ray Tracing model becomes a physical - geometric optics hybrid method. There have been many of these created over the past three decades such as the *Modified Kirchhoff Approximation* (MKA), the *Improved Geometric Optics Method* (IGOM) and the *Ray Tracing with Diffraction of Facets* (RTDF), all of which will be discussed later in this report.

A more recent development in physical-geometric optics models has been to model ray bundles (i.e. beams) instead of rays. Beams have finite transverse size and their shape and size can be determined at any point in their propagation. An early beam tracing model was developed by Borovoi and Grishin [53] and recent ones by Bi et al. [54,55] and Konoshonkin [56]. In Beam Tracing, the intersection of plane parallel beams with crystal facets are traced rather than rays, beams are divided when they illuminate multiple facets. Due to the difficulties associated with beam splitting algorithms, these existing methods have only been applied to convex crystals where beam re-entry is not possible. Tracing beams rather than rays is computationally cheaper as one need not track the path of millions of rays, just a few hundred beams. Much like in Ray Tracing, a beam is assigned a Stokes or Jones vector which is altered by its interaction with the crystal.

The focus of this work is to develop a Beam Tracing model that can be applied to ice crystals such as those found in cirrus, including spheroidal particles and concave particles. The phase of beams will be traced throughout their interaction with the crystal and the angularly resolved far-field amplitude post scattering will be determined through application of a diffraction integral over a beam's cross section.

Chapter 3

Ice Crystals and Cirrus Clouds

> Three glorious suns, each one a perfect sun; Not separated with the racking clouds, But sever'd in a pale clear-shining sky.
>
> William Shakespeare, in Henry VI

Cirrus clouds derive their name from their wispy appearance, with the word *cirrus* having its origins in Latin, meaning "curl-like fringe or tuft". They form at altitudes greater than six kilometres and consist of ice crystals of varying shapes and sizes. It was stated in the introduction that due to their large global coverage their impact on the Earth's radiation budget could be substantial. It has been reported that cirrus represent around 25% of all high clouds [57], their coverage is around 30% at mid-latitudes [1] and around 70% in the tropics [2].

The interaction of cirrus with incident shortwave radiation from the sun, and longwave radiation from the earth's surface and lower altitude clouds affects the Earth's climate. Reflection of shortwave radiation, and transmission of longwave radiation into space leads to cooling. Trapping thermal radiation leads to a greenhouse effect and therefore warming. In this way cirrus can make positive (warming) or negative (cooling) contributions to radiative forcing. In order to determine this contribution, the scattering properties of the constituent ice crystals needs to be understood. This task has proved troublesome due to the range of shapes and sizes that are found in cirrus ice. For example, in mid-latitude cirrus, a lower size limit of 10μm has been reported [58], with an upper size limit of 4000μm given in [59]. For the smaller sizes it is difficult for traditional *in-situ* measurement techniques to distinguish shape features, an issue which can be partly addressed through indirect techniques as employed by the Small Ice Detector (SID) probes discussed in Section 3.1.3.

The formation of ice crystals in cirrus is described by two mechanisms. *Homogeneous nucleation* takes place in the absence of Ice Nuclei (IN) and therefore requires lower temperatures and higher supersaturation. If ice nuclei, such as, aerosol are present *heterogeneous nucleation* can arise. Cooled water vapour (or super-cooled droplets) can freeze on to the surface in a process called vapour deposition leading to the formation of ice crystals. In order to better understand the bulk optical proper-

ties of cirrus, a good understanding of the underlying cloud microphysics is needed. This is because the optical properties are linked to the particle size distribution, ice crystal habit and complexity within the cloud. Heterogeneous nucleation tends to lead to fewer, but larger, ice crystals since it removes water vapour from the cloud. On the other hand, homogeneous nucleation tends to lead to smaller particles.

3.1 Ice Crystals

Ice crystal shape depends on a range of environmental factors. Ice crystals will naturally form hexagonal structures exhibiting six-fold symmetry. However in nature one encounters a range of crystal structures, known as ice crystal *habits* or *morphologies*. A habit diagram [60, 61] displays crystal type as a function of ice supersaturation and temperature (but does not contain any information regarding size or complexity). Figure 3.1 is the recent habit diagram taken from [61] where it is reported that columnar type crystals (i.e. those with an aspect ratio greater than unity) form at temperatures less than $-40°$ and plate like structures are observed in the temperature range between $-20°$ and $-40°$. This report will focus on columnar type structures only.

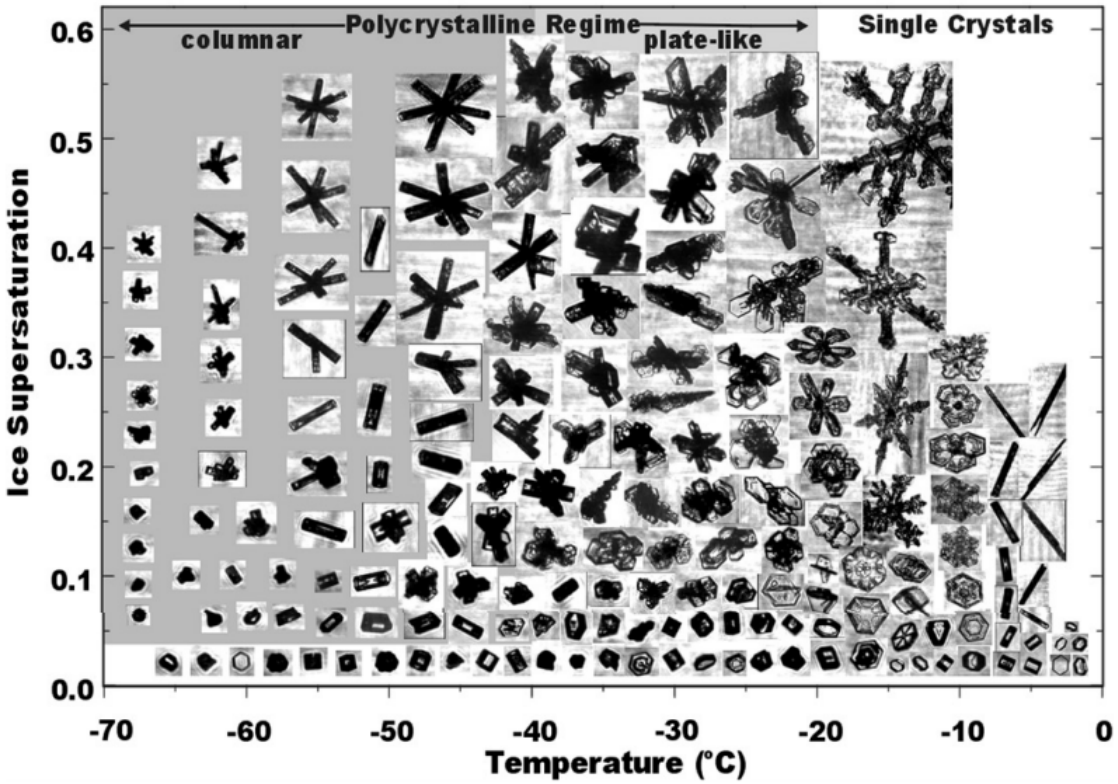

Figure 3.1: An ice crystal habit diagram, taken from [61].

3.1.1 Scattering by Ice Crystals

Modelling scattering by atmospheric ice crystals has been the subject of research for the last forty years and detailed reviews have been given by Baran [62, 63]. Approximating nonspherical particles by ellipsoidal and circular cylinders was investigated

by Macke and Mishchenko [24]. In this study while side-scattering properties were similar, the forward and backscattering regions differed greatly from a hexagonal column. The halo feature, characteristic of hexagonal columns, was not observed in most cases. Furthermore, the asymmetry parameter was found to be lower for the simplified shapes meaning that they are not suitable as proxies. It should be noted though that the circular cylinder did yield comparable results when the particle was absorbing.

Approximating hexagonal columns as volume equivalent spheres or surface area equivalent spheres has been shown to be unsatisfactory [25, 64, 65]. In the former case this is due to there being too little surface area from which to scatter. In the second case there is too much volume and subsequently too much absorption. Both lead to large asymmetry parameters which are not representative of measured data. A more involved approach modelling an infinite circular cylinder as a collection of independent spheres was shown to be promising by Grenfell and Warren [66] with generally good agreement in the extinction efficiency and single scattering albedo across a range of wavelengths. Agreement was less good for the asymmetry parameter.

For small particles, spheres have previously been assumed, however even small ice crystals are nonspherical. Deviations from spheres to more nonspherical shapes has been investigated using Chebyshev particles [67], Gaussian random spheres [68] and droxtals [69]. While these are interesting, it is widely accepted that approximating complex geometries by simpler ones does not lead to representative results. As such, the emphasis is now on modelling scattering by accurate computational particle geometries, reflecting those observed *in-situ*.

3.1.2 Laboratory Studies

Controlled studies of ice growth and morphology in laboratories is troublesome for a range of reasons. For one, recreating the conditions found in the atmosphere is non-trivial although complex cloud chambers do exist where it is possible to control environmental factors such as temperature and humidity. The advantage of using cloud chambers is that they allow for free growth of ice crystals but it is not possible to track the development of a single ice crystal.

Ice growth at the end of fibres does allow for investigations of single ice crystal growth, but it is impossible to say whether the presence of the fibre affects the process, this effect is known as *nucleation bias*. One can bypass the use of a fibre and grow the crystals directly on a substrate. Here the substrate is kept at a low temperature and water vapour is supplied to facilitate ice growth. This technique has been applied to study growth within the confines of a Scanning Electron Microscope (SEM) [6, 7]. The problem of nucleation bias persists with this type of growth and in addition new issues arise such as electron impact on the surface.

While both of these techniques are useful for studying the growth and morphology of ice they do not provide a means to investigate the scattering properties of individual ice crystals in a controlled manner. Ulanowski et al. [8,9] created ice crys-

tal analogues which have the same optical properties of ice but are stable at room temperature. Complex structures were made from fluorosilicates, the adjustment of growth parameters used allowed for the formation of a wide variety of crystal shapes and sizes. Simple cylindrical analogues can be made by heating, and subsequently stretching, glass tubes. Alternatively one can use optical fibres (an example of optical fibre scattering is shown in Figure 3.2). Because analogues are stable at room temperature it is possible to make measurements of size under an optical microscope and then place them within the detection mechanism of a laboratory version of the SID-3 probe, discussed in Section 3.1.3, or an electrodynamic balance [8,9], allowing for the study of scattering by individual crystals, see Figure 3.4.

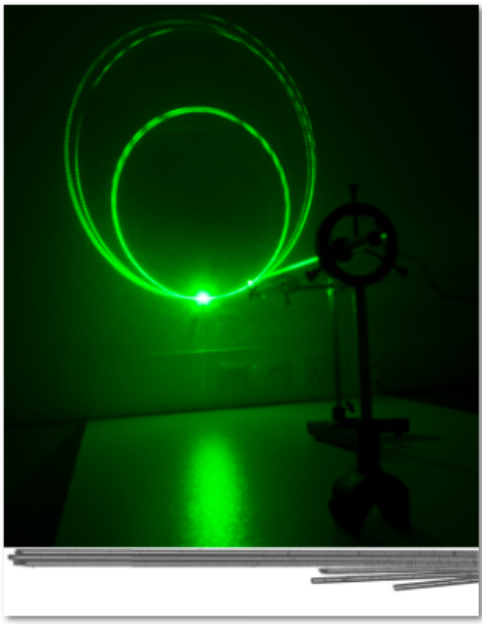

Figure 3.2: A bunch of optical fibres (bottom panel) are illuminated by a green laser. The resulting scattering pattern is seen on the wall. Notice the three distinct rings corresponding to the two fibre bundles. Interference fringes are also visible.

3.1.3 Remote Sensing and *In-Situ* Measurements

Remote sensing involves using ground or satellite instruments. Lidar, the shorter wavelength range analogue to radar, is a powerful technique that can be used to determine cloud optical depth, as well as properties of the ice crystals in cirrus (as well as other cloud types). Multi-wavelength lidar can use a quantity known as the *colour ratio* to estimate particle size distribution by recording the intensity of the backscattered light at two different wavelengths. Lidar instruments which use polarised light can measure the depolarisation to investigate particle properties such as thermodynamic phase, orientation and habit [64,70,71]. Furthermore, combining observations performed in both the radar and lidar regimes can reduce the uncertainty in retrieved microphysical properties of ice clouds [72].

Investigating ice crystals *in-situ* has evolved from collection from an open cockpit by Weickmann to direct imaging using instruments. A variety of optical array probes exist such as the Cloud Particle Imager (CPI) which captures the shadow

cast by a passing ice crystal. Direct imaging is size limited (issues arise when the particle is smaller than 100μm) and suffers from optical effects such as constrained depth of field at small sizes and aberrations. Detecting crystal habit from direct imaging requires high resolution, correctly focussed images. Otherwise errors can arise when trying to size particles [73]. In addition to this, diffraction fringes will often be seen in the images, further hampering efforts to determine habit, although this can be overcome by using an incoherent light source, as is done in the Particle Habit Imaging and Polar Scattering (PHIPS) probe [74]. Given that ice crystals display sizes over a large range (from micron scale to centimetre scale) the existence of sizing issues at the smaller end of the scale does not impose to much of a restriction in their use.

The SID probes [75] (the latest manifestation of which is SID-3) are *in-situ* probes that use an indirect technique to measure and size small ice crystals, see Figure 3.3. Particles enter the probe and pass through a 532nm laser beam, the resulting scattered light travels through a beam splitter dividing it into two parts (in a ratio of 92:8). The smaller proportion is used to trigger the recording of the scattering pattern as well as estimate the size. The larger proportion is detected in the angular range $6° - 25°$ which contains the 22° halo. The peak intensity of this halo is useful since it suggests that the particle which passed the laser was a large and smooth hexagonal prism. The absence or weakening of the halo is indicative of rough, small, or complex ice [9, 11].

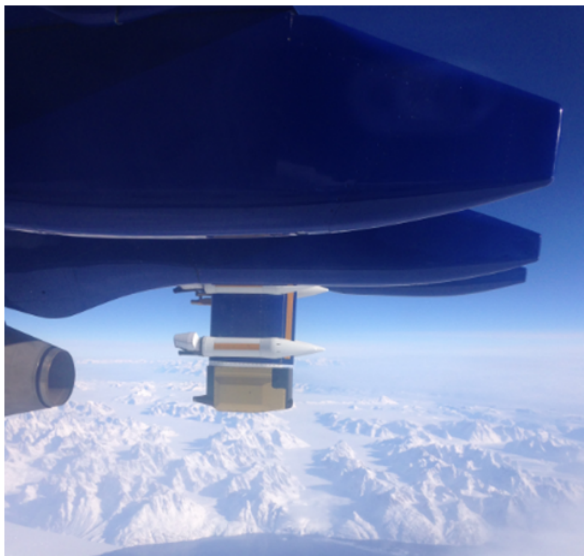

Figure 3.3: The SID-2 and SID-3 probes (both encased in white canisters), attached to the wing of the FAAM BAE-146 aircraft, over Greenland. Within the gold box is a CPI. (Photograph courtesy of Jenna Thornton).

Most probes relate the intensity of the scattered light to the diameter of the particle by using its scattering cross section C_{sca}. However, this is a function of size, shape and refractive index, all of which have to be assumed if one is to derive a diameter from the intensity, adding to the uncertainties with the measurement. This is further complicated by using Mie scattering profiles as the reference intensity for deriving particle diameter, since this assumes that the illuminated particle was spherical,

which is not the case with ice. Not only that, but the scattering cross section is not linearly related to particle size, meaning that particles of different size can have the same scattering cross section. All of this means that using intensity for particle sizing can be unreliable. As such, SID-3 also records a two-dimensional scattering pattern through the use of a Charged Coupled Device (CCD), see Figure 3.4. These patterns are affected by particle shape, complexity and roughness so can reveal a lot more information than traditional image capture techniques. However, one is then presented with the inverse problem of trying to identify an ice crystal by its scattering pattern. To aid in this, particle scattering databases have been created [76]. One of the principal aims of this project is to be able to aid in the creation of such databases, by having a model which can work over a large size range, and accurately model scattering in the SID detection range of $6° - 25°$.

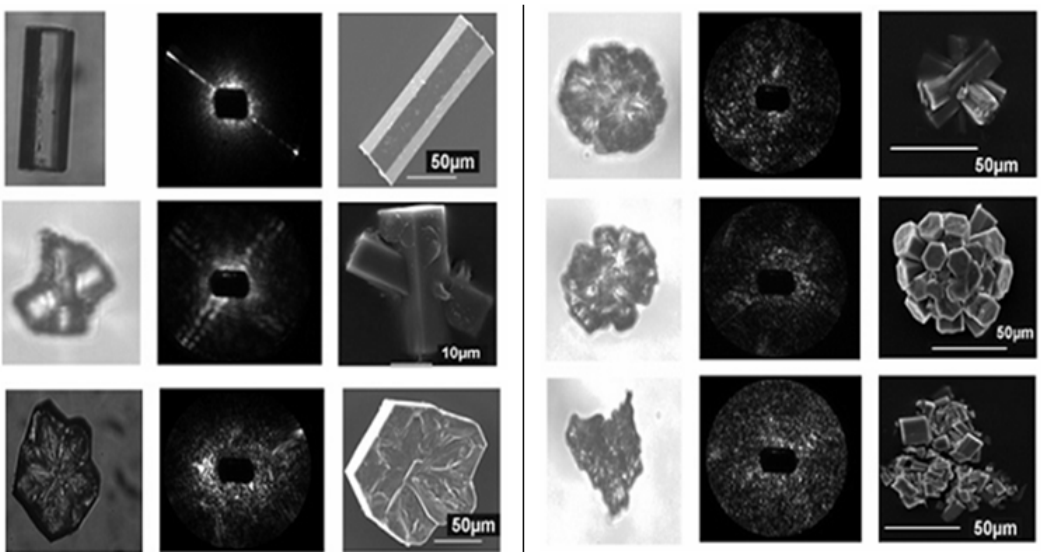

Figure 3.4: A variety of ice crystal analogues (optical microscope image on the left, Scanning Electron Microscope (SEM) on the right) and their scattering patterns (centre). Notice how crystal complexity leads to a speckly scattering pattern. The presence of such speckle can be used to infer crystal size [77] (images provided by Jenna Thornton).

Due to the high speed of aircraft during *in-situ* measurement ice crystals can shatter on instruments leading to an increase in the recorded number of small crystals [78]. While modern probes are designed with anti-shatter tips, older data will show a bias. Attempts to correct for the over-recording of small ice crystals have been investigated, including the creation of algorithms [79] which alter the measured particle size distributions retrospectively.

3.1.4 Crystal Complexity

Deviations from pristine polyhedra and spheres is common. Crystal complexity is the umbrella term that covers features such as roughness, inclusions, indentations and protrusions. Examples of complex pristine particles include rosettes and capped columns, which are thought to form when hexagonal ice crystals are transported to regions which favour plate growth [61]. The effect of crystal complexity on light

scattering depends on the particle size. For smaller particles, external diffraction dominates the forward scattering region and so complexity has little effect. Small quasi-spherical particles have been observed in mid-latitude cirrus. However, as particle size increases compared to the wavelength a smoothing of the phase function is observed [9, 80] leading to a decrease in the asymmetry parameter for complex crystals compared to smooth hexagonal prisms.

Recent satellite observations [81] revealed that a significant proportion of ice crystal in cirrus display evidence of surface roughness; similar observations have been made by *in-situ* measurements [11]. Modelling the scattering properties of rough particles has been performed with Ray Tracing [50] by changing the local surface normal when a ray intersects, which alters the ray's propagation direction. While this technique does result in a smoothing of the phase function (indicative of a rough particle) it is non-repeatable and does not allow for ray re-entry. Due to the random surface modifications, the surface of the 'model crystal' is not closed. Modelling scattering by roughened hexagonal columns with roughness properties derived from dust particles was presented in [82] (provided in Appendix G) where we showed that a two-scale roughness mechanism does indeed lead to a decrease in the asymmetry parameter for large enough size parameters (apart from the one exception at $x = 100$, single scale roughness has a similar, but smaller effect) through the use of ADDA computations.

Hollow hexagonal columns were shown to increase the asymmetry parameter [83] due to the cavities reducing backscattering. Smith et al. [84], using the Manchester cloud chamber and ray tracing computations, showed that the type of hollow column affects the asymmetry parameter. In particular, hollow columns with stepped indents in the basal facet were found to decrease the asymmetry parameter, while those with regular indents increased it. Hexagonal crystals with inclusions were investigated by Macke et al. [85]. It was seen that when the inclusions were non-absorbing the phase function was smoothed and the asymmetry parameter was reduced. However, when the particles contained absorbing inclusions, e.g. soot, it was shown that the asymmetry parameter was increased due to the decrease in internal reflection.

3.2 Optical Phenomena

Despite the range of crystal habits combined with forms of complexity, the existence of the 22° atmospheric halo is evidence of the presence of pristine hexagonal prisms in the atmosphere. The 22° halo is caused by incident light passing through two prism facets on a hexagonal column. The rarer 46° halo requires light to be incident on a prism facet and to leave through a basal facet. Hexagonal plate crystals which are sufficiently large that drag forces align their basal facets parallel to the horizon can be attributed as the cause of the parhelia, commonly known as sun dogs. More exotic halos, such as the 28° Scheiner's halo have been explained through light scattering from cubic ice crystals. Such ice crystals form at very low temperatures ($T < -100°$) and are thought to arise because of stacking faults in the hexagonal lattice structure of ice [86] which itself is hypothesised to occur when rapid homogeneous nucleation takes place.

The presence of pristine hexagonal ice in the atmosphere is not sufficient to lead

to halos, it has been reported in the literature that the crystals must have a size parameter of at least $x = 100$ [87]. This minimum size is due to diffraction; if the crystal becomes too small then diffraction becomes sufficiently strong to spread out the halo peak to such an extent that it no longer becomes distinguishable. Even with this minimum size requirement, the relative rarity of the atmospheric halo further adds evidence to the suggestion that atmospheric ice displays sufficient complexities as to smooth out the resultant phase functions [88, 89]. The proportion of complexities due to surface roughness, inclusions, indents or complex geometries remains to be determined and will likely continue as an active area of research.

Chapter 4

Beam Tracing

> Night had fallen, but the moon was so bright that it could compete with the orb whose light it reflected...
>
> Miguel de Cervantes,
> in Don Quixote

In Section 2.8.2 the idea of beam tracing was introduced as a physical optics method for modelling electromagnetic scattering. The creation of such a model has been the main research goal of this project. This chapter will outline in detail how the model works and how it is able to calculate various light scattering parameters.

4.1 From Ray-Tracing to Beam-Tracing

In the Monte Carlo ray tracing code written by Macke [50] random points are chosen in the plane $z = constant$ above the crystal from which rays are spawned propagating in the $-z$ direction. A given ray may not intersect the crystal as the x, y dimensions of the 'start plane' are determined by the maximum x, y dimensions of the crystal, as is shown in Figure 4.1.

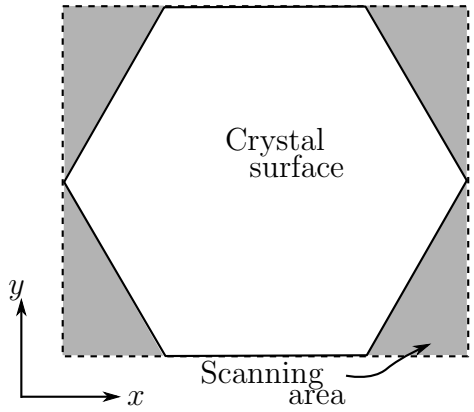

Figure 4.1: The scanning area in Macke's code is almost always larger than the crystal's projected area. As such, there are regions where propagating rays (here, the rays are propagating into the page) miss the crystal entirely (the shaded regions in the figure).

If a sufficiently large number of rays were used, then it is conceivable that every possible ray-crystal surface intersection would occur, leaving the entire surface 'scanned', with some intersections occurring multiple times. If identical hit points are removed then the contour of the crystal surface would then serve as a boundary for these rays, defining a ray bundle. In the limit of each of these rays having an infinitesimal area, one would arrive at a beam, see Figure 4.2.

A beam is a three dimensional entity in space but for beam tracing one need only consider the area defined by the intersection of a crystal facet and a beam, giving rise to polygonal beam cross sections. The corners of the cross section are referred to as *beam vertices*, these combined with a beam's propagation vector provide all the necessary tools to begin beam tracing. However, since this technique is to be applied to electromagnetic scattering, other properties of the beams will be needed which will be introduced towards the end of this chapter.

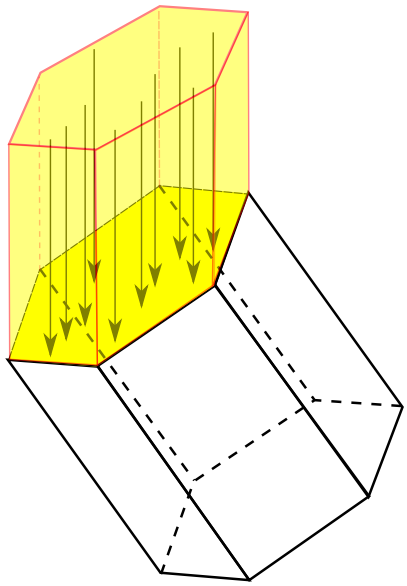

Figure 4.2: The rays scan out a region on the crystal surface, given enough rays the entire region would be scanned and one would have a well defined ray-bundle, or *beam*.

4.2 Particle Input Files

The model is written in Fortran and requires four input files: one for the scattering particle geometry; one involving electromagnetic properties; one for the rotation angles and one defining the scattering angle bins. Each input file can be written in Notepad.

4.2.1 Crystal Files

Scattering particle geometries are saved as a '.crystal' file. Particles must be facetted which requires curved surfaces to be approximated by a large number of polygonal facets. Crystal files contain (in order):

1. Number of facets on the first line.
2. Number of vertices on each facet, with each facet beginning on a new line.
3. Comma delimited (x, y, z) coordinates of each vertex, with each vertex going on its own line.

In order for the code to correctly calculate the surface normals, it is important that the vertices be given in a clockwise order when the facet is viewed from the outside of the crystal. This means, for example, that the vertices of the two basal facets of a hexagonal prism will not be given in the same order.

4.2.2 Electromagnetic Properties

Files with the extension '.file' contain the majority of user determined parameters that the code is to use. These quantities are listed below, in the order in which they are given.

1. The name of the particle geometry file (the .crystal file).
2. The wavelength of the incident light, the real part of the refractive index and the imaginary part, each quantity separated by a comma.
3. The number of crystal orientations.
4. The maximum number of beam recursions to be considered.
5. The maximum number of total internal reflections allowed.

The number of beam recursions, or *order*, p (see Section 2.8.1 and Figure 2.4), is one of the methods used by the model to determine at what point to stop tracing a given beam. It is possible for a beam with a small cross section to find itself totally internally reflected many times. As such, a user defined cut off is used to prevent the code from running indefinitely, the default being ten. However, since no energy is lost when a beam is totally internally reflected (so long as there is no absorption) the code could cut off an energetic beam which has been totally internally reflected if it exceeded the number of beam recursions set. For this reason, if a beam is totally internally reflected the beam recursion counter is not increased.

4.2.3 Euler Angles

The particle is situated at the centre of a 'laboratory coordinate system' with its 'particle coordinate system' overlapping this (z-axis along the cylinder axis of the prism). The direction of propagation of the incident wave is always considered to be in the $-z$ while the particle itself with its coordinate system is rotated. The rotation is described by the three Euler angles:

1. A rotation of α about the z-axis creating two new axes x' and y'.
2. A rotation of β about the x'-axis creating two new axes y'' and z'.
3. A rotation of γ about the $z'' = Z$ axis creating two new axes X and Y of the particle coordinate system.

Positive angles represent clockwise rotations when looking in the positive direction of the axis. These rotations, applied to a hexagonal column, are shown in Figure 4.3. While one can allow the code to randomly choose the particle orientation, if investigating scattering by ice crystals in fixed orientation, e.g. for comparison with *in-situ data*, then manual angle input is required. Likewise, if comparing results from two separate light scattering models, averaged over multiple orientations (as is done in this work between a Ray Tracing code and the Beam Tracer) it is useful to use the same set of Euler angles for both models. For this reason it is possible to save the Euler angles in a separate, comma delimited, text file to be read in by the code. The Euler angle rotation matrix is applied to each of the crystal vertex coordinates to yield their rotated positions with respect to the original (x, y, z) laboratory coordinate system. To that end, if a crystal vertex has position vector $\mathbf{x}_{\text{old}} = (x_o, y_o, z_o)^T$ then its new position is given by [90]:

$$\mathbf{x}_{\text{new}} = \mathbf{E}\mathbf{x}_{\text{old}}, \tag{4.1}$$

where $\mathbf{E}$ is the Euler angle rotation matrix,

$$\mathbf{E} = \begin{pmatrix} -\cos\beta\sin\alpha\sin\gamma + \cos\alpha\cos\gamma & -\cos\beta\sin\alpha\cos\gamma - \cos\alpha\sin\gamma & \sin\beta\sin\alpha \\ \cos\beta\cos\alpha\sin\gamma + \sin\alpha\cos\gamma & \cos\beta\cos\alpha\cos\gamma - \sin\alpha\sin\gamma & -\sin\beta\cos\alpha \\ \sin\beta\sin\gamma & \sin\beta\cos\gamma & \cos\beta \end{pmatrix}. \tag{4.2}$$

While Euler angles are the default rotation mechanism for the crystal geometry in the beam tracing code, they are not the only way of performing a rotation. For example, later when discussing comparison between results from the beam tracer and ADDA, a two stage rotation was used instead of Euler angles.

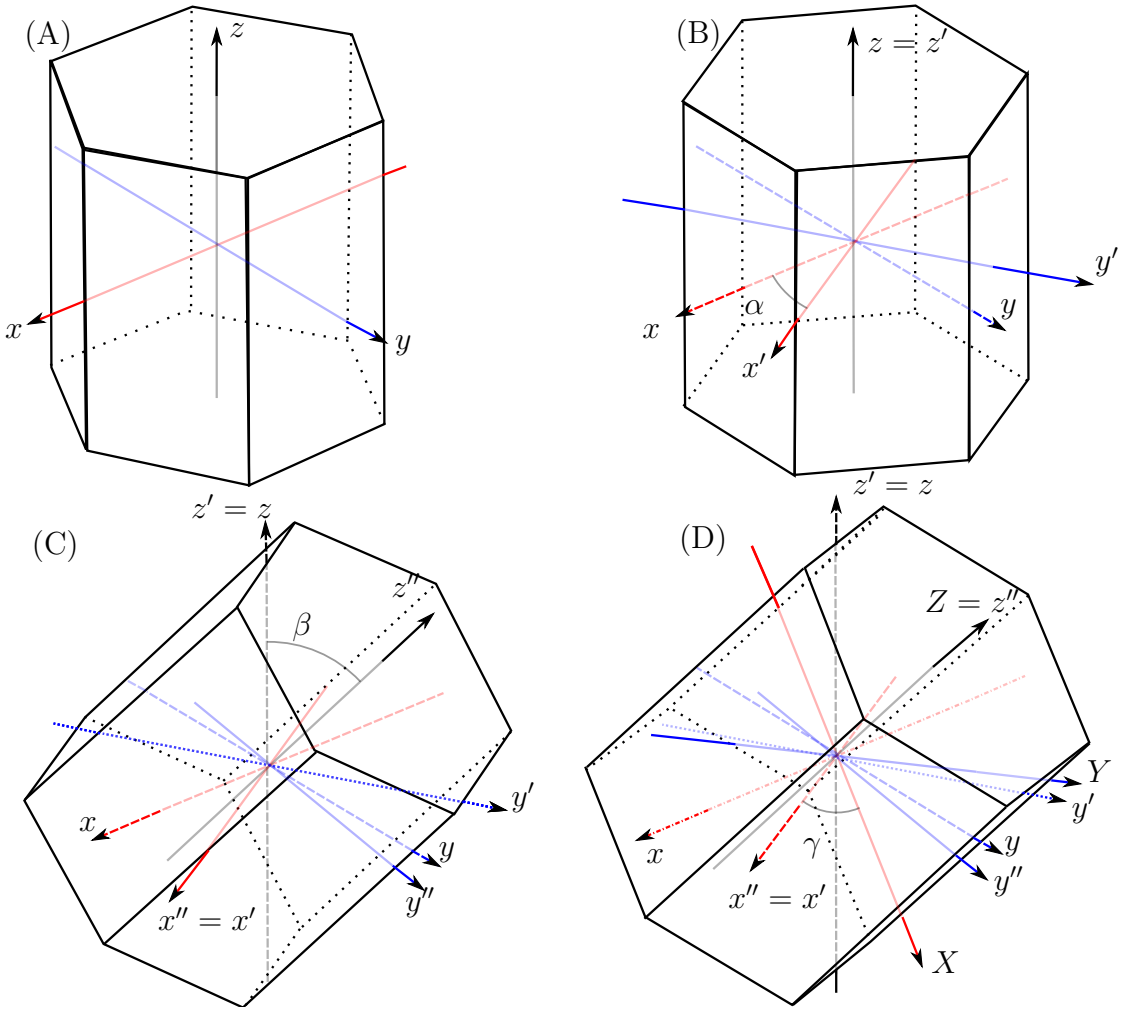

Figure 4.3: Rotation of a hexagonal column using the Euler angles. (A) is the original crystal orientation, (B) shows the first rotation by α about the z axis, (C) shows the second rotation by β about the x' axis, (D) shows the third rotation by γ about the $z'' = Z$ axis. The rotated axes are denoted by X, Y, Z.

4.2.4 Scattering Angle Bins

While the azimuthal bin size is set constant at 1° across the range $0° \leq \phi \leq 360°$ the scattering angle size is variable. This is because certain regions may require greater resolution than others. For example, in its current form the bin sizes are set

to equal that used in ADDA computations to ensure fair comparisons. The input file requires the complete list of scattering angles.

4.3 The Division of Beams

The propagation of a beam is described entirely by its propagation unit vector $\hat{\mathbf{k}}$. Changes to its direction due to reflection and refraction are described by Equations 2.35 and 2.36 introduced in section 2.8.1. A propagating beam, when incident on the surface of the crystal, may illuminate a region which extends over multiple facets. Since a beam cannot propagate in two directions simultaneously, it follows that the incident beam will have to be split before reflection and transmission can take place. An algorithm was written to take an incident beam and split it into N new beams, where N denotes the number of illuminated facets. The algorithm will be outlined in this section.

4.3.1 A Note on Terminology

An incident beam is equally well referred to as being the *parent beam*, when it intersects the crystal its *child beams* are referred to as *beamlets*. Child beams will consist of the reflected and transmitted beamlets. We refrain from using the term *sub-beams* until further division due to absorption is discussed.

4.3.2 Determination of the Illuminated Region

It was stated earlier that existing beam tracing models that have been presented in the literature have been restricted to convex, facetted polyhedra. It was desired that this beam tracer should be capable of handling particles such as cylinders, spheroidals and indented particles. In this section we will discuss how beam tracing is performed, first on a hexagonal column with flat basal facets, and then on a hexagonal column with an indented basal facet; both columns will be smooth.

The surface normals of the crystal facets are all pointing out of the crystal volume. For external illumination a facet with surface normal $\hat{\tau}$ will be illuminated if $\arccos(\hat{\mathbf{k}}_0^i \cdot \hat{\tau}) > 90°$, that is if the surface normal points towards the beam source. In practice, the incident wave is propagating in the direction $\hat{\mathbf{k}}_0^i = (0, 0, -1)^T$ which means that any surface normal with a positive z component is considered illuminated.

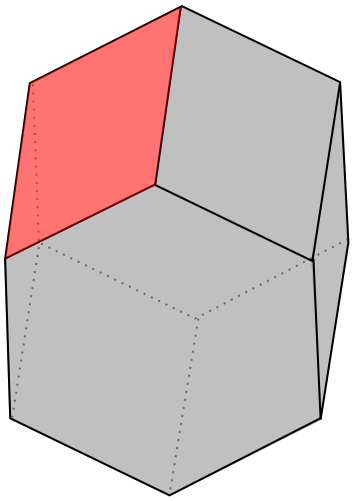

Figure 4.4: The red region indicates a beam cross section illuminated by the incident wave, which is propagating into the page. This beam would undergo reflection and transmission, the latter will require beam splitting.

We will investigate how the beam formed by illuminating the facet shown in red in Figure 4.4 would be split. The externally reflected beam would not interact with the crystal again and therefore can be considered scattered. The transmitted beam however, would intersect the crystal and as such we wish to determine the region it would illuminate. In order to do this, we introduce the set B_i of position vectors of the beam vertices $\mathbf{b}$, for the i^{th} beam,

$$B_i = \{\mathbf{b}_{i,1}, \mathbf{b}_{i,2}, ..., \mathbf{b}_{i,n}\}, \tag{4.3}$$

with the number of beam vertices being denoted by n. One can envisage rays passing through each of these beam vertices in the direction of transmission, the intersection of these rays with the crystal would then define the vertices of the newly illuminated region, which may be across several facets meaning that the beam has to be split. There are six stages to beam splitting:

1. Determine all candidate facets, i.e. those facets which could be illuminated by the incoming beam.
2. Project the beam, and all candidate facets, on to the beam splitting plane.
3. Find the intersection between each projected beam edge with each edge of each projected facet.
4. Check to see if any projected crystal vertex is bound by the projected beam cross section.
5. Check to see if any projected beam vertex is bound by each projected facet.
6. Project each new point back on to the crystal.

Step 1: Determining candidate facets.

Candidate facets are again determined through use of surface normals. However, unlike external incidence, a facet will be illuminated if $\arccos(\hat{\mathbf{k}} \cdot \hat{\tau}) < 90°$. This is

because the surface normals point out of the crystal volume, therefore to be illuminated the angle between the propagation vector and the surface normal has to be acute.

Step 2: Projection on to the beam splitting plane.

Beam splitting is performed by projecting the beam, and all candidate facets on to the *beam splitting plane*, which is the plane perpendicular to the direction of propagation of the beam. The general expression to project a point with position vector $\mathbf{x}$ on to a plane through the origin of the coordinate system and perpendicular to $\hat{\mathbf{k}}$ is:

$$\mathbf{x}' = \mathbf{x} - (\hat{\mathbf{k}} \cdot \mathbf{x})\hat{\mathbf{k}}. \tag{4.4}$$

Throughout the rest of this chapter, primed quantities will be in reference to position vectors of points given in this beam splitting plane. Projecting a beam vertex $\mathbf{b}_i$ in to the beam splitting plane is therefore achieved by replacing $\mathbf{x}$ in Equation 4.4; likewise for crystal vertices $\mathbf{v}$. Figure 4.5 shows the incident beam, in red, being projected on to the beam splitting plane, along with the candidate facets, which are coloured individually. Blue dashed lines are shown passing through each beam vertex in the direction of propagation $\hat{\mathbf{k}}^t$. The left panel illustrates that the beam splitting plane is perpendicular to the direction of propagation (the beam splitting plane has been translated in the direction of $\hat{\mathbf{k}}^t$ for better visualisation). The black circles in the right panel are the points of intersection between a ray passing through the beam vertex and the crystal, the position vector of such points is found through Steps 3-6.

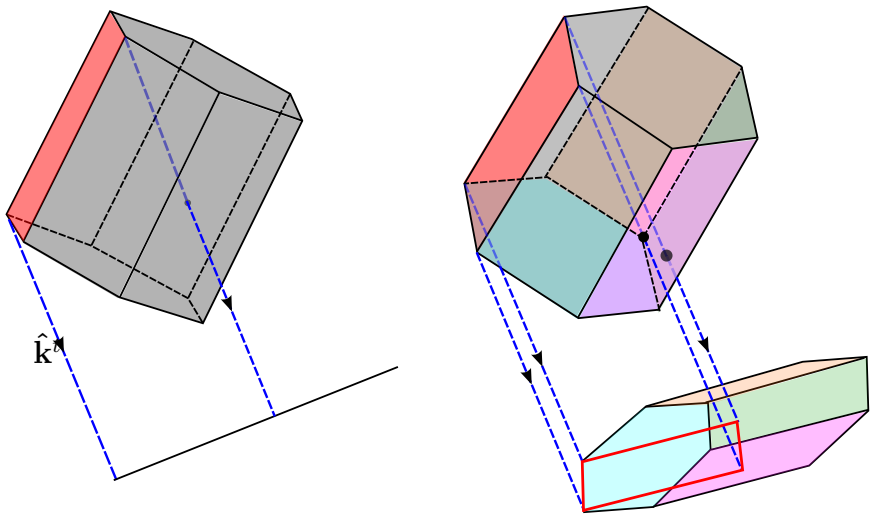

Figure 4.5: A beam cross section being projected on to the beam splitting plane, which is perpendicular to the direction of propagation (the blue dashed lines). The thick red lines are the projection of the beam edges and the black lines are the projections of the candidate facets. An additional translation of the plane in the direction of propagation has been made to aid visualisation.

Step 3: Intersections of projected beam edges with projected crystal edges.

Once in the beam splitting plane, we seek the intersections (if they exist) between

the projections of the beam edges, and the projections of the edges of the candidate facets. To that end, let the edge of a beam cross section be denoted by

$$\mathbf{l}' = \mathbf{b}_i + \mu(\mathbf{b}'_{i+1} - \mathbf{b}'_i) = \mathbf{b}'_i + \mu\mathbf{a}' \qquad \mu \in \mathbb{R}. \tag{4.5}$$

Likewise, let the edge joining two crystal vertices be given by:

$$\mathbf{e}' = \mathbf{v}'_j + \nu(\mathbf{v}'_{j+1} - \mathbf{v}'_j) = \mathbf{v}'_j + \nu\mathbf{c}' \qquad \nu \in \mathbb{R}. \tag{4.6}$$

Equating these two equations and rearranging we have:

$$\mu\mathbf{a}' - \nu\mathbf{c}' = \mathbf{v}' - \mathbf{b}'_i = \widetilde{\mathbf{r}}. \tag{4.7}$$

The system of equations given by Equation 4.7 is overloaded and so can be solved using matrices,

$$\underbrace{\begin{pmatrix} a_x & c_x \\ a_y & c_y \\ a_z & c_z \end{pmatrix}}_{\mathbf{A}} \underbrace{\begin{pmatrix} \mu \\ \nu \end{pmatrix}}_{\mathbf{B}} = \underbrace{\begin{pmatrix} \widetilde{r}_x \\ \widetilde{r}_y \\ \widetilde{r}_z \end{pmatrix}}_{\mathbf{C}}. \tag{4.8}$$

In order to solve this system using matrices it is necessary to reduce the size of $\mathbf{A}$ so that it is square. To do this, we choose to use only the xy components, calling the reduced matrix $\bar{\mathbf{A}}$. The values of μ and ν are then given by:

$$\mathbf{B} = \bar{\mathbf{A}}^{-1}\mathbf{C}. \tag{4.9}$$

If no solution is found using the xy components then the xz components are used, likewise if these yield no solution we try the yz. If still no solution is found, then the lines do not intersect meaning that the beam does not illuminate any portion of the crystal edge. Of course, it is possible that the lines may intersect outside of the projection of the crystal. Therefore a check is made to ensure that

$$\mu \leq ||\mathbf{b}'_{i+1} - \mathbf{b}'_i||^2,$$
$$\nu \leq ||\mathbf{v}'_{j+1} - \mathbf{v}'_j||^2.$$

If satisfied, the intersection between the beam edge and the crystal edge in the beam splitting plane can then be found by substitution of μ into Equation 4.5 (or ν into Equation 4.6). This process is repeated for all beam edges and all candidate facet edges, every time a successful intersection is found the facet and the point of intersection are stored. Figure 4.6 denotes these points of intersection with blue crosses.

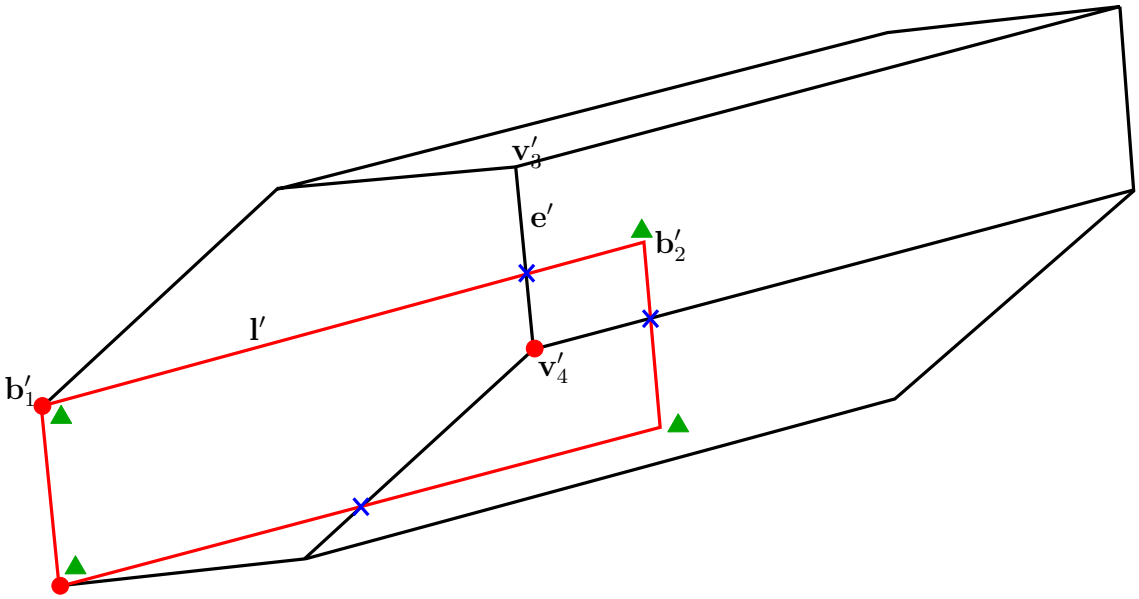

Figure 4.6: Projection plane: Points found through the three stages of beam splitting (the crystal orientation is the same as Figure 4.4, but the viewing angle has been changed for ease of viewing). Two beam vertices $\mathbf{b}'_1$ and $\mathbf{b}'_2$ are labelled, as are two facet vertex projections $\mathbf{v}'_3$ and $\mathbf{v}'_4$. The markers indicate at which stage a given point will be found by the algorithm; blue crosses mark points found through considering line intersections; red filled circles are facet vertices bound by the beam (red lines) and green triangles are beam vertices bound by a crystal facet.

Step 4: Projected crystal vertex check.

The next stage is to determine whether any of the projected candidate facet vertices are within the beam's cross sectional area. Tests to determine whether a given point is bounded by some area defined by vertices $\mathbf{r}_1, ..., \mathbf{r}_n$, n being the number of vertices, are common throughout the beam tracing algorithm. The technique makes use of vectors which are perpendicular to the boundary. These so-called *edge vectors* are in the same plane as the bounded area and as such will be perpendicular to the normal of the plane $\hat{\mathbf{n}}$. It follows that a vector perpendicular to the edge joining the vertices $\mathbf{r}'_i$ and $\mathbf{r}'_{i+1}$, $i = 1, ..., n$ would be given by:

$$\mathbf{q}_i = \hat{\mathbf{n}} \times (\mathbf{r}_{i+1} - \mathbf{r}_i), \tag{4.10}$$

note that when $i = n$, $i + 1 = 1$. Next, let the vector $\mathbf{p}$ be the vector from a vertex to the point being investigated $\mathbf{x}$, that is:

$$\mathbf{p}_i = \mathbf{x} - \mathbf{r}_i. \tag{4.11}$$

If $\mathbf{x}$ is within the area, then $\hat{\mathbf{p}}_i \cdot \hat{\mathbf{q}}_i \leq 0$ for all pairs of vectors $\hat{\mathbf{p}}_i$, $\hat{\mathbf{q}}_i$. This condition states that the angle φ between the two vectors will be greater than or equal to 90° when $\mathbf{x}$ is within the area, see Figure 4.7.

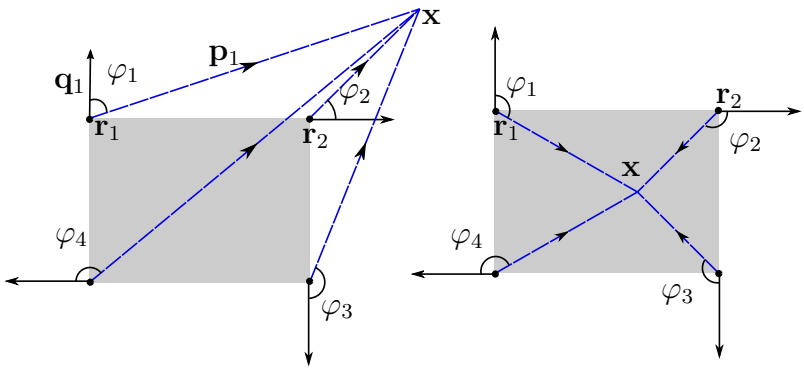

Figure 4.7: A test to determine if a point is within a bounded region. If $\mathbf{x}$ is within the shaded area, the angle φ_l between each pair of vectors $\mathbf{p}_l, \mathbf{q}_l$ will be larger than 90°. For clarity, only one pair of vectors has been labelled.

Applying the above test with $\hat{\mathbf{n}} = \hat{\mathbf{k}}^t$ and $\mathbf{r}_i = \mathbf{b}'_i$ in Equation 4.10, and $\mathbf{x} = \mathbf{v}'_j$ in Equation 4.11 (i.e. is the crystal vertex $\mathbf{v}'_j$ within the region define by the projection of the beam vertices?) yields, in this instance, three additional points indicated by red circles in Figure 4.6.

Step 5: Projected beam vertex check.

Next consider the converse situation, beam vertices bounded by crystal facets. The process for doing this is in essence the same as described for step 4, but the test point is now a beam vertex, not a crystal vertex. Therefore Equations 4.10 and 4.11 use $\hat{\mathbf{n}} = \hat{\mathbf{k}}^t$, $\mathbf{r}_j = \mathbf{v}'_j$ and $\mathbf{x} = \mathbf{b}'_i$. The points revealed by this process are denoted in Figure 4.6 by the green triangles.

Step 6: Projecting points back on to the crystal.

Once steps 1-5 have been carried out a set of points, and the corresponding facets, will have been found. These position vectors have to be projected back on to the crystal. Let the position vector of a stored point in the projection plane be $\mathbf{x}'$, its corresponding point on the crystal is given by:

$$\mathbf{x} = \mathbf{x}' + \frac{(\mathbf{v}' - \mathbf{x}')}{\hat{\mathbf{k}} \cdot \hat{\tau}} \hat{\mathbf{k}}, \tag{4.12}$$

where $\hat{\tau}$ is the surface normal of the facet associated with the point $\mathbf{x}'$. Repeating this for all points and grouping by facet then gives the coordinates of the new beams' vertices. There is one final adjustment that may need to be made, the beam splitting process may duplicate points. In order to avoid errors when calculating phase it is important that duplicated points are removed from the beam vertex coordinate arrays (the error in calculating phase arises because duplicated points will affect the location of the midpoint of the beam cross section). The resulting beams are shown in Figure 4.8.

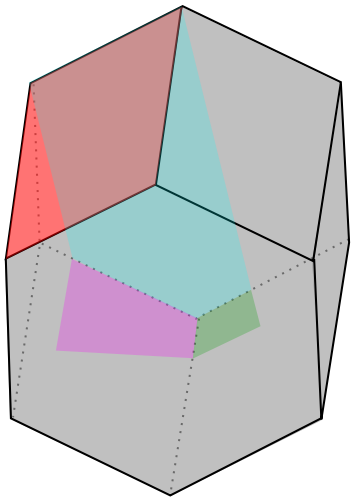

Figure 4.8: Three new beams formed as a consequence of beam splitting.

4.3.3 Vertex Order

The arrangement of the beam vertices in an array can have a profound effect on the shape of the beam as shown in Figure 4.9. For the beam to be a closed polygon we require the points to be in clockwise order *when viewed in the direction of propagation*, i.e. from the 'source' of the beam. While the second part of this criterion does not affect the shape of the beam, it does affect the sign of the line integral used in calculating the amplitude of the diffracted field (see Section 5.4.2).

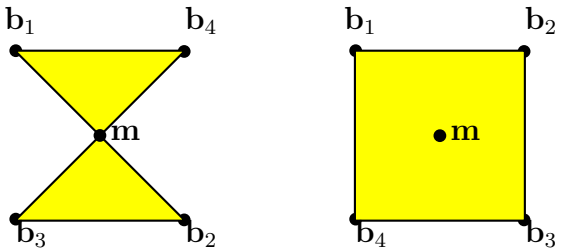

Figure 4.9: The order of beam vertices can drastically affect the shape resulting beam cross section.

The position vector of the midpoint $\mathbf{m}$ of a beam cross section is the average of the beam vertex position vectors,

$$\mathbf{m} = \frac{1}{n}\sum_{j=1}^{n} \mathbf{b}_j. \tag{4.13}$$

To sort the points into clockwise order, let $\mathbf{u}_j = \mathbf{b}_j - \mathbf{m}$ be a vector from the centre of a beam's cross section to the i^{th} beam vertex, then $\cos\Theta_j = \hat{\mathbf{u}}_1 \cdot \hat{\mathbf{u}}_{j+1}$ is the angle between two vectors in the plane.

This scalar product will only return an angle $\Theta \in [0, \pi]$, to extend this range to $\Theta \in [0, 2\pi]$ one can use the cross product. The product $\hat{\mathbf{u}}_{j+1} \times \hat{\mathbf{u}}_1$ will give a vector perpendicular to the beam's cross section on the facet, as such $(\hat{\mathbf{u}}_{j+1} \times \hat{\mathbf{u}}_1) \cdot \hat{\tau}$ will

either be equal to 1 or -1 leading to the following condition:

$$\Theta_j = \begin{cases} \cos^{-1}(\hat{\mathbf{u}}_1 \cdot \hat{\mathbf{u}}_{j+1}) & \text{if } (\hat{\mathbf{u}}_{j+1} \times \hat{\mathbf{u}}_1) \cdot \hat{\tau} = 1 \\ 2\pi - \cos^{-1}(\hat{\mathbf{u}}_1 \cdot \hat{\mathbf{u}}_{j+1}) & \text{if } (\hat{\mathbf{u}}_{j+1} \times \hat{\mathbf{u}}_1) \cdot \hat{\tau} = -1 \end{cases} \tag{4.14}$$

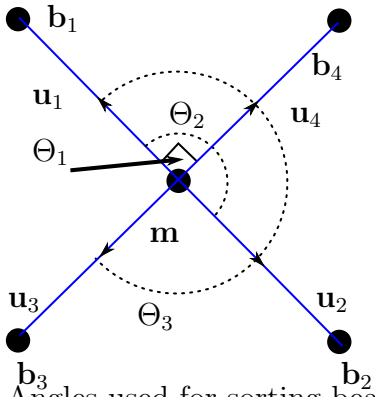

Figure 4.10: Angles used for sorting beam vertices.

Sorting these angles into ascending order will give the points in such an order as to ensure the beam cross section is a closed polygon. The next stage is to ensure that the points have been sorted into clockwise order as viewed from the 'source'. To do this let $\mathbf{p} = \mathbf{b}_2 - \mathbf{b}_1$ and $\mathbf{q} = \mathbf{b}_3 - \mathbf{b}_2$. If the points are in clockwise order as viewed in the direction of propagation $\hat{\mathbf{k}}$, then $\hat{\mathbf{n}} \cdot \hat{\mathbf{k}}$ will be greater than zero, where $\mathbf{n} = \mathbf{p} \times \mathbf{q}$, see Figure 4.11. If this result is negative, then the order of the points in the array is reversed. The special case of $\hat{\mathbf{n}} \cdot \hat{\mathbf{k}} = 1$ occurs when the surface normal to the facet is parallel to the direction of beam propagation.

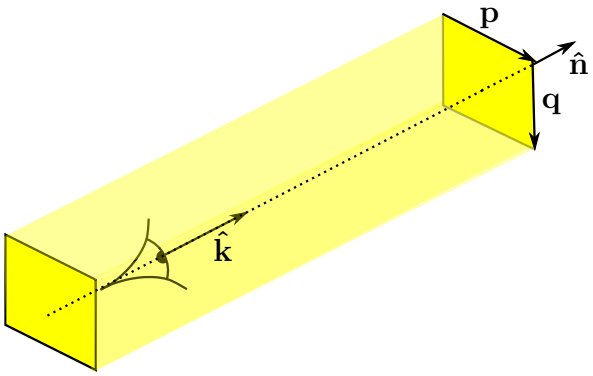

Figure 4.11: If the beam vertices are arranged in the clockwise direction when viewed from the source, then the test vector $\hat{\mathbf{n}}$ should point away from the beam source

4.4 Adapting the Beam Splitting Algorithm to Handle Concavities

Concave particles, such as the one shown in Figure 4.12, present a number of challenges for beam tracing models and as such existing codes have dealt explicitly with convex particles [54, 56]. The two most obvious problems being shadowing by the

indent and beam re-entry. The beam tracer has been adapted to deal with both of these problems, this section outlines how it handles them.

Figure 4.12: An example of an indented column which can be used in the beam tracer

4.4.1 Partial Blocking of the Incident Wave

It was stated in the previous section that the initial beam cross sections were equal to those crystal facets whose surface normals had a positive z coordinate as the incident wave propagates in the direction $\hat{\mathbf{k}} = (0, 0, -1)^T$. However, for indented particles some facets may be partially, or totally, blocked by other upward facing facets, see Figure 4.13.

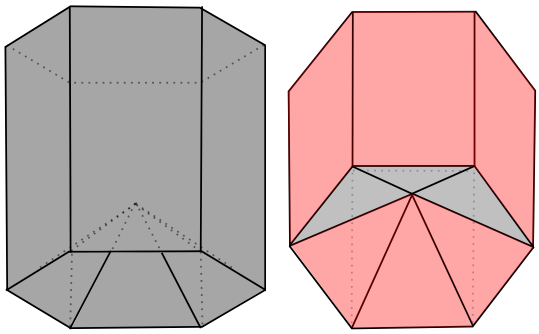

Figure 4.13: An indented column seen from two different viewing angles. In the left configuration the incident wave is into the page, a portion of the indent would be blocked by one of the prism facets. The right configuration shows the initial beams found using the old "upward facing facet" criterion.

Finding the shadow region is a four step process.

1. Test each candidate crystal vertex to see if it is blocked by any other candidate facet.
2. Project each blocked facet and the blocking facet into the beam splitting plane.
3. Seek intersection between the projections of the crystal edges.
4. Project points, along with intersections, back on to the blocked facet. Sort into clockwise order.

As step one of this procedure is the only new step to be discussed the other three will be omitted. Steps 2-4 were outlined in Section 4.3.2.

Step 1: Determining if any crystal vertices are overshadowed.

To determine the shadow region each illuminated candidate facet is considered in turn and compared with all other candidate facets. For comparison we see if a ray passing through each vertex of a given candidate facet intersects with any other candidate facet when the ray is travelling back towards the beam source (i.e. its propagation direction is $-\hat{\mathbf{k}}_0^i$). A ray can be written as a vector line equation, passing through a beam vertex $\mathbf{b}$ parallel to the reverse direction. A point on this line is given by:

$$\mathbf{x} = \mathbf{b} - \mu\hat{\mathbf{k}}_o^i. \tag{4.15}$$

In a similar manner, a crystal facet can be considered a bound region in $\mathbb{R}^3$. The position vector of a point on the facet will therefore satisfy

$$(\mathbf{x} \cdot \hat{\tau}) = 0. \tag{4.16}$$

Substitution of Equation 4.15 into Equation 4.16 and solving for μ leads to a Equation for the intersection of the ray with a given crystal facet,

$$\mathbf{x} = \mathbf{b} - \left(\frac{\mathbf{b} \cdot \hat{\tau}}{\hat{\mathbf{k}}_0^i \cdot \hat{\tau}}\right)\hat{\mathbf{k}}_0^i. \tag{4.17}$$

If this point is bound by the crystal facet it means that the beam vertex $\mathbf{b}$ is blocked by the facet and as such it is removed from the initial beam array. The facet is then identified as having been blocked, in the same way the other facet is identified as blocking. A shadow boundary must exist on the blocked facet, to find it all blocked facets and all blocking facets are projected on to the beam splitting plane, as shown in Figure 4.14. The line intersections can then be found in the same way as was done in Step 3 of Section 4.3.2.

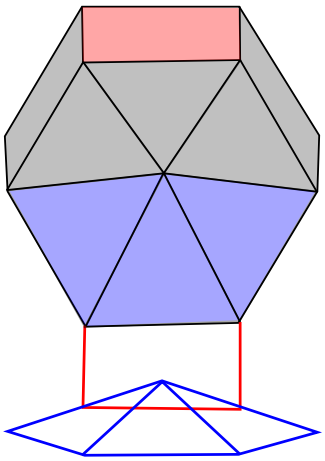

Figure 4.14: The three blue facets have been found to be 'blocked' by the red prism facet and as such all are projected into the beam splitting plane (which again has been translated). The coloured lines reflect the colour of the projected facet. By finding the line intersections between the red and blue lines the shadow region can be determined.

Once the line intersections are known the points are projected back on to the blocked facet. Each set of beam vertices is then sorted into clockwise order to ensure correct beam shape. This process yields the shapes of the initial beams on facets which were partially blocked by other facets. The result is shown in Figure 4.15.

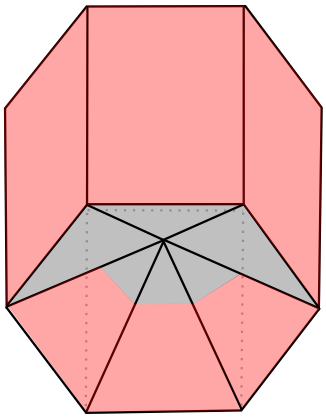

Figure 4.15: The upper prism facet has blocked some of the incident wave and stopped full illumination of the triangular facets which make up the indent. As a consequence of this shadowing the beam shapes are deformed. Beams are shown in red.

4.4.2 Beam Re-entry

The next stage to consider is beam re-entry, to do this, we will consider external reflection from an indented column in a slightly different orientation as the one given above (in this case, there was no shadowing). In Figure 4.16 the red beam is to be reflected, the direction of reflection is shown by a blue arrow and it can be seen that the arrow intersects again with the crystal. We wish to determine the shape of the beam that intersects, and the shape of the beam which does not (i.e. is scattered).

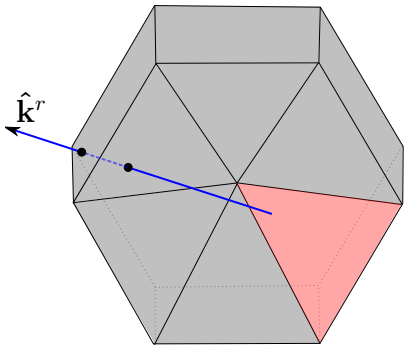

Figure 4.16: The red beam is externally reflected in the direction of the blue arrow (incident wave propagates into the page). Some portion of this beam will re-enter the crystal.

The steps involved in handling beam re-entry are:

1. Identifying candidate facets.
2. Project beam and candidate facets on to the beam splitting plane.

3. Find line intersections.
4. Check the intersections to see if they are shared by two candidate facets.
5. Check to see if beam vertices are bound by projected candidate facets.
6. Check to see if crystal vertices are bound by the projected beam cross section.
7. Project points back on to the crystal.

Steps 2 and 3 have been discussed in Section 4.3.2 and so are omitted in the following discussion.

Step 1: Identifying candidate facets.

Additional criteria are needed to determine which facets could potentially be illuminated. A surface normal criterion is used, requiring that $\arccos(\hat{\mathbf{k}}^r \cdot \hat{\tau}) > 90°$ i.e. the surface normal points towards the beam source. The problem with using this criterion on its own is that facets 'behind' the beam would also be considered. To get round this issue, let the vector $\mathbf{M}$ be the vector from the midpoint of the currently illuminated facet to the centre of the candidate facet. To be considered as potentially illuminated the requirement that $\arccos(\mathbf{M} \cdot \hat{\mathbf{k}}^r) < 90°$ must be satisfied. If a facet meets both of these criteria then it is projected, along with the beam cross section, on to the beam splitting plane, see Figure 4.17.

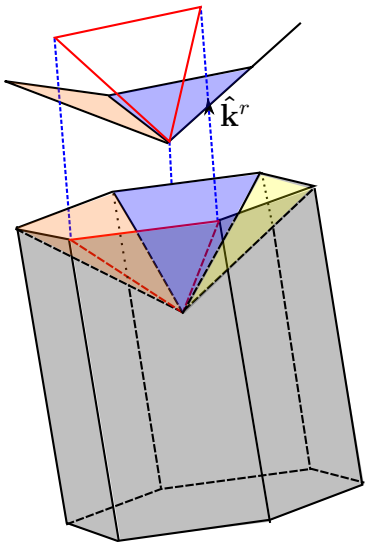

Figure 4.17: The same crystal as in Figure 4.16 seen from a different angle. Projections of the beam (red) and candidate facets (orange, blue and yellow) in the beam splitting plane (which again has been translated by a constant amount in the direction of propagation) have been included.

Normal beam splitting then takes place; line intersections between projections of the beam edges with projections of the facet edges are sought. In this instance, there are two intersections, marked by blue crosses in Figure 4.18.

Step 4: Classifying points found through line intersections.

The blue crosses would be shared by both the beam that re-enters, and the beam that is scattered. As such, they will be projected back on to the crystal in two places, once on the current facet (i.e. the facet on which the parent was beam reflected) and also on to the newly illuminated facet. However, if the crystal edge had been shared by two candidate facets then projecting the point back on to the old facet would lead to problems. In particular, if more beam vertices are supplied than what are necessary to define the beam shape, phase issues can arise due to the incorrect determination of the beam centre. Therefore, for each intersection found a test is performed to see if the edge the point is on is shared by two projected candidate facets. If it is, then the point will only be projected on to the newly illuminated candidate facets. If not, then it is projected on to the old facet, and the candidate facet. In the case discussed here, the blue crosses are on a crystal edge which is not shared. They therefore mark the edge which separates the beam that is scattered from the beam that re-enters.

Step 5: Testing to see if beam vertices are bound by facet projections

A ray passing through a beam vertex which is bound by facet projections would re-intersect that facet, (green triangle in Figure 4.18). If the vertex is not bound then a ray would propagate away from the crystal (red circles in Figure 4.18).

Step 6: Testing to see if crystal vertices are bound by beam projection

Any crystal vertex which is bound by the projection of the beam would be illuminated by that beam. This point is stored, along with its facet. In this instance, no such point is found.

Step 7: Projecting back on to the crystal

The mechanism for this has been discussed already. However, in this case the points associated with the scattered beam have to be projected back on to the parent facet, so that its cross section is known for modelling diffraction.

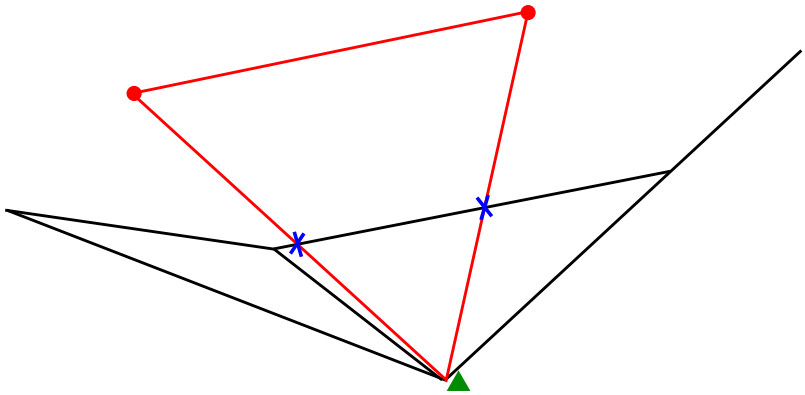

Figure 4.18: Splitting the reflected beam. Beam vertices found through line intersections are marked by blue crosses, these points are shared by the scattered beam and the beam that intersects. Beam vertices which are not bound by facet projections will belong to the beam which is scattered (red circles); whereas beam vertices which are bound would belong to the beam which intersects (green triangle).

In this way the reflected beam has been split as shown in Figure 4.19.

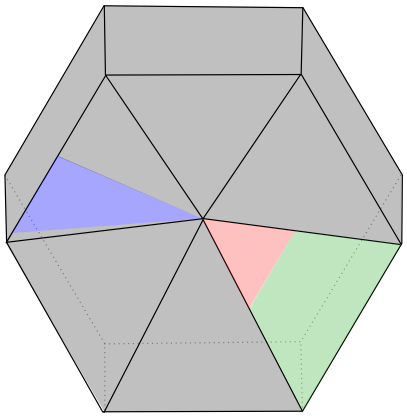

Figure 4.19: The externally reflected beam is split into parts which intersect with the crystal again (red) and those which are scattered (green). The region illuminated by external reflection off the facet is shown in blue.

4.4.3 Transmission into an Indented Column

For transmission, once candidate facets have been identified, the model divides them into three sets. The first set contains those facets which could potentially have a shadow region on them, the second set contains those facets which are blocking some portion of the transmitted beam and the third set are the facets which neither block, nor are blocked. For each set, the process is then the same as for reflection, they are projected on to the beam splitting plane and line intersections are sought. For each blocked facet, the shadow portion is removed by considering the symmetric difference between coordinate sets. As before, a list of steps is given.

1. Identifying candidate facets.

2. Identify potential blocking facets and their corresponding overshadowed facets. Find any unblocked facets

3. Project beam and the blocked facet on to the beam splitting plane.
4. Find line intersections.
5. Check to see if beam vertices are bound by projected candidate facets.
6. Check to see if crystal vertices are bound by the projected beam cross section.
7. Project beam and corresponding blocking facets on to the beam splitting plane.
8. Repeat steps 4-6.
9. Find the symmetric difference between the resulting coordinate sets.
10. Repeat steps 3-9 until all blocked facets have been considered.
11. Project the beam and any unblocked facets on to the beam splitting plane.
12. Repeat steps 4-6.
13. Project all new beams back on the crystal.
14. Project points back on to the crystal.

Consider the situation shown in Figure 4.20 where a single beam is being transmitted into the crystal. As with external incidence, the indent will block some of the transmitted beam from reaching the lower prism facet. Step 1 is the same as for reflection and so will not be repeated here, we move straight on to Step 2.

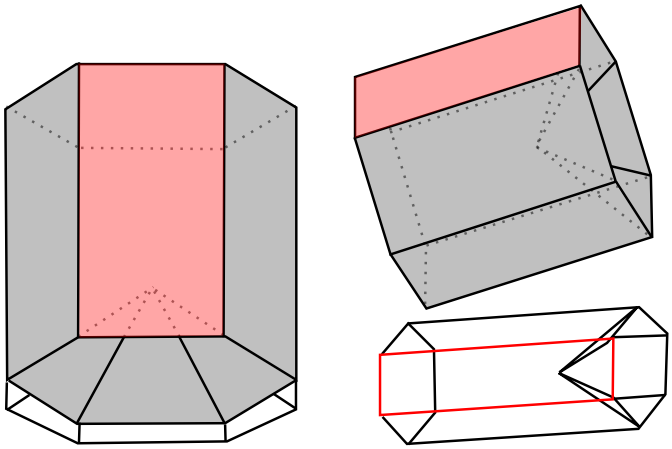

Figure 4.20: Two views of an indented crystal and a beam undergoing transmission. The thick red line is the projection of the beam and the black lines are the projections of all the candidate facets.

Step 2: Identifying and dividing facet groups.

For external shadowing 'back-rays' were used originating from each vertex of each candidate facet. A similar approach is used here, but instead of back rays normal rays are used. The intersection between rays passing through a candidate facet, in the direction $\hat{\mathbf{k}}^t$ with each other candidate facet are sought. If a successful intersection is found, i.e. one which is within the confines of the facet, then the facet from

which the ray originated is classed as being 'blocking' and the facet which was intercepted is considered as 'blocked'. This process is repeated until all candidate facets have being grouped. At which stage two sets are defined, those which are blocking the transmitted beam, and those which are blocked, i.e. are overshadowed. It is important that for each potentially blocked facet, the facets which may block some of the beam are also stored. Any facet which neither blocks, or is itself blocked, is stored separately.

Steps 3-6 have been discussed before. The difference now is that the process is performed on different facet groups. We will consider one such grouping, shown in Figure 4.21. One of the prism facets has been identified as being potentially blocked, the facets which could block the transmitted beam are coloured. These two facet groups, along with the beam (shown in red) are projected on to the beam splitting plane, Figure 4.22.

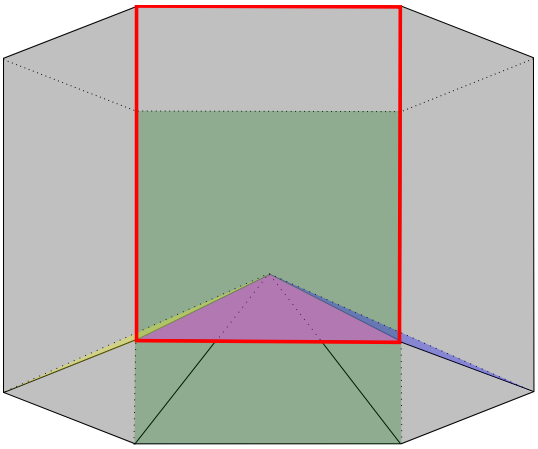

Figure 4.21: Two facet groups, the facet shown in green is partially blocked by the facets shaded in yellow, magenta and blue. The transmitted beam cross section is shown in red.

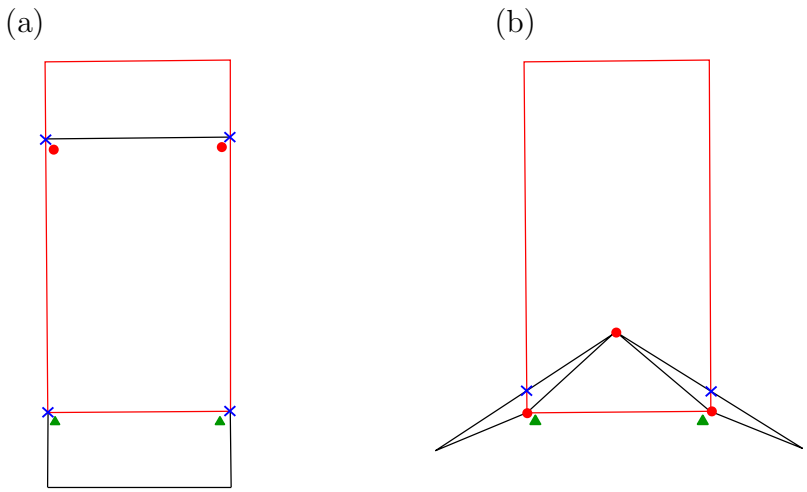

Figure 4.22: (a) Projection of facets which are potentially blocked by other facets [given in (b)] along with the beam, shown in red. (b) Blocking facets and beam in the beam splitting plane. As in Figure 4.6 blue crosses indicate new beam vertices found by line intersections; red circles are crystal vertex projections bound by the beam cross section and green triangles are beam vertices bound by facet projections.

Step 9: Removing the shadow portion

Once Steps 3-8 have been carried out the result is two sets of position vectors. The first set, denoted by X, contains the position vectors of new beam vertices (in the beam splitting plane) on the potentially blocked facet. Likewise, the set of position vectors found through investigating blocking facets is denoted by Y. If the beam is blocked by any facets then there will be at least one vertex common to both sets X and Y. If no such vector exists then the beam is not blocked and each set can be projected back on to the crystal. However, if the beam is blocked then the position vectors of the illuminated region, on the blocked facet, are given by the symmetric difference between the sets X and Y, defined as:

$$\widetilde{X} = X \oplus Y = (X \setminus Y) \cup (Y \setminus X), \tag{4.18}$$

where $\setminus$ denotes the set difference and $\cup$ the set union. This operation yields the position vectors which are not shared by either set, Figure 4.23 shows the process. In panel (a) the illuminated region on the prism facet is given, at this stage blocking has yet to be considered. The vertices, indicated by black circles, are stored in the set X. Panel (b) gives the same but for the blocking facets, the colours reflecting those used in Figure 4.21; these vertices are stored in the set Y. In panel (c) the two sets are overlaid; (d) shows the resulting set found once the symmetric difference has been taken. The position vectors in $\widetilde{X}$ can then be projected back onto the crystal through use of Equation 4.12. Those position vectors in Y are grouped by facet and then projected back on to the crystal, giving rise to new beams (in this case three).

This process is repeated for all potentially blocked facets. If the same blocking facet is investigated more than once, it is not projected back on to the crystal as this would lead to beam duplication leading to errors.

For those candidate facets which were not blocked and did not block any others the process is the same as for previous cases. The transmitted beam thus considered would illuminated regions on five different facets, leading to five new beams, which are shown in Figure 4.24. The additional beam, coloured cyan, arises during Steps 11 and 12.

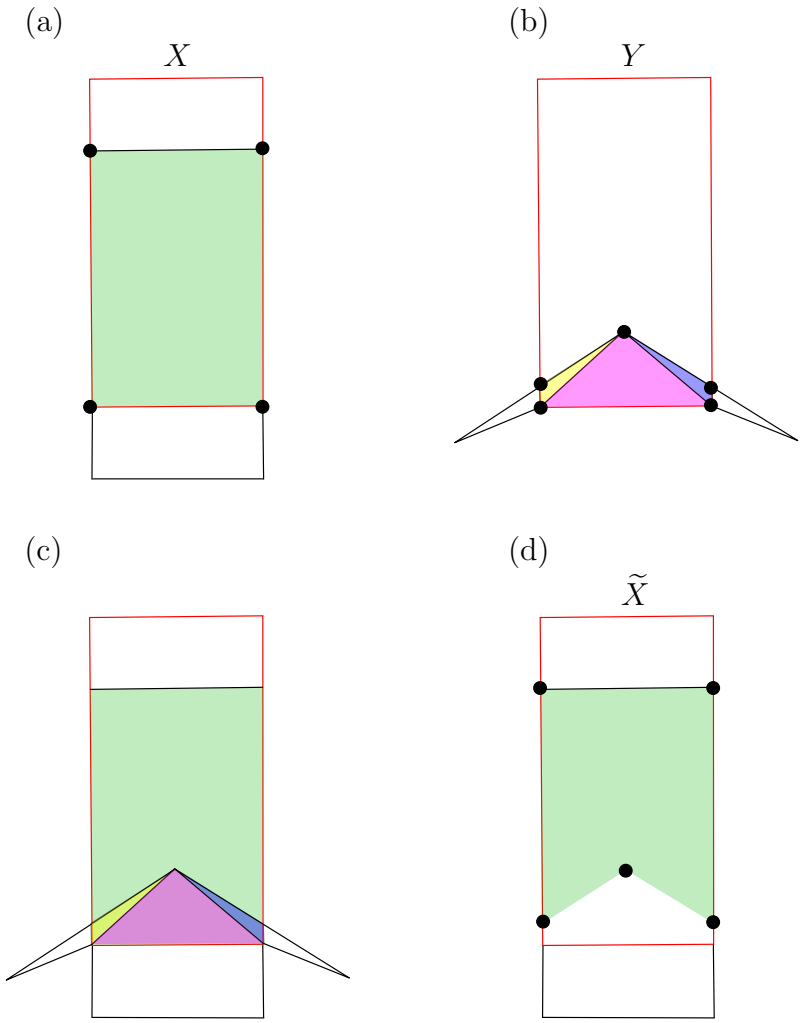

Figure 4.23: The process of removing the blocked portion of the transmitted beam. (a) The illuminated region on the prism facet ignoring blocking. (b) The illuminated region on the blocking facets. (c) Parts (a) and (b) overlaid. (d) the removal of the blocked region.

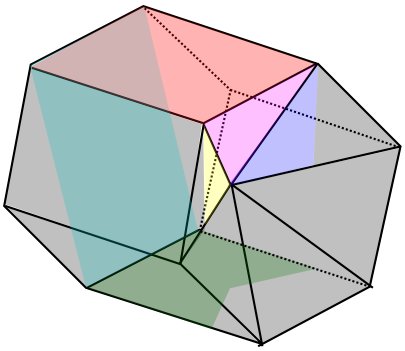

Figure 4.24: Five new beams are spawned in this case from the beam transmitted through the top prism facet.

The process outlined in this section allows the beam tracing model to be applied to particles which have concavities or shadow regions; which significantly increases the range of crystal habits it can be applied to. The discussion so far has focussed on geometric considerations of the model. In the sections to follow physical properties of beams will be explained and how they are implemented in the model.

4.5 The Amplitude Scattering Matrix

The *amplitude scattering matrix* was discussed in Section 2.5 and is repeated below for convenience in Equation 4.19. In order to determine the amplitude scattering matrix for the ice-crystal, we associate with each beam an amplitude matrix. This describes the effect the crystal has had on the incident electric field vector of the beam. The sum of all the beams' amplitude matrices then gives rise to the θ and ϕ resolved amplitude scattering matrix,

$$\begin{pmatrix} E_{\parallel}^{s} \\ E_{\perp}^{s} \end{pmatrix} = \frac{\exp(ikR)}{-ikR} \begin{pmatrix} S_2 & S_3 \\ S_4 & S_1 \end{pmatrix} \begin{pmatrix} E_{\parallel}^{i} \\ E_{\perp}^{i} \end{pmatrix}. \tag{4.19}$$

In the trivial case that there is no ice-crystal and hence no scattering, the incident field would be unchanged and the scattering matrix would be equal to the 2×2 identity matrix. This section outlines how a beam's amplitude matrix is altered as it interacts with the ice-crystal. In order to do this, it is necessary to first discuss the various planes used throughout the beam tracing process.

4.5.1 Reference Plane and Incident Field

The incident wave is travelling in the negative z direction and has its electric field amplitude vectors decomposed with respect to a reference plane, which is chosen to be the xz plane. The polarisation vectors, along with the direction vector form an orthogonal trio,

$$\hat{\mathbf{k}} = \hat{\mathbf{e}}_{\perp} \times \hat{\mathbf{e}}_{\parallel}. \tag{4.20}$$

Unit vectors parallel and perpendicular are:

$$\hat{\mathbf{e}}_{\parallel} = [1, 0, 0]^T, \tag{4.21a}$$

$$\hat{\mathbf{e}}_{\perp} = [0, 1, 0]^T. \tag{4.21b}$$

Which describe the polarisation of the incident beam. New polarisation vectors are found each time there is a beam-facet interaction.

4.5.2 Plane of Incidence and Fresnel Matrices

The Fresnel amplitude coefficients, discussed in Section 2.3 provide the means to determine the proportion of a wave's amplitude which is transmitted or reflected. By expressing them in matrix form, they can be used in conjunction with the Jones calculus. The *Fresnel transmission matrix*, $\mathbf{T}$, and the *Fresnel reflection matrix*, $\mathbf{R}$ are given by

$$\mathbf{T} = \begin{pmatrix} t_{\parallel} & 0 \\ 0 & t_{\perp} \end{pmatrix}, \tag{4.22a}$$

$$\mathbf{R} = \begin{pmatrix} r_{\parallel} & 0 \\ 0 & r_{\perp} \end{pmatrix}. \tag{4.22b}$$

Whenever a beam encounters a crystal facet these matrices can be used to determine the amplitude matrices of the reflected and transmitted beams. However, the Fresnel coefficients apply to amplitudes expressed with respect to a *plane of incidence*. The plane of incidence is the name given to the plane which contains the local surface normal and the three propagation vectors corresponding to the directions of incidence, reflection and transmission, as seen in Figure 4.25.

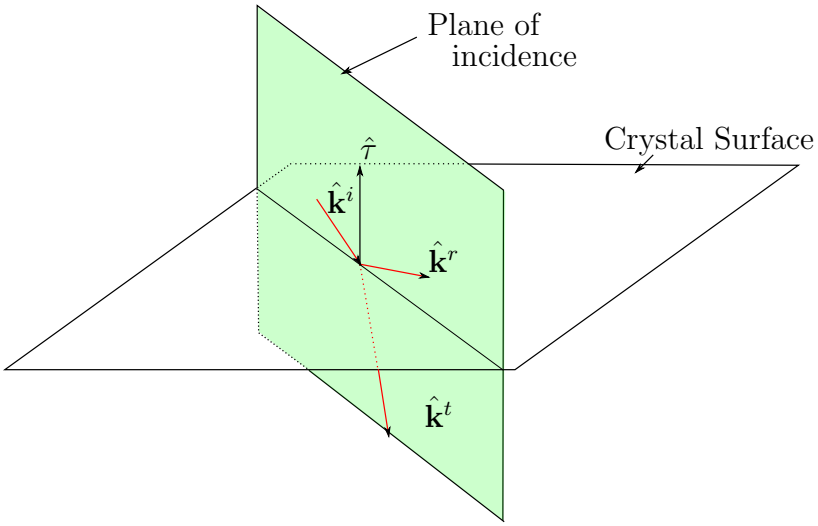

Figure 4.25: The plane of incidence contains the surface normal and the three geometric optics propagation vectors.

The incident beam's amplitude matrix was expressed with respect to the last plane of incidence (in the case of external incidence, this is the reference plane). To go from this plane to the new plane we apply a rotation matrix which rotates the polarisation vectors of the beam into the new plane of incidence. The rotation matrix has the form:

$$\mathbf{L} = \begin{pmatrix} \cos\Theta & \sin\Theta \\ -\sin\Theta & \cos\Theta \end{pmatrix} \tag{4.23}$$

which describes a counter-clockwise rotation by an angle $\Theta \in [0, \pi]$ when looking in the direction of propagation. In order to perform this rotation, a vector perpendicular to the new plane of incidence is required. Since this plane contains the surface

normal and the incident propagation vector, the new perpendicular vector can be found using:

$$\mathbf{e}'_{\perp} = \hat{\mathbf{k}}^i \times \hat{\tau}. \tag{4.24}$$

As the rotation serves to rotate the old perpendicular vector and align it with the new it follows that:

$$\cos\Theta = \hat{\mathbf{e}}'_{\perp} \cdot \hat{\mathbf{e}}_{\perp}. \tag{4.25}$$

Figure 4.26 provides a schematic of the rotation discussed. Since the rotation angle is restricted in its range between 0 and π, the sense of the rotation has to be properly considered. The intersection between the old and new planes of incidence defines a line on which lies the vector in the direction of incidence, $\hat{\mathbf{k}}^i$. As the new perpendicular electric field vectors are both perpendicular to this vector, their cross product will either be parallel or anti-parallel to it. If the cross product is parallel, then the rotation is clockwise and the negative sign in Equation 4.23 goes with the upper right sine. The inverse statement is true for the anti-parallel case in which the rotation is considered anti-clockwise and as such Equation 4.23 is unchanged. Incorporating this criterion gives a modified form of Equation 4.23 namely:

$$\mathbf{L} = \begin{pmatrix} \cos\Theta & \xi\sin\Theta \\ -\xi\sin\Theta & \cos\Theta \end{pmatrix} \tag{4.26}$$

where,

$$\xi = \begin{cases} 1 & \text{if } (\hat{\mathbf{e}}_{\perp} \times \hat{\mathbf{e}}'_{\perp}) \cdot \hat{\mathbf{k}}^i = -1 \\ -1 & \text{if } (\hat{\mathbf{e}}_{\perp} \times \hat{\mathbf{e}}'_{\perp}) \cdot \hat{\mathbf{k}}^i = 1. \end{cases} \tag{4.27}$$

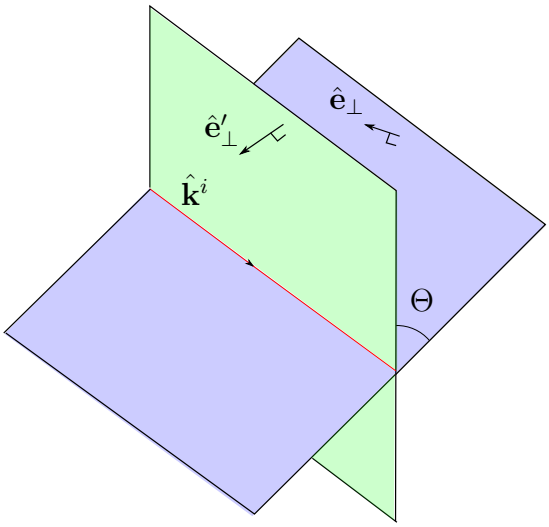

Figure 4.26: The angle Θ is the angle between the two planes of incidence. Here, the blue and green planes are the old and new planes of incidence respectively.

It follows immediately from Equation 4.20 that the new parallel polarisation vector is given by:

$$\mathbf{e}'_{\parallel} = \hat{\mathbf{k}}^r \times \hat{\mathbf{e}}'_{\perp}. \tag{4.28}$$

With the rotation matrix determined, it is now possible to apply the Fresnel matrices given in Equations 4.22a and 4.22b to determine the amplitude matrix $\mathbf{M}$ of the transmitted and reflected beams,

$$\mathbf{M}^t = \mathbf{T} \cdot \mathbf{L} \cdot \mathbf{I} = \begin{pmatrix} t_\parallel & 0 \\ 0 & t_\perp \end{pmatrix} \begin{pmatrix} \cos\Theta & \xi \sin\Theta \\ -\xi \sin\Theta & \cos\Theta \end{pmatrix} \begin{pmatrix} 1 & 0 \\ 0 & 1 \end{pmatrix}, \tag{4.29a}$$

$$\mathbf{M}^r = \mathbf{R} \cdot \mathbf{L} \cdot \mathbf{I} = \begin{pmatrix} r_\parallel & 0 \\ 0 & r_\perp \end{pmatrix} \begin{pmatrix} \cos\Theta & \xi \sin\Theta \\ -\xi \sin\Theta & \cos\Theta \end{pmatrix} \begin{pmatrix} 1 & 0 \\ 0 & 1 \end{pmatrix}. \tag{4.29b}$$

The elegance of this is that the process of rotations followed by application of Fresnel matrices can be applied for every new beam-crystal facet interaction while a beam is propagating through the crystal, i.e. as many times as given in the input file. When the beam leaves the crystal a final rotation is needed into the *scattering plane*.

4.5.3 Scattering Plane

The scattering plane is defined as the plane which contains the initial incident propagation vector $\hat{\mathbf{k}}_0$ (which for this work is always $\hat{\mathbf{k}}_0 = [0, 0, -1]$) and the direction of scattering $\hat{\mathbf{k}}^s$, see Figure 4.27. Rotating into the scattering plane is a two-stage procedure and here the formalism laid out by Hovenier and van der Mee [91] is followed.

The first stage is to rotate from the last plane of incidence to the scattering plane. The rotation angle is found using a similar approach to that used to determine Θ in Equation 4.25; namely that a vector perpendicular to the scattering plane is found first which is then used to determine the rotation angle. The scattering plane contains both $\hat{\mathbf{k}}_0$ and $\hat{\mathbf{k}}_s$ which means that their cross product will yield such a vector,

$$\mathbf{e}_\perp^s = \hat{\mathbf{k}}_0 \times \hat{\mathbf{k}}^s. \tag{4.30}$$

This can then be used to calculate the rotation angle in precisely the same way as in Equation 4.25 to rotate the polarisation vectors into the scattering plane.

A second rotation is required to take the reference plane into the scattering plane. The perpendicular vectors needed for this are already known from Equations 4.21b and 4.30. Taking the scalar product between these provides the rotation angle needed to get from the reference plane to the scattering plane.

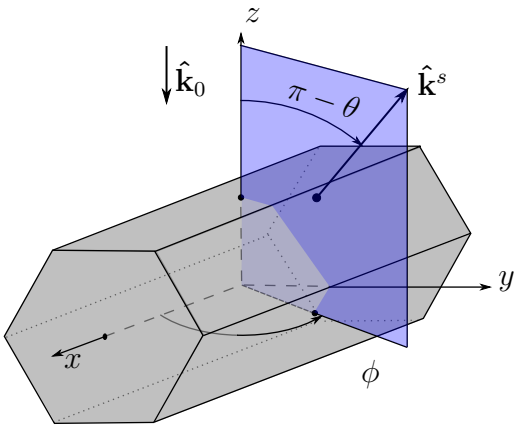

Figure 4.27: The scattering plane, shown in blue, is the plane that contains the incident ($\hat{\mathbf{k}}_0$ and scattered $\hat{\mathbf{k}}^s$ propagation vectors). Also shown are the scattering angle θ and azimuthal angle ϕ.

Let the rotation matrix which rotates the plane of incidence to the scattering plane be denoted by $\mathbf{L}_s$. Similarly, let the rotation from the reference plane to the scattering plane be denoted by $\mathbf{L}_p$. Then, the amplitude matrix of the externally reflected beam is

$$\mathbf{M}^r = \mathbf{L}_s \cdot \mathbf{R} \cdot \mathbf{L} \cdot \mathbf{I} \cdot \mathbf{L}_p. \tag{4.31}$$

Note that the rotation $\mathbf{L}_p$ has to be pre-multiplied since its purpose is to align the reference plane to the scattering plane.

4.5.4 Higher Order Events

At the end of Section 4.5.2 it was alluded to that the process of applying the Fresnel matrices in conjunction with rotations allows the amplitude matrix of a beam to be traced as it propagates through the crystal. Then, in Section 4.5.3 the extra rotations necessary to place the polarisation vectors of the scattered beam into the scattering plane were given. Combining these it becomes possible to write the general form for the amplitude matrix of a beam, propagating away from the crystal, after an arbitrary number of internal reflections.

$$\mathbf{M} = \mathbf{L}_s \cdot \mathbf{T}_2 \cdot \mathbf{L}_{n-1} \ldots \cdot \mathbf{R}_2 \cdot \mathbf{L}_2 \cdot \mathbf{R}_1 \cdot \mathbf{L}_1 \cdot \mathbf{T}_1 \cdot \mathbf{L}_0 \cdot \mathbf{I} \cdot \mathbf{L}_p. \tag{4.32}$$

4.5.5 The Total Amplitude Scattering Matrix

It can be imagined that surrounding the particle is a sphere whose radius is large compared to that of the particle. The radius of this sphere is sufficiently large that we can consider any two beams which propagate away from the crystal in a particular direction (θ, ϕ) to hit the sphere at the same point; their combined amplitude matrices provide the scattering matrix elements for that direction. For now, phase effects are ignored and it is assumed that the beams undergo no diffraction as they propagate away from the crystal; both of these will be addressed later on. With this current restriction in place, the amplitude scattering matrix of the crystal, in the direction (θ, ϕ) is:

$$\mathbf{S}(\theta, \phi) = \sum_{i=1}^{N} A_i \cdot \mathbf{M}_i(\theta, \phi), \tag{4.33}$$

where the summation is performed over all beams. The multiplicative factor A_i is the cross sectional area of the beam which will be discussed in Section 4.6.1. In the geometric optics regime, there would be many scattering directions where the elements of the scattering matrix for that direction would be zero. This is because geometric optics leads only to discrete scattering directions corresponding to the directions of scattered beams. Later, it will be seen that diffraction changes this.

While the beam amplitude components are necessary for determining the intensity of beams, as well as the angular distribution of the scattered light and its polarisation properties, they on their own do not provide the quantities desired from the beam tracer. The next section outlines various properties of the beams themselves which help give rise to a more complete model.

4.6 Beam Properties

Associated with each beam are a number of physical properties which are necessary for informative modelling of light scattering. This section discusses these along with their implementation within the model.

4.6.1 Beam Cross-sectional Area

Unlike a ray which has infinitesimal area, the beam has a clearly defined area when it intersects a plane. For planar surfaces with non-curved edges a beam's cross section can be determined from Stokes' theorem. Consider a beam cross section with n vertices with position vectors $\mathbf{b}_1 \dots \mathbf{b}_n$, its centre having position vector $\mathbf{m}$. By using the centre as a reference point, the cross section can be divided into triangles as is shown in Figure 4.28.

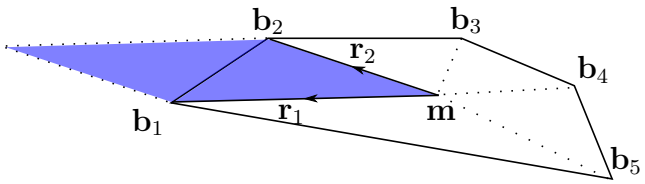

Figure 4.28: Division of a beam cross section into triangles.

The vectors from the centre to the beam vertices as are labelled as $\mathbf{r}_1 \dots \mathbf{r}_n$. The magnitude of the cross product can be geometrically interpreted as the signed area of the parallelogram formed by the two vectors. However, since the cross section may not lie in the xy plane, it is necessary to include the normal vector to the surface which is intersecting the beam as well as taking the absolute (which ensures that the area is positive). The area of the beam cross section on the facet is therefore given by

$$A = \frac{1}{2} \left| \sum_{j=1}^{n} (\mathbf{b}_j \times \mathbf{b}_{j+1}) \cdot \hat{\tau} \right|. \tag{4.34}$$

Note that when $j = n$, $j + 1 = 1$. It is necessary to divide by two since it is the area of the individual triangles that is required, not the parallelograms.

Knowing the cross sectional area of the beam allows for the beam's irradiance to be calculated by using its amplitude matrix.

4.6.2 Irradiance and Energy

The irradiance of an electromagnetic wave is proportional the square of its amplitude. In terms of a beam's amplitude matrix, the following relation (used in determining the first element of the 4×4 phase matrix, see Section 2.5) is used to determine its irradiance:

$$I = \frac{1}{2}(|S_2|^2 + |S_3|^2 + |S_4|^2 + |S_1|^2). \tag{4.35}$$

Conservation of energy required for beams at a boundary is that the irradiance of the incident beam must equal the sum of the irradiances of the reflected and transmitted beam:

$$I^i = I^r + \frac{m_1 \cos\vartheta_i}{m_2 \cos\vartheta_t} I^t, \tag{4.36}$$

where I represents the irradiance of the given beam and the superscripts have their usual meaning. The quotient next to the transmitted intensity takes into account the fact that the energy density is less in the transmitted beam. As beams have a finite cross section their power can be determined; the power of a given beam, illuminating a facet with surface normal $\hat{\tau}$, is given by

$$P_i = I_i \times A_i(\hat{\mathbf{k}}_i \cdot \hat{\tau}), \tag{4.37}$$

where A is the beam cross sectional area on the facet. The term in brackets projects the area on to a plane perpendicular to the direction of propagation of the beam. This is of course necessary since a beam illuminating a surface at a grazing angle may have a large cross section, but low irradiance which would increase as the angle of incidence decreased. The power of the parent beam is redistributed between its children giving rise to the following energy conservation requirement:

$$P_{\text{parent}} = \sum P_{\text{children}}. \tag{4.38}$$

Equation 4.36 can then be rewritten in terms of beam power,

$$P^i = \sum P^r_{\text{children}} + \frac{m_1}{m_2} \sum P^t_{\text{children}}, \tag{4.39}$$

with the cosines no longer needed since the projected areas are now included implicitly in the power calculations. The summations take place over all child beams formed through the reflection / transmission. Working under the assumption of the particles being convex, only one process will lead to the formation of beamlets, either external transmission or internal reflection.

It is necessary to provide a numerical cut-off; a criterion which determines whether a beam should continue being traced. In ray tracing, one traditionally uses the irradiance. The temptation would therefore be to use irradiance in the beam tracing model, or potentially even the beam cross section. However, doing so would cause the following two problems:

1. Low intensity, large area beams would be ignored, and
2. High intensity, small area beams would be ignored.

By using the power both of these issues are resolved. When a beam's power falls below a threshold value of $P_j < 10^{-5}$ W the code no longer considers its propagation and it is traced no further.

4.6.3 Phase

Associated with a beam is its phase which is needed to model interference effects. The key assumption in modelling the phase of the beams is that they can be treated as plane waves at all points in their travel. As a direct consequence of this assumption the phase is constant anywhere on the plane perpendicular to the beam's propagation direction. The assumption of constant phase across a cross section is extended to cases where the cross section is formed via intersection with a crystal facet. For normal incidence, the approximation is exact, however, if the beam is incident at large, oblique angles to the facet the resulting cross section will have significant phase variation over the cross section reducing the accuracy of the approximation, see Figure 4.29.

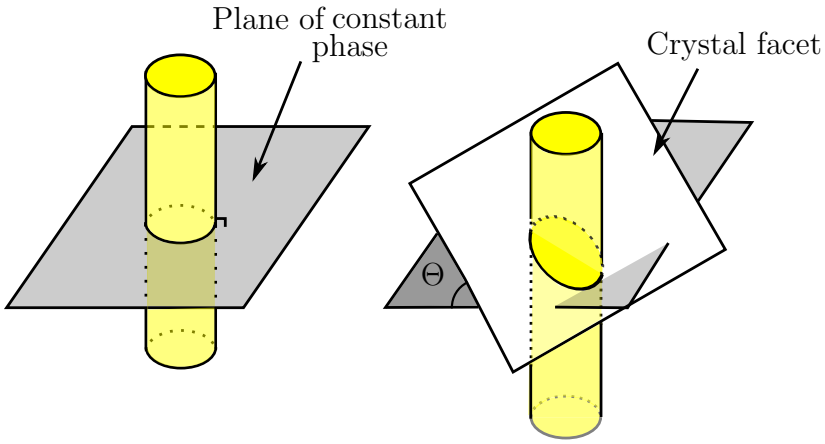

Figure 4.29: The Beam Tracer assumes constant phase over the cross section. When the intersecting facet is perpendicular to the beam the approximation is exact, as shown in the left panel. However, when the beam intersects the facet at some angle Θ the approximation gets weaker, becoming less valid as the angle Θ increases, shown in the right panel.

Maintaining this assumption the beam's phase can be determined by knowing the beam's optical path length. To determine this one must find the total path that a ray striking the centre of the beam, travelling parallel to the beam would have taken. It is important to stress that this is not the same as finding the distance from the parent beam's mid-point to the child beam's mid-point. If one does this then the ray which passes through both these mid-points is not necessarily travelling parallel to the beam. Figure 4.30 visualises this, the incident beam propagates in the direction $\hat{\mathbf{k}}^i$ illuminating the region shown. The beam then refracts into the crystal whereupon it illuminates two regions, defining two new beam cross sections. The centre of each of the three cross sections are indicated by a filled black circle,

the two dashed lines join the centres of beams 2 and 3 with the parent beam centre. These lines are not parallel to the direction of transmission of $\hat{\mathbf{k}}^t$ and therefore a ray travelling along them would not be propagating in the direction $\hat{\mathbf{k}}^t$. Therefore one needs to find the location on the parent beam's cross section where a ray would have passed to intersect the centre of the new beam. These rays are shown in red and green. The distance from these points to the reference plane is then found.

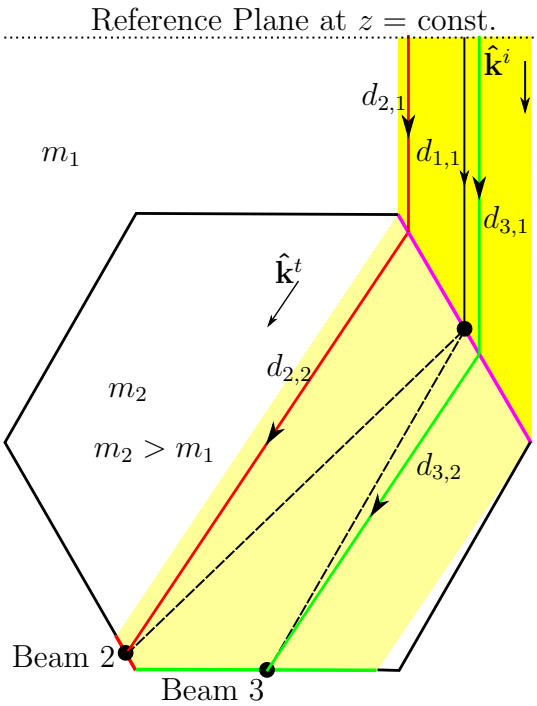

Figure 4.30: A parent beam leads to new child beams. To correctly determine the phase of the new beams it is not sufficient to take the distance between the centre of each child beam's cross section (child beam cross sections are shown in red and green) to the centre of parent beam's cross section (shown in magenta). This is because rays travelling along such paths (black dashed lines) would not be parallel to the propagation vector. Instead one has to find the position on the parent beam's cross section where a ray would have passed to intersect the centre of a given child beam's cross section. Such rays are shown in red and green.

The optical path length is defined as:

$$\Lambda = \int m(s)\mathrm{d}s \tag{4.40}$$

Where ds is a path element. However, since we are considering homogenous ice-crystals we assume that the refractive index is not a function of position while inside (or outside of) the particle. As such, Equation 4.40 reduces to:

$$\Lambda = m \cdot d \tag{4.41}$$

with d being the distance travelled in the medium of refractive index m. With this in mind, the total optical path for the i^{th} beam, of order p, can be approximated as:

$$m_1 \cdot d_{i,1} + m_2 \sum_{j=2}^{p} d_{i,j}. \tag{4.42}$$

Where the summation is performed over all internal beam-facet interactions. Note that the determination of the central ray path has to be re-evaluated for each new beamlet formed as a consequence of internal reflection.

In Equation 4.42 the presence of the refractive indices serves to modify the distance due to the change in the wavelength of the beam. When the beam exits the crystal its phase delay with respect to a reference ray is calculated and added to the optical path. This reference ray propagates from the centre of the particle in the same direction as the outgoing beam, as shown in Figure 4.31.

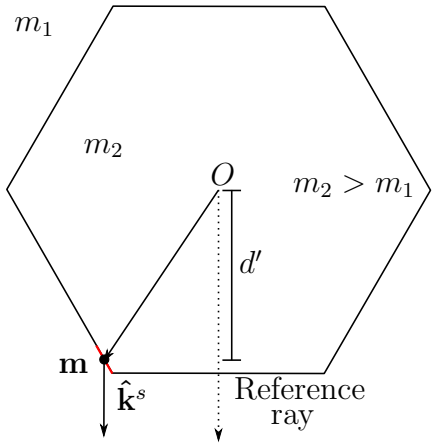

Figure 4.31: The phase delay is found through comparison with a reference ray which originates at the centre of the crystal and propagates in the direction of the scattered beam $\hat{\mathbf{k}}^s$.

With the centre of the crystal at the origin and denoting the position vector of the centre of the beam cross section as $\mathbf{m}$, the phase delay distance d' is the length of the projection of the vector $\mathbf{m}$ onto the scattering direction vector $\hat{\mathbf{k}}^s$, that is:

$$d' = \mathbf{m} \cdot \hat{\mathbf{k}}^s. \tag{4.43}$$

This is about the difference in the path lengths to infinity between the ray starting at the crystal surface and the reference ray. In Figure 4.31, the ray from the surface has to travel a distance $d' = \mathbf{m} \cdot \hat{\mathbf{k}}^s$ less than the reference ray. Therefore its contribution is subtracted from the total optical path. As such, for the i^{th} beam the total optical path is:

$$\Lambda_i = m_1(d_{i,1} - \mathbf{m} \cdot \hat{\mathbf{k}}^s) + m_2 \sum_{j=2}^{p} d_{i,j}. \tag{4.44}$$

If the particle has concavities then Equation 4.44 has to be modified to take into account portions of the beam's history when it may have been propagating outside

of the crystal, becoming:

$$\Lambda_i = m_1(d_{i,1} - \mathbf{m} \cdot \hat{\mathbf{k}}^s) + \sum_{j=2}^{p} \Xi_j d_{i,j}, \tag{4.45}$$

where

$$\Xi_j = \begin{cases} m_1 & \text{if portion of beam's journey was outside the crystal.} \\ m_2 & \text{if portion of beam's journey was inside the crystal.} \end{cases} \tag{4.46}$$

The phase of this beam is then:

$$\psi = \frac{2\pi}{\lambda}\Lambda_i. \tag{4.47}$$

The beam's amplitude matrix is adjusted to include this phase information,

$$\mathbf{M}' = e^{-i\psi}\mathbf{M}. \tag{4.48}$$

4.7 Modelling Absorption

Absorption is the process of wave energy being transformed in heat, the decrease in wave energy leads to attenuation of the wave as it propagates through the medium. While ice is mainly transparent in the optical and the infra-red, depending on wavelength it does exhibit some weakly absorbing properties. Warren et al. [92] detailed the real and imaginary parts of the complex refractive index of ice from the ultraviolet to the microwave region. The beam tracing model does not consider how the crystal is affected by absorbing electromagnetic energy, i.e. melting of the ice crystal, it only models the attenuation of the beam. The refractive index of an absorbing medium is a complex quantity where the imaginary part describes how strongly it absorbs, e.g.

$$\widetilde{m} = m_r + \mathrm{i}m_i. \tag{4.49}$$

Which is sometimes written as:

$$\widetilde{m} = m(1 + \mathrm{i}\kappa). \tag{4.50}$$

Note that if we had chosen the time harmonic factor $\exp(\mathrm{i}\omega t)$ instead of $\exp(-\mathrm{i}\omega t)$ in Equation 2.7 then the imaginary component in the above equations would have been negative. Absorption leads to the attenuation of the amplitude of the beam inside the medium, however it also leads to wave inhomogeneities meaning that the planes of constant amplitude do not coincide with the planes of constant phase (see e.g. [15]). The Poynting vector, indicating the direction of propagation of the wave is perpendicular to the latter. Furthermore, the presence of a complex refractive index leads to a non-geometrical interpretation of Snell's law.

This section will give alternative formulas for the transmission angle and the Fresnel equations. Furthermore, a description of how absorption alters the shapes of incident beams will be given and the method for further sub-division of beams will be described.

4.7.1 Modified Snell's Law

At an air-ice interface we can set the refractive index of air to be approximately unity. Denoting the complex refractive index of ice as $\widetilde{m}$, Snell's law can be written as:

$$\sin\vartheta_t = \frac{\sin\vartheta_i}{\widetilde{m}_2}. \tag{4.51}$$

Whereupon the geometric interpretation fails, after all a complex angle has no meaning in this context. Macke [50] uses a modified Snell's law which can be traced to Born and Wolf [15] which is the same approach taken in the beam tracer. An alternative method is the *effective refractive index* [93], we only use the former as it has been shown to be the same as the latter [94].

When an electromagnetic wave propagates inside an absorbing medium the planes of constant amplitude deviate from the planes of constant phase; a property known as *wave inhomogeneity*. The planes of constant amplitude will be parallel to the boundary since amplitude decays with distance. The planes of constant phase however will not necessarily coincide with these. The angle of transmission we use is the angle between the normals to these planes, and the normal to the surface. In this way we write a modified Snell's law as:

$$\sin\vartheta_t' = \frac{\sin\vartheta_i}{\sqrt{\sin^2\vartheta_i + m^2q^2(\cos\gamma - \kappa\sin\gamma)^2}} = \frac{\sin\vartheta_i}{m'}. \tag{4.52}$$

Here, q and γ are real constants which are found by considering the direction of transmission. A full explanation of these, and a derivation of Equation 4.52, is given in Appendix C. This is the form of Snell's law that is used in the beam tracing algorithm. In much the same way as it is possible to arrive at an equation for the planes of constant phase we can get expressions for the amplitude and phase of the reflected and transmitted components.

4.7.2 Fresnel's Generalised Equations

The electromagnetic boundary conditions and the interface separating the two media are the same as for the non-absorbing case leading to the generalised Fresnel amplitude coefficients given below:

$$r_\perp = \frac{\widetilde{m}_1\cos\vartheta_i - \sqrt{\widetilde{m}_2^2 - \widetilde{m}_1^2\sin^2\vartheta_i}}{\widetilde{m}_1\cos\vartheta_i + \sqrt{\widetilde{m}_2^2 - \widetilde{m}_1^2\sin^2\vartheta_i}} \tag{4.53a}$$

$$r_\parallel = \frac{\widetilde{m}_2^2\cos\vartheta_i - \widetilde{m}_1\sqrt{\widetilde{m}_2^2 - \widetilde{m}_1^2\sin^2\vartheta_i}}{\widetilde{m}_2^2\cos\vartheta_i + \widetilde{m}_1\sqrt{\widetilde{m}_2^2 - \widetilde{m}_1^2\sin^2\vartheta_i}} \tag{4.53b}$$

$$t_\perp = \frac{2\widetilde{m}_1\cos\vartheta_i}{\widetilde{m}_1\cos\vartheta_i + \sqrt{\widetilde{m}_2^2 - \widetilde{m}_1^2\sin^2\vartheta_i}} \tag{4.53c}$$

$$t_\parallel = \frac{2\widetilde{m}_1\widetilde{m}_2\cos\vartheta_i}{\widetilde{m}_2\cos\vartheta_i + \widetilde{m}_1\sqrt{\widetilde{m}_2^2 - \widetilde{m}_1^2\sin^2\vartheta_i}} \tag{4.53d}$$

Note that when the refractive indexes are real, these equations reduce back to the regular forms given in Equations 2.12a-2.12d. The corresponding matrix represen-

tation remains unchanged, that is:

$$\mathbf{T} = \begin{pmatrix} t_{\parallel} & 0 \\ 0 & t_{\perp} \end{pmatrix} \tag{4.54a}$$

$$\mathbf{R} = \begin{pmatrix} r_{\parallel} & 0 \\ 0 & r_{\perp} \end{pmatrix}. \tag{4.54b}$$

However, the matrices are now complex quantities. We now have means to calculate the propagation direction in an absorbing medium as well as amplitudes. It should be stated that while in this way we model the change in propagation direction we do not model wave inhomogeneity. It has been reported in the literature though that the effect of wave inhomogeneity on the scattering properties of a particle are likely to be small [93]. The justification for this is that inhomogeneity is only significant when particles are highly absorbing, but for such particles such little light escapes the particle (i.e. is not absorbed) that any effects will be dwarfed by contributions from external diffraction and reflection.

4.8 Incorporating Absorption into the Beam Tracer

The most straightforward effect of absorption is the attenuation of the beam as it propagates through the crystal, its amplitude matrix is adjusted as follows:

$$\mathbf{M}'_j = \exp(-km_i d_j)\mathbf{M}_j. \tag{4.55}$$

Here d_j is the distance the beam has travelled inside the crystal, it is taken to be the same as the phase distance (see Section 4.6.3). The approximation of equal intensity across a beam's cross section is no longer valid for an absorbing crystal as can be seen in Figure 4.32. Denoting the intensity of the incoming beam by I_0 the intensity at some distance d is given by Beer's law:

$$I = I_0 \exp(-2km_i d). \tag{4.56}$$

Note that the argument in the exponent is different in Equations 4.55 and 4.56. This is because in the former electric field amplitudes are being considered whereas in the latter it is modelling the change in intensity ($I \propto |E|^2$). As an approximation, the beam is sub-divided into regions which have a proportional drop in intensity $\Delta I = I/I_0$. The length corresponding to a percentage drop is found by rearranging Equation 4.56,

$$d = -\frac{1}{2km_i} \ln(\Delta I). \tag{4.57}$$

Decreasing the size of the allowed change in intensity ΔI will increase the number of regions which the cross section is to be divided into. One can therefore think of ΔI as a resolution, decreasing ΔI increases the resolution of the beam tracer. As absorption is an exponential decay, dividing the beam cross section does not results in strips of equal width.

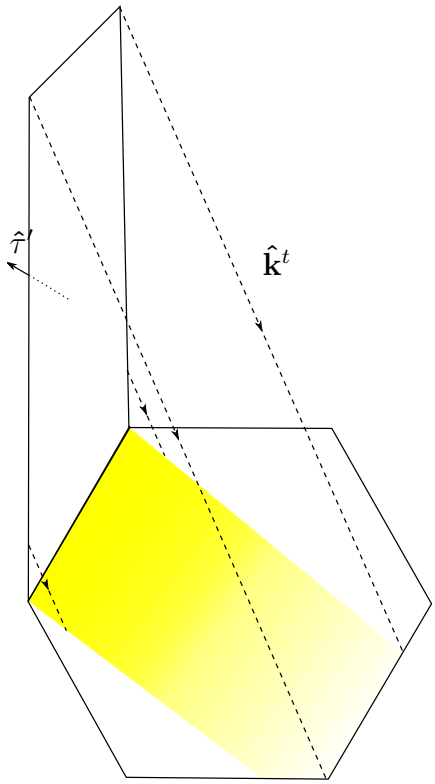

Figure 4.32: The intensity of a beam decreases as the distance it has travelled through the crystal increases. This leads to an intensity variation over the cross section of the beam with the surface it is illuminating.

In order to sub-divide the incident beam we make use of two vectors, one in the direction of constant intensity and one the projection of the propagation vector $\hat{\mathbf{k}}^t$ on the intersected facet. Let

$$\mathbf{k}^t_{\text{proj}} = \hat{\mathbf{k}}^t - (\hat{\mathbf{k}}^t \cdot \hat{\tau})\hat{\tau} \tag{4.58}$$

be the aforementioned projection, whereas before $\hat{\tau}$ is the surface normal. On the crystal surface there will exist lines of constant distance from the previously illuminated facet, to determine a vector in the direction of constant intensity, project the previous illuminated facet's surface normal $\hat{\tau}'$ on to the new facet,

$$\mathbf{u} = \hat{\tau}' - (\hat{\tau}' \cdot \hat{\tau})\hat{\tau}. \tag{4.59}$$

This vector can then be used to yield a vector in the direction of constant intensity (see Figure 4.33),

$$\mathbf{w} = \hat{\mathbf{u}} \times \hat{\tau}. \tag{4.60}$$

For a start point the code chooses the beam vertex corresponding to the least distance travelled $\mathbf{v}$ (if there are two such vertices, either one will do). The position vector of a point on the line through $\mathbf{v}$ at which the intensity has dropped by the factor ΔI is

$$\mathbf{r} = \mathbf{v} + d \sin\vartheta_i \hat{\mathbf{k}}^t_{\text{proj}} \tag{4.61}$$

The additional $\sin\vartheta_i$, where ϑ_i is the angle of incidence, term takes into account that the distance d from Equation 4.57 corresponds to the length of the ray from the previous facet to the currently illuminated one, see Figure 4.33. From the point

$\mathbf{r}$ we seek the intersection of the line $\ell = \mathbf{r} + \xi\hat{\mathbf{w}}$ with the edges of the beam cross section. In particular two solutions are sought which are within the region bounded by the beam which is determined using the method described in 4.3.2 (see Figure 4.7).

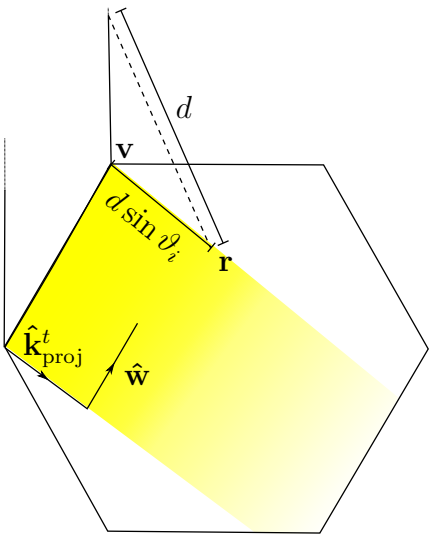

Figure 4.33: Vectors used in the division of a beam due to absorption. The vector $\hat{\mathbf{w}}$ points in the direction of constant intensity.

Repeating this process as many times as required to achieve the desired intensity resolution results in additional beam vertex points. An example result is shown in Figure 4.34 where blue dots represent the additional beam vertices. In this set up, the transmitted beam was through the upper basal facet and it illuminated facet 4. The refractive index was set as $\widetilde{m} = 1.31 + 0.01i$ which leads to absorption, represented by the decrease in intensity. The red lines join pairs of points which have the same intensity and the intensity variation across each strip is set at $\Delta I = 0.1$. The non-linearity of the intensity decay gives rise to strips of varying width.

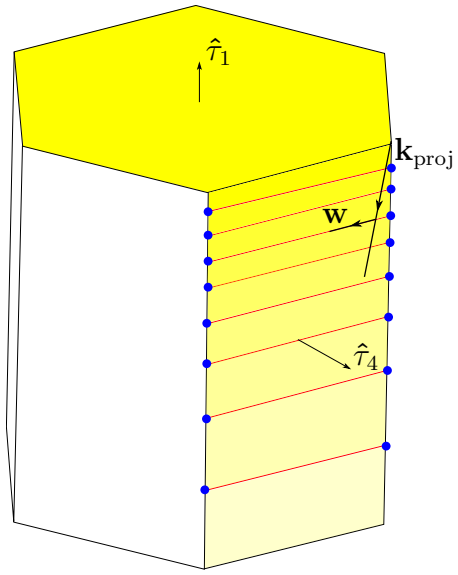

Figure 4.34: The beam formed via transmission through facet 1 is further split after illuminating facet 4.

By associating with each point $\mathbf{r}_j$ its intensity I_j the code can group the points according to their intensity. The advantage of performing the grouping this way is that it can then handle situations where the sub-beams may not necessarily be rectangular in nature. The original beam, referred to as the *master-beam* is no longer traced, its amplitude matrix is passed to each of the sub-beams which is then altered in accordance to Equation 4.55 where the distance d is found through the back tracing process described in Subsection 4.6.3. Note that the direction of the polarisation vectors for each of the sub-beams is the same as for the master-beam.

4.9 Beam Tracing Closing Remarks

So far the beam tracer describes a geometric optics approach to modelling scattering with some interference effects modelled by summing amplitudes which contain phase information instead of intensities. To test the idea of beam tracing, the model was tested with interference turned off, against Macke's ray tracing code [50] with diffraction switched off. This test was to determine how the geometric optics properties of the beam tracer compared, the results are given in Section 6.1. In the next chapter incorporating external diffraction, and diffraction of the outgoing beams is discussed. By including beam spreading in this way the model moves away from geometric optics towards physical optics.

Chapter 5

Diffraction

> ...ere yet Mr F appeared a misty shadow on the horizon paying attentions like the well-known spectre of some place in Germany beginning with a B...
>
> Charles Dickens,
> in Little Dorrit

Consider a plane wave incident on an aperture in an infinite screen such that the normal to the aperture is parallel to the direction of incidence. The geometric optics approximation would predict that a screen placed behind the aperture, at some distance R, would have an illuminated region the shape and size of which would be identical to the aperture Σ, see Figure 5.1.

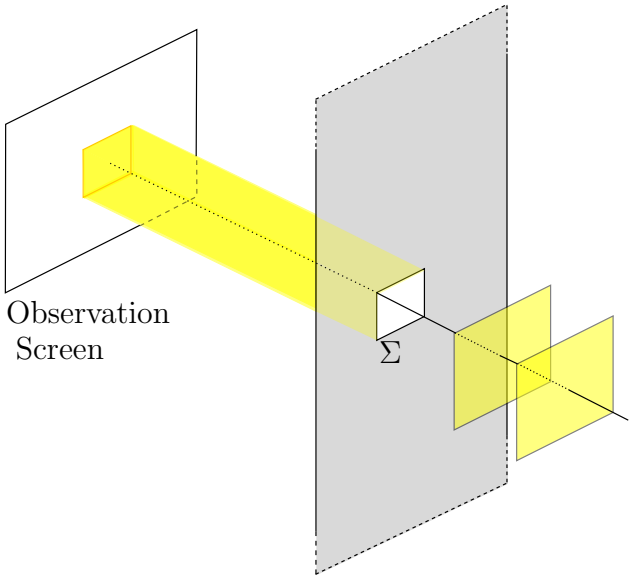

Figure 5.1: The geometric optics prediction for aperture illumination.

However, in situations where the wavelength of the incident light is comparable to the width of the aperture this is not observed. Instead, a diffraction pattern emerges, the features of which vary depending on the distance from the aperture

to the screen; the angle between directions of incidence and observation; and the shape of the aperture itself. If the point of observation is close to the aperture, then we observe *Fresnel* or near-field diffraction. Whereas, if the distance from the aperture to the point of observation is large then we observe *Fraunhofer* or far-field diffraction. While there is no clear cut transition from the near-field to the far-field, a general rule of thumb is to use the Fresnel number $F_{\#}$:

$$F_{\#} = \frac{a^2}{L\lambda}, \tag{5.1}$$

where a is the characteristic size of the aperture and L is the distance to the observation point. If $F_{\#} \ll 1$, then one can use the Fraunhofer approximation, however if $F_{\#} \approx 1$ then the Fresnel approach is necessary. In the context of atmospheric optics, we can make use of the Fraunhofer formulation since the distance from the scattering objects, i.e. ice crystals in the atmosphere, to the detector is large.

This chapter first presents the key developments in the history of diffraction theory before discussing the Fraunhofer approximation and the Kirchhoff approximation. The way in which diffraction has been implemented into light scattering models is then discussed, followed by the principles behind diffraction in the beam tracing model.

5.1 Historical Overview

The earliest mention of diffraction is attributed to the Jesuit father Grimaldi, who in 1665, investigated the shadow region formed by an object blocking sunlight which had passed through a small hole in a shutter. He observed coloured fringes and noted that the edges of the shadow were larger than expected. Grimaldi named this phenomenon *diffractio* [95] from where we get the term diffraction. The popular corpuscular theory of the time could not explain this effect. Huygens in 1678 made the first step to explaining diffraction when he postulated that:

> *Every point on a propagating wavefront serves as the source of spherical, secondary wavelets, such that the wavefront at some later time is the envelope of these wavelets.*

The argument of Huygens however was incomplete, including no reference to phase or wavelength. Young, in a demonstration to the Royal Society in 1803, presented a variation of his now famous double-slit experiment. He showed that although the shadow itself was divided into parallel fringes, the middle was always white due to interference. Fresnel added to Young's interference idea, winning the 1819 French Academy of Science's Grand Prix. The wave theory of light was not without its critics, most notably Poisson who, in an attempt to discredit the argument using mathematics, predicted the existence of bright spot in the centre of a shadow of an illuminated disk. The existence of "Poisson's spot" was confirmed soon after by Arago. The combination of Huygen's postulate with Fresnel's addition led to what is now known as the *Huygens-Fresnel Principle* [14]:

> *Every unobstructed point of a wavefront, at a given instant, serves as a source of spherical secondary wavelets (with the same frequency as that*

> *of the primary wave). The amplitude of the optical field at any point is the superposition of all these wavelets (considering their amplitudes and relative phases).*

The crux of which is to say that diffraction arises due to interference. Kirchhoff in 1882 was the first to start working towards a mathematical theory of diffraction. He showed that it is possible to calculate the amplitude of some scalar field at a position within a volume through knowledge of the field and its normal derivative on the limiting surface. The approach however has certain mathematical inconsistencies which have to be removed. Further progress on a mathematical theory of diffraction was made by Sommerfeld, from whom we get our modern definition of diffraction:

> *Any deviation of light rays from rectilinear paths which cannot be interpreted as reflection or refraction.*

This definition of diffraction makes clear that geometric optics would not be able to explain diffraction, and it is therefore a true wave phenomenon. Modern efforts to solve diffraction problems usually focus on trying to find an analytic expression for a given geometry. However, due to complexities only a few exact solutions are known, e.g. for a half plane. Diffraction by electromagnetic waves is further complicated by the electric and magnetic fields being coupled and therefore being a vector wave rather than a simple, scalar wave. However, For a large number of situations, diffraction of light can be treated using the scalar formalism outlined in Section 5.2.2.

5.2 Near and Far-Field Approximation

5.2.1 Fresnel Diffraction

Fresnel diffraction arises when the plane of observation is near to the diffracting obstacle. Analytical expressions in the Fresnel regime are complicated by the presence of a quadratically varying phase term. This term arises due to the diffracted wavefronts still being spherical when they reach the point of observation. In the beam tracing model Fresnel diffraction is not considered, neglecting these effects should only have a minor effect since it can be shown that for modelling light scattering by atmospheric ice crystals the observations are taking place in the far-field.

Consider ice particles with a characteristic size of the order $a \sim 100\mu$m illuminated by laser light with wavelength $\lambda \sim 0.5\mu$m. In remote sensing there may be several kilometres between the scattering object and the observation distance, thus $L \sim 10^3$m. We have as an approximation

$$F_{\text{remote}-\text{sensing}} \approx \frac{(100 \cdot 10^{-6})^2}{0.5 \cdot 10^{-6} \cdot 10^3} = 2 \times 10^{-5},$$

which suggests that for simulating the scattered light detected by remote sensing equipment, the far field approximation is suitable. For *in-situ* measurements we consider the SID probes. The distance between the scattering object and the detector is approximately $2 \cdot 10^{-2}$m and the incident light has wavelength $\lambda = 0.532\mu\text{m} \sim$

0.5μm. If we consider an ice particle of characteristic size $a = 50\mu$m (which is roughly in the middle of the sizeable range for the SID probes), then the Fresnel number is,

$$F_{\text{in-situ}} \approx \frac{(50 \cdot 10^{-6})^2}{0.5 \cdot 10^{-6} \cdot 2 \cdot 10^{-2}} = 0.0250,$$

which is still two orders of magnitude away from 1. The beam tracer should therefore be able to reproduce scattering patterns similar to those captured by the SID probes. We have demonstrated that the far-field approximation is valid for our present investigation. We note that beams propagating inside the crystal would undergo some deflection because of Fresnel diffraction however the beam tracer makes no attempt to model this.

5.2.2 The Helmholtz-Kirchhoff Integral - Scalar Diffraction Theory

If one is only interested in the intensity of diffracted light then the scalar approach of Kirchhoff is a good first approximation. A component of either **E** or **B** is assigned to the scalar function ψ which is assumed to be time harmonic, for example:

$$\psi(\mathbf{x}, t) = E_x \exp(-\mathrm{i}\omega t). \tag{5.2}$$

As is customary throughout the time harmonic factor is not written and $\psi(\mathbf{x}, t)$ is given a function of position only, $\psi(\mathbf{x})$. Kirchhoff's approximation uses Green's theorem, Equation 5.3, to express $\psi(\mathbf{x})$ inside an arbitrary closed volume V in terms of the field and its normal derivative on the surface. We start with Green's theorem for any two scalar fields $\psi(\mathbf{x})$ and $\phi(\mathbf{x})$,

$$\oint_{S'} (\phi \nabla\psi - \psi\nabla\phi)\mathrm{d}\mathbf{S} = \oint_{V} (\phi\nabla^2\psi - \psi\nabla^2\phi)\mathrm{d}V. \tag{5.3}$$

The surface S' consists of two surfaces S_ϵ and S, the surface normals of which point out of the bounded volume. Both ψ and ϕ satisfies the scalar Helmholtz equation,

$$(\nabla^2 + k^2)\psi = 0, \qquad \psi \in V \tag{5.4}$$

$$(\nabla^2 + k^2)\phi = 0, \qquad \phi \in V. \tag{5.5}$$

We wish to determine the value of $\psi(\mathbf{x})$ at some point inside V, see Figure 5.2. Derivations are found in many texts, e.g. [15, 21]; for the variable ϕ we use the Green's function corresponding to outgoing spherical waves originating at P_0

$$\phi = G = \frac{e^{\mathrm{i}kR}}{R}. \tag{5.6}$$

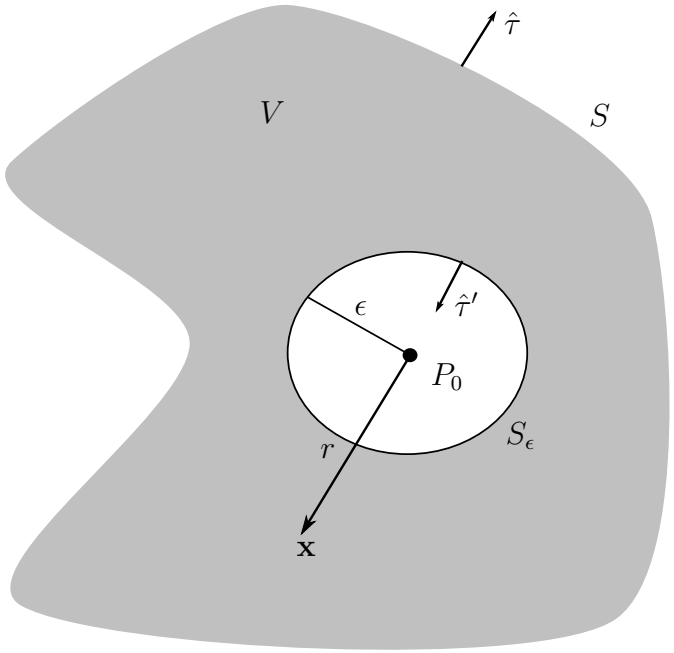

Figure 5.2: Geometry considered for deriving the Kirchhoff integral formula.

The singularity which emerges at the source, i.e. when $R = 0$, causes $\phi = G$ to no longer satisfy Equation 5.5. It is for this reason that the surface integral is evaluated over a compound surface $S' = S + S_\epsilon$, where S_ϵ is a small surface around the point P_0; the volume over which the integration is taking place being the volume between S and S_ϵ. In this way the requirement that ϕ satisfies the scalar Helmholtz equation within the volume is re-established. Since ψ and ϕ satisfy the scalar Helmholtz equation the volume integral is equal to zero. Separating the surface integral into its two components,

$$\oint_S (G\nabla\psi - \psi\nabla G)\mathrm{d}\mathbf{S} = -\oint_{S_\epsilon} (G\nabla\psi - \psi\nabla G)\mathrm{d}\mathbf{S}_\epsilon. \tag{5.7}$$

and noting that in the limit $\epsilon \to 0$ the integral on the right hand side of Equation 5.7 is $4\pi\psi$, we get the Kirchhoff integral, Equation 5.8,

$$\psi(\mathbf{x}) = \frac{1}{4\pi}\oint_S \left(\psi\nabla\frac{e^{\mathrm{i}kr}}{r} - \frac{e^{\mathrm{i}kr}}{r}\nabla\psi\right)\cdot\hat{\tau}\mathrm{d}s. \tag{5.8}$$

Kirchhoff's integral formula provides a means to calculate $\psi(\mathbf{x})$ in terms of a linear combination of its value and normal derivative on the bounding surface. However these values are often not known and so one has to use the following boundary conditions:

1. Both ψ and $\nabla\psi\cdot\hat{\mathbf{n}}$ vanish everywhere on S, except in the aperture.
2. In the aperture, ψ and $\nabla\psi\cdot\hat{\mathbf{n}}$ take the same value as they would in the absence of the surface.

Applying these boundary conditions to Equation 5.8 leads to the *Kirchhoff approximation* integral formula:

$$\psi(\mathbf{x}) = \frac{1}{4\pi}\int_{\text{apertures}} \left(\psi\nabla\frac{e^{\mathrm{i}kr}}{r} - \frac{e^{\mathrm{i}kr}}{r}\nabla\psi\right)\cdot\hat{\tau}\,\mathrm{d}s \tag{5.9}$$

The only difference between Equations 5.8 and 5.9 is that in the Kirchhoff approximation the integral takes place only over the aperture, not the entire surface. Jackson [21] points out that there are mathematical inconsistencies with this approximation. Namely that if any scalar potential which satisfies the scalar Helmholtz equation has zero values for both itself and its normal derivative on any finite surface then it is necessarily zero everywhere; this causes the second boundary condition to become invalid. This inconsistency arises due to the boundary conditions being over-specified. Therefore changing the Green function and the boundary condition to either a Dirichlet type ($G = 0$ on S), or Neumann type ($\partial G/\partial n = 0$ on S) will remove the inconsistency. Alternatively, one can model the diffraction as a *saltus* problem and assume the screen is black, i.e. no reflection or transmission, as was done by Kottler [96, 97]. The Kirchhoff Approximation in an altered form has been used by Muinonen in creating the Modified Kirchhoff Approximation which will be discussed in Section 5.3.

As a closing comment, if we consider a point source illuminating a single aperture in an infinite screen we arrive at the following expression,

$$\psi(\mathbf{x}) = \frac{1}{\lambda\mathrm{i}}\int_S \frac{e^{\mathrm{i}k(r+r')}}{r\cdot r'}\left(\frac{(\hat{\mathbf{k}}^{\text{inc}}\cdot\hat{\tau}) + (\hat{\mathbf{k}}^{\text{diff}}\cdot\hat{\tau})}{2}\right)\mathrm{d}S. \tag{5.10}$$

Where r and r' are the distances from the area element in the aperture to the points of observation and source respectively; $\hat{\mathbf{k}}^{\text{inc}}$ and $\hat{\mathbf{k}}^{\text{diff}}$ are vectors in the direction of incidence and observation. The term in brackets is the obliquity factor. It explains why the backward propagating wave predicted by the Huygens-Fresnel principle is not observed.

Fraunhofer Approximation

The so-called Fraunhofer approximation uses the Helmholtz-Kirchhoff integral to evaluate the amplitude of the diffracted wave at small angles in the far-field. Here, the phase difference between neighbouring points in the aperture (i.e. spherical wave point sources) is linear and so one can apply a two-dimensional Fourier transform of the aperture function, which describes the amplitude of the incident wave over the aperture [98]. While computationally the Fraunhofer approximation is easily implemented, its restrictions to small scattering angles means that it is unsuitable for the beam tracing model where we require knowledge of the diffracted field over all space.

5.2.3 Vector Diffraction Theory

The polarisation of the diffracted field is not modelled by scalar diffraction theory. In the beam tracer a vector diffraction formulation was used since in reality the electric and magnetic fields are coupled and so cannot be treated separately. A vector analogue to the Kirchhoff integral given in Equation 5.8 for a perfectly thin, conducting screen with apertures has the form [21]:

$$\mathbf{E}(\mathbf{x}) = \frac{1}{2\pi}\nabla \times \int_S (\hat{\tau} \times \mathbf{E})\frac{e^{ikR}}{R}\mathrm{d}a', \tag{5.11}$$

where R is the distance from the point on the surface to the point of observation. We can expand the kR term so long as $r \gg d$, where d is the characteristic size of the diffracting system as follows:

$$kR = kr - \mathbf{k}\cdot\mathbf{x}' + \frac{1}{2r}[kr'^2 - (\mathbf{k}\cdot\mathbf{x}')^2] + ... \tag{5.12}$$

where $\mathbf{k} = k\hat{\mathbf{k}}$ is the wave vector. In the beam tracing model we are only concerned with the far-field (Fraunhofer) region which means we can neglect third order and higher terms. Furthermore, diffracting apertures will be planar as the crystal facets are planar. With these two restriction we can rewrite Equation 5.11 as:

$$\mathbf{E}(\mathbf{x}) = \frac{ie^{ikr}}{2\pi r}\mathbf{k} \times \int_S \hat{\tau} \times \mathbf{E}(\mathbf{x}')e^{-i\mathbf{k}\cdot\mathbf{x}'}\mathrm{d}a' \tag{5.13}$$

where the terms are defined according to Figure 5.3.

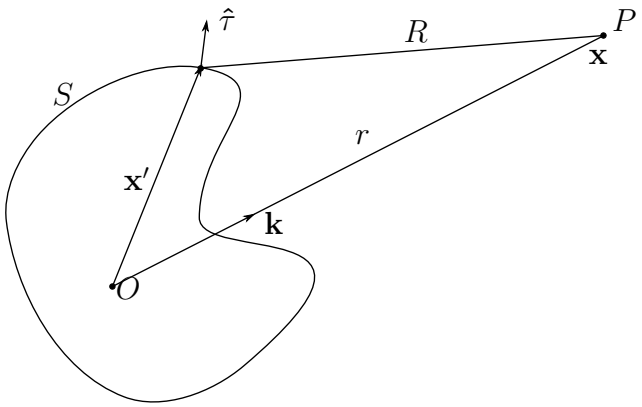

Figure 5.3: The set-up for deriving a vector analogue to the scalar Helmholtz-Kirchhoff integral.

Equation 5.13 serves as the basis for modelling diffraction in the beam tracer, which is discussed in Section 5.4. The integral is performed over the aperture through which the incident wave propagates. The presence of the wave-vector $\mathbf{k}$ means that this approach is capable of modelling diffraction at oblique incidence which will be shown to be important if the model is to be used to aid in the identification of particles from their 2D light scattering patterns.

5.3 Modelling Diffraction in Light Scattering Models

The popularity of Geometric Optics for modelling light scattering by larger sized particles has led to the development of numerous methods to incorporate diffraction approximations into ray tracing codes. We discuss some of these here, along with their advantages and limitations. It is customary to separate ray tracing and external diffraction such that the scattered field in a given direction is the sum of

the contributions from each component. For example, if we denote the intensity as a function of angle by P we would have:

$$P(\theta) = P^{\text{diff}}(\theta) + P^{\text{GO}}(\theta), \tag{5.14}$$

where the superscripts relate to contributions from diffraction and geometric optics. In this way hybrid geometric-physical optics models are created.

The Geometrical Theory of Diffraction proposed by Keller [99] extends the idea of ray tracing to include diffraction by edges and surfaces. To do this he introduces diffraction coefficients, the values of which depend on the type of diffraction taking place, i.e. edge or surface diffraction. A ray which is incident obliquely on an edge gives rise to a cone of diffracted rays, similarly a ray incident normal to the edge leads to rays which lie in a plane perpendicular to the edge. It is essentially a scalar approach and has been used by the engineering community (e.g. [100, 101]) but has been generally overlooked by researchers in atmospheric light scattering.

The Kirchhoff Approximation was used by Muinonen [102] to add a physical optics correction when investigating light scattering by randomly oriented crystalline structures. Originally, this approach was based on the scalar Kirchhoff integral (Equation 5.8) and was applied only to the phase function. This technique was further improved by Muinonen [103] by using a vector form of Kirchhoff's diffraction integral (Equation 5.13) and was named the *Modified Kirchhoff Approximation* (MKA). It contains three simplifications:

1. The reflected, transmitted and diffracted amplitudes are added without regard to phase.

2. The diffracted amplitude is calculated in the far field by modelling diffraction by a circular aperture of equal area to the facet from which the ray leaves.

3. External diffraction is calculated in the far-field by assuming a size distribution of circular projected areas that is equal to the distribution of the real projected areas.

The approximation of treating facets as equivalent circular apertures is done for the mathematical convenience of using Bessel's functions in calculating diffracted amplitudes. However, as facets become increasingly elongated the approximation gets less and less accurate. In addition, the assumption of random orientations means that it is not applicable to studying particles which adopt a preferred orientation.

Yang and Liou [45, 46] formulated the *Improved Geometric Optics Method* (IGOM). Ray tracing is used to determine the electric and magnetic near fields of wavelets on the surface of the scatterer, taking into account their phase. Then, by invoking an electromagnetic equivalence theorem the near field can be rewritten in terms of electric and magnetic current densities before being mapped to the far field. The method was compared with FDTD and good agreement was found, down to a size parameter of 20. The method is however, more computationally expensive than pure geometric optics.

A ray tracing code developed by Macke modelled external diffraction as diffraction at normal incidence on an equal area circular aperture [104]. This was improved by removing the equivalent circular aperture approximation and instead considering normal incidence diffraction on the projected cross section [50]. However, rays which left the crystal were not diffracted.

Hesse and Ulanowski [12] built on Macke's ray tracing code by introducing diffraction of scattered rays. The time averaged Poynting vector was used to determine the direction of the far-field energy flow lines. From this a deflection angle was derived which was used to modify the scattering direction of an outgoing ray. The technique has become known as the Ray Tracing with Diffraction on Facets (RTDF) model. Initially, RTDF was only for infinitely long hexagonal columns at normal incidence which in essence meant it was a 2D problem. It was extended to three dimensions by Clarke et al. [105] and was further improved by Hesse [106] by changing the approximation for the deflection angle to incorporate the method of Prosser [107].

Beam tracing models have been developed by Bi et al. [54, 55] where a volume integral approach was used to determine the far-field diffracted amplitude, as opposed to the surface integral methods discussed so far. These integrals have to be analytically solved for a given beam and are performed over a beam's volume which is computationally expensive. The model does however yield very good results when compared to T-Matrix.

Diffraction by highly absorbing particles was investigated by Hesse et al. [108], external diffraction was modelled by treating the upward facing facets as independent apertures and combining the diffracted amplitude of beams passing through each one. To do this, the vector Kirchhoff integral given in Equation 5.11 was transformed into a line integral by application of Green's theorem in the plane. It was shown that modelling diffraction this way led to the formation of curved diffraction arcs as the incident beams were modelled with oblique incidence, rather than normal incidence on the projected cross section. The work was further improved [109] by introducing a *diffraction amplitude matrix* to better model the degree of linear polarisation in the scattered field. These techniques will be discussed in the next section as they provide the basis for modelling diffraction in the beam tracer.

This brief overview of diffraction demonstrates the variety of techniques which have been employed. Combining ray-tracing with diffraction on the projected cross section has become known as *Classical Geometric Optics*. It this case the incident light is normal to the aperture, which leads to diffraction arcs perpendicular to each edge. While some models have incorporated diffraction of outgoing rays/beams, this is still very much an active research area.

5.4 Diffraction in the Beam Tracing Model

Apart from the time saving capabilities of tracing beams opposed to rays, physical insights are gained through knowledge of the beam's cross section, amplitude and phase. In the model, diffraction of outgoing beams is performed by treating diffraction at oblique incidence on a planar aperture whose dimensions match those

of the beam's cross section on the facet. The Kirchhoff Approximation is used to model the amplitude of the electric field in the Fraunhofer region through means of a surface integral which maps the near-field to the far-field. The field amplitude in the near field is taken to be the phase dependent amplitude which is known from beam tracing. We build upon the work done by Hesse et al. [108, 109], by including the diffraction of beams which have undergone internal interactions with the crystal; as opposed to just external diffraction and reflection.

5.4.1 The Aperture Coordinate System

Diffraction in the Beam Tracing model requires the diffracting aperture, i.e. the beam cross section on the facet, to be parallel to the xy plane. A coordinate system centred in the middle of the aperture is called *aperture system* and coordinates given with respect to it are denoted by (x', y', z'). Rotation into the aperture system is performed in three stages. The first two rotations align the surface normal with the the z-axis and the third rotates the propagation vector of the incident beam in to the $x'z'$ plane. Initially, we perform a rotation about the z-axis about an angle $\Theta_1 = \arctan(\tau_y/\tau_x)$ using the rotation matrix:

$$\mathbf{L}_1^c = \begin{pmatrix} \cos\Theta_1 & -\sin\Theta_1 & 0 \\ \sin\Theta_1 & \cos\Theta_1 & 0 \\ 0 & 0 & 1 \end{pmatrix}. \tag{5.15}$$

The superscript c denoting that this is a coordinate transformation. The rotated surface normal ($\tau' = \mathbf{L}_1^c\hat{\tau}$) can then be aligned parallel to the z-axis by performing a rotation by $\Theta_2 = \arctan(\tau'_x/\tau'_z)$ about the y-axis using the rotation matrix:

$$\mathbf{L}_2^c = \begin{pmatrix} \cos\Theta_2 & 0 & \sin\Theta_2 \\ 0 & 1 & 0 \\ -\sin\Theta_2 & 0 & \cos\Theta_2 \end{pmatrix}. \tag{5.16}$$

Finally a second rotation about the z-axis rotates the vector $\mathbf{k}' = \mathbf{L}_2^c \cdot \mathbf{L}_1^c \cdot \hat{\mathbf{k}}$ into the $x'z'$ plane by an angle $\Theta_3 = \arctan(k'_y/k'_z)$:

$$\mathbf{L}_3^c = \begin{pmatrix} \cos\Theta_3 & -\sin\Theta_3 & 0 \\ \sin\Theta_3 & \cos\Theta_3 & 0 \\ 0 & 0 & 1 \end{pmatrix}. \tag{5.17}$$

The sequence of rotations $\mathbf{L}_3^c \cdot \mathbf{L}_2^c \cdot \mathbf{L}_1^c$ is applied to the beam vertices, the surface normal, the polarisation vectors and the incident beam's propagation. An example set up is shown in Figure 5.4.

5.4.2 Evaluating the Diffraction Integral

We consider a perfectly conducting screen with an aperture in the $x'y'$ plane, its surface normal $\hat{\tau}$ being parallel to the z' axis. The incident beam propagates in the $x'z'$ plane with direction vector $\hat{\mathbf{K}}$, drawing an angle α with the surface normal. This choice of direction removes the negative in the exponential term in Equation 5.13:

$$\mathbf{E}(\mathbf{x}) = \frac{ie^{ikr}}{2\pi r}\mathbf{k} \times \int_S \mathbf{n} \times \mathbf{E}(\mathbf{x}')e^{i\mathbf{k}\cdot\mathbf{x}'}\mathrm{d}S'. \tag{5.18}$$

The diffraction setup is shown in Figure 5.4. It has been shown [108] that the surface integral in 5.18, after bracketing a polarisation dependent factor, can be written as:

$$F = \int_S \exp\{ik[x'(\sin\alpha + \cos\varphi' \sin\theta') + y' \sin\varphi' \sin\theta']\}\mathrm{d}x'\mathrm{d}y', \tag{5.19}$$

where θ' is the angle between the incident and scattered direction vectors and φ' is the angle from the positive x' axis to the projection of $\hat{\mathbf{k}}$ on the $x'y'$ plane.

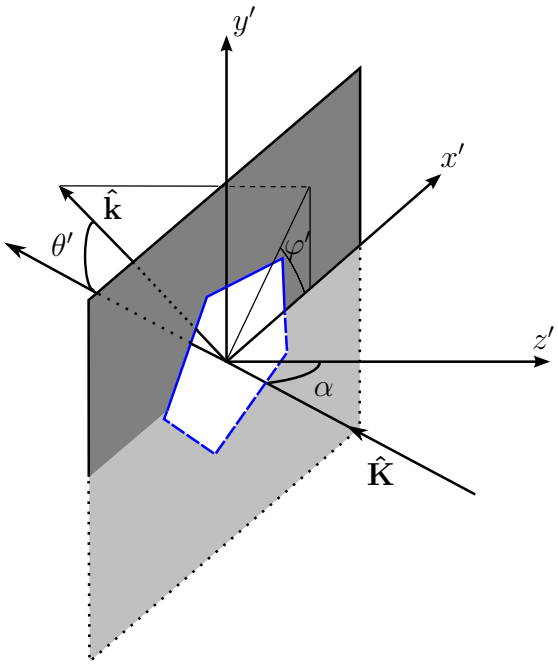

Figure 5.4: The aperture-centred coordinate system used in modelling diffraction. The aperture is in the $x'y'$ plane and the plane of incidence is the $x'z'$ plane.

Green's theorem in the plane, given in Equation 5.20, relates a given surface integral to a line integral around the surface's boundary.

$$\oint_{\partial S} P\mathrm{d}x + Q\mathrm{d}y = \int_S \left(\frac{\partial Q}{\partial x} - \frac{\partial P}{\partial y}\right) \mathrm{d}x\mathrm{d}y. \tag{5.20}$$

Through the use of Green's theorem we rewrite Equation 5.19 as:

$$F = -\oint_{\partial S} \frac{e^{ik[x'(\sin\alpha+\cos\varphi'\sin\theta')+y'\sin\varphi'\sin\theta']}}{2ik\sin\varphi'\sin\theta'}\mathrm{d}x' + \oint_{\partial S} \frac{e^{ik[x'(\sin\alpha+\cos\phi'\sin\theta')+y'\sin\varphi'\sin\theta']}}{2ik(\sin\alpha+\cos\varphi'\sin\theta')}\mathrm{d}y'. \tag{5.21}$$

The advantage of writing the diffraction integral this way is that the line integrals can be approximated as straight line integrals between adjacent aperture vertices (i.e. beam vertices). When a beam leaves the crystal we first apply Equations 5.15-5.17 to move into the aperture system before applying Equation 5.21 for a range of θ' and φ' angles (depending on the bin resolution in use in the model). For each scattering direction $\hat{\mathbf{k}} = (\theta', \varphi')$ it is also necessary to determine the path difference as described in Section 4.6.3. The beam's amplitude matrix is then redistributed over all scattering angles.

5.4.3 Polarisation of the Diffracted Wave

The polarisation treatment in [108] was an approximation valid for small scattering angles. To model the polarisation components of the diffracted field over the whole scattering sphere we apply the method of Karczewski and Wolf [110], where a relation between the incident and diffracted polarisation vectors is given. They showed that the electric field at some point P in the Fraunhofer region can be written as:

$$\mathbf{E}^s(P) = \hat{\mathbf{k}} \times (\mathbf{F} \times \mathbf{E}^i) + (\mathbf{F} \times \mathbf{B}^i) - \hat{\mathbf{k}} \cdot (\mathbf{F} \times \mathbf{B}^i)\hat{\mathbf{k}} \tag{5.22}$$

where $\mathbf{E}^i$ and $\mathbf{B}^i$ are complex amplitude vectors of the incident electric and magnetic field respectively. Note that because the incident wave is planar, $\mathbf{B}^i = \mathbf{K} \times \mathbf{E}^i$, where $\mathbf{K}$ is the direction of incidence. The vector $\mathbf{F}$ is written as:

$$\mathbf{F} = \left(\frac{ik_0}{4\pi} \exp[ik_0 r_0]/r_0 \right) \hat{\tau} \int_S \exp[ik_0(\hat{\mathbf{K}} - \mathbf{k}) \cdot \mathbf{R}] \mathrm{d}S. \tag{5.23}$$

Note that Equations 5.19 and 5.23 are the same except for the bracketed, constant term in Equation 5.23 which shows that the fields in the Fraunhofer region take the form of outgoing spherical waves propagating away from the aperture.

The relation between the incident and scattered electric field amplitudes is found by considering the electric and magnetic components of Equation 5.22 separately. The derivation is lengthy and is provided in Appendix D. However, the resulting expressions are:

$$E^s_\parallel = F(a_1 E^i_\parallel + b_1 E^i_\perp), \tag{5.24a}$$
$$E^s_\perp = F(a_2 E^i_\parallel + b_2 E^i_\perp), \tag{5.24b}$$

where the terms a_1, a_2, b_1, b_2 are defined as follows:

$$a_1 = -\left(K_z \sqrt{\frac{1-k_y^2}{1-K_y^2}} + k_z \sqrt{\frac{1-K_y^2}{1-k_y^2}} \right), \tag{5.25a}$$
$$b_1 = k_x k_y \sqrt{\frac{1-K_y^2}{1-k_y^2}} - K_x K_y \sqrt{\frac{1-k_y^2}{1-K_y^2}}, \tag{5.25b}$$
$$a_2 = K_x K_y \sqrt{\frac{1-k_y^2}{1-K_y^2}} - k_x k_y \sqrt{\frac{1-K_y^2}{1-k_y^2}}, \tag{5.25c}$$
$$b_2 = -\left(K_z \sqrt{\frac{1-k_y^2}{1-K_y^2}} + k_z \sqrt{\frac{1-K_y^2}{1-k_y^2}} \right). \tag{5.25d}$$

We express Equations 5.24a-5.24b as a matrix:

$$\begin{pmatrix} E^s_\parallel \\ E^s_\perp \end{pmatrix} = F \begin{pmatrix} a_1 & b_1 \\ a_2 & b_2 \end{pmatrix} \begin{pmatrix} E^i_\parallel \\ E^i_\perp \end{pmatrix} \tag{5.26}$$

The 2×2 matrix is termed the *diffraction amplitude matrix* [109] in this work and is denoted by $\mathbf{D}$. It takes the form of a scattering matrix and relates the amplitude of the diffracted wave's electric field vectors to those of the incident wave. The field

amplitudes for the incident wave are expressed in the plane of incidence, in the same way as necessary to apply the Fresnel amplitude matrices. The factor F takes care of amplitude variation over the angular range and is evaluated using the line integrals given in Equation 5.21. To bring this all together the next section illustrates how diffraction is modelled in the beam tracer.

5.5 Modelling Diffraction

We now show how the diffraction model is implemented in three different scenarios: external diffraction, diffraction after external reflection and diffraction after transmission. The crystal has a size parameter of $x = 100$ with refractive index $m = 1.31 + 0.0\text{i}$, its orientation is shown below in Figure 5.5 and the incident wave travels into the page.

Figure 5.5: The diffraction results are given for a transparent crystal in this orientation.

5.5.1 External Diffraction

We approximate external diffraction as diffraction on upward facing facets, each of which is treated independently. In doing this we invoke Babinet's principle of complementary screens which states that [111]:

The intensity of the diffracted field from an aperture is the same as that from a complementary screen.

The amplitude of a wave diffracted through an aperture in the far-field would have the form $M(\theta, \phi)$. Removing the screen then requires the amplitude to be the unobstructed value which in turn suggests that an amplitude $-M(\theta, \phi)$ has been added. Ergo, if there is no screen and just an obstruction of the same shape and size as the original aperture (i.e. the complementary screen), its diffracted field would have an amplitude $-M(\theta, \phi)$. Since the intensity is proportional to the amplitude squared, both cases will yield identical diffraction patterns. The change in sign of amplitude corresponds to a phase shift of π between the two cases which means that in using Babinet's principle, we must subtract the external diffraction amplitude from the beam diffraction amplitudes. Babinet's principle allows us to model diffraction due to a crystal facet (obstacle) as diffraction by an aperture of equal shape and size

(complementary screen) as shown in Figure 5.6.

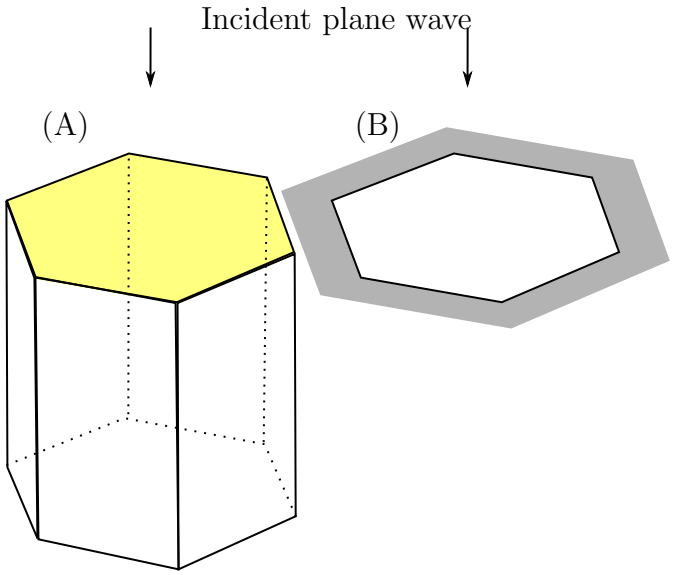

Figure 5.6: Babinet's principle applied to the case of external diffraction on the upward facing basal facet. (A) is the complementary screen and (B) is the corresponding aperture. There is a phase shift of π between the cases.

The amplitude matrix associated with external diffraction is the identity matrix. We first rotate the crystal facet, surface normal and incident propagation vector into the aperture system through application of Equations 5.15-5.17. We then rotate the amplitude matrix into the plane of incidence. Diffraction is applied by considering a range of diffraction directions $\hat{\mathbf{k}}$ corresponding to the scattering direction and each direction is then rotated into the aperture system. For each direction the elements of the diffraction amplitude matrix are found along with the value for the diffraction integral. Three additional rotations are performed, the first $\mathbf{L}_0$ rotates the reference plane into the plane of incidence; the second rotates the plane of incidence into the scattering plane, $\mathbf{L}_1$; the final rotation rotates the reference plane into the scattering plane, $\mathbf{L}_p$ (see Section 4.5.3). For a given scattering direction (θ, ϕ) the contribution of the diffracted wave's amplitude to the external diffraction amplitude matrix is:

$$\mathbf{S}^{\text{ext}}(\theta, \phi) = \mathbf{L}_1 \cdot F(\theta, \phi) \cdot \mathbf{D}(\theta, \phi) \cdot \mathbf{L}_0 \cdot \mathbf{I} \cdot \mathbf{L}_p \tag{5.27}$$

In Equation 5.27 the dependence of F and $\mathbf{D}$ on the scattering angles has been written explicitly for understanding, usually these are not given. External diffraction does not polarise the incident wave in any way and neither is it dependent on the refractive index of the medium.

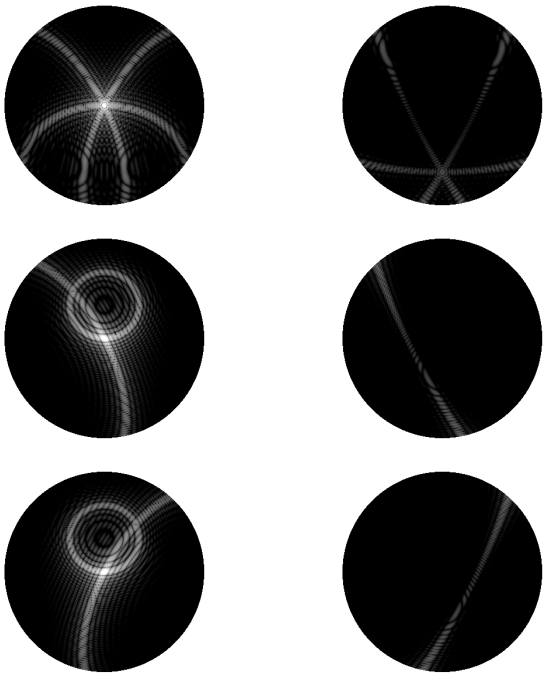

Figure 5.7: External diffraction patterns. The first column corresponds to scattering into the forward hemisphere, the second into the backward hemisphere. The three rows show the external diffraction patterns arising from facets, in the first row the illuminated basal facet, and then the two prism facets, see Figure 5.5.

Figure 5.7 shows the external diffraction intensity patterns from the three illuminated facets, see Figure 5.5. As is to be expected, most of the diffracted light is in the forward hemisphere. The curving of the diffraction arcs due to the oblique incidence can be seen. Combining the amplitudes of the contributions from the individual beam facing facets then gives the total external diffracted field, the diffraction pattern in Figure 5.8. We see that the curved arcs from the two prism facets both overlap with arcs from the basal facet; this is due to the shared edges. Note further how the ring structure is formed from the contributions from the two prism facets which share one edge.

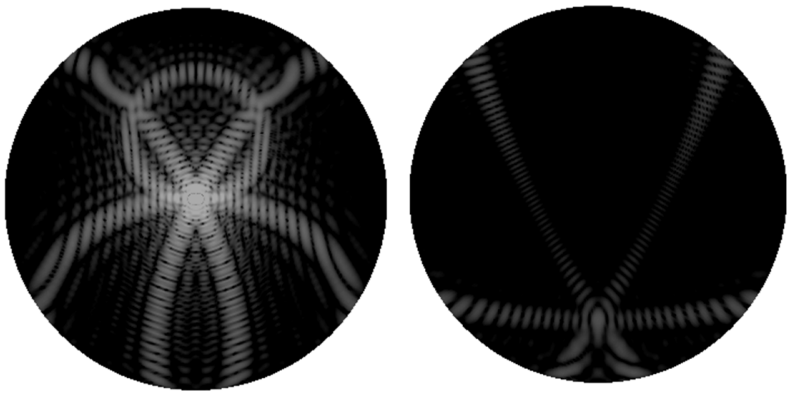

Figure 5.8: Total external diffraction pattern.

5.5.2 Beam Diffraction

We consider beam diffraction in two parts. First we look at the case of diffraction of the externally reflected beam. We then consider the diffraction of a beam which has travelled through the crystal.

External Reflection

External reflection is handled in very much the same way as external diffraction, however we modify Equation 5.27 so that the Fresnel reflection matrix $\mathbf{R}$ is included,

$$\mathbf{S}(\theta, \phi) = \mathbf{L}_s \cdot F \cdot \mathbf{D} \cdot \mathbf{R} \cdot \mathbf{L}_0 \cdot \mathbf{I} \cdot \mathbf{L}_p. \tag{5.28}$$

Note the similarity to Equation 4.31, however this new form includes diffraction. The direction of incidence is now the direction of the reflected wave, that is $\hat{\mathbf{K}} = \hat{\mathbf{k}}^{\text{refl}}$. For a given facet the 'aperture' is the same for both external diffraction and reflection. This would suggest that the form of the externally diffracted beam should resemble the diffraction post reflection beam.

Diffraction After Transmission

Next we consider the case of a beam which has passed through the crystal with no internal reflections. The amplitude matrix for such a beam would be:

$$\mathbf{M} = \mathbf{T}_2 \cdot \mathbf{L}_1 \cdot \mathbf{T}_1 \cdot \mathbf{L}_0 \cdot \mathbf{I}. \tag{5.29}$$

The rotation matrix $\mathbf{L}_0$ expresses the polarisation vectors with respect to the first plane of incidence during the first beam facet interaction, i.e. inward transmission into the crystal. The beam then propagates into the crystal before intersecting a different facet. The rotation $\mathbf{L}_1$ then rotates from the old plane of incidence to the new one. The two transmission matrices $\mathbf{T}_1$ and $\mathbf{T}_2$ handle the amplitude changes at the boundaries.

The amplitude matrix for this beam is currently given with respect to the plane of incidence for the second beam-crystal interaction (i.e. perpendicular to the facet the beam is exiting from). We rotate into the aperture coordinate system before applying the diffraction amplitude matrix and the diffraction integral. For each scattering direction considered we have:

$$\mathbf{S}_i(\theta, \phi) = \mathbf{L}_s \cdot F \cdot \mathbf{D} \cdot \mathbf{T}_2 \cdot \mathbf{L}_1 \cdot \mathbf{T}_1 \cdot \mathbf{L}_0 \cdot \mathbf{I} \cdot \mathbf{L}_p. \tag{5.30}$$

5.6 Combining Diffracted Amplitudes

As Babinet's principle was applied to external diffraction a phase shift of π will exist between the externally diffracted field and the scattered beam fields. As such, the contribution from external diffraction is subtracted. For a given scattering direction, the global amplitude matrix (i.e. the crystal's amplitude matrix) is:

$$\mathbf{S}(\theta, \phi) = \sum_{i=1}^{N} \mathbf{S}_i^{\text{beams}}(\theta, \phi) - \sum \mathbf{S}^{\text{ext}}(\theta, \phi). \tag{5.31}$$

In this way the amplitude scattering matrix of the crystal is determined by using the beam tracing model.

5.7 Diffraction Closing Remarks

This chapter outlined how diffraction has been incorporated into various light scattering models and justified the use of the Fraunhofer approximation. It also explained how a diffraction formalism was derived and applied to the beam tracing model using a vector form of the Kirchhoff integral to evaluate the electric field amplitude in the far field. The need to subtract the external diffraction amplitude, determined through an application of Babinet's principle, was also given.

Chapter 6

Results

> The sun is alone, except in thick weather, when there sometimes appear to be two, but one is a mock sun.
>
> Henry David Thoreau,
> in Walden

6.1 Validating the Geometric Optics Component

To validate the geometric optics aspects of the Beam Tracing model a comparison study was carried out using for reference the Ray Tracing code developed by Macke [50]. Physical optics features of the Beam Tracer were turned off (e.g. phase tracing and diffraction) while diffraction was not included in the Ray Tracing calculations. Calculations using geometric optics on particles in fixed orientation would lead to discrete scattering events which would not be very insightful, therefore both codes were averaged over 1000 different orientations. The Euler angles used in both models were the same.

The Ray Tracing code uses a fixed number of rays per orientation, these rays spawn at random (x, y) positions in a plane $z = const$ above the crystal. The maximum (x, y) dimensions are determined from the crystal itself. This means that the 'scanning area' considered in the Ray Tracer likely changes with each orientation. Furthermore, the chosen number of rays does not necessarily mean that that number of rays intersects with the crystal. Consider the two orientations shown in Figure 6.1, the red lines represent the 'scanning area' in Macke's code where rays can originate from and black lines are crystal edges.

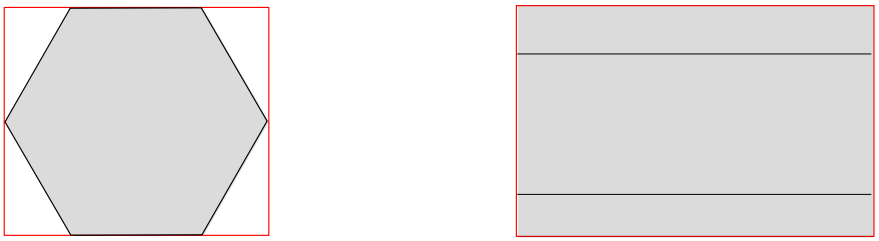

(a) The crystal is standing on a basal facet. (b) The crystal laying on a prism facet.

Figure 6.1: Two particular orientations, with the incident light going into the page.

In case (a) some rays would not hit the crystal whereas in case (b) all rays would. However, in both situations the same number of rays would be used despite the scanning area being much larger is case (b). This led to errors when comparing beams to rays since the Beam Tracer can be considered as including every possible ray trajectory. The Ray Tracing model was altered to keep the *ray density* constant. Let ρ be the number of rays per unit area A:

$$\rho = \frac{N_r}{A}, \tag{6.1}$$

where N_r is the user set number of rays to be used. Upon initialisation, the Ray Tracer calculates the ray density for each orientation keeping track of the largest ray density $\rho_{\max}$ found. This is then set as the value to be kept constant for each orientation. Once this has been determined, for each orientation a new number of rays is calculated for that orientation such that the ray density is constant:

$$N_r' = \rho_{\max} \times A. \tag{6.2}$$

Every time a ray is scattered in the direction (θ, ϕ) its phase matrix is added to the global phase matrix for the crystal; in this way the Phase matrix is developed as more rays are scattered. In Beam Tracing calculations the Amplitude matrix is built up in the same way before being transformed into the Phase matrix via Equations A.1a-A.1p. The phase matrix elements are then multiplied by the beam's projected area in the direction of scattering. The resulting phase functions calculated from both methods is given in Figure 6.2 where the agreement is excellent and the 22° halo peak is prominent. Computationally speaking, the Beam Tracer was a factor 70 quicker than the ray tracer, although no diffraction was used. This test proved two aspects of the Beam Tracing model, firstly that it was correctly splitting beams and determining their propagation distances. Secondly, the Ray Tracing model uses the Stokes formalism, rather than Jones formalism (although in this test phase effects were turned off); the P_{11} elements matching confirmed that the Jones formalism had been correctly implemented in the Beam Tracing model.

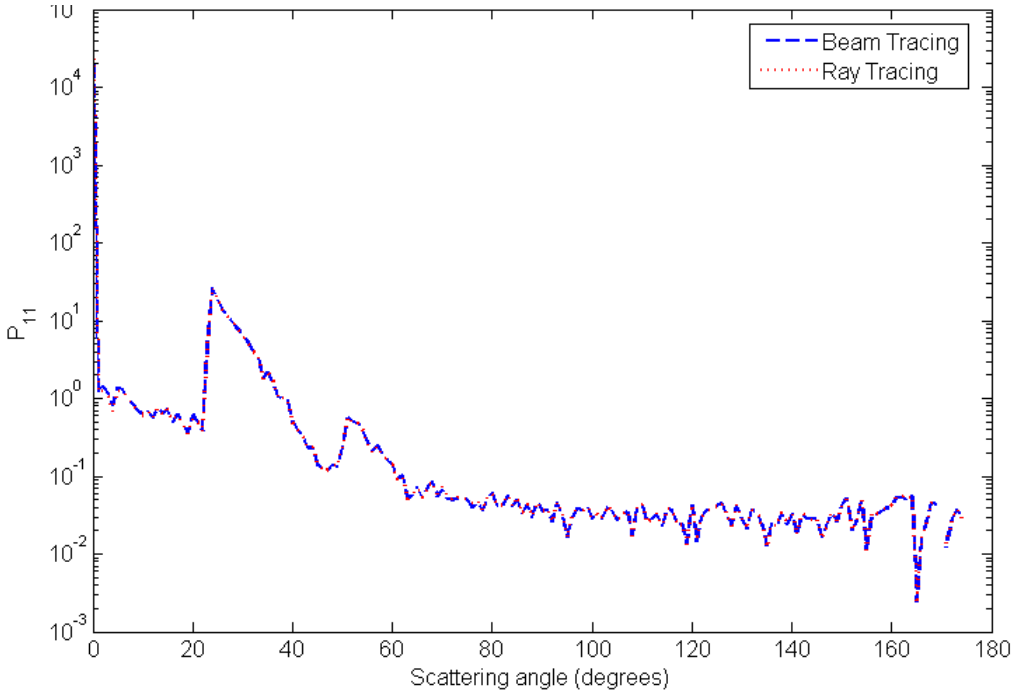

Figure 6.2: Comparison of Beam Tracing and Ray Tracing results for a hexagonal column of size parameter $x = 100$ over 1000 orientations. For Ray Tracing the initial number of rays per orientation was set as $N_r = 1000$.

There are some interesting features in the geometric optics plot. The intensity in the direct forward direction is very high, this is caused by light propagating through plane parallel facets and is known as the *delta transmission peak* [64]. The absence of diffraction means that there is no broadening of this peak. Furthermore, the phase function is made of a series of discrete points, and is not continuous as can be seen near backscattering.

6.2 Comparison to ADDA

Results gained using the ADDA implementation of the Discrete-Dipole Approximation (see Section 2.7.3) for four fixed orientations at four different size parameters were compared to Beam Tracing results.

Four orientations of a transparent hexagonal crystal of unity aspect ratio, given in Figure 6.4, will be considered with four size parameters of 20, 40, 60 and 100. The ADDA data, provided by Antti Penttilä of the University of Helsinki, contains the azimuthally resolved P_{11} and $-P_{12}/P_{11}$ scattering matrix elements; relating to the intensity and degree of polarisation of the scattered light. Both two-dimensional and one-dimensional (azimuthally averaged) results from the Beam Tracer are compared to ADDA. Also calculated is the asymmetry parameter. A limited orientation average is also carried out, but is not intended to be representative of random orientation.

A detailed discussion will be given for only one case, the hexagonal column of size parameter 100 in orientation (a) in Figure 6.4. Once the features have been

established a broader discussion on the effects of size and orientation will be given. Further comparisons will be made against ADDA results for an absorbing hexagonal column, and an absorbing indented hexagonal column, both of which will also be in orientation (a).

6.2.1 ADDA Data

In these simulations, the orientation of the incident beam is changed with the crystal remaining fixed in its original position, in which the crystal axis is aligned with the x axis. This differs from the Beam Tracer where the crystal is physically rotated (through use of the Euler angles, see Section 4.2.3) and the direction of the incident beam remains constant. Initially, the incident beam propagates in the direction of positive x. The first rotation is about the z axis in the xy plane. The second rotation is about the x axis, these rotations are depicted in Figure 6.3. Note that whereas the complete set of paths swept by the incident vector after the first rotation is a circle, for the second rotation it is a cone.

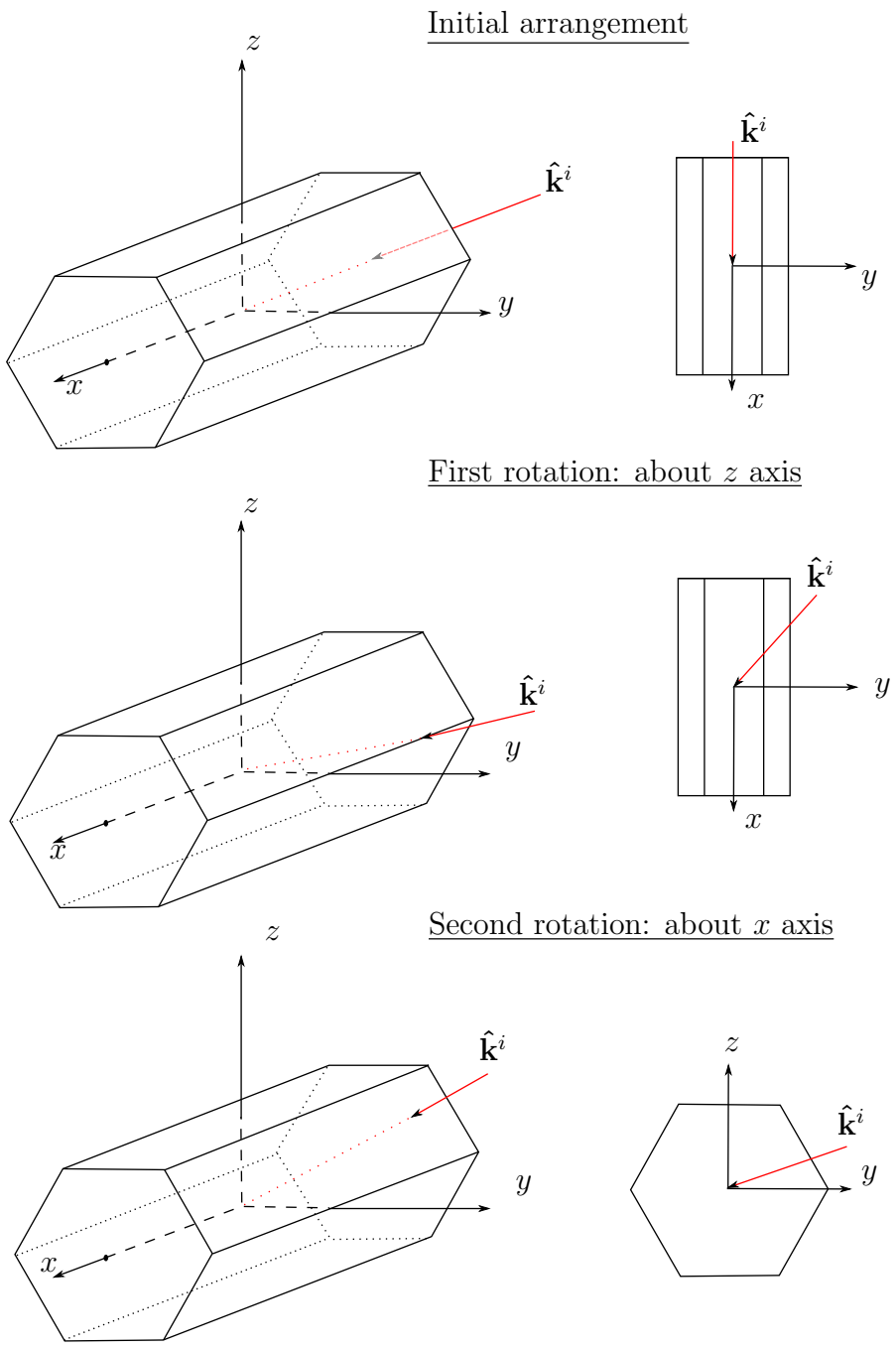

Figure 6.3: The orientation of the incident beam in the DDA simulations is adjusted by two rotations, as shown.

The four rotations that are considered for the transparent case are given in Figure 6.4. For the absorbing columns only data for orientation (a) was provided.

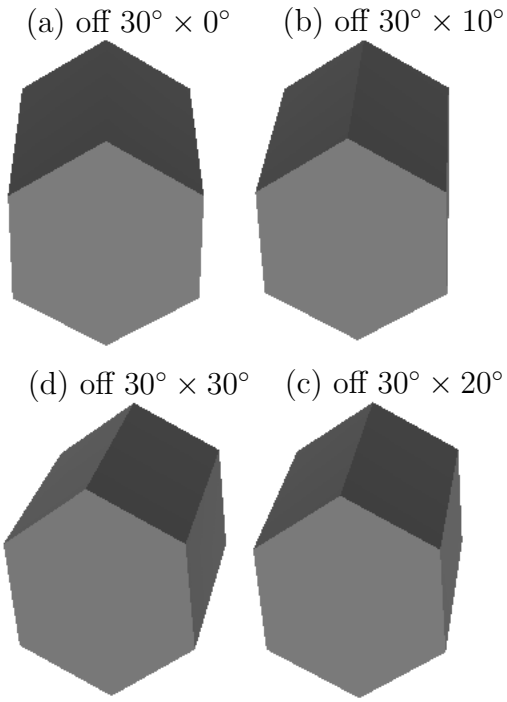

Figure 6.4: The four crystal orientations considered for a solid, transparent hexagonal column. The angles refer to the rotations of the incident beam about the z-axis and x-axis respectively, as shown in Figure 6.3.

6.2.2 Output Data

The scattering matrix is normalised so that the first element integrated over the entire scattering sphere is unity. The ADDA data contains differential scattering cross sections and is therefore not normalised so post processing was necessary, which ensured fair comparison between the two models. Furthermore, the ADDA computations had variable angular resolution in scattering angle with 205 angular bins between $0° - 180°$ (allowing for higher angular resolution close to direct forward and backscattering) and constant bin size of $1°$ in azimuthal angle; a list of the scattering bins used is given in Appendix E. The same angular resolution was used in the Beam Tracing computations.

Normalising was performed using Equation 2.23 in a discretised form, given in Equation 6.3.

$$P'_{11}(\theta,\phi) = \frac{4\pi P_{11}(\theta,\phi)}{\sum_{j=1}^{360}\sum_{i=1}^{205} P_{11}(\theta_i,\phi_j)\sin\theta_i\Delta\theta_i\Delta\phi_j}. \tag{6.3}$$

The degree of linear polarisation is found via:

$$\text{dlp} = -\frac{P_{12}}{P_{11}}. \tag{6.4}$$

Both the P_{11} and dlp were azimuthally averaged to get one-dimensional functions dependent on the scattering angle only. From the one-dimensional P_{11} the asymmetry parameter could be directly calculated using:

$$g = \int P'_{11}(\theta)\cos\theta \mathrm{d}\theta. \tag{6.5}$$

Two-dimensional scattering patterns are used to give scattering information over the entire scattering sphere. Forward ($\theta \in [0°, 90°]$) and backward ($\theta \in [90°, 180°]$) scattering patterns are given separately. Figure 6.5 provides a means to aid in reading the two-dimensional scattering patterns which will be presented.

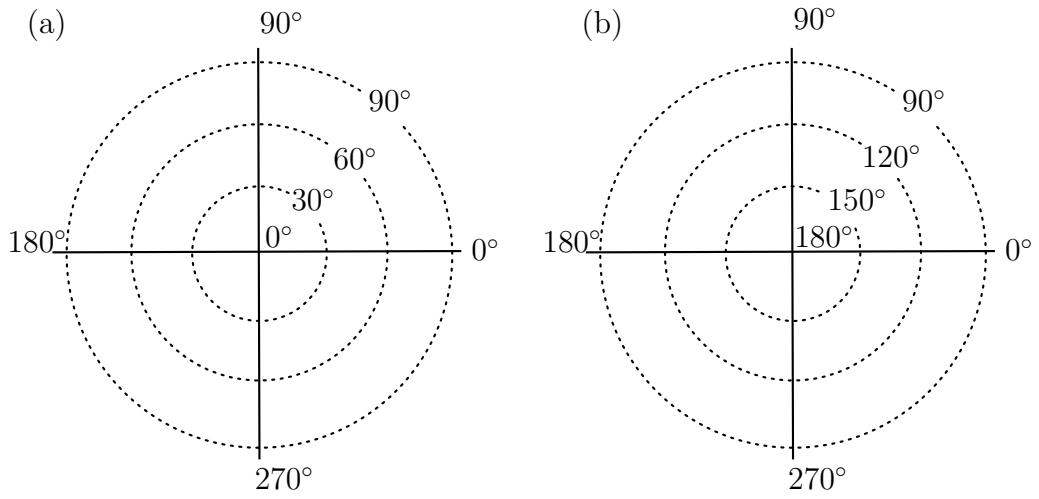

Figure 6.5: The forward and backward scattering hemispheres expressed as polar plots, with concentric rings denoting constant scattering angle, θ.

Geometric optics cannot be used to study ice crystals in fixed orientation due to the finite number of scattering directions. Usually, geometric optics is applied to randomly oriented crystals. The resulting scattering matrix elements do not have any azimuthal dependency and plots of intensity against scattering angle are commonly referred to as *phase functions*. As the Beam Tracer incorporates far field diffraction it is not limited to randomly oriented crystals and so can be applied to fixed orientation, as is done in this thesis. To avoid confusion, we do not refer to one-dimensional P_{11} plots as phase functions, instead using the term azimuthally averaged P_{11}.

In the following sections, plots of intensity (P_{11}) will be presented in a logarithmic (base 10) scale; degree of linear polarisation plots will be in a linear scale. Colourbars for the two-dimensional scattering patterns are reserved only for total scattering, i.e. scattering patterns resulting from considering all beams. When two-dimensional patterns are presented without colourbars it should be understood that these are for qualitative use only, to aid with description.

6.3 Results for Transparent, Smooth, Pristine, Hexagonal Columns

We will consider, in detail, scattering from a hexagonal column in orientation (a) of Figure 6.4 of size parameter 100. Two-dimensional intensity patterns derived from the Beam Tracer and ADDA are given in Figure 6.6 (top and bottom row respectively). There is generally good agreement between the two, with common bright features visible in both. The agreement is worst at side-scattering angles

around 90° where dark patches are present in the Beam Tracing results and not in the corresponding ADDA pattern.

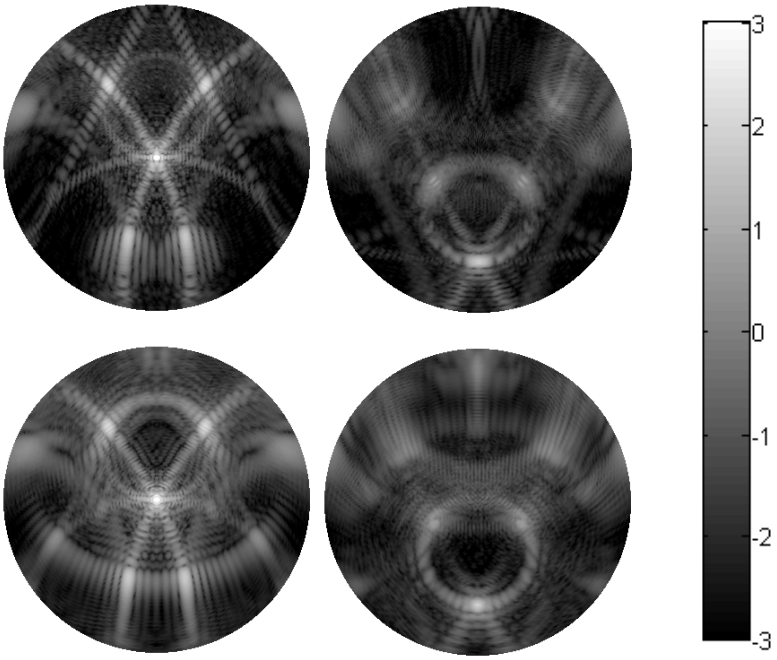

Figure 6.6: Beam Tracing (top row) and ADDA (bottom row) two-dimensional intensity distributions.

The incident light undergoes external diffraction which is shown in Figure 6.7. The external diffraction pattern has an intensely bright centre in the forward scattering direction. Diffraction fringes are visible in the scattering pattern, especially along the bright arcs, with very little light scattered in directions away from these.

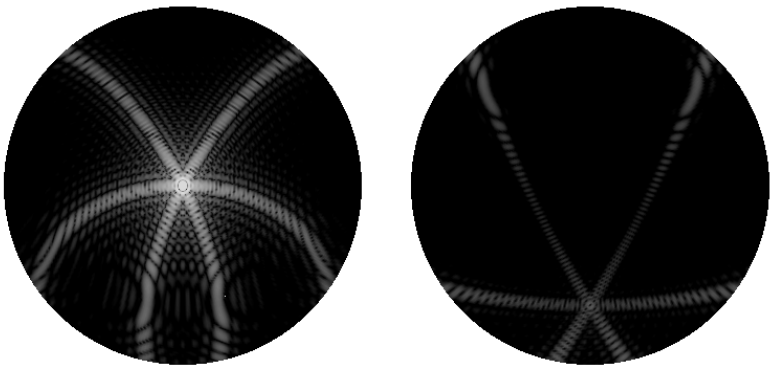

Figure 6.7: External diffraction of the incident wave around the crystal.

Geometric optics terminology can be used to aid in the interpretation of two-dimensional scattering patterns, attributing bright regions to reflection and transmission of beams. In the following it will be shown how the overall scattering pattern develops due to different beams. To aid in this, Figure 6.8 displays an annotated version of the Beam Tracing 2D intensity pattern originally given in Figure 6.6. The numbers correspond to the twelve main beams which contribute to the overall scattering pattern. The origins of these twelve beams will be discussed.

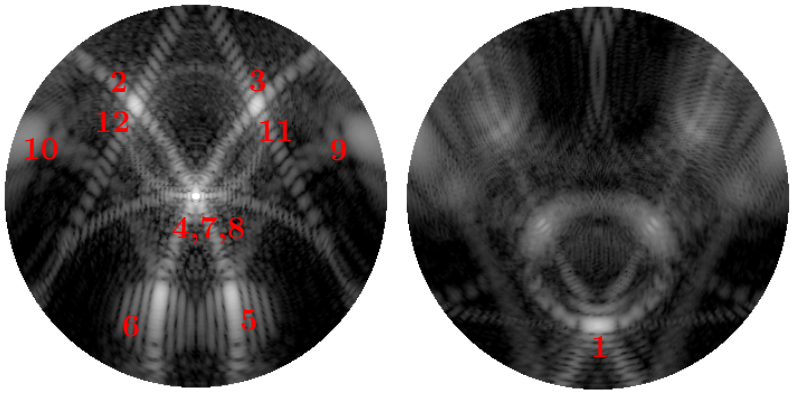

Figure 6.8: Annotated version of the Beam Tracing results given in Figure 6.6

The incident wave illuminates two prism facets and one basal facet. Due to the symmetry of the hexagonal column and orientation, the two beams formed by the two prism facets will lead to symmetric beams throughout their propagation within the crystal. The three initial beams are shown in Figure 6.9 (the incident light is into the page). The three blue beams in Figure 6.9 are externally reflected leading to beams propagating in the directions $(120°, 270°)$, $(51°, 124°)$ and $(51°, 56°)$ which are labelled 1-3 on Figure 6.8.

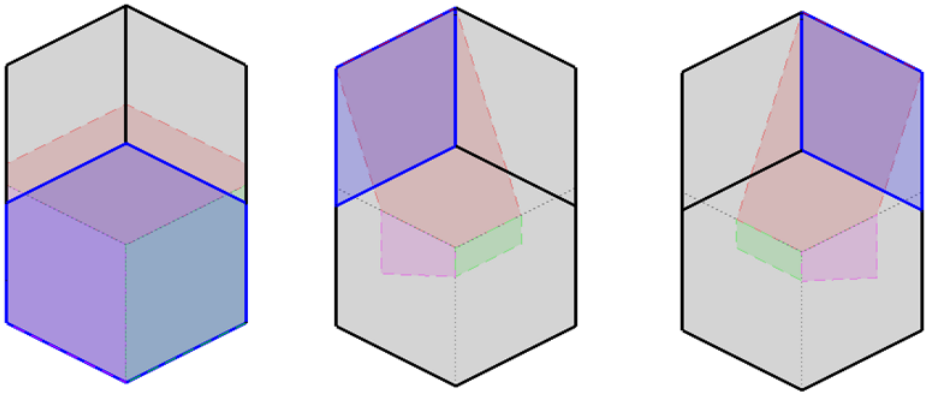

Figure 6.9: Transmission leads to nine new beams. Blue denotes the parent beam in each case, that is, the beam that is transmitted into the crystal.

The reflected beams each undergo diffraction as they scatter. The 'aperture' through which they diffract has the same shape as the beam's cross section on the facet. The diffraction patterns of beams 1-3 is given in Figure 6.10. The symmetric nature of the reflected beams is visible in their respective diffraction patterns (second and third row). The bright spots are in the geometric optics scattering direction, i.e. in the direction of reflection.

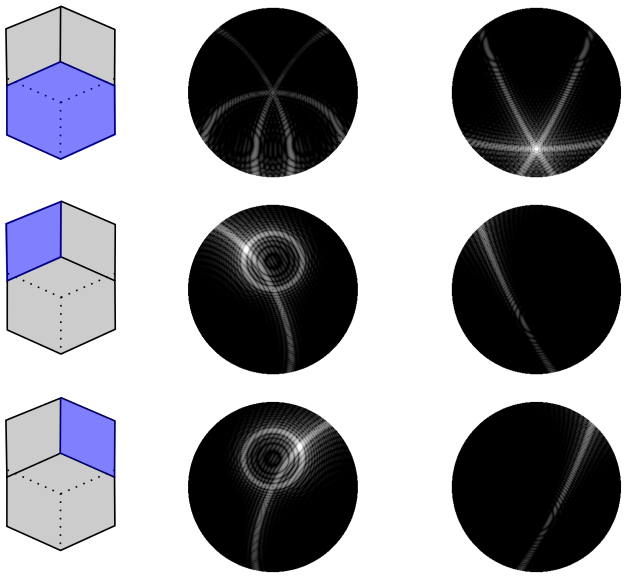

Figure 6.10: Individual scattering patterns arising due to the diffraction of beams 1-3. Diffraction of the beam reflected off the basal facet is given in the top row. The second and third are diffraction of the reflected beams off the two prism facets.

The combined scattering pattern of external diffraction and reflection is found by combining the associated amplitude matrices and is given in Figure 6.11. The similarity to the external diffraction pattern given in Figure 6.7 is due to them both being formed from the same apertures. However, in the combined scattering pattern there are additional bright features due to reflection.

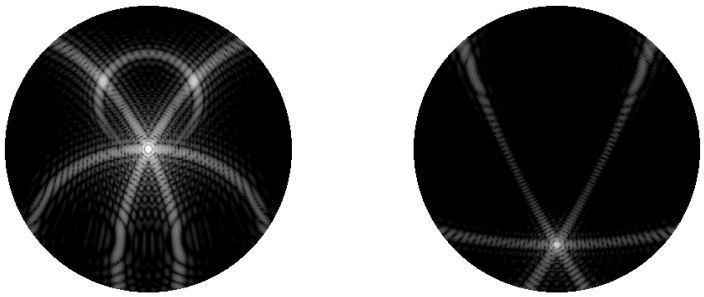

Figure 6.11: Resulting scattering pattern when the externally reflected beams are combined with external diffraction added.

Transmission into the crystal leads to the formation of new beams, shown in red, green and magenta in Figure 6.9. Due to the crystal being transparent, first order transmission events carry the majority of the incident energy. The beam shown in red in the left panel of Figure 6.9 is scattered into the direct forward ($\theta = 0°$), in geometric optics terms it is responsible for the *delta transmission peak* [64]. The large size of this beam, combined with its zero transmission angle, results in it carrying approximately 25% of the incident energy, the largest of any single beam. On Figure 6.8 it is labelled as point 4; its individual diffraction pattern is shown in Figure 6.12.

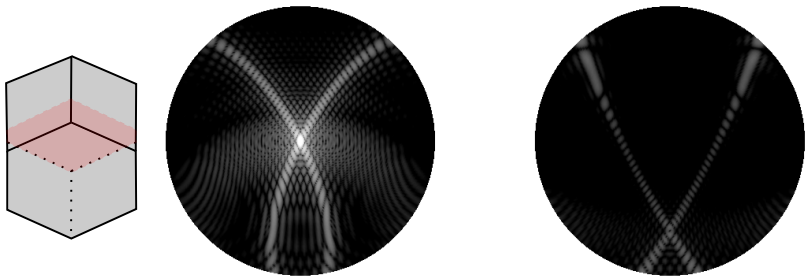

Figure 6.12: Individual scattering patterns arising due to the diffraction of beam 4.

Note that the diffraction arcs seen in Figure 6.12 can also be seen in the previous figures because of the common facet edges. The combined amplitudes of beams 1-4, with external diffraction are given in Figure 6.13.

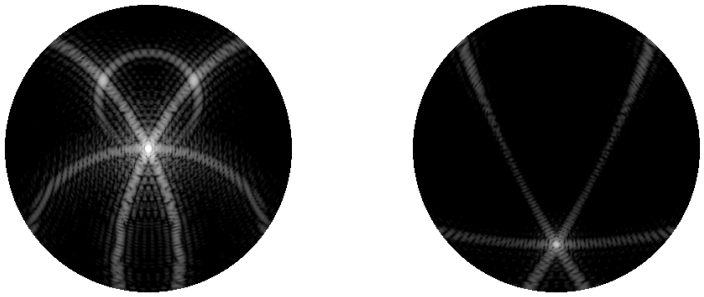

Figure 6.13: Combined scattering pattern of beams 1-4.

The addition of the transmitted beam leads to increased interference in the centre two arcs, with diffraction minima present in the region around $(90°, 270°)$. The magenta and green beams also formed through transmission on the basal facet both undergo total internal reflection at a prism.

The remaining two cases [middle and right panel of Figure 6.9] corresponding to transmission through the prism facets are symmetric, leading to symmetric beam paths. Such beam pairs will have identical scattering angles, but differing azimuthal angles. In addition when they scatter in either the direct forward or backward direction they will have identical path lengths and so will add constructively. Their two dimensional features will be symmetric about the plane $\phi = 90°$ so we will focus on case (b) only, giving the corresponding scattering directions for case (c) in square brackets.

The largest beam formed via transmission through the prism facet is the shown in red. Its subsequent transmission (it also undergoes internal reflection) out of the basal facet leads to a scattered beam in the direction $(51°, 290°)$ [$(51°, 250°)$]. These points are labelled 5 and 6 on Figure 6.8, with individual scattering patterns given in Figure 6.14.

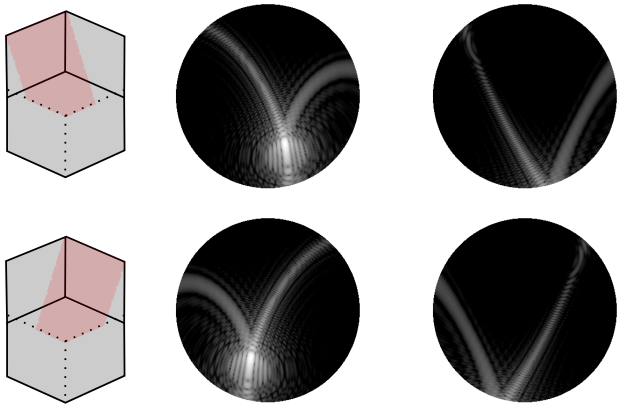

Figure 6.14: Individual scattering patterns from beams 5 and 6.

Including these beams in the overall scattering pattern we arrive at Figure 6.15. Most of the notable features from the total scattering pattern are now visible. The two arcs which pass though the new peaks (marked by a red dotted line) do not overlap any of the existing arcs in the scattering pattern. This is because two of the edges of the beam's cross section on the facet are not along crystal edges (see red region of centre panel of Figure 6.9). As the number of internal interactions increases, the cross section of beams gets smaller and so the likelihood of one of a given beam's edges running along a crystal edge also decreases. This in turn leads to more small non-overlapping diffraction arcs, which cause the hazy appearance in the scattering pattern, as these small beams diffracted fields interfere.

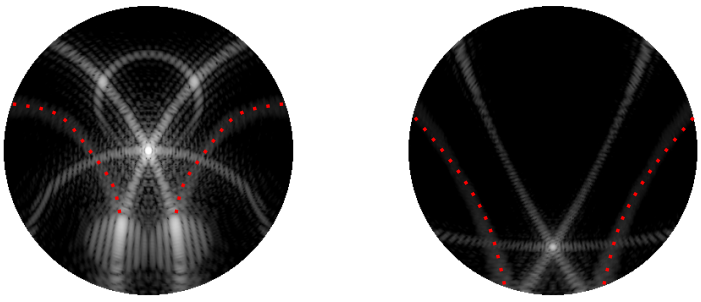

Figure 6.15: Combined scattering pattern of beams 1-6, with external diffraction added.

The green beam in the middle and right panels in Figure 6.9 is transmitted out of the crystal in the direct forward direction (points 7 and 8 on Figure 6.8). These beams are quite low intensity with each carrying about 3% of the incident energy. Their scattering patterns are given in Figure 6.16.

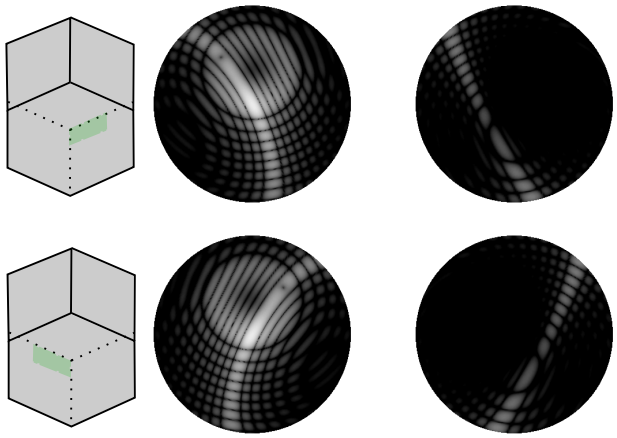

Figure 6.16: Individual scattering patterns from beams 7 and 8.

The magenta beam undergoes total internal reflection leading to a new beam intersecting with the basal facet (see Figure 6.17). The transmitted part of this beam leaves in the direction $(88°, 18°)$ $[(88°, 162°)]$ labelled as point 9 [and 10] in Figure 6.8.

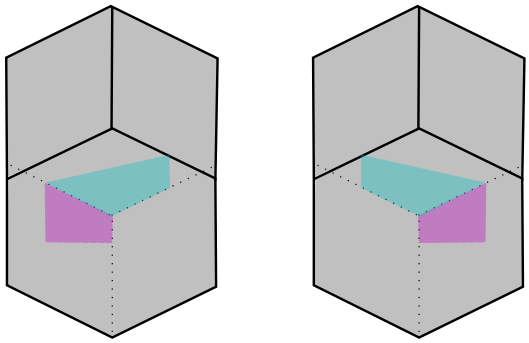

Figure 6.17: Total internal reflection leads to a new beam illuminating a portion on the basal facet.

The resulting diffraction pattern from these beams is given in Figure 6.18. These contributions are significant as they cause the blurred features seen in the forward scattering patterns at $\phi \approx 20°$ and $\phi \approx 160°$ visible in both the ADDA and Beam Tracer results. Not only this, but their contribution to the backscattering hemisphere is greater than that of any other beam discussed so far.

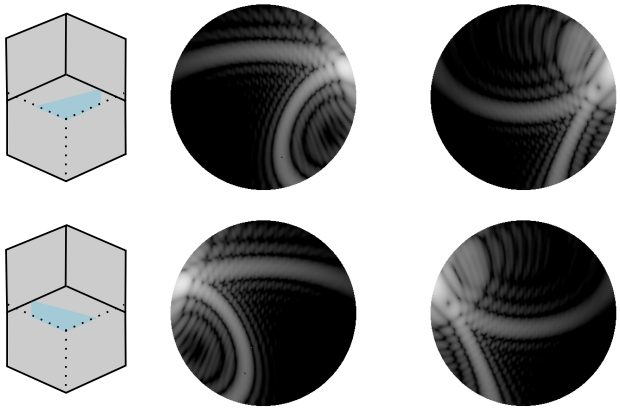

Figure 6.18: Individual scattering patterns from beams 9 and 10.

Combining beams 1-9 with external diffraction forms the pattern shown in Figure 6.19. At this point the majority of the features seen in the total forward scattering pattern (Figure 6.6) are visible. The backscattering hemisphere has not developed the complexity observed, but this is due to the analysis outlined so far neglecting higher order internal reflection events.

Figure 6.19: Combined scattering pattern of beams 1-10, with external diffraction added.

The strong peaks at $(51°, 56°)$ and $(51°, 124°)$ seen in the overall pattern cannot be attributed to external reflection alone. This is because the crystal is non-absorbing and therefore weakly reflecting. Returning to the left most configuration in Figure 6.8, the magenta and green beams, which were totally internally reflected, form beams on the basal facet illuminating a region as shown in Figure 6.20. These then propagate out of the crystal in the directions of $(51°, 56°)$ and $(51°, 124°)$ each carrying approximately 15% of the incident energy; these are labelled as points 11 and 12 on Figure 6.8.

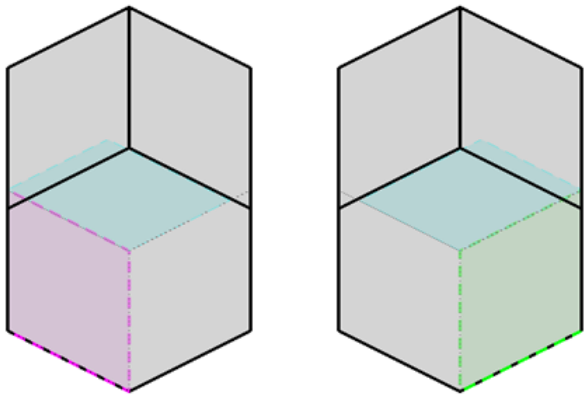

Figure 6.20: Total internal reflection off the prism facets leads to beams which propagate in the same direction as two of the externally reflected beams.

The diffraction patterns associated with these beams are given in Figure 6.21. The bright peak corresponds to the direction of transmission (which is also the same as the direction of external reflection). It is interesting to note how these patterns differ to those formed by the externally reflected beams (Figure 6.10). Despite there being no shared crystal edges both pairs of patterns share a common diffraction arc. This is because part of the transmitted beam cross section is parallel to the edge of the upper prism facets. Whereas the reflected beam had a ring-like feature in its scattering pattern the diffraction pattern for this transmitted beam is a larger arc. This is because the vector in the direction of transmission draws a large angle with the facet edge than was the case for extenal reflection.

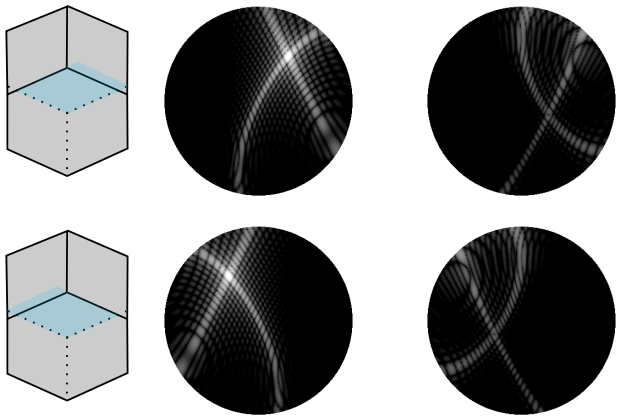

Figure 6.21: Individual scattering patterns from beams 11 and 12. The roughly square like beam cross section leads to a diffraction pattern similar to that seen for a square aperture, with curvature being caused by oblique incidence.

Figure 6.22 gives the scattering pattern formed by beams 1-12 with external diffraction. Internal reflections will lead to the formation of additional features, most of which will be in the backscattering hemisphere.

Figure 6.22: Combined scattering pattern of beams 1-12, with external diffraction added

Higher order internal reflection events, followed by outward refraction, lead to small contributions in other scattering directions. In terms of energy these twelve beam paths account for 87% of the incident power. An individual breakdown is given in Figure 6.23, where the scattering directions associated with a given beam are given along the upper x-axis.

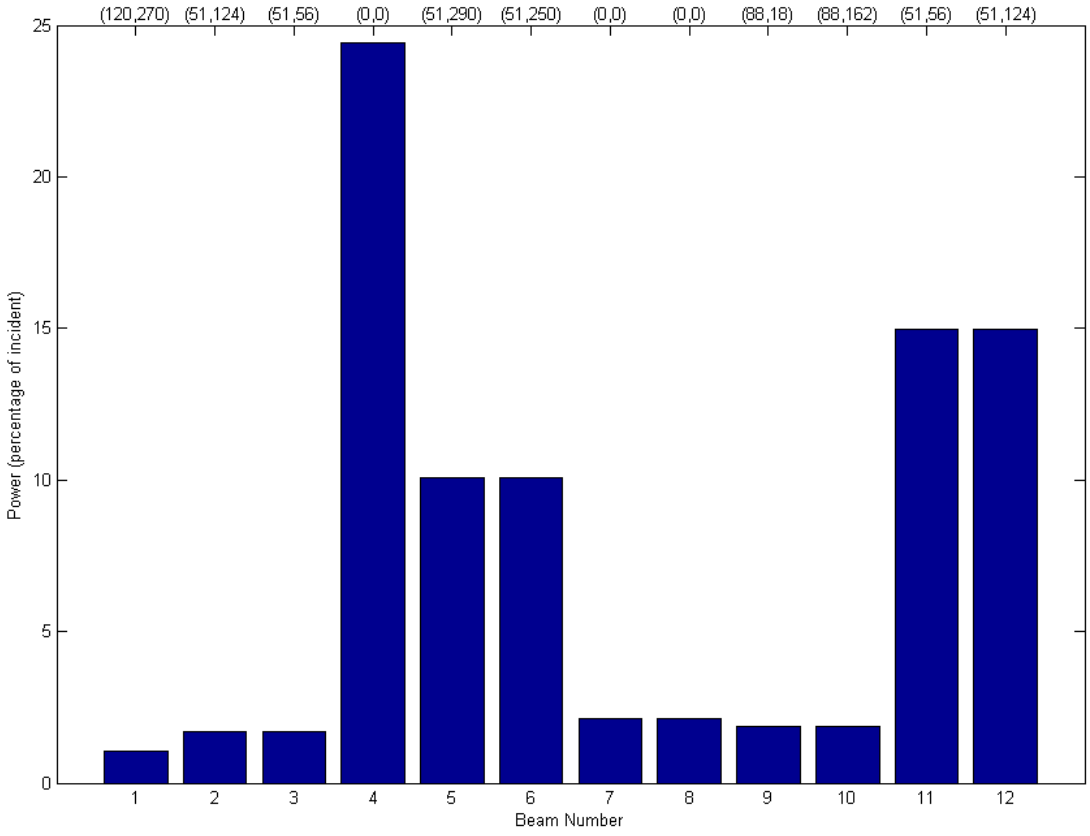

Figure 6.23: The power carried away from the crystal by the twelve beam paths discussed. The scattering angles are given along the top of the chart.

Azimuthally averaging the two-dimensional scattering patterns removes the azimuthal dependency on scattering, see Figure 6.24. The large peak at 51° is formed predominantly by beams 2,3,5,6 11 and 12 which together carry more energy than

beams scattered into the direct forward direction. However, direct forward is still greater because of the contribution of external diffraction. General agreement between the Beam Tracing model and DDA is good, especially in geometric optics scattering directions. However, Beam Tracing does not seem to be able to carry sufficient energy away from the GO scattering direction, highlighting a limitation of the diffraction approximation used. This is most noticeable towards the direct backscattering. There are no geometric optics beams associated with this direction for this particle orientation, the closest being at 151°. The difference between Beam Tracing and DDA in the neighbouring region is quite clear, especially at direct backscattering.

It is also noteworthy that there seems to be a slight shift in the peak at 151° between Beam Tracing and DDA. This is potentially due to the effects of Fresnel diffraction on deflecting the propagation of beams inside the crystal. The Beam Tracing model only considers the far-field diffraction of beams as they scatter, there is no modelling of internal deflection.

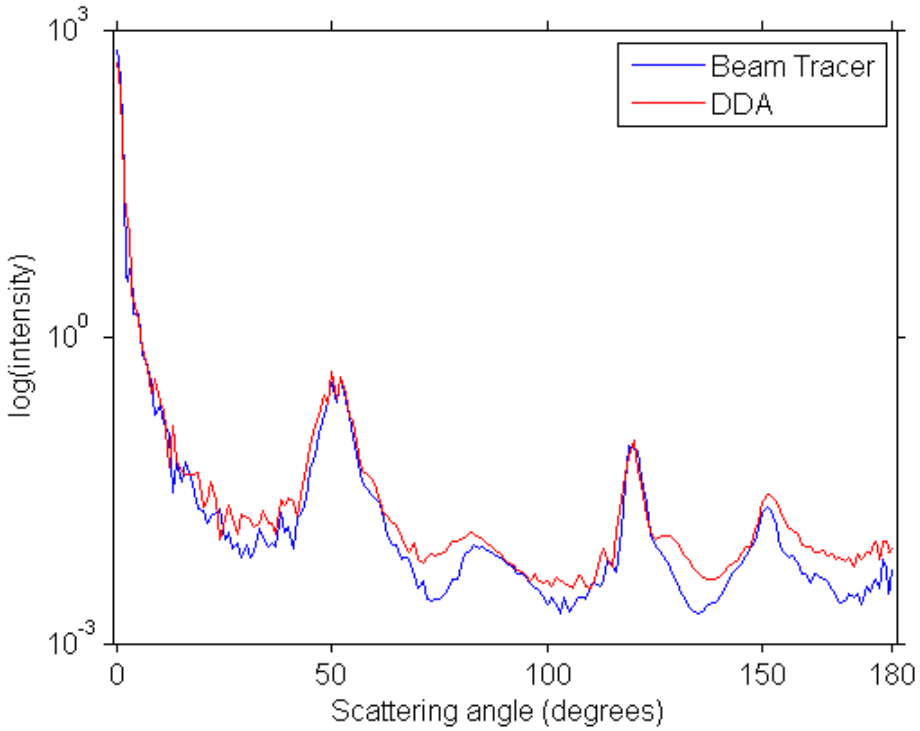

Figure 6.24: Azimuthally averaged P_{11} for the size parameter 100 particle currently being discussed.

Since the dlp is found through the ratio of the P_{11} and P_{12} elements, in regions of low intensity small errors in P_{11} will lead to large dlp values. In this way, small (or low intensity) beams can have a significant effect on the dlp. This all means that a beam-by-beam analysis is not informative when discussing dlp plots. However, a general property of beams is that their polarisation patterns form a cone about the scattering plane. Figure 6.25 gives the two polarisation patterns from the two beams externally reflected by prism facets.

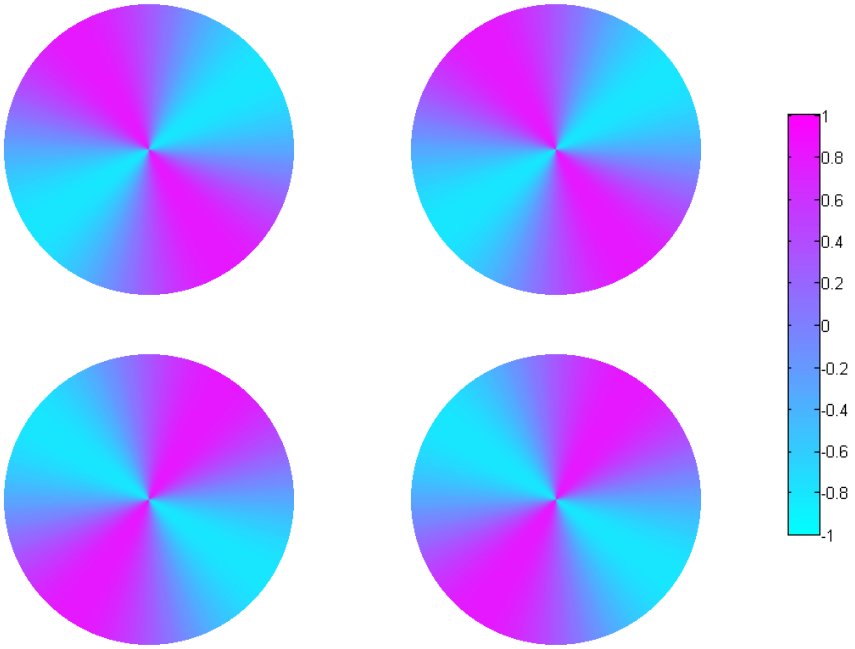

Figure 6.25: External reflection leads to the formation of positive degree of linear polarisation cones about the respective scattering angles.

The degree of linear polarisation derived from both Beam Tracing and ADDA is presented in Figure 6.26. It is difficult to extract anything meaningful from the plot, but regions of close to zero polarisation are seen in the forward scattering hemisphere, while the backward scattering hemisphere is generally negatively polarised with respect to the scattering plane. The ADDA forward scattering hemisphere shows a strong negatively polarised region in the azimuthal range $180° \leq \phi \leq 360°$ in the same fan like structure seen in the intensity plot (bottom row of Figure 6.6). This fine structure was not present in the corresponding Beam Tracing plot which is believed to be caused by the Kirchhoff diffraction approximation employed in the model.

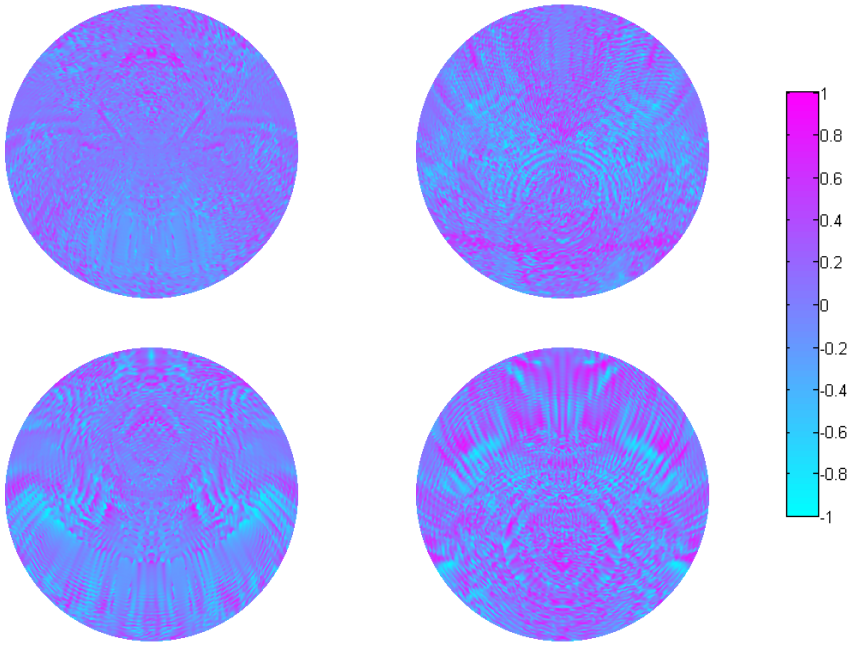

Figure 6.26: Two-dimensional degree of linear polarisation derived using Beam Tracing (top row) and ADDA (bottom row)

Azimuthally averaged dlp results are given in Figure 6.27. Both Beam Tracing and ADDA show near zero polarisation across the entire scattering angle range. There is quite good agreement, except in the region between $130° \leq \theta \leq 180$. This could be due to the lack of geometric optics scattering directions in this range.

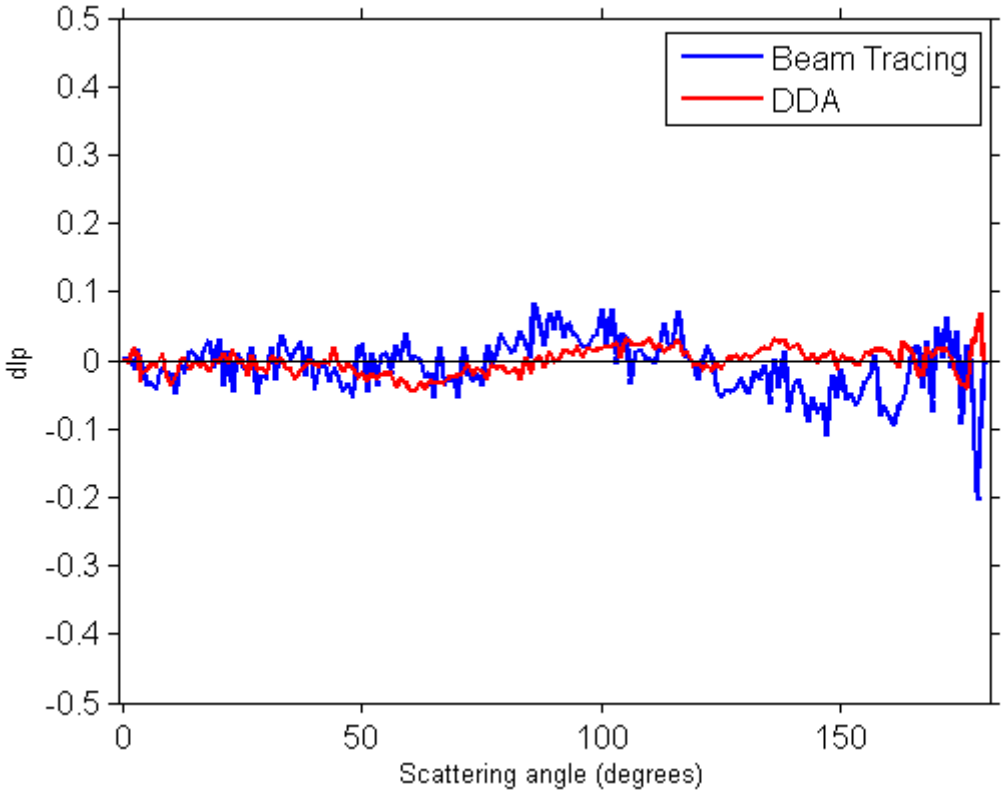

Figure 6.27: Azimuthally averaged dlp.

6.3.1 Effects of Size and Orientation

We now discuss, in broad terms, the effects of changing size and orientation on the scattering properties of the hexagonal ice crystals. Figure 6.31 contains azimuthally averaged P_{11} for the sixteen cases for which DDA data were available; with corresponding dlp patterns in Figure 6.32. The four rows correspond to the four particle size parameters (20, 40, 60 and 100) and the four columns correspond to the orientations given in Figure 6.3.

Changing orientation refers to moving from orientation (b) to (d) of Figure 6.4, exposing more facets to the incident wave. As the direction of incidence is rotated about the $x-$ axis by 10° we see the breakdown of the symmetry about the plane $\phi = 90°$ in the scattering pattern, see Figure 6.28. The two peaks associated with external reflection and transmission also move away from $\theta = 51°$, one increases in scattering angle while the other decreases, illustrated by the blue and red dashed lines respectively. This change is seen in the one-dimensional, azimuthally averaged intensity pattern (Figure 6.31) by the splitting of the 51° peak (2nd column of the 4th row). The splitting of this peak and the shifting of some beams to a higher scattering angle of roughly 55° helps decrease the difference between the DDA and Beam Tracer in the side scattering region. However, there is a significant difference between the two models in the direct backscattering. This is an anomalous result in comparison to all other sizes and orientations where the differences in the backscattering are not so severe.

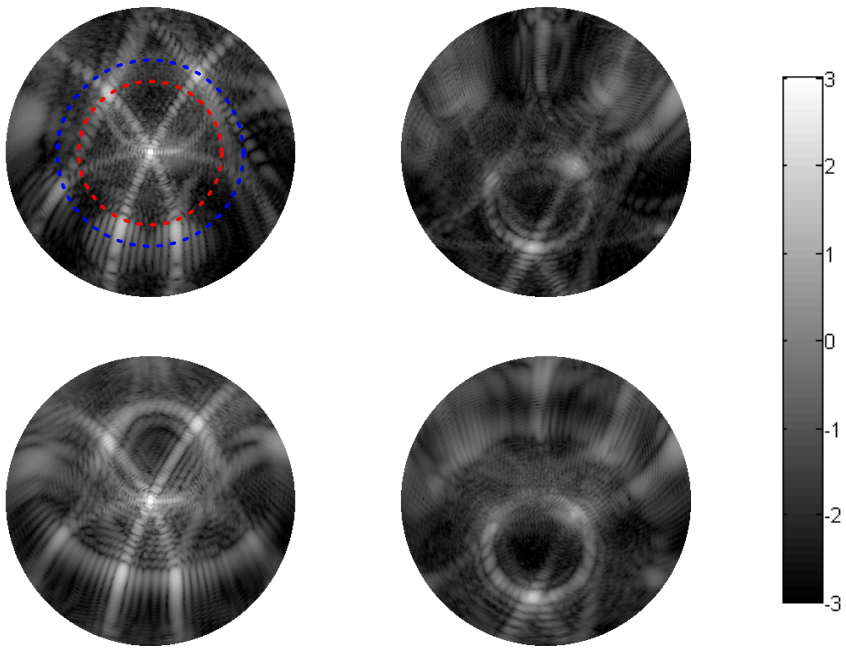

Figure 6.28: Two-dimensional scattering patterns for size parameter 100 in orientation (b). The top row is data acquired using DDA, the bottom row Beam Tracing. Columns denote forward and backward scattering respectively.

Continuing to rotate the incident beam about the $x-$axis, the original 51° continues to move away in the averaged phase function. Notice how the diffraction arc that runs through the peak in the red circle is straightening out, this is due to the angle between the incident beam and (inward facing) surface normal decreasing. In addition to this, a bright spot separates from the direct forward due to reflection from the now visible third prism facet. This peak travels along the closed arc joining the two existing reflection peaks, and the direct forward. These peaks are all connected due to their shared edges between neighbouring facets, which lead to the bright diffraction arcs.

At the maximum rotation of 30° of the incident beam about the x-axis, there are three prismatic reflection peaks (points 1-3), and three transmission peaks (point 5). This crystal orientation demonstrates strongest retro-reflections. As the beam paths are symmetric the beams themselves will add in phase leading to the pronounced peak in the direct backscattering (point 7); an in-depth discussion of this can be found in [112]. Note that the reflection peak from the basal facet (point 8) lies on a diffraction arc which also passes through point 1. This is again due to the shared edge between the basal facet and the prism facet. In the Beam Tracing 2D pattern, the diffraction approximation is recognisable from the presence of the two diffraction arcs passing through point 1. They are analogous to diffraction from a rectangular aperture. The effect is not seen in the ADDA pattern, however, only the arc also passing through the direct forward direction and which is shared with external diffraction is visible. The non-appearance of the other arc is presumably due to phase effects smearing it out. Due to the additional transmission peak near side scattering (points 5), the fan like structure is more pronounced in the Beam

Tracing model than for the orientation shown in Figure 6.6. This is because the additional scattering direction is able to compensate for limited angular range of the diffracted beam.

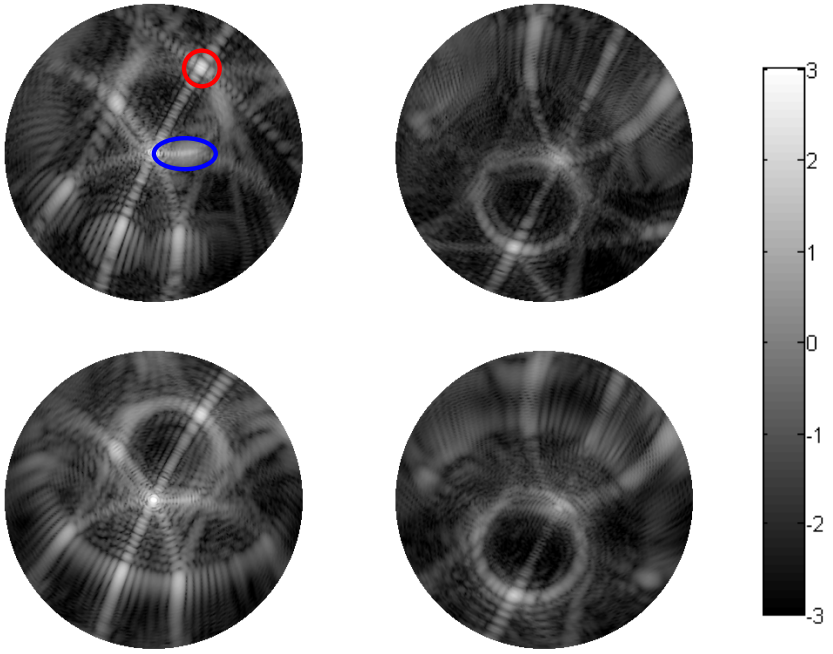

Figure 6.29: Same as Figure 6.28 but for orientation (c)

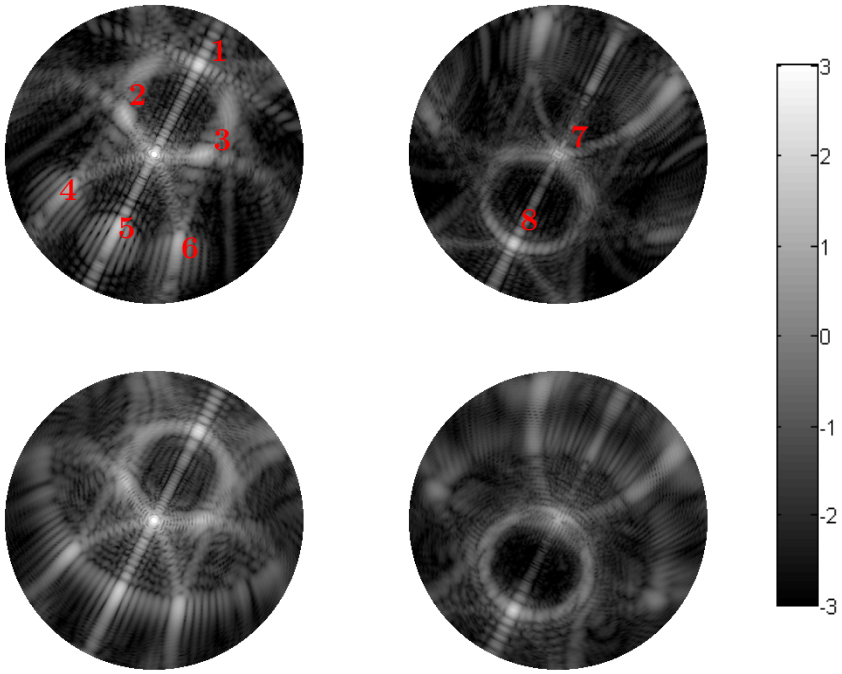

Figure 6.30: Same as Figures 6.28 and 6.29 but for orientation (d)

This rotation also re-established a plane of symmetry, now at $\phi = 60°$. In general, symmetry properties of the crystal are reflected in symmetry properties of the scattering pattern. The symmetric reflection peaks are much closer to forward scattering, at around 25°. The one dimensional pattern, in the fourth column of the bottom row of Figure 6.31 shows excellent agreement over most of the scattering range. For this orientation the number of available beam paths (and related beam cross sections) are largest. For non-skew rays inverse ray paths should lead to constructive interference, but as explained in [112], some symmetric 'skewed' beam paths will undergo destructive interference due to phase shifts of π.

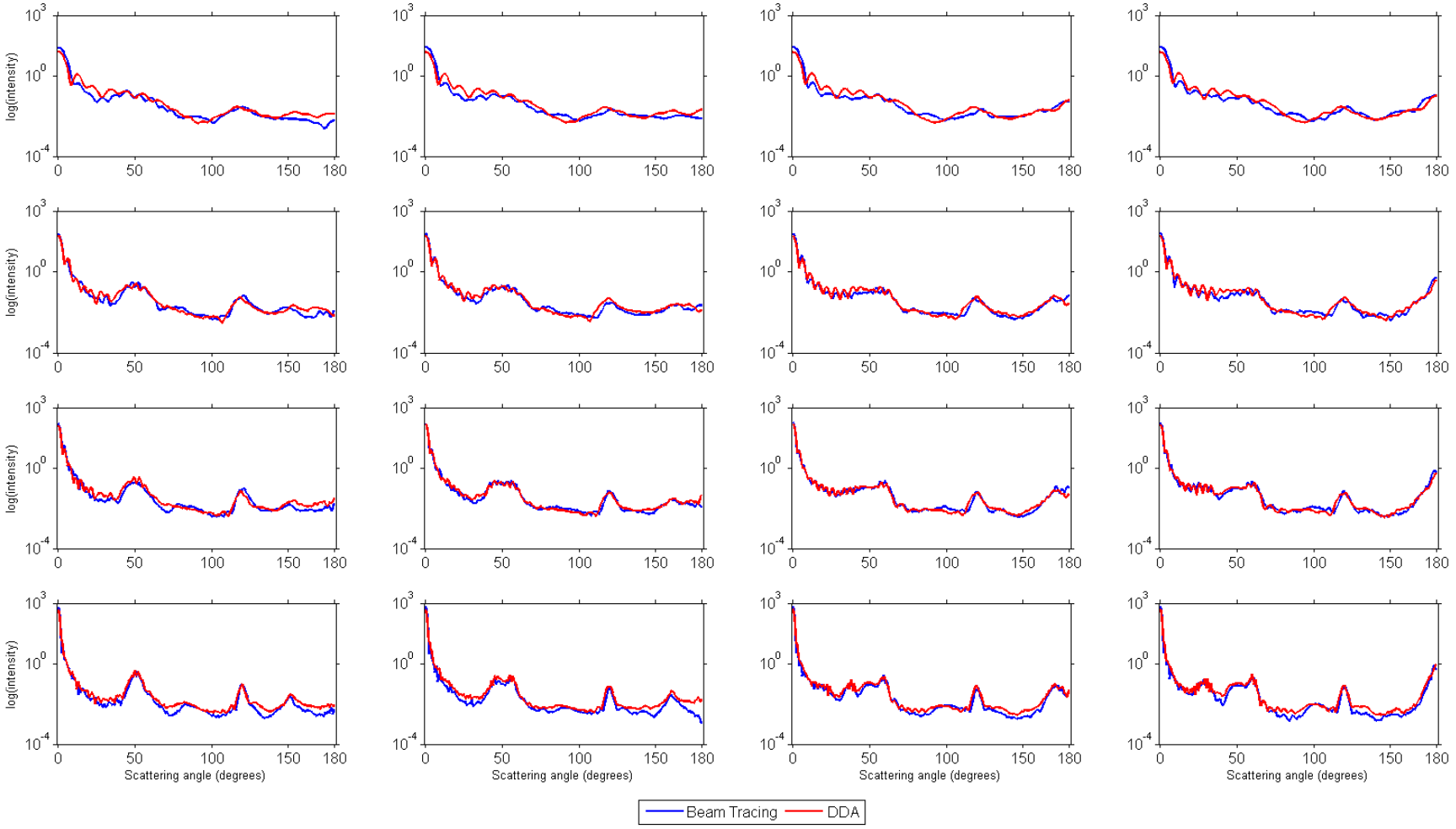

Figure 6.31: Azimuthally averaged P_{11} elements calculated using the Beam Tracer (blue) and ADDA (red). Rows correspond to particle size parameters $x = 20,\ 40,\ 60$ and 100. Columns correspond to particle orientations (a) - (d).

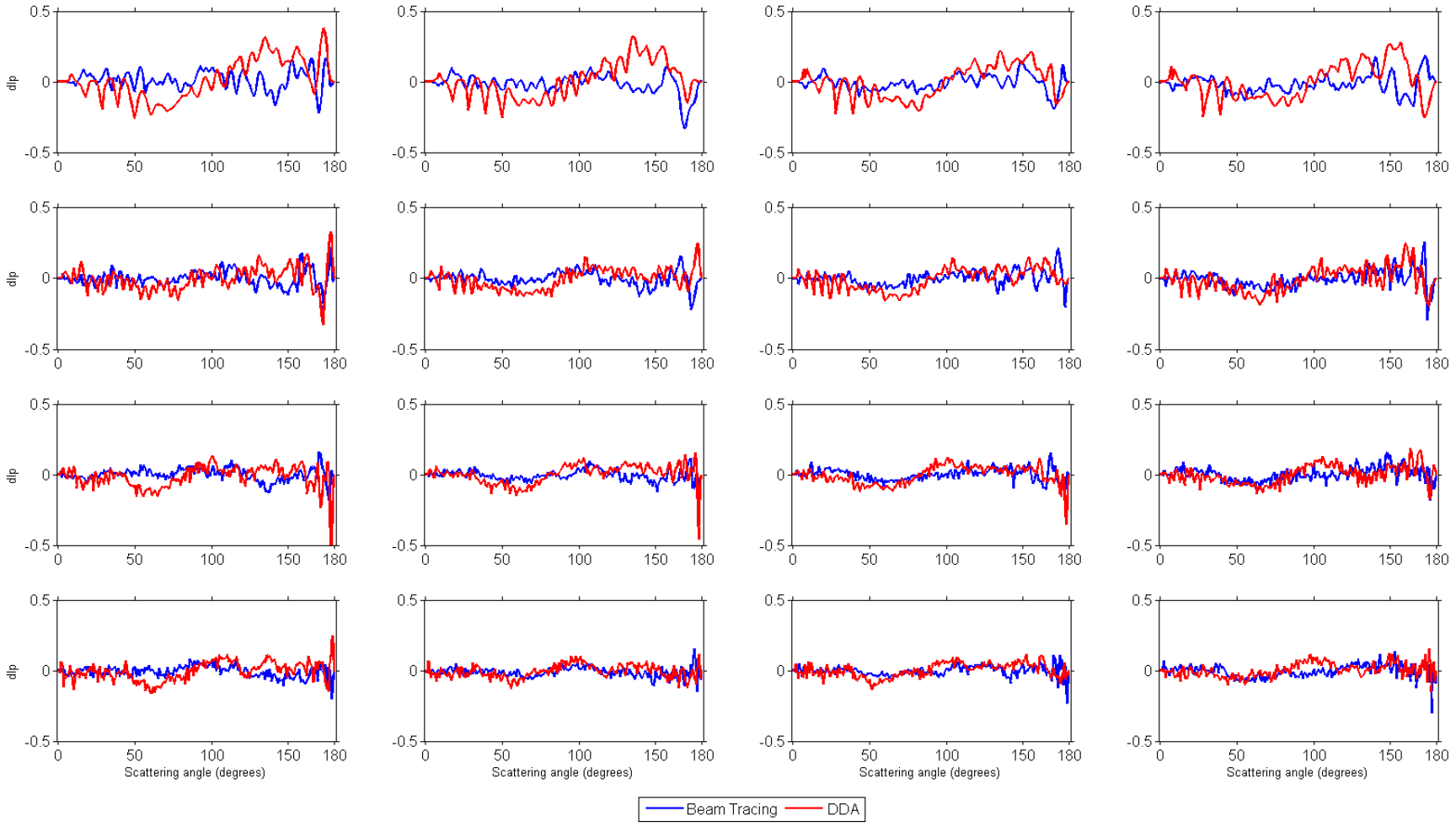

Figure 6.32: Same as Figure 6.31, but for degree of linear polarisation.

Next, we discuss the effects of size on scattering patterns. The treatment of electromagnetic scattering as a process of reflection and transmission of localised beams breaks down with decreasing size parameter as the geometric optics approximation becomes invalid. However, the treatment of diffraction (both external, and of scattered beams) should help mitigate this. For all cases, we see good agreement of the Beam Tracer with ADDA, especially at size parameter 60 (third row of Figure 6.31). With decreasing size parameter, the strength of the geometric peaks decreases, while the width of the peaks increases as a consequence of diffraction. At the smallest size parameter, the geometric optics peaks have all but been removed and washed out by diffraction. Figure 6.33 gives the two-dimensional intensity patterns for the crystal in orientation (d). This orientation is chosen since it displays the largest number of clearly defined geometric optics peaks. The first two columns in Figure 6.33 are the forward scattering hemisphere results for the Beam Tracer and for ADDA, respectively; the final two being the backward scattering results. The expected consequences of size on diffraction are observable, such as the increase in diffraction fringes with decreasing size and the corresponding increase in diffraction peak width. The geometric optics scattering peaks become less apparent with decreasing size and at size parameter 20 they are all but removed. In the backward scattering hemispheres this is most pronounced. The broad width of the diffraction peak associated with reflection off the basal facet is clear by the 'smudge' like feature in the 3rd and 4th columns. Again there is generally good agreement between the two (as reflected in the fourth column of Figure 6.31).

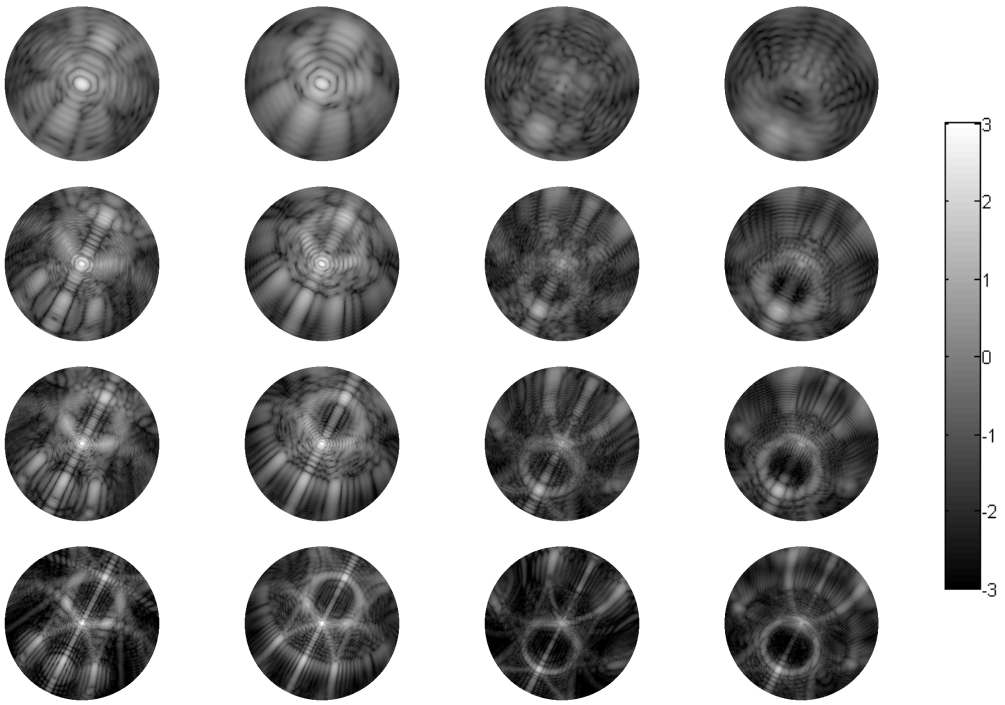

Figure 6.33: The effect of changing particle size parameter on the two-dimensional scattering pattern. From left to right the columns are Beam Tracer forward, ADDA forward, Beam Tracer backward, ADDA backward. From top to bottom we have $x = 20,\ 40,\ 60$ and 100.

Asymmetry parameters were calculated for all orientations and sizes and the resulting values, together with percentage differences with respect to ADDA, are given in Table 6.1. From size parameter 40 there is an increase of asymmetry parameter with size. The smallest percentage difference occurs for size parameter 60; for all cases the percentage difference between the two is less than 10%.

	Off 30×0			Off 30×10		
	g_{BT}	g_{DDA}	$\Delta g(\%)$	g_{BT}	g_{DDA}	$\Delta g(\%)$
$x = 20$	0.775	0.7243	7.00	0.7848	0.7208	8.88
$x = 40$	0.6974	0.7097	-1.73	0.7396	0.6997	5.70
$x = 60$	0.7400	0.7105	4.15	0.7221	0.7263	-0.58
$x = 100$	0.8108	0.7645	6.06	0.8355	0.7611	9.78
	Off 30×20			Off 30×30		
	g_{BT}	g_{DDA}	$\Delta g(\%)$	g_{BT}	g_{DDA}	$\Delta g(\%)$
$x = 20$	0.7710	0.7172	7.50	0.7593	0.7147	6.24
$x = 40$	0.7326	0.6923	5.82	0.7297	0.6877	6.11
$x = 60$	0.7260	0.7226	0.47	0.7263	0.7101	2.28
$x = 100$	0.8162	0.7686	6.19	0.8123	0.7471	8.73

Table 6.1: Comparison of asymmetry parameter predictions between DDA and the Beam Tracer.

We can perform a limited orientation average of these results, but do so with the caveat that such a limited sample is not representative of a hexagonal column in random orientation, the resulting azimuthally averaged P_{11} are given in Figure 6.34; with dlp given in Figure 6.35.

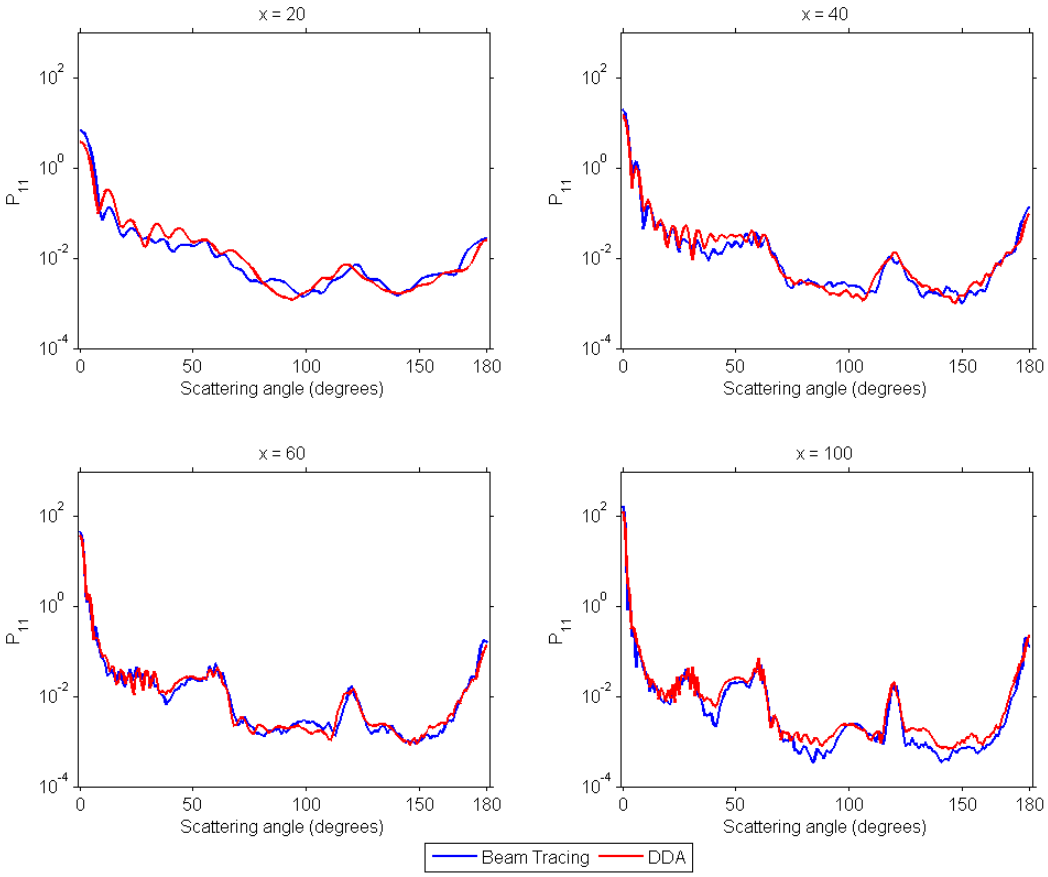

Figure 6.34: P_{11} averaged over the four orientations shown in Figure 6.4. The agreement between beam tracing and ADDA is clearly improved by orientation averaging.

The orientation averaged P_{11} show overall very good agreement, with a fair agreement seen at the smallest size parameter. The anomalous result in backscattering for one of orientations at size parameter 100 is all but removed because of this averaging. It seems that the negative dlp values close to direct backscattering caused by skew rays, which are very strong in geometric optics (see [113]) are much weaker in ADDA. This might indicate that the assumption of the applicability of geometric optics for beam propagation inside the crystal is not entirely justified. However, they too are improved by averaging, with both Beam Tracing Results and ADDA taking near zero values. The values for the asymmetry parameter are also improved by this averaging, see Table 6.2 with errors below 8% for all. While such small scale orientation averaging should be treated with a pinch of salt, the results are encouraging and suggest that the Beam Tracer could be a computationally cheap way of modelling particles in random orientation; as each orientation took around one minute to model.

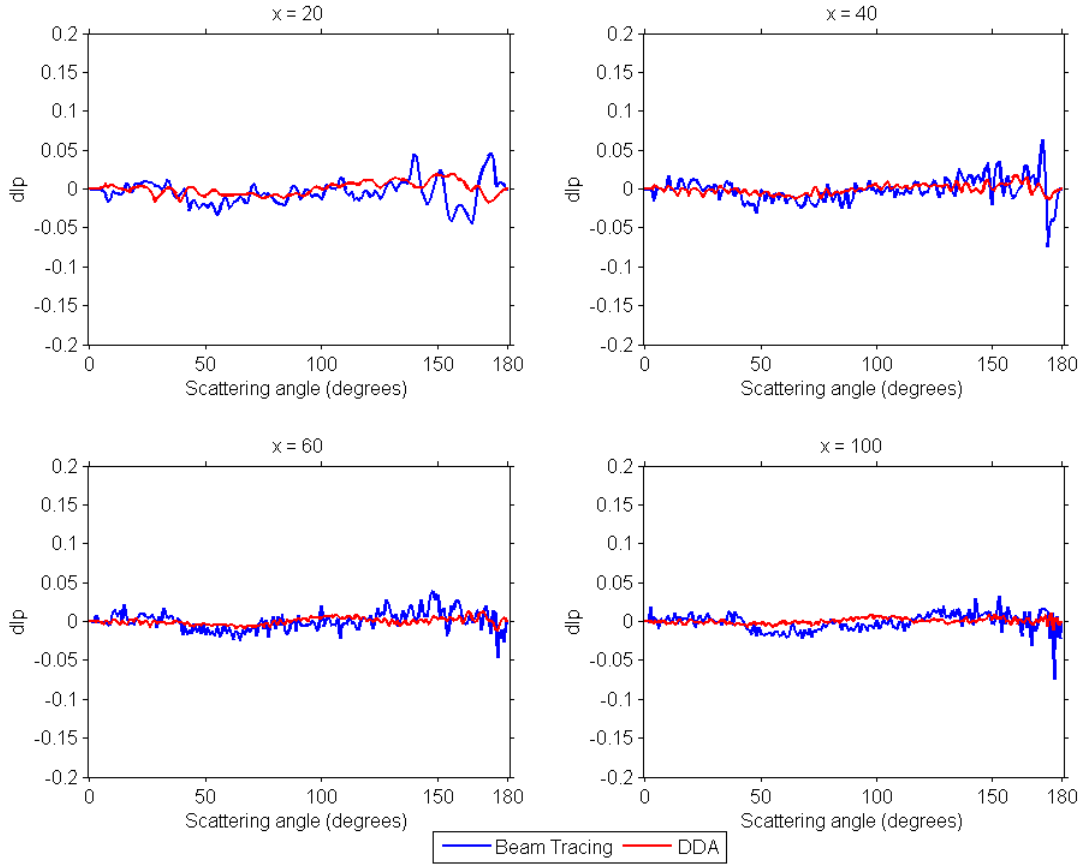

Figure 6.35: dlp averaged over the four orientations shown in Figure 6.4 and size parameters $x = 20, 40, 60$ and 100. For all size parameters there is near zero dlp across all scattering angles.

	$\bar{g}_{BT}$	$\bar{g}_{DDA}$	$\Delta\bar{g}(\%)$
$x = 20$	0.7725	0.7193	7.41
$x = 40$	0.7248	0.6974	3.97
$x = 60$	0.7286	0.7174	1.58
$x = 100$	0.8187	0.7603	7.69

Table 6.2: Orientation averaged asymmetry parameters

Figure 6.36 is a graphical representation of the data in Table 6.2. The error bars are found by the standard deviation of the asymmetry parameter over the four orientations for each size. There is a trend of increasing asymmetry parameter with size. In general the Beam Tracer predicts higher values than ADDA, most likely due to the difference in forward scattering. The best agreement between the two methods can be seen at $x = 60$.

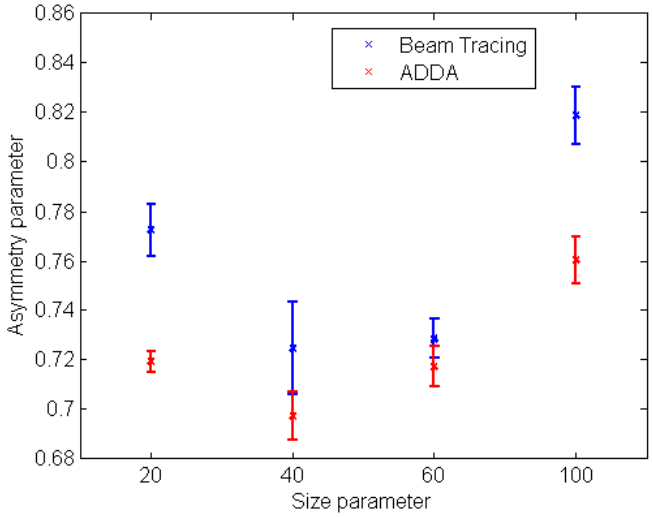

Figure 6.36: Comparison between the range of values predicted by the two methods for the asymmetry parameter averaged over the four orientations. Error bars give the standard deviation over the four measurements.

6.3.2 Analysis of the Accuracy of the Beam Tracer for Modelling Smooth, Transparent Hexagonal Columns.

From the two-dimensional scattering patterns we see that the Beam Tracer is able to produce results of qualitative similarity to those acquired through ADDA. Bright regions due to geometric optics scattered beams, curved bright arcs and diffraction fringes are clearly visible in these patterns. The one-dimensional, azimuthally averaged plots also show generally good agreement, with differences mainly in the side scattering region. For the transparent crystals, these were improved by orientation averaging. In order to better analyse differences in the two methods, Figures 6.37 and 6.38 give the absolute difference and percentage difference for the transparent cases. the absolute difference is given by:

$$\Delta(\theta) = |P_{11}^{\mathrm{BT}}(\theta) - P_{11}^{\mathrm{DDA}}(\theta)|. \tag{6.6}$$

From Figure 6.37 the largest contribution to the error between the two methods is in the direct forward. In all cases the raw error quickly drops off to very small values. This error in the forward direction suggests that either (a) forward diffraction is too strong, potentially caused by the approximation of treating diffraction by the crystal as diffraction by apertures and so ignoring its three-dimensional nature. Given that instruments scarcely measure in the direct forward due to saturation of the imaging system, errors in this region are not of great concern if the Beam Tracer is to be used for analysis of SID data (which is in the range $\theta \in [6°, 25°]$). Furthermore, we note that the structure of the forward scattering lobe predicted by the Beam Tracer is very good when compared to ADDA. In Lidar multiple scattering investigations this is an important quantity to measure, indicating a potential application of the model.

Percentage differences can be a more useful way to compare methods. We define the percentage difference to be:

$$\Delta^{\%}(\theta) = \frac{P_{11}^{\mathrm{BT}}(\theta) - P_{11}^{\mathrm{DDA}}(\theta)}{P_{11}^{\mathrm{DDA}}(\theta)} \times 100. \tag{6.7}$$

Positive percentage differences will denote scattering angles where the Beam Tracer gives higher values than ADDA. The highest difference between the two methods occurs at the smallest size parameter due to the breakdown of the geometric optics approximation. Similar values for percentage differences comparing the Physical-Geometric Optics Hybrid (PGOH) method of Bi et al. and ADDA have been reported [55].

Phase variations across a beam cross section, discussed in Section 4.6.3, could cause differences between the methods. For large beam cross sections incident at oblique angles there would be significant phase variations over the cross section. The Beam Tracing model assumes that the phase across the beam cross section is constant and is equal to the phase at the centre on the facet. A consequence of this can be seen in the contribution of beams 11 and 12 (in Figure 6.21) to the overall scattering pattern shown in Figure 6.6 where the diffraction arcs extend to larger scattering angles than is seen in the corresponding ADDA results. Division of this beam into sub-beams of quasi constant phase may reduce this effect and it is encouraged to investigate this.

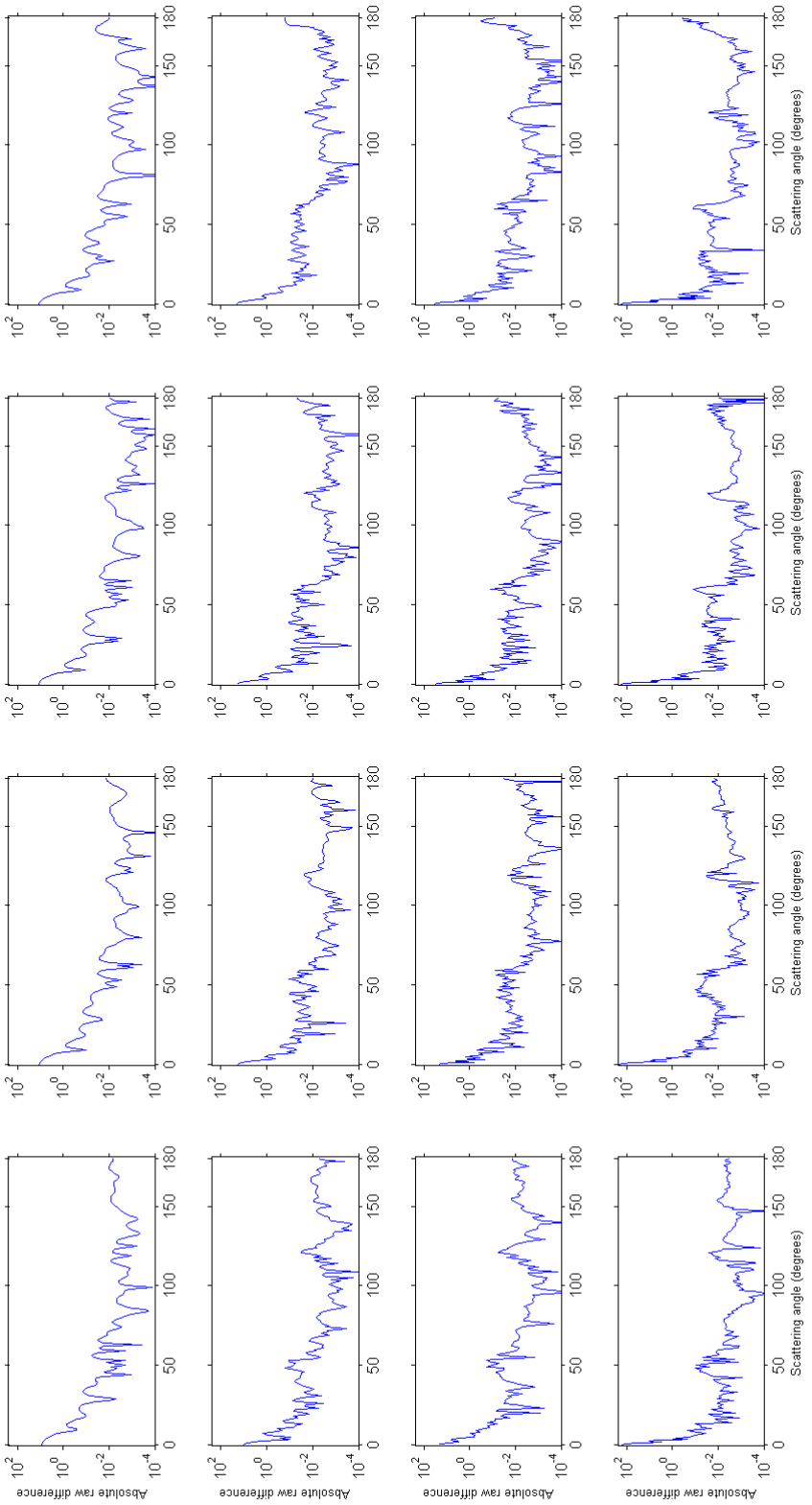

Figure 6.37: Absolute values of the differences between normalised P_{11} elements from the Beam Tracer and ADDA for transparent, pristine hexagonal columns. From top to bottow rows correspond to the four size parameters $x = 20, 40, 60$ and 100. The columns, from left to right, correspond to the orientations (a)-(d) given in Figure 6.4).

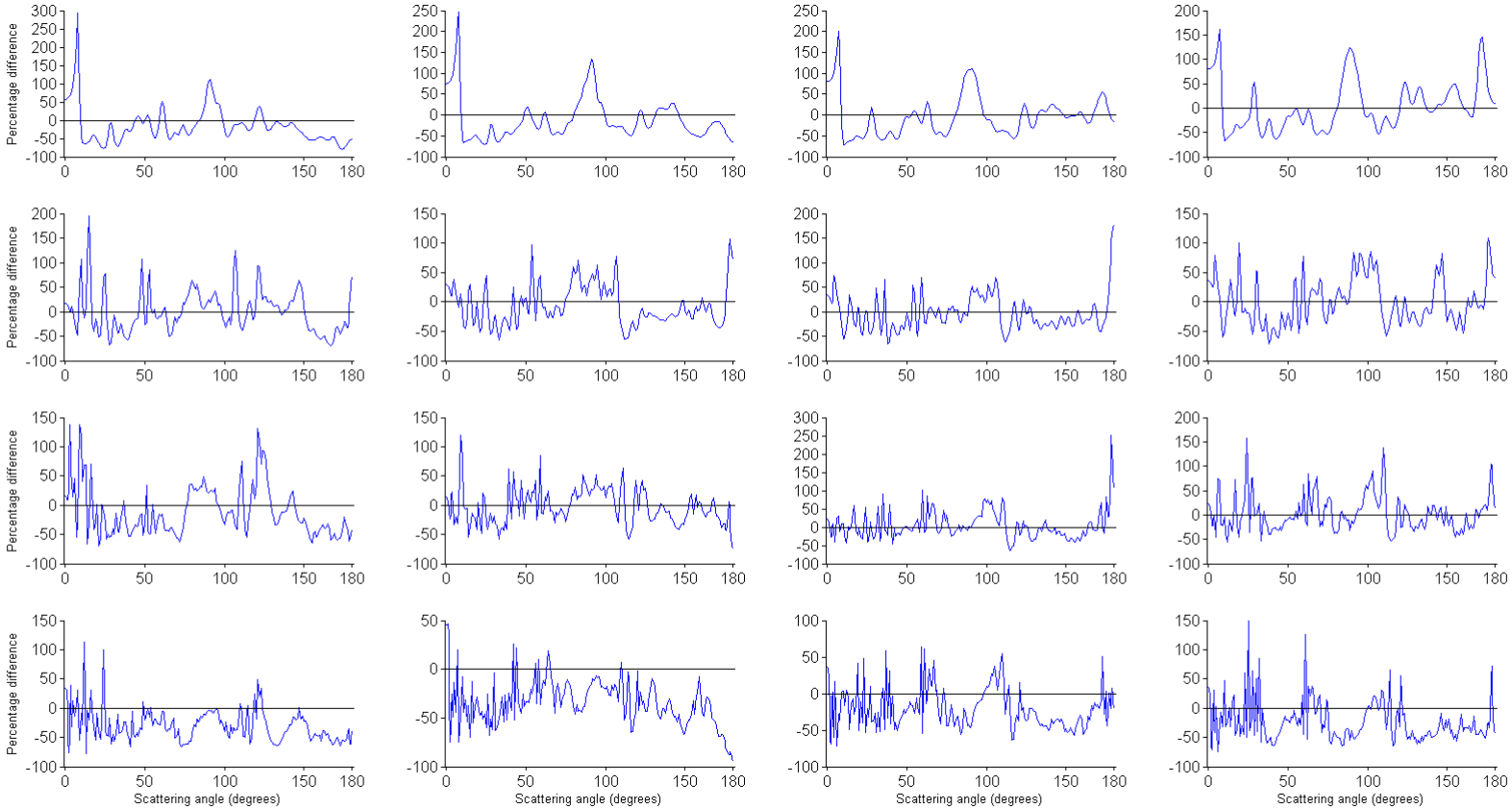

Figure 6.38: Percentage difference in P_{11} values from the Beam Tracer and ADDA for transparent, pristine hexagonal columns. From top to bottow rows correspond to the four size parameters $x = 20, 40, 60$ and 100. The columns, from left to right, correspond to the orientations (a)-(d) given in Figure 6.4).

6.4 Results for an Absorbing, Smooth, Pristine Hexagonal Column

The absorbing hexagonal column has a size parameter of 20π and is illuminated by incident light of wavelength 500nm in orientation (a) of Figure 6.4. It is set to be highly absorbing, with a refractive of $m = 1.31 + \mathrm{i}0.1$ which means that the scattering pattern is dominated by external diffraction and reflection. Figure 6.39 gives the two-dimensional P_{11} from the Beam Tracer and ADDA methods. The central bright peak in the forward scattering is due to external diffraction, the other three peaks being due to reflection off the two prism facets and the basal facet. There is also noticeable absence of the transmission peaks due to absorption. Due to the lack of transmitted beams there is less interference. The effect this has on the scattering pattern is that there is noticeably more dark patches, associated with low light intensity in these scattering directions.

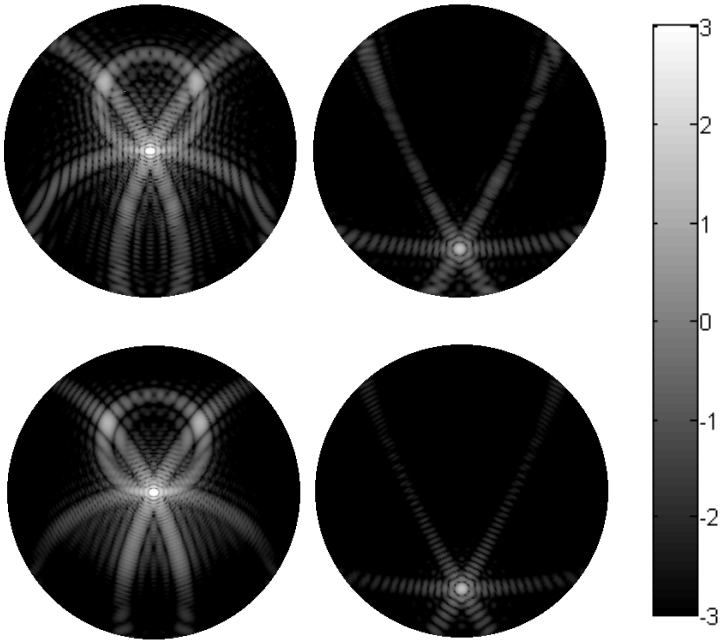

Figure 6.39: Two-dimensional P_{11} for the highly absorbing hexagonal column of size parameter100 in orientation (a); Beam Tracing (top row) and ADDA (bottom row).

In the forward scattering hemisphere there are two fuzzy patches in the diffraction arcs either size of $\phi = 270$, these can be associated with transmission through the upper prism facets (earlier, these were called beams 5 and 6). Whereas in the transparent case, this led to spatially extended beams exiting the basal facet, absorption attenuates this beam leading to its sub-division (see Section 4.7). Only a small proportion of the incident beam is able to propagate out, hence the absence of a bright transmission peak.

Two dimensional dlp patterns are given in Figure 6.40. In the forward scattering hemisphere regions of strong positive polarisation associated with external reflection can be seen around $(51°, 56°)$ and $(51°, 124°)$ corresponding to external reflection off

the two prism facets. The strong negative polarisation seen in the lower half of the ADDA image is not so prominent in the results from the Beam Tracer, which predicts close to zero polarisation. The side scattering region is positively polarised due to reflection from the basal facet, with polarisation decreasing towards direct backscattering. This is seen in both sets of results, although more prominently in the ADDA case, in the Beam Tracing case the negatively polarised ripples are more apparent. A left/right asymmetry can be seen in the backscattering hemisphere (compare for example, the regions either side of the plane $\phi = 90°$ at $\theta \approx 150°$) for the results from the Beam Tracer which is not seen in the ADDA results.

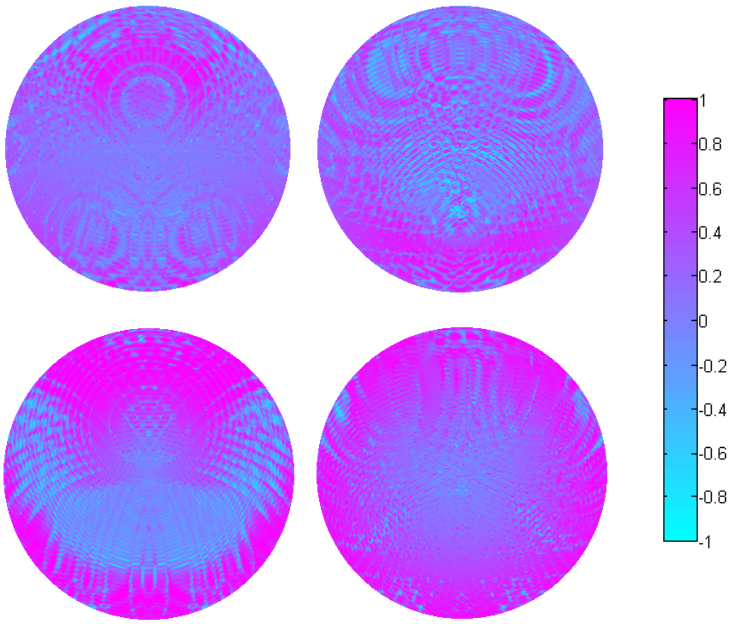

Figure 6.40: Two-dimensional dlp for the highly absorbing hexagonal column. Beam Tracing (top row) and ADDA (bottom row).

The azimuthally averaged P_{11} results in Figure 6.41 include the normalised contribution from external diffraction and diffraction of the reflected beam. We see that the addition of further beam interactions leads to a deviation in the backscattering which is not seen when considering just external diffraction and reflection. It must therefore be associated with transmission. A potential cause is the model's improper handling of wave inhomogeneity, leading to improper modelling of beam phase in absorbing crystals. This could lead to artificial constructive interference, thus giving rise to the peak at 143° (this is likely related to the asymmetry in the two-dimensonal dlp pattern given in Figure 6.40). The strong decline in the backscattering is due to the absorption removing internally reflected beams. The side scattering region displays the largest departure between the two models, with the Beam Tracer being too large here. The central diffraction arc in Figure 6.39 is much stronger in the Beam Tracing model, extending to larger scattering angles that the ADDA results predict. This arc is associated with external diffraction, suggesting that it is too strong.

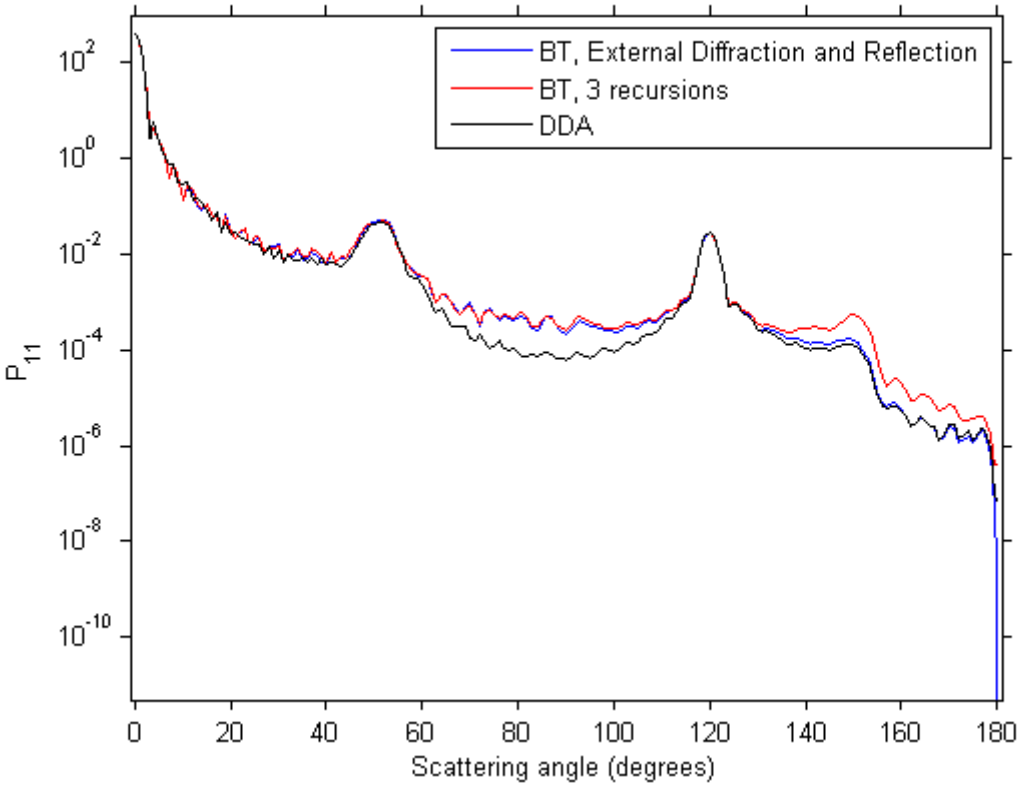

Figure 6.41: Azimuthally averaged P_{11} for the absorbing hexagonal column. ADDA results are given in black and two Beam Tracing results corresponding to external diffraction and reflection only (shown in blue) and including a single transmission through the crystal (shown in red) are given as comparison.

6.5 Results for an Absorbing, Smooth, Indented Hexagonal Column

The absorbing indented column, shown in Figure 6.42 has a size parameter of 60, it is in orientation (a). The indent is 30% of the total length and is present in one basal facet only, the other being unaffected. The incident light again has a wavelength of 500nm and the refractive index is $m = 1.31 + \mathrm{i}0.2$.

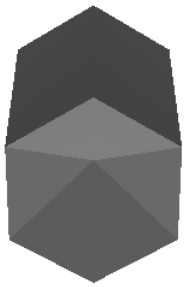

Figure 6.42: The absorbing, smooth, hexagonal column with one indented facet, as used in the model, incident light propagates into the page.

Two-dimensional P_{11} patterns are given in Figure 6.43. As with the pristine column, forward scattering is dominated by external diffraction and reflection off the prism facets. As with the transparent and absorbing cases there are two bright peaks at $(51°, 56°)$ and $(51°, 51°)$ corresponding to external reflection off two prism facets. Whereas before there was reflection off a basal facet in the direction $(120°, 270°)$, there is now reflection off six triangular facets. These six facets are best discussed in three pairs, corresponding to the rows in Figure 6.44. For the pair in the top row the entire beam (shown in green) re-intersects the crystal illuminating regions spread over two facets (shown in blue and pink). The two pink beams then undergo reflection again, scattering in the directions $(111°, 305°)$ and $(111°, 235°)$ respectively. Likewise for the two blue beams, which go in the directions $(130°, 263°)$ and $(130°, 277°)$. The beams shown in the middle row of Figure 6.44 both scatter upon reflection (with no portion re-intersecting the crystal), propagating in the directions $(147°, 3°)$ and $(147°, 177°)$. On the two-dimensional scattering pattern, Figure 6.43 these two points are recognisable by their pristine, i.e. not smeared, appearance. Those beams shown in the third row of Figure 6.44 do partially intersect the crystal, leaving a portion to propagate away. The division of the beam into parts which do, and do not, intersect is represented by the green and red regions on the triangular facet. The parts which are scattered go in the directions $(91°, 324°)$ and $(91, 216°)$. The intersected beams, shown in blue, undergo external reflection again and then propagate away from the crystal in the directions $(117°, 320°)$ and $(117°, 220°)$.The presence of four beams in the vicinity of around $(115°, 270°)$ leads to widespread interference, which can be seen by the haziness in the backward hemisphere of Figure 6.43.

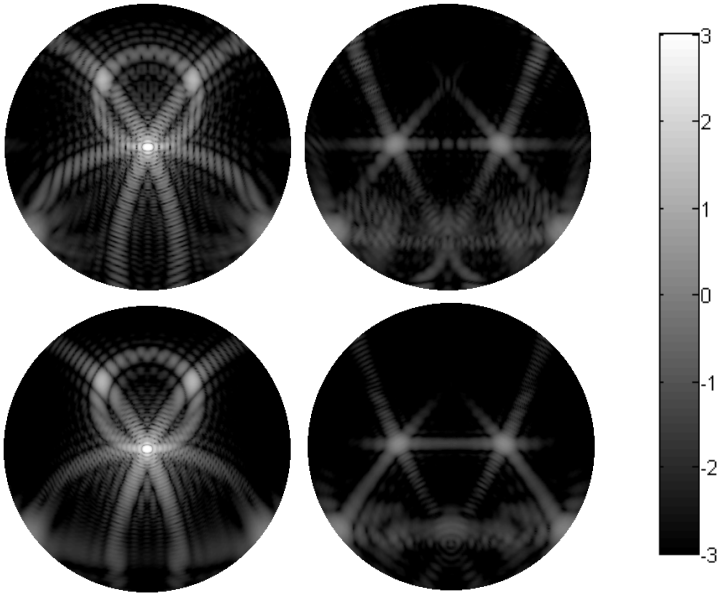

Figure 6.43: Two-dimensional P_{11} for the highly absorbing indented hexagonal column of size parameter100 in orientation (a); Beam Tracing (top row) and ADDA (bottom row).

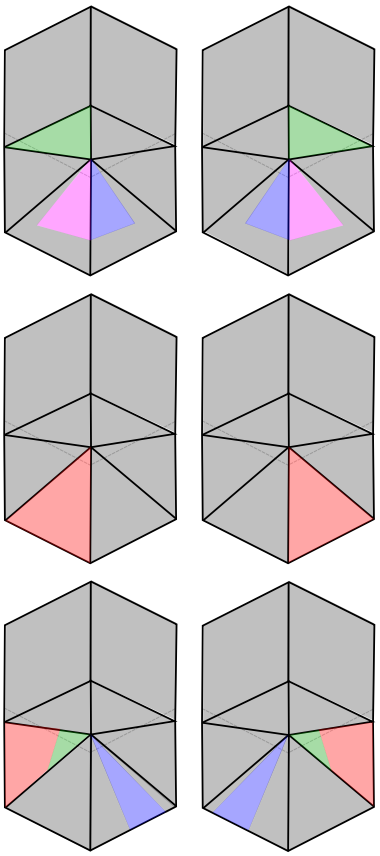

Figure 6.44: Reflection from inside the indent. The top row shows two reflected beams which are entirely intersected by the indent. The middle row shows two reflected beams which do not re-intersect. The bottom row shows two reflected beams which partially intersect other facets. The green portion of the facet corresponds to the portion of the beam that does re-intersect, the red indicating scattering away from the crystal.

Polarisation plots in Figure 6.45 suggest that the indent has little effect on the polarisation of light scattered into the forward hemisphere. However, there is now positive polarisation around $(91°, 324°)$ and $(91, 216°)$ due to the small beams which, after external reflection do not intersect the crystal (green beams in the bottom row of Figure 6.44. There is a noticeable absence of positive polarisation around $(85°, 270°)$ in the Beam Tracing results, but not in the ADDA results. Regions of positive polarisation are also present in the backscattering, again due to external reflection. Interference between scattered beams can be seen in the region around $(115°, 270°)$, as was the case for intensity.

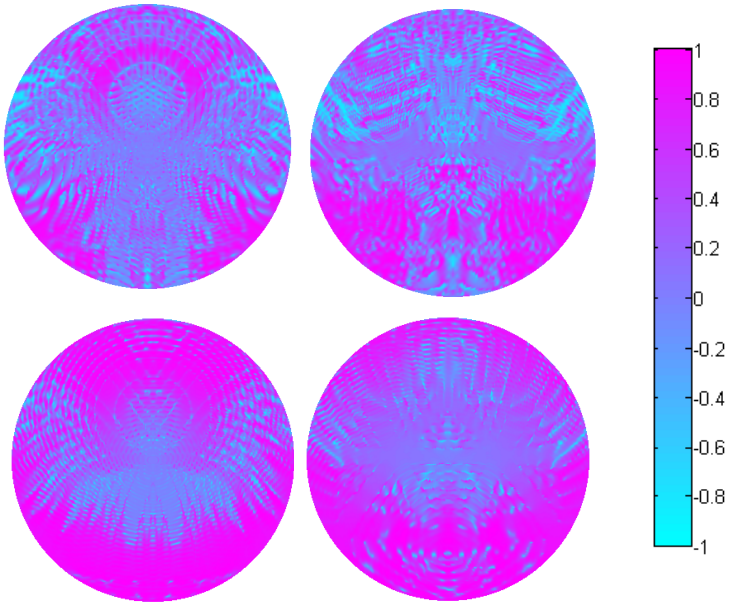

Figure 6.45: Two-dimensional dlp for the highly absorbing indented hexagonal column of size parameter100 in orientation (a) Beam Tracing (top row) and ADDA (bottom row).

The azimuthally averaged P_{11}, given in Figure 6.46 shows very good agreement at all scattering angles except near to direct backscattering, where oscillations appear. These can also be seen in the two-dimensional pattern in the upper right panel of Figure 6.43; where diffraction minima can be seen in the arc joining the two bright reflection peaks. Similar minima are not observed in the corresponding ADDA case.

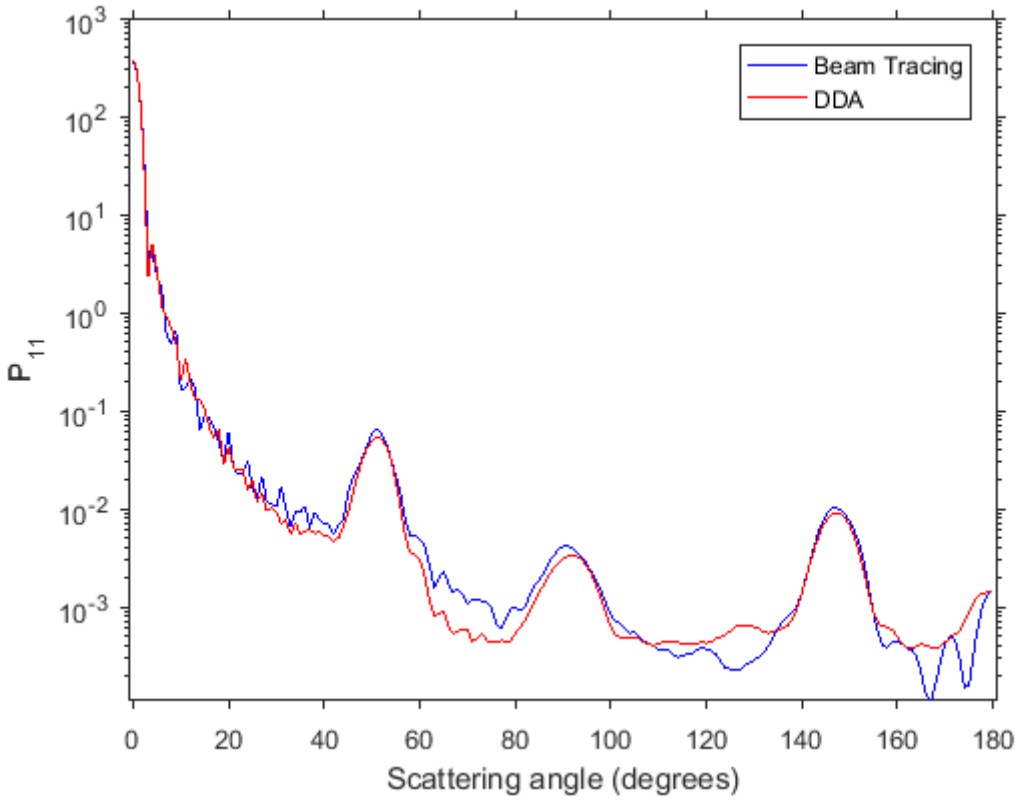

Figure 6.46: Azimuthally averaged P_{11} for the highly absorbing, smooth, indented hexagonal column.

Chapter 7

Discussion and Future Outlook

> "Ah," said the jailer, "do not always brood over what is impossible, or you will be mad in a fortnight".
>
> Alexandre Dumas,
> in The Count of Monte Cristo

The project sought to address the need for a computationally cheap, accurate and versatile Beam Tracing model for electromagnetic scattering by atmospheric ice. This report has detailed the development of the Beam Tracer. Demonstrations of the model were performed on a range of hexagonal columns of different sizes, orientations and refractive indexes; with results compared to ADDA. While this report focussed on its application to smooth hexagonal columns (transparent pristine, absorbing pristine and absorbing with an indented basal facet) the model is able to handle facetted approximations to shapes like spheroids and cylinders, as well as more complicated shapes like rosettes. Existing Beam Tracing methods have been developed for transparent, smooth, pristine hexagonal columns, e.g. [53, 56], and other models, e.g. [54, 55], have included absorption as well as extending the model to handle smooth, pristine polyhedra. However, in these models, the sub-division of beams does not take place, i.e. it is assumed that the intensity over the cross section of an attenuated beam is constant. As such, to the author's best knowledge, no other Beam Tracing code in the literature has demonstrated the same versatility as the one developed here.

The Beam Tracer is computationally cheap, usually taking around one minute for a typical particle such as a transparent hexagonal prism. In terms of computational time, the model is independent of size parameter (so long as the particle is scaled equally) meaning there is, in principal, no upper size limit. The smallest size parameter used in comparison studies was 20, where differences in P_{11} and dlp between the Beam Tracer and ADDA were apparent. Where differences between the models were observed, it was found that limited orientation averaging reduced the errors quite significantly. This suggests that the Beam Tracer could be a useful tool in modelling light scattering by randomly oriented crystals.

The key feature of the model, the beam splitting process, was discussed in detail,

including how it can be viewed as an extension of ray tracing. For validation of the geometric optics component of the Beam Tracer a comparison to a modified Ray Tracer [50] was carried out. The phase function, averaged over 1000 orientations, for a hexagonal column was compared with identical agreement seen. The necessity of phase tracing to allow for interference effects to be seen in two-dimensional scattering patterns was outlined. Finally, the incorporation of a surface integral formulation of a vector Kirchhoff approximation for modelling diffraction enabled the model to leave the confines of geometric optics, resulting in beams spreading out as they propagate away from the crystal. Included in the diffraction implementation was the use of a diffraction amplitude matrix, which enabled the polarisation of the diffracted wave to be modelled. The combination of all these resulted in good agreement between ADDA and the Beam Tracer.

While the beam splitting process makes use of similar techniques found in ray tracing models it is important to emphasise some of the differences between them. Ray tracing requires that the scattering particle be much larger than the wavelength of the incident light in order for the wave effects to be ignored, which simplifies the problem significantly but does so at a cost to the overall accuracy. Beam Tracing is built on wave optics, taking into account phase, interference and diffraction of plane parallel beams meaning its basis is more physical than geometric optics. Because wave effects are inherent to the model, there is in principle no lower size limit, which in addition to there being no upper size limit means that Beam Tracing is potentially a very powerful technique, applicable over all particle size parameters. When complex particles are considered ray tracing requires that the number of incident rays increases as particle complexity increases to ensure that all ray paths are traced and that enough rays traverse them to realistically probe the illuminated regions. If not enough rays are used then intensity peaks in the resulting intensity patterns may be missed. Beam Tracing does not suffer this issue since contained within a beam cross section are all the possible ray paths that would lead to the illuminated region.

Using the Beam Tracer to create scattering databases has been achieved through utilising cluster computing. An example script to generate a database of scattering properties of hexagonal columns of varying size parameter is given in Appendix F. A lower size parameter is decided by the user and the upper size parameter is determined by the number of nodes used in the execution. The code creates a hexagonal column for the given size parameter and passes this to the Beam Tracer. The results are stored in individual directories, the names of which are the size parameter of the crystal file. Once a database has been created, one can (in the case of comparison with SID images) compare the two-dimensional scattering patterns from the probe and the Beam Tracer. Performing this task manually would most likely not be fruitful, so an automated process is preferable, see [76]. The idea behind these algorithms is that intensity values from a recorded image are compared with those in the database. If a similar match can be found then the particle can be considered identified, within a confidence interval. Future developments in this area could include the use of neural networks, exploiting machine learning, to better perform analysis of measured scattering patterns in conjunction with scattering databases. Improved habit retrieval algorithms will in turn lead to more informed choices for ice crystal geometries used to derive parameters for climate models.

The model should provide a means to create an updated scattering database of two-dimensional patterns that can be used to aid in the retrieval of particle size, habit and orientation from *in-situ* probes such as SID-3, or the recently developed Aerosol Ice Interface Transition Spectrometer (AIITS) *in-situ* probe. This probe was attached to a NASA Global Hawk [1] and took part in the Coordinated Airborne Studies in the Tropics (CAST) campaign. Like the SID probes it captures two-dimensional forward scattering patterns, but also measures polarisation. This additional aspect makes AIITS useful in determining whether the particle is a droplet or not, as droplets do not depolarise.

It was seen that the approximation of equal phase over a beam cross section results in the transmitted beams' diffraction patterns contributing too strongly in their localised region to the overall scattering pattern. This could potentially be mitigated through further division of beams, dividing them into regions of quasi-constant phase in a similar way as was done for absorption. This would hopefully improve the agreement between Beam Tracing and exact methods. It was seen that the model showed better agreement when there was an increase in the number of geometric optics scattering directions. This is likely for the same reason, with diffraction effects being too tightly confined around the scattering direction of the beam.

Near to far-field mapping was achieved through the use of a surface integral. The Vector Kirchhoff approximation used is derived by starting with Green's Theorem, from which one can derive an alternative, volume integral diffraction formalism. It has been shown in the literature [55] that the volume integral method leads to better agreement in the side scattering region for the P_{11} element. However, it is more computationally expensive. An interesting future avenue of research would be investigating what effect incorporating a volume integral form of diffraction would have on the beam tracing model.

Increasingly the atmospheric community is exploring the effects of surface roughness on light scattering. The Beam Tracing model has not been tested on particles with surface roughness, this is an area for further investigation. The large number of small facets would likely lead to substantial computational demand arising from the increased number of plane projections and line intersections. The beam tracing model, in its current form, would likely not be applicable to particles displaying significant roughness. That said, it is conceivable that a variation of the Beam Tracing model could be devised in the future to be used on rough particles. While the computational demands would be greater than for smooth cases, it is likely that the demands would still be less than more exact methods. A possible technique that could be used to reduce the computational burden would be to use bounding boxes, as was done by McCall [114] for the RTDF model.

On a more philosophical note, the Paris summit of December 2015 hopefully saw the commencement of a global initiative towards tackling climate change. The work of

[1] http://www.herts.ac.uk/research/centres-and-groups/cair/particle-instruments-and-diagnostics/aiits

the atmospheric research community cannot be understated in making this happen and their role has likely never been as important as it is now. The onus lays with scientists, of multiple disciplines, to come together and collaborate to help and avoid what would be, no-doubt, a disaster for mankind if climate change went unchecked. The study of atmospheric ice, the development of accurate probes, the creation of computer models and so forth all have a role to play in this. For, while the knowledge bank is forever growing, there is still much to be learned.

Chapter 8

Bibliography

[1] C. Stubenrauch, A. Chédin, G. Rädel, N. Scott, and S. Serrar, "Cloud properties and their seasonal and diurnal variability from tovs path-b," *Journal of climate*, vol. 19, no. 21, pp. 5531–5553, 2006.

[2] H. Nazaryan, M. P. McCormick, and W. P. Menzel, "Global characterization of cirrus clouds using calipso data," *Journal of Geophysical Research: Atmospheres*, vol. 113, no. D16, 2008.

[3] Intergovernmental Panel On Climate Change, *The Physical Science Basis: Working Group I Contribution to the Fifth Assessment Report of the Intergovernmental Panel on Climate Change*. Cambridge University Press, 2013.

[4] R. J. Hogan, A. J. Illingworth, and H. Sauvageot, "Measuring crystal size in cirrus using 35-and 94-GHz radars," *Journal of Atmospheric and Oceanic Technology*, vol. 17, no. 1, pp. 27–37, 2000.

[5] B. H. Cole, P. Yang, B. A. Baum, J. Riedi, and L. C. Labonnote, "Ice particle habit and surface roughness derived from PARASOL polarization measurements," *Atmospheric Chemisty and Physics*, vol. 14, pp. 3739–3750, 2014.

[6] W. Pfalzgraff, R. Hulscher, and S. Neshyba, "Scanning electron microscopy and molecular dynamics of surfaces of growing and ablating hexagonal ice crystals," *Atmospheric Chemistry and Physics*, vol. 10, no. 6, pp. 2927–2935, 2010.

[7] G. Ritter, *The growth and morphology of small ice crystals in a diffusion chamber*. PhD thesis, University of Hertfordshire, Hatfield, UK, 2015.

[8] Z. Ulanowski, E. Hesse, P. H. Kaye, A. J. Baran, and R. Chandrasekhar, "Scattering of light from atmospheric ice analogues," *Journal of Quantitative Spectroscopy and Radiative Transfer*, vol. 79, pp. 1091–1102, 2003.

[9] Z. Ulanowski, E. Hesse, P. H. Kaye, and A. J. Baran, "Light scattering by complex ice-analogue crystals," *Journal of Quantitative Spectroscopy and Radiative Transfer*, vol. 100, no. 1, pp. 382–392, 2006.

[10] A. Korolev and G. Isaac, "Roundness and aspect ratio of particles in ice clouds," *Journal of the atmospheric sciences*, vol. 60, no. 15, pp. 1795–1808, 2003.

[11] Z. Ulanowski, P. H. Kaye, E. Hirst, R. Greenaway, R. J. Cotton, E. Hesse, and C. T. Collier, "Incidence of rough and irregular atmospheric ice particles from small ice detector 3 measurements," *Atmospheric Chemistry and Physics*, vol. 14, no. 3, pp. 1649–1662, 2014.

[12] E. Hesse and Z. Ulanowski, "Scattering from long prisms computed using ray tracing combined with diffraction on facets," *Journal of Quantitative Spectroscopy and Radiative Transfer*, vol. 79, pp. 721–732, 2003.

[13] K. Sassen, "The polarization lidar technique for cloud research: A review and current assessment," *Bulletin of the American Meteorological Society*, vol. 72, no. 12, pp. 1848–1866, 1991.

[14] E. Hecht, *Optics*. Addison Wesley, 1998.

[15] M. Born and E. Wolf, *Principles of optics: electromagnetic theory of propagation, interference and diffraction of light*. Cambridge University Press Archive, 2000.

[16] M. I. Mishchenko, "Gustav mie and the fundamental concept of electromagnetic scattering by particles: a perspective," *Journal of Quantitative Spectroscopy and Radiative Transfer*, vol. 110, no. 14, pp. 1210–1222, 2009.

[17] R. C. Jones, "A new calculus for the treatment of optical systems," *J. Opt. Soc. Am.*, vol. 31, pp. 488–493, Jul 1941.

[18] D. Clarke and Grainger, *Polarized Light and Optical Measurement: International Series of Monographs in Natural Philosophy*, vol. 35. Pergamon Press, 1971.

[19] C. F. Bohren and D. R. Huffman, *Absorption and scattering of light by small particles*. John Wiley & Sons, 2008.

[20] H. Van De Hulst, "On the attenuation of plane waves by obstacles of arbitrary size and form," *Physica*, vol. 15, no. 8, pp. 740–746, 1949.

[21] J. D. Jackson, *Classical electrodynamics*. Wiley, 1999.

[22] S. Groth, A. Baran, T. Betcke, S. Havemann, and W. Śmigaj, "The boundary element method for light scattering by ice crystals and its implementation in bem++," *Journal of Quantitative Spectroscopy and Radiative Transfer*, vol. 167, pp. 40–52, 2015.

[23] O. B. Toon, E. Browell, S. Kinne, and J. Jordan, "An analysis of lidar observations of polar stratospheric clouds," *Geophysical Research Letters*, vol. 17, no. 4, pp. 393–396, 1990.

[24] A. Macke and M. I. Mishchenko, "Applicability of regular particle shapes in light scattering calculations for atmospheric ice particles," *Applied Optics*, vol. 35, no. 21, pp. 4291–4296, 1996.

[25] K. Liou and Y. Takano, "Light scattering by nonspherical particles: Remote sensing and climatic implications," *Atmospheric Research*, vol. 31, no. 4, pp. 271–298, 1994.

[26] T. Rother, K. Schmidt, and S. Havemann, "Light scattering on hexagonal ice columns," *JOSA A*, vol. 18, no. 10, pp. 2512–2517, 2001.

[27] G. Mie, "Beiträge zur Optik trüber Medien, speziell kolloidaler Metallösungen," *Annalen der physik*, vol. 330, no. 3, pp. 377–445, 1908.

[28] J. D. Keener, K. J. Chalut, J. W. Pyhtila, and A. Wax, "Application of Mie theory to determine the structure of spheroidal scatterers in biological materials," *Optics letters*, vol. 32, no. 10, pp. 1326–1328, 2007.

[29] S. Röser and H. Staude, "The zodiacal light from 1500 a to 60 micron-Mie scattering and thermal emission," *Astronomy and Astrophysics*, vol. 67, pp. 381–394, 1978.

[30] P. Waterman, "Matrix formulation of electromagnetic scattering," *Proceedings of the IEEE*, vol. 53, no. 8, pp. 805–812, 1965.

[31] M. I. Mishchenko, G. Videen, V. A. Babenko, N. G. Khlebtsov, and T. Wriedt, "T-matrix theory of electromagnetic scattering by particles and its applications: a comprehensive reference database," *J. Quant. Spectrosc. Radiat. Transfer*, vol. 88, no. 1-3, pp. 357–406, 2004.

[32] M. I. Mishchenko, N. T. Zakharova, N. G. Khlebtsov, G. Videen, and T. Wriedt, "Comprehensive thematic T-matrix reference database: A 2014–2015 update," *Journal of Quantitative Spectroscopy and Radiative Transfer*, 2015.

[33] B. R. Johnson, "Invariant imbedding T-matrix approach to electromagnetic scattering," *Applied Optics*, vol. 27, no. 23, pp. 4861–4873, 1988.

[34] L. Bi, P. Yang, G. W. Kattawar, and M. I. Mishchenko, "Efficient implementation of the invariant imbedding T-matrix method and the separation of variables method applied to large nonspherical inhomogeneous particles," *Journal of Quantitative Spectroscopy and Radiative Transfer*, vol. 116, pp. 169–183, 2013.

[35] L. Bi and P. Yang, "Accurate simulation of the optical properties of atmospheric ice crystals with the invariant imbedding t-matrix method," *Journal of Quantitative Spectroscopy and Radiative Transfer*, vol. 138, pp. 17–35, 2014.

[36] E. M. Purcell and C. R. Pennypacker, "Scattering and absorption of light by nonspherical dielectric grains," *The Astrophysical Journal*, vol. 186, pp. 705–714, 1973.

[37] B. T. Draine, "The discrete-dipole approximation and its application to interstellar graphite grains," *The Astrophysical Journal*, vol. 333, pp. 848–872, 1988.

[38] M. A. Yurkin and A. G. Hoekstra, "The discrete-dipole-approximation code adda: capabilities and known limitations," *Journal of Quantitative Spectroscopy and Radiative Transfer*, vol. 112, no. 13, pp. 2234–2247, 2011.

[39] A. G. Hoekstra and P. Sloot, "New computational techniques to simulate light scattering from arbitrary particles," *Particle & particle systems characterization*, vol. 11, no. 3, pp. 189–193, 1994.

[40] M. A. Yurkin and A. G. Hoekstra, "The discrete dipole approximation: an overview and recent developments," *Journal of Quantitative Spectroscopy and Radiative Transfer*, vol. 106, no. 1, pp. 558–589, 2007.

[41] P. Yang, L. Bi, B. A. Baum, K.-N. Liou, G. W. Kattawar, M. I. Mishchenko, and B. Cole, "Spectrally consistent scattering, absorption, and polarization properties of atmospheric ice crystals at wavelengths from 0.2 to 100 μ m," *Journal of the Atmospheric Sciences*, vol. 70, no. 1, pp. 330–347, 2013.

[42] J. Um and G. M. McFarquhar, "Formation of atmospheric halos and applicability of geometric optics for calculating single-scattering properties of hexagonal ice crystals: Impacts of aspect ratio and ice crystal size," *Journal of Quantitative Spectroscopy and Radiative Transfer*, vol. 165, pp. 134–152, 2015.

[43] A. Penttilä, E. Zubko, K. Lumme, K. Muinonen, M. A. Yurkin, B. Draine, J. Rahola, A. G. Hoekstra, and Y. Shkuratov, "Comparison between discrete dipole implementations and exact techniques," *Journal of Quantitative Spectroscopy and Radiative Transfer*, vol. 106, no. 1, pp. 417–436, 2007.

[44] K. Yee, "Numerical solution of initial boundary value problems involving Maxwell's equations in isotropic media," *IEEE Transactions on Antennas and Propagation*, vol. 14, no. 3, pp. 302–307, 1966.

[45] P. Yang and K. Liou, "Light scattering by hexagonal ice crystals: comparison of finite-difference time domain and geometric optics models," *JOSA A*, vol. 12, no. 1, pp. 162–176, 1995.

[46] P. Yang and K. Liou, "Geometric-optics–integral-equation method for light scattering by nonspherical ice crystals," *Applied Optics*, vol. 35, no. 33, pp. 6568–6584, 1996.

[47] S. N. Chandler-Wilde, I. G. Graham, S. Langdon, and E. A. Spence, "Numerical-asymptotic boundary integral methods in high-frequency acoustic scattering," *Acta numerica*, vol. 21, pp. 89–305, 2012.

[48] A. Buffa and R. Hiptmair, "Galerkin boundary element methods for electromagnetic scattering," in *Topics in computational wave propagation*, pp. 83–124, Springer, 2003.

[49] S. Groth, *Numerical and asymptotic methods for scattering by penetrable obstacles*. PhD thesis, University of Reading, Reading, UK, 2016.

[50] A. Macke, J. Mueller, and E. Raschke, "Single scattering properties of atmospheric ice crystals," *Journal of the Atmospheric Sciences*, vol. 53, no. 19, pp. 2813–2825, 1996.

[51] H. C. Hulst and H. Van De Hulst, *Light scattering by small particles*. Courier Corporation, 1957.

[52] B. De Greve, "Reflections and refractions in ray tracing," 2004.

[53] A. G. Borovoi and I. A. Grishin, "Scattering matrices for large ice crystal particles," *JOSA A*, vol. 20, no. 11, pp. 2071–2080, 2003.

[54] L. Bi, P. Yang, G. W. Kattawar, Y. Hu, and B. A. Baum, "Scattering and absorption of light by ice particles: solution by a new physical-geometric optics hybrid method," *Journal of Quantitative Spectroscopy and Radiative Transfer*, vol. 112, no. 9, pp. 1492–1508, 2011.

[55] L. Bi, P. Yang, G. W. Kattawar, Y. Hu, and B. A. Baum, "Diffraction and external reflection by dielectric faceted particles," *Journal of Quantitative Spectroscopy and Radiative Transfer*, vol. 112, no. 2, pp. 163–173, 2011.

[56] A. V. Konoshonkin, N. V. Kustova, and A. G. Borovoi, "Beam-splitting code for light scattering by ice crystal particles within geometric-optics approximation," *Journal of Quantitative Spectroscopy and Radiative Transfer*, vol. 164, pp. 175–183, 2015.

[57] A. Guignard, C. Stubenrauch, A. Baran, and R. Armante, "Bulk microphysical properties of semi-transparent cirrus from airs: a six year global climatology and statistical analysis in synergy with geometrical profiling data from cloudsat-calipso," *Atmospheric Chemistry and Physics*, vol. 12, no. 1, pp. 503–525, 2012.

[58] A. Vogelmann and T. Ackerman, "Relating cirrus cloud properties to observed fluxes: A critical assessment," *Journal of the atmospheric sciences*, vol. 52, no. 23, pp. 4285–4301, 1995.

[59] A. J. Heymsfield and L. M. Miloshevich, "Parameterizations for the cross-sectional area and extinction of cirrus and stratiform ice cloud particles," *Journal of the atmospheric sciences*, vol. 60, no. 7, pp. 936–956, 2003.

[60] C. Magono, W. Chung, *et al.*, "Meteorological classification of natural snow crystals," *Journal of the Faculty of Science, Hokkaido University. Series 7, Geophysics*, vol. 2, no. 4, pp. 321–335, 1966.

[61] M. P. Bailey and J. Hallett, "A comprehensive habit diagram for atmospheric ice crystals: Confirmation from the laboratory, airs ii, and other field studies," *Journal of the Atmospheric Sciences*, vol. 66, no. 9, pp. 2888–2899, 2009.

[62] A. J. Baran, "A review of the light scattering properties of cirrus," *Journal of Quantitative Spectroscopy and Radiative Transfer*, vol. 110, no. 14, pp. 1239–1260, 2009.

[63] A. J. Baran, "From the single-scattering properties of ice crystals to climate prediction: A way forward," *Atmospheric Research*, vol. 112, pp. 45–69, 2012.

[64] Y. Takano and K.-N. Liou, "Solar radiative transfer in cirrus clouds. part i: Single-scattering and optical properties of hexagonal ice crystals," *Journal of the Atmospheric Sciences*, vol. 46, no. 1, pp. 3–19, 1989.

[65] P. Chỳlek and G. Videen, "Longwave radiative properties of polydispersed hexagonal ice crystals," *Journal of the atmospheric sciences*, vol. 51, no. 2, pp. 175–190, 1994.

[66] T. C. Grenfell and S. G. Warren, "Representation of a nonspherical ice particle by a collection of independent spheres for scattering and absorption of radiation," *Journal of Geophysical Research: Atmospheres*, vol. 104, no. D24, pp. 31697–31709, 1999.

[67] A. Mugnai and W. J. Wiscombe, "Scattering from nonspherical Chebyshev particles. i: cross sections, single-scattering albedo, asymmetry factor, and backscattered fraction," *Applied Optics*, vol. 25, no. 7, pp. 1235–1244, 1986.

[68] K. Muinonen, E. Zubko, J. Tyynelä, Y. G. Shkuratov, and G. Videen, "Light scattering by gaussian random particles with discrete-dipole approximation," *Journal of Quantitative Spectroscopy and Radiative Transfer*, vol. 106, no. 1, pp. 360–377, 2007.

[69] P. Yang, B. A. Baum, A. J. Heymsfield, Y. X. Hu, H.-L. Huang, S.-C. Tsay, and S. Ackerman, "Single-scattering properties of droxtals," *Journal of Quantitative Spectroscopy and Radiative Transfer*, vol. 79, pp. 1159–1169, 2003.

[70] R. M. Schotland, K. Sassen, and R. Stone, "Observations by lidar of linear depolarization ratios for hydrometeors," *Journal of Applied Meteorology*, vol. 10, no. 5, pp. 1011–1017, 1971.

[71] V. Noel, D. M. Winker, M. McGill, and P. Lawson, "Classification of particle shapes from lidar depolarization ratio in convective ice clouds compared to in situ observations during crystal-face," *Journal of Geophysical Research: Atmospheres*, vol. 109, no. D24, 2004.

[72] R. J. Hogan, M. E. Brooks, A. J. Illingworth, D. P. Donovan, C. Tinel, D. Bouniol, and J. P. V. P. Baptista, "Independent evaluation of the ability of spaceborne radar and lidar to retrieve the microphysical and radiative properties of ice clouds," *Journal of Atmospheric and Oceanic Technology*, vol. 23, no. 2, pp. 211–227, 2006.

[73] P. J. Connolly, M. J. Flynn, Z. Ulanowski, T. Choularton, M. Gallagher, and K. Bower, "Calibration of the cloud particle imager probes using calibration beads and ice crystal analogs: The depth of field," *Journal of Atmospheric and Oceanic Technology*, vol. 24, no. 11, pp. 1860–1879, 2007.

[74] A. Abdelmonem, M. Schnaiter, P. Amsler, E. Hesse, J. Meyer, and T. Leisner, "First correlated measurements of the shape and light scattering properties of cloud particles using the new particle habit imaging and polar scattering (PHIPS) probe," *Atmospheric Measurement Techniques*, vol. 4, no. 10, pp. 2125–2142, 2011.

[75] P. H. Kaye, E. Hirst, R. S. Greenaway, Z. Ulanowski, E. Hesse, P. J. DeMott, C. Saunders, and P. Connolly, "Classifying atmospheric ice crystals by spatial light scattering," *Optics letters*, vol. 33, no. 13, pp. 1545–1547, 2008.

[76] C. Stopford, *Ice crystal classification using two dimensional light scattering patterns*. PhD thesis, University of Hertfordshire, Hatfield, UK, 2010.

[77] Z. Ulanowski, E. Hirst, P. H. Kaye, and R. Greenaway, "Retrieving the size of particles with rough and complex surfaces from two-dimensional scattering patterns," *Journal of Quantitative Spectroscopy and Radiative Transfer*, vol. 113, no. 18, pp. 2457–2464, 2012.

[78] A. Korolev, E. Emery, J. Strapp, S. Cober, G. Isaac, M. Wasey, and D. Marcotte, "Small ice particles in tropospheric clouds: Fact or artifact? airborne icing instrumentation evaluation experiment," *Bulletin of the American Meteorological Society*, vol. 92, no. 8, pp. 967–973, 2011.

[79] P. Field, A. Heymsfield, and A. Bansemer, "Shattering and particle interarrival times measured by optical array probes in ice clouds," *Journal of Atmospheric and Oceanic Technology*, vol. 23, no. 10, pp. 1357–1371, 2006.

[80] C. Liu, R. L. Panetta, and P. Yang, "The effects of surface roughness on the scattering properties of hexagonal columns with sizes from the rayleigh to the geometric optics regimes," *Journal of Quantitative Spectroscopy and Radiative Transfer*, vol. 129, pp. 169–185, 2013.

[81] B. Cole, P. Yang, B. Baum, J. Riedi, and L. C-Labonnote, "Ice particle habit and surface roughness derived from parasol polarization measurements," *Atmospheric Chemistry and Physics*, vol. 14, no. 7, pp. 3739–3750, 2014.

[82] C. Collier, E. Hesse, L. Taylor, Z. Ulanowski, A. Penttilä, and T. Nousiainen, "Effects of surface roughness with two scales on light scattering by hexagonal ice crystals large compared to the wavelength: Dda results," *Journal of Quantitative Spectroscopy and Radiative Transfer*, 2016.

[83] P. Yang, Z. Zhang, G. W. Kattawar, S. G. Warren, B. A. Baum, H.-L. Huang, Y. X. Hu, D. Winker, and J. Iaquinta, "Effect of cavities on the optical properties of bullet rosettes: Implications for active and passive remote sensing of ice cloud properties," *Journal of Applied Meteorology and Climatology*, vol. 47, no. 9, pp. 2311–2330, 2008.

[84] H. R. Smith, P. J. Connolly, A. J. Baran, E. Hesse, A. R. Smedley, and A. R. Webb, "Cloud chamber laboratory investigations into scattering properties of hollow ice particles," *Journal of Quantitative Spectroscopy and Radiative Transfer*, vol. 157, pp. 106–118, 2015.

[85] A. Macke, M. I. Mishchenko, and B. Cairns, "The influence of inclusions on light scattering by large ice particles," *Journal of Geophysical Research: Atmospheres*, vol. 101, no. D18, pp. 23311–23316, 1996.

[86] W. F. Kuhs, C. Sippel, A. Falenty, and T. C. Hansen, "Extent and relevance of stacking disorder in ice ic," *Proceedings of the National Academy of Sciences*, vol. 109, no. 52, pp. 21259–21264, 2012.

[87] M. I. Mishchenko and A. Macke, "How big should hexagonal ice crystals be to produce halos?," *Applied Optics*, vol. 38, no. 9, pp. 1626–1629, 1999.

[88] P. Yang and K. Liou, "Single-scattering properties of complex ice crystals in terrestrial atmosphere," *Contributions to Atmospheric Physics*, vol. 71, no. 2, pp. 223–248, 1998.

[89] Z. Ulanowski, "Ice analog halos," *Applied Optics*, vol. 44, no. 27, pp. 5754–5758, 2005.

[90] G. B. Arfken, H. J. Weber, and F. E. Harris, *Mathematical methods for physicists: a comprehensive guide*. Academic press, 2011.

[91] J. Hovenier and C. Van der Mee, "Fundamental relationships relevant to the transfer of polarized light in a scattering atmosphere," *Astronomy and Astrophysics*, vol. 128, pp. 1–16, 1983.

[92] S. G. Warren and R. E. Brandt, "Optical constants of ice from the ultraviolet to the microwave: A revised compilation," *Journal of Geophysical Research: Atmospheres*, vol. 113, no. D14, 2008.

[93] P. Yang and K. Liou, "Effective refractive index for determining ray propagation in an absorbing dielectric particle," *Journal of Quantitative Spectroscopy and Radiative Transfer*, vol. 110, no. 4, pp. 300–306, 2009.

[94] L. Taylor, "Light scattering by particles relevant to atmospheric research," *Unpublished Manuscript*, 2012.

[95] O. Darrigol, *A history of optics from Greek antiquity to the nineteenth century*. Oxford University Press, 2012.

[96] F. Kottler, "Diffraction at a black screen, part I: Kirchhoff's theory," *Progress in Optics*, vol. 31, pp. 281–281, 1993.

[97] F. Kottler, "Diffraction at a black screen, part II: Electromagnetic theory," *Progress in Optics*, vol. 31, pp. 331–331, 1993.

[98] M. Nieto-Vesperinas, *Scattering and diffraction in physical optics*. Wiley New York, 1991.

[99] J. B. Keller, "Geometrical theory of diffraction," *JOSA*, vol. 52, no. 2, pp. 116–130, 1962.

[100] J. Achenbach, A. Gautesen, and H. McMaken, "Application of geometrical diffraction theory to scattering by cracks," 1978.

[101] D. Laurenson, S. McLaughlin, and A. Sheikh, "The application of ray tracing and the geometrical theory of diffraction to indoor channel modelling," in *Global Telecommunications Conference, 1993, including a Communications Theory Mini-Conference. Technical Program Conference Record, IEEE in Houston. GLOBECOM'93., IEEE*, pp. 1242–1246, IEEE, 1993.

[102] K. Muinonen, K. Lumme, J. Peltoniemi, and W. M. Irvine, "Light scattering by randomly oriented crystals," *Applied Optics*, vol. 28, no. 15, pp. 3051–3060, 1989.

[103] K. Muinonen, "Scattering of light by crystals: a modified Kirchhoff approximation," *Applied Optics*, vol. 28, no. 15, pp. 3044–3050, 1989.

[104] A. Macke, "Scattering of light by polyhedral ice crystals," *Applied Optics*, vol. 32, no. 15, pp. 2780–2788, 1993.

[105] A. J. Clarke, E. Hesse, Z. Ulanowski, and P. H. Kaye, "A 3D implementation of ray tracing combined with diffraction on facets: Verification and a potential application," *Journal of Quantitative Spectroscopy and Radiative Transfer*, vol. 100, no. 1, pp. 103–114, 2006.

[106] E. Hesse, "Modelling diffraction during ray tracing using the concept of energy flow lines," *Journal of Quantitative Spectroscopy and Radiative Transfer*, vol. 109, no. 8, pp. 1374–1383, 2008.

[107] R. Prosser, "The interpretation of diffraction and interference in terms of energy flow," *International Journal of Theoretical Physics*, vol. 15, no. 3, pp. 169–180, 1976.

[108] E. Hesse, A. Macke, S. Havemann, A. Baran, Z. Ulanowski, and P. H. Kaye, "Modelling diffraction by facetted particles," *Journal of Quantitative Spectroscopy and Radiative Transfer*, vol. 113, no. 5, pp. 342–347, 2012.

[109] E. Hesse, C. Collier, A. Penttilä, T. Nousiainen, Z. Ulanowski, and P. H. Kaye, "Modelling light scattering by absorbing smooth and slightly rough facetted particles," *Journal of Quantitative Spectroscopy and Radiative Transfer*, vol. 157, pp. 71–80, 2015.

[110] B. Karczewski and E. Wolf, "Comparison of three theories of electromagnetic diffraction at an aperture. part i: Coherence matrices," *JOSA*, vol. 56, no. 9, pp. 1207–1210, 1966.

[111] J. F. James, *A student's guide to Fourier transforms: with applications in physics and engineering*. Cambridge University Press, 2011.

[112] A. Borovoi, N. Kustova, and A. Konoshonkin, "Interference phenomena at backscattering by ice crystals of cirrus clouds," *Optics Express*, vol. 23, no. 19, pp. 24557–24571, 2015.

[113] Y. Takano and K. Jayaweera, "Scattering phase matrix for hexagonal ice crystals computed from ray optics," *Applied Optics*, vol. 24, no. 19, pp. 3254–3263, 1985.

[114] D. McCall, *Measurement and Modelling of Light Scattering by Small to Medium Size Parameter Airborne Particles*. PhD thesis, University of Hertfordshire, Hatfield, UK, 2010.

Appendices

Appendix A

Scattering Matrix Elements

The equations below relate the elements of the amplitude scattering matrix and the elements of the phase matrix [19].

$$P_{11} = \frac{1}{2}(|S_1|^2 + |S_2|^2 + |S_3|^2 + |S_4|^2) \tag{A.1a}$$
$$P_{12} = \frac{1}{2}(|S_2|^2 - |S_1|^2 + |S_4|^2 - |S_3|^2) \tag{A.1b}$$
$$P_{13} = \mathrm{Re}\{S_2 S_3^* + S_1 S_4^*\} \tag{A.1c}$$
$$P_{14} = \mathrm{Im}\{S_2 S_3^* - S_1 S_4^*\} \tag{A.1d}$$
$$P_{21} = \frac{1}{2}(|S_2|^2 - |S_1|^2 - |S_4|^2 + |S_3|^2) \tag{A.1e}$$
$$P_{22} = \frac{1}{2}(|S_2|^2 + |S_1|^2 - |S_4|^2 - |S_3|^2) \tag{A.1f}$$
$$P_{23} = \mathrm{Re}\{S_2 S_3^* - S_1 S_4^*\} \tag{A.1g}$$
$$P_{24} = \mathrm{Im}\{S_2 S_3^* + S_1 S_4^*\} \tag{A.1h}$$
$$P_{31} = \mathrm{Re}\{S_2 S_4^* + S_1 S_3^*\} \tag{A.1i}$$
$$P_{32} = \mathrm{Re}\{S_2 S_4^* - S_1 S_3^*\} \tag{A.1j}$$
$$P_{33} = \mathrm{Re}\{S_1 S_2^* + S_3 S_4^*\} \tag{A.1k}$$
$$P_{34} = \mathrm{Im}\{S_2 S_1^* + S_4 S_3^*\} \tag{A.1l}$$
$$P_{41} = \mathrm{Im}\{S_2^* S_4 + S_3^* S_1\} \tag{A.1m}$$
$$P_{42} = \mathrm{Im}\{S_2^* S_4 - S_3^* S_1\} \tag{A.1n}$$
$$P_{43} = \mathrm{Im}\{S_1 S_2^* - S_3 S_4^*\} \tag{A.1o}$$
$$P_{44} = \mathrm{Re}\{S_1 S_2^* - S_3 S_4^*\} \tag{A.1p}$$

Appendix B

Aspect Ratio and Particle Size Parameter

B.1 Aspect Ratio

The aspect ratio of a hexagonal column is the ratio of its length L to its diameter D,

$$\text{Aspect ratio} = \frac{L}{D}. \tag{B.1}$$

For this report, it is kept at a value of unity. When particle size parameters are changed, both the length and diameter are scaled accordingly.

B.2 Particle Size Parameter

Since there are many ways to describe a particle's size a commonly used alternative quantity known as the *size parameter* is used. It is defined in the following way:

$$x = \frac{2\pi r}{\lambda} = kr, \tag{B.2}$$

where r is the characteristic size and λ is the wavelength. The choice of r can either be the particle radius, or its length. We use the radius as the particle characteristic size. The advantages of using the particle size parameter rather than just a pure size value is that it allows for scaling by either size or wavelength.

Appendix C

Complex Snell's Law

We give here a derivation of the modification made to Snell's law used in the beam tracer. The derivation below is the same as that found in *Principles of Optics* [15], but more detail is given here.

To begin with, we rewrite the complex refractive index as

$$\hat{m} = m(1 + \mathrm{i}\kappa). \tag{C.1}$$

In this form the imaginary part of the refractive index m_i becomes $m_i = m\kappa$. Maintaining the assumption used throughout that the second medium is air we wish to express the complex Snell's law,

$$\sin\vartheta_t = \frac{1}{\hat{m}}\sin\vartheta_i, \tag{C.2}$$

in such a way that all quantities involved are real. To that end we choose the plane of incidence to be the xz plane, with the air-ice interface being the plane $z = 0$. The space dependent part of the phase in the absorbing medium is given by $\hat{k}(\mathbf{r}\cdot\hat{\mathbf{k}}^t)$, where $\hat{k}$ is the complex wavenumber, $\mathbf{r}$ is the position vector of some point and $\hat{\mathbf{k}}^t$ is a unit vector in the direction of transmission. Expressing $\hat{\mathbf{k}}^t$ in component form we have:

$$k_x^t = \sin\vartheta_t, \quad k_y^t = 0, \quad k_z^t = \cos\vartheta_t. \tag{C.3}$$

Combining Equations C.3 - C.1 we have:

$$k_x^t = \frac{1 - i\kappa}{m(1+\kappa^2)}\sin\vartheta_i, \tag{C.4}$$

$$k_z^t = \sqrt{1 - \frac{(1-\kappa^2)}{m^2(1+\kappa^2)^2}\sin^2\vartheta_i + i\frac{2\kappa}{m^2(1+\kappa^2)^2}\sin^2\vartheta_i}. \tag{C.5}$$

Next, we write k_z^t in amplitude-phase form

$$k_z^t = \cos\vartheta_t = qe^{\mathrm{i}\gamma} \qquad q, \gamma \in \mathbb{R}. \tag{C.6}$$

To gain expressions for q and γ we square Equations C.5 and C.6 and make use of Eulers relation ($Ae^{\mathrm{i}\alpha} = A(\cos\alpha + \mathrm{i}\sin\alpha)$):

$$(k_z^t)^2 = q^2e^{\mathrm{i}2\gamma} = q^2\cos(2\gamma) + \mathrm{i}\sin(2\gamma) \tag{C.7}$$

$$(k_z^t)^2 = 1 - \frac{(1-\kappa^2)}{m^2(1+\kappa^2)^2}\sin^2\vartheta_i + \mathrm{i}\frac{2\kappa}{m^2(1+\kappa^2)^2}\sin^2\vartheta_i. \tag{C.8}$$

Comparing real and imaginary parts we have:

$$q^2\cos(2\gamma) = 1 - \frac{(1-\kappa^2)}{m^2(1+\kappa^2)^2}\sin^2\vartheta_i \tag{C.9}$$

$$q^2\sin(2\gamma) = \frac{2\kappa}{m^2(1+\kappa^2)^2}\sin^2\vartheta_i. \tag{C.10}$$

These two equations, with two unknowns, can then be solved to gain expressions for q and γ. To yield q we square both equations and add them:

$$q^4 = \left(1 - \frac{(1-\kappa^2)}{m^2(1+\kappa^2)^2}\sin^2\vartheta_i\right)^2 + \left(\frac{2\kappa}{m^2(1+\kappa^2)^2}\sin^2\vartheta_i\right)^2. \tag{C.11}$$

Square rooting this and substituting into Equation C.9 we then get an expression for γ:

$$\gamma = \frac{1}{2}\left[\frac{1 - \frac{(1-\kappa^2)}{m^2(1+\kappa^2)^2}\sin^2\vartheta_i}{\sqrt{\left(1 - \frac{(1-\kappa^2)}{m^2(1+\kappa^2)^2}\sin^2\vartheta_i\right)^2 + \left(\frac{2\kappa}{m^2(1+\kappa^2)^2}\sin^2\vartheta_i\right)^2}}\right]. \tag{C.12}$$

Returning to the space dependent part of the phase we require that $\hat{k}(\mathbf{r}\cdot\hat{\mathbf{k}}^t) = const$ for some point $\mathbf{r} = (x, 0, z)$ on the plane of constant phase. Evaluating this product we get:

$$\begin{aligned}
\hat{k}(\mathbf{r}\cdot\hat{\mathbf{k}}^t) &= \frac{\omega}{c}m(1+\mathrm{i}\kappa)(xk_x^t + zk_z^t) \\
&= \frac{\omega}{c}m(1+\mathrm{i}\kappa)\left[\frac{x(1-i\kappa)}{m(1+\kappa^2)}\sin\vartheta_i + z(q\cos\gamma + \mathrm{i}q\sin\gamma)\right] \\
&= \frac{\omega}{c}[x\sin\vartheta_i + zmq(\cos\gamma - \kappa\sin\gamma) + \mathrm{i}mzq(\kappa\cos\gamma + \sin\gamma)].
\end{aligned} \tag{C.13}$$

The planes of real phase are given by setting the real part of Equation C.13 to a constant value. That is:

$$x\sin\vartheta_i + zmq(\cos\gamma - \kappa\sin\gamma) = const \tag{C.14}$$

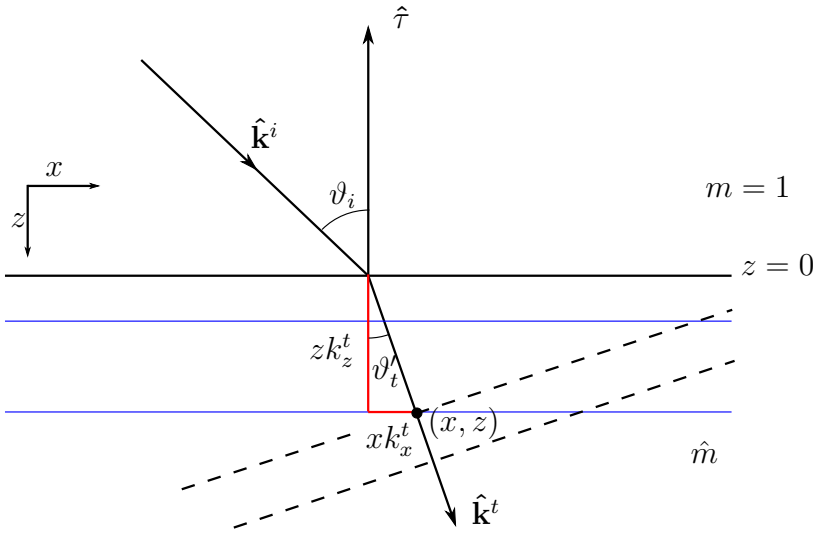

Figure C.1: Transmission into an absorbing medium, planes of constant amplitude (blue) are parallel to the boundary and deviate from the planes of constant phase (black dashed lines).

Through considering Figure C.1 we can deduce that the angle between the planes of constant phase and the surface normal is given by:

$$\cos\vartheta_t' = \frac{mq(\cos\gamma - \kappa\sin\gamma)}{\sqrt{\sin^2\vartheta_i + m^2q^2(\cos\gamma - \kappa\sin\gamma)^2}}, \tag{C.15}$$

$$\sin\vartheta_t' = \frac{\sin\vartheta_i}{\sqrt{\sin^2\vartheta_i + m^2q^2(\cos\gamma - \kappa\sin\gamma)^2}}. \tag{C.16}$$

If we write the denominator in the above equations as m' then we arrive at an expression in a similar form to Snell's law:

$$\sin\vartheta_t' = \frac{\sin\vartheta_i}{m'}. \tag{C.17}$$

We see that in this form the transmission angle ϑ_t', which corresponds to the direction the transmitted ray would need to make to be perpendicular to the planes of constant phase, depends on the material properties and the incidence angle ϑ_i. The beam tracer users the above form of Snell's law.

Appendix D

Elements of the Diffraction Amplitude Matrix

Here a complete derivation of Equation 5.16 from the paper by Karczewski and Wolf [110] is given. This equation forms the elements of the diffraction amplitude matrix which is used in the Beam Tracing model to evaluate the polarisation of the diffracted beam. In this section the notation from the paper is used. As such, note the following when comparing this section to the rest of the thesis:

- The vectors $\hat{\mathbf{L}}$ and $\hat{\mathbf{M}}$ are equivalent to $\hat{\mathbf{e}}^i_{\parallel}$ and $\hat{\mathbf{e}}^i_{\perp}$.
- The vectors $\hat{\mathbf{l}}$ and $\hat{\mathbf{m}}$ are equivalent to $\hat{\mathbf{e}}^s_{\parallel}$ and $\hat{\mathbf{e}}^s_{\perp}$.
- The field vector $\mathbf{A}$ is equivalent to $\mathbf{E}$.

An incident plane electromagnetic wave is incident on an aperture. The centre of the Aperture is at O, we introduce a rectangular coordinate axis at this point with the direction Oz perpendicular to the screen, pointing into the region in which the wave is propagating.

We introduce the right handed triad $\hat{\mathbf{k}}, \hat{\mathbf{l}}, \hat{\mathbf{m}}$ where $\hat{\mathbf{k}}$ is the direction of observation. we force the vector $\hat{\mathbf{l}}$ to lie in the xz plane such that

$$\hat{\mathbf{l}} = l_x\hat{\mathbf{x}} + l_z\hat{\mathbf{z}}. \tag{D.1}$$

Furthermore, since we have defined unit vectors we have

$$\hat{\mathbf{k}}^2 = \hat{\mathbf{l}}^2 = \hat{\mathbf{m}}^2 = 1. \tag{D.2}$$

Also, we have the orthogonality relationships

$$\hat{\mathbf{k}} \cdot \hat{\mathbf{l}} = \hat{\mathbf{m}} \cdot \hat{\mathbf{l}} = \hat{\mathbf{k}} \cdot \hat{\mathbf{m}} = 0, \qquad \hat{\mathbf{k}} \times \hat{\mathbf{l}} = \hat{\mathbf{m}}. \tag{D.3}$$

This is different to the system used in the Beam Tracer $\hat{\mathbf{k}} \times \hat{\mathbf{m}} = \hat{\mathbf{l}}$. As such, the $\hat{\mathbf{l}}$ vector is negative for our work. This document has corrected for this

It is convenient to express the components of $\hat{\mathbf{l}}$ & $\hat{\mathbf{m}}$ in terms of $\hat{\mathbf{k}}$. First, we have $\hat{\mathbf{k}} = k_x\hat{\mathbf{x}} + k_y\hat{\mathbf{y}} + k_z\hat{\mathbf{z}}$. Before doing this note that from equation D.1 we have

$$\hat{\mathbf{l}} \cdot \hat{\mathbf{l}} = l_x^2 + l_z^2 = 1 \rightarrow l_z = \sqrt{1 - l_x^2}. \tag{D.4}$$

Also note that:

$$\hat{\mathbf{k}} \cdot \hat{\mathbf{k}} = k_x^2 + k_y^2 + k_z^2 = 1 \rightarrow k_x^2 + k_z^2 = 1 - k_y^2. \tag{D.5}$$

We can now get expressions for the components of $\hat{\mathbf{l}}$.

$$\begin{aligned} \hat{\mathbf{k}} \cdot \hat{\mathbf{l}} = k_x l_x + k_z + l_z &= 0 \\ k_x l_x &= -k_z l_z \end{aligned}$$

Substitution into Equation D.4 yields,

$$\begin{aligned} k_x l_x &= -k_z \sqrt{1 - l_x^2} \\ k_x^2 l_x^2 &= k_z^2 (1 - l_x^2) \\ k_x^2 l_x^2 + k_z^2 l_x^2 &= k_z^2 \\ l_x^2 (k_x^2 + k_z^2) &= k_z^2. \end{aligned}$$

Substituting this into Equation D.5,

$$\begin{aligned} l_x^2 (1 - k_y^2) &= k_z^2 \\ l_x &= \frac{k_z}{\sqrt{1 - k_y^2}}. \end{aligned}$$

Which can be used to get l_z,

$$\begin{aligned} k_x l_x &= -k_z l_z \\ l_z &= -\frac{k_x l_x}{k_z} \\ l_z &= -\frac{k_z}{\sqrt{1 - k_y^2}} \times \frac{k_x}{k_z} \\ l_z &= -\frac{k_x}{\sqrt{1 - k_y^2}}. \end{aligned}$$

At this point we multiply $\hat{\mathbf{l}}$ by -1. This compensates for the formalism discussed in the paper using $\hat{\mathbf{k}} \times \hat{\mathbf{l}} = \hat{\mathbf{m}}$, rather than $\hat{\mathbf{k}} \times \hat{\mathbf{m}} = \hat{\mathbf{l}}$.

$$\hat{\mathbf{l}} = -\frac{k_z}{\sqrt{1 - k_y^2}} \hat{\mathbf{x}} + \frac{k_x}{\sqrt{1 - k_y^2}} \hat{\mathbf{z}}.$$

Next we decompose $\hat{\mathbf{m}}$, to do this we use the fact that $\hat{\mathbf{k}} \times \hat{\mathbf{l}} = \hat{\mathbf{m}}$

$$\hat{\mathbf{k}} \times \hat{\mathbf{l}} = \begin{vmatrix} \hat{\mathbf{x}} & \hat{\mathbf{y}} & \hat{\mathbf{z}} \\ k_x & k_y & k_z \\ -\frac{k_z}{\sqrt{1-k_y^2}} & 0 & \frac{k_x}{\sqrt{1-k_y^2}} \end{vmatrix}$$

Evaluating the cross product we get:

$$\hat{\mathbf{k}} \times \hat{\mathbf{l}} = \frac{k_y k_x}{\sqrt{1 - k_y^2}} \hat{\mathbf{x}} - \left(\frac{k_x^2}{\sqrt{1 - k_y^2}} + \frac{k_z^2}{\sqrt{1 - k_y^2}} \right) \hat{\mathbf{y}} + \frac{k_y k_z}{\sqrt{1 - k_y^2}} \hat{\mathbf{z}}$$

$$= \frac{k_y k_x}{\sqrt{1-k_y^2}}\hat{\mathbf{x}} - \frac{(k_x^2+k_z^2)}{\sqrt{1-k_y^2}}\hat{\mathbf{y}} + \frac{k_y k_z}{\sqrt{1-k_y^2}}\hat{\mathbf{z}}.$$

Then using equation D.5 we get:

$$= \frac{k_y k_x}{\sqrt{1-k_y^2}}\hat{\mathbf{x}} - \frac{(1-k_y^2)}{\sqrt{1-k_y^2}}\hat{\mathbf{y}} + \frac{k_y k_z}{\sqrt{1-k_y^2}}\hat{\mathbf{z}}$$
$$\therefore \hat{\mathbf{m}} = \frac{k_x k_y}{\sqrt{1-k_y^2}}\hat{\mathbf{x}} - \sqrt{1-k_y^2}\hat{\mathbf{y}} + \frac{k_y k_z}{\sqrt{1-k_y^2}}\hat{\mathbf{z}}$$

Combining all of this we have

	$\hat{\mathbf{x}}$	$\hat{\mathbf{y}}$	$\hat{\mathbf{z}}$
$\hat{\mathbf{k}}$:	k_x	k_y	k_z
$\hat{\mathbf{l}}$:	$-\frac{k_z}{\sqrt{1-k_y^2}}$	0	$\frac{k_x}{\sqrt{1-k_y^2}}$
$\hat{\mathbf{m}}$:	$\frac{k_x k_y}{\sqrt{1-k_y^2}}$	$-\sqrt{1-k_y^2}$	$\frac{k_y k_z}{\sqrt{1-k_y^2}}$

For the incident field, we introduce another right handed orthogonal system defined in strictly the same manner as the diffracted field vectors. These vectors are $\hat{\mathbf{K}}, \hat{\mathbf{L}}, \hat{\mathbf{M}}$, again we have $\hat{\mathbf{L}}$ in the xz plane. By doing this we have analogous expressions for the components (that is, the lower case letters are replaced by their upper case counterparts).

Next we find the components of the electric and magnetic amplitude vectors of the incident field with respect to the xyz axes. Let A_K, A_L, A_M be the components of the electric amplitude vector in the $\hat{\mathbf{K}}, \hat{\mathbf{L}}, \hat{\mathbf{M}}$ directions. Since $\mathbf{A}$ is perpendicular to the direction of propagation we have $A_K = 0$. The component of $\mathbf{A}$ with respect to the x direction is.

$$\begin{aligned} A_x &= A_K K_x + A_L L_x + A_M M_x \\ &= 0 + \frac{K_z}{\sqrt{1-K_y^2}} A_L + \frac{K_x K_y}{\sqrt{1-K_y^2}} A_M \\ A_x &= \frac{K_z}{\sqrt{1-K_y^2}} A_L + \frac{K_x K_y}{\sqrt{1-K_y^2}} A_M \end{aligned} \tag{D.6}$$

For A_y we have

$$\begin{aligned} A_y &= A_K K_y + A_L L_y + A_M M_y \\ &= 0 + 0 + A_M M_y \\ A_y &= -\sqrt{1-K_y^2} A_M \end{aligned} \tag{D.7}$$

and for A_z

$$\begin{aligned} A_z &= A_K K_z + A_L L_z + A_M M_z \\ &= 0 - \frac{K_x}{\sqrt{1-K_y^2}} A_L + \frac{K_y K_z}{\sqrt{1-K_y^2}} A_M \\ A_z &= -\frac{K_x}{\sqrt{1-K_y^2}} A_L + \frac{K_y K_z}{\sqrt{1-K_y^2}} A_M \end{aligned} \tag{D.8}$$

Since $\mathbf{B} = \hat{\mathbf{K}} \times \mathbf{A}$ we have:

$$\hat{\mathbf{K}} \times \mathbf{A} = \begin{vmatrix} \hat{\mathbf{k}} & \hat{\mathbf{l}} & \hat{\mathbf{m}} \\ 1 & 0 & 0 \\ 0 & A_L & A_M \end{vmatrix} = -A_M \hat{\mathbf{l}} + A_L \hat{\mathbf{m}}.$$

We see that $B_L = -A_M$ and $B_M = A_L$. We then get the corresponding values for $\mathbf{B}$ defined with respect to the xyz axes.

$$\begin{aligned} B_x &= -\frac{K_z}{\sqrt{1-K_y^2}} A_M + \frac{K_x K_y}{\sqrt{1-K_y^2}} A_L \\ B_y &= -\sqrt{1-K_y^2} A_L \\ B_z &= \frac{K_x}{\sqrt{1-K_y^2}} A_M + \frac{K_y K_z}{\sqrt{1-K_y^2}} A_L \end{aligned} \tag{D.9}$$

With all this done, we can begin to find the components of the electric field with respect to the coordinate system in the diffracted space ($\hat{\mathbf{k}}, \hat{\mathbf{l}}, \hat{\mathbf{m}}$ system). From the so called *m-theory* we have:

$$\mathbf{E}^{(m)}(P) = 2\hat{\mathbf{k}} \times (\mathbf{F} \times \mathbf{A}) \tag{D.10}$$

Where $\mathbf{F}$ is given by:

$$\mathbf{F} = C\hat{n} \iint_a \exp[ik_0(\hat{\mathbf{K}} - \hat{\mathbf{k}}) \cdot \mathbf{R}] \mathrm{d}S,$$

where $C = (ik_0/4\pi)[\exp(ik_0 r_0)/r_0]$. Also, the scalar part of $\mathbf{F}$ is the classical Fraunhofer diffraction pattern (F in the thesis). Note that $\hat{\mathbf{n}} =< 0, 0, 1 >^T$, this means that $\mathbf{F}$ only has a z component.

We now evaluate the product given in equation D.10.

$$\mathbf{F} \times \mathbf{A} = \begin{vmatrix} \hat{\mathbf{x}} & \hat{\mathbf{y}} & \hat{\mathbf{z}} \\ 0 & 0 & F \\ A_x & A_y & A_z \end{vmatrix} = -FA_y \hat{\mathbf{x}} + FA_x \hat{\mathbf{y}}$$

and the second product

$$2\hat{\mathbf{k}} \times (\mathbf{F} \times \mathbf{A}) = 2 \begin{vmatrix} \hat{\mathbf{x}} & \hat{\mathbf{y}} & \hat{\mathbf{z}} \\ k_x & k_y & k_z \\ -FA_y & FA_x & 0 \end{vmatrix} = 2(-k_z FA_x \hat{\mathbf{x}} - k_z FA_y \hat{\mathbf{y}} + (k_x FA_x + k_y FA_y)\hat{\mathbf{z}}).$$

However, this has been found with respect to the xyz axes and we want it with respect the diffraction space. Therefore, we set up the following equation

$$2\hat{\mathbf{k}} \times (\mathbf{F} \times \mathbf{A}) = \alpha \hat{\mathbf{l}} + \beta \hat{\mathbf{m}},$$

where α and β are two scalars to be found. Equating the two

$$\alpha \hat{\mathbf{l}} + \beta \hat{\mathbf{m}} = 2(-k_z FA_x \hat{\mathbf{x}} - k_z FA_y \hat{\mathbf{y}} + (k_x FA_x + k_y FA_y)\hat{\mathbf{z}})$$

Expressing this in component form gives:

$$\alpha l_x + \beta m_x = -2k_z F A_x. \tag{D.11}$$
$$\beta m_y = -2k_z F A_y \tag{D.12}$$
$$\alpha l_z + \beta m_z = 2(k_x F A_x + k_y F A_y) \tag{D.13}$$

From Equation D.12 we have

$$\beta = -\frac{2Fk_z}{m_y} A_y.$$

Now using equation D.6 and the expression for m_y we get:

$$\beta = -\frac{2Fk_z}{-(1-k_y^2)^{\frac{1}{2}}} \times \left[-(1-K_y^2)^{\frac{1}{2}}\right] A_M$$

$$\therefore \beta = -2Fk_z \left(\frac{1-K_y^2}{1-k_y^2}\right)^{\frac{1}{2}} A_M \tag{D.14}$$

Substituting Equation D.14 into Equation D.11,

$$\alpha l_x + \beta m_x = -2k_z F A_x$$
$$\alpha l_x - 2Fk_z \left(\frac{1-K_y^2}{1-k_y^2}\right)^{\frac{1}{2}} A_M m_x = -2k_z F \left(\frac{K_z}{\sqrt{1-K_y^2}} A_L + \frac{K_x K_y}{\sqrt{1-K_y^2}} A_M\right)$$
$$\alpha \frac{k_z}{(1-k_y^2)^{\frac{1}{2}}} - \frac{2Fk_x k_y k_z}{(1-k_y^2)^{\frac{1}{2}}} \left(\frac{1-K_y^2}{1-k_y^2}\right)^{\frac{1}{2}} A_M = -\frac{2Fk_z K_z}{(1-K_y^2)^{\frac{1}{2}}} A_L - \frac{2FK_x K_y k_z A_M}{(1-K_y^2)^{\frac{1}{2}}}$$
$$\alpha k_z - 2Fk_x k_y k_z \left(\frac{1-K_y^2}{1-k_y^2}\right)^{\frac{1}{2}} A_M = -2Fk_z K_z \left(\frac{1-k_y^2}{1-K_y^2}\right)^{\frac{1}{2}} A_L -$$
$$2FK_x K_y k_z \left(\frac{1-k_y^2}{1-K_y^2}\right)^{\frac{1}{2}} A_M$$
$$\alpha - 2Fk_x k_y \left(\frac{1-K_y^2}{1-k_y^2}\right)^{\frac{1}{2}} A_M = -2FK_z \left(\frac{1-k_y^2}{1-K_y^2}\right)^{\frac{1}{2}} A_L -$$
$$- 2FK_x K_y \left(\frac{1-k_y^2}{1-K_y^2}\right)^{\frac{1}{2}} A_M$$

$$\therefore \alpha = 2F \left\{-K_z \left(\frac{1-k_y^2}{1-K_y^2}\right)^{\frac{1}{2}} A_L + A_M \left[k_x k_y \left(\frac{1-K_y^2}{1-k_y^2}\right)^{\frac{1}{2}} - K_x K_y \left(\frac{1-k_y^2}{1-K_y^2}\right)^{\frac{1}{2}}\right]\right\}. \tag{D.15}$$

Next we use the result from the *e-theory*

$$\mathbf{E}^{(e)}(P) = 2\{\mathbf{F} \times \mathbf{B} - [\hat{\mathbf{k}} \cdot (\mathbf{F} \times \mathbf{B}]\hat{\mathbf{k}}\}. \tag{D.16}$$

Since the product $\mathbf{F} \times \mathbf{B}$ appears twice, we first do this:

$$\mathbf{F} \times \mathbf{B} = \begin{vmatrix} \hat{\mathbf{x}} & \hat{\mathbf{y}} & \hat{\mathbf{z}} \\ 0 & 0 & F \\ B_x & B_y & B_z \end{vmatrix} = -FB_y\hat{\mathbf{x}} + FB_x\hat{\mathbf{y}}$$

$$\begin{aligned} [\hat{\mathbf{k}} \cdot (\mathbf{F} \times \mathbf{B})]\hat{\mathbf{k}} &= [-FB_yk_x + FB_xk_y]\hat{\mathbf{k}} \\ &= (-FB_yk_x^2 + FB_xk_xk_y)\hat{\mathbf{x}} + (-FB_yk_xk_y + FB_xk_y^2)\hat{\mathbf{y}} + \\ &\quad (-FB_yk_xk_z + FB_xk_yk_z)\hat{\mathbf{z}} \\ \{\mathbf{F} \times \mathbf{B} - [\hat{\mathbf{k}} \cdot (\mathbf{F} \times \mathbf{B})]\hat{\mathbf{k}}\} &= 2\{-FB_y\hat{\mathbf{x}} + FB_x\hat{\mathbf{y}} + (FB_yk_x^2 - FB_xk_xk_y)\hat{\mathbf{x}} + \\ &\quad (FB_yk_xk_y - FB_xk_y^2)\hat{\mathbf{y}} + (FB_yk_xk_z - FB_xk_yk_z)\hat{\mathbf{z}}\}. \end{aligned}$$

As before, we set up a corresponding vector equation, with two unknown coefficients, γ, δ that we seek to find. We have

$$2\hat{\mathbf{k}} \times (\mathbf{F} \times \mathbf{A}) = \gamma\hat{\mathbf{l}} + \delta\hat{\mathbf{m}}.$$

Written in component form

$$\gamma l_x + \delta m_x = 2F(-B_y + B_yk_x^2 - B_xk_yk_x) \tag{D.17}$$

$$\delta m_y = 2F(B_x + Byk_xk_y - B_xk_y^2) \tag{D.18}$$

$$\gamma l_z + \delta m_z = 2F(B_yk_xk_z - B_xk_yk_z), \tag{D.19}$$

where once again we have made use of the fact that $l_y = 0$. From Equation D.18,

$$\delta = \frac{2F}{m_y}\left[B_x(1 - k_y^2) + B_yk_xk_y\right],$$

and making use of the expression for m_y

$$\begin{aligned} &= 2F\left[\frac{(1 - k_y^2)}{[-(1 - k_y)^{\frac{1}{2}}]} + \frac{B_yk_xk_y}{[-(1 - k_y^2)^{\frac{1}{2}}]}\right] \\ &= 2F\left[-B_x(1 - k_y^2)^{\frac{1}{2}} - B_y\frac{k_xk_y}{(1 - k_y^2)^{\frac{1}{2}}}\right]. \end{aligned}$$

Using Equation D.9 for expressions of B_x, B_y

$$= 2F\left[K_z\left(\frac{1 - k_y^2}{1 - K_y^2}\right)^{\frac{1}{2}}A_M - K_xK_y\left(\frac{1 - k_y^2}{1 - K_y^2}\right)^{\frac{1}{2}}A_L + k_xk_y\left(\frac{1 - K_y^2}{1 - k_y^2}\right)^{\frac{1}{2}}A_L\right].$$

$$\therefore \delta = 2F\left\{\left[K_z\left(\frac{1 - k_y^2}{1 - K_y^2}\right)^{\frac{1}{2}}\right]A_M + \left[k_xk_y\left(\frac{1 - K_y^2}{1 - k_y^2}\right)^{\frac{1}{2}} - K_xK_y\left(\frac{1 - k_y^2}{1 - K_y^2}\right)^{\frac{1}{2}}\right]A_L\right\}. \tag{D.20}$$

Next we use Equation D.19 to get,

$$\begin{aligned}\gamma &= \frac{2F}{l_z}\left(B_y k_x k_z - B_x k_y k_z\right) - \frac{\delta m_z}{l_z} \\ &= \frac{2F(1-k_y^2)^{\frac{1}{2}}}{k_x}\left(B_y k_x k_z - B_x k_y k_z\right) - \frac{\delta k_y k_z}{k_x}.\end{aligned}$$

Again, using Equation D.9 for expressions of B_x, B_y:

$$\begin{aligned}=&\frac{2F}{k_x}\left\{\left[K_z\left(\frac{1-k_y^2}{1-K_y^2}\right)^{\frac{1}{2}} k_y k_z\right] A_M - \right. \\ &\left. A_L\left[k_y k_z K_x K_y\left(\frac{1-k_y^2}{1-K_y^2}\right)^{\frac{1}{2}} + k_z k_x (1-K_y^2)^{\frac{1}{2}}(1-k_y^2)^{\frac{1}{2}}\right]\right\} \\ &= -\frac{2F k_y k_z}{k_x}\left\{\left[K_z\left(\frac{1-k_y^2}{1-K_y^2}\right)^{\frac{1}{2}}\right] A_M + \right. \\ &\left.\left[k_x k_y\left(\frac{1-K_y^2}{1-k_y^2}\right)^{\frac{1}{2}} - K_x K_y\left(\frac{1-k_y^2}{1-K_y^2}\right)^{\frac{1}{2}}\right] A_L\right\}\end{aligned}$$

For ease, consider each component separately, starting with A_M:

$$\frac{2F}{k_x}\left[K_z\left(\frac{1-k_y^2}{1-K_y^2}\right)^{\frac{1}{2}} k_y k_z\right] A_M - \frac{2F k_y k_z}{k_x}\left[K_z\left(\frac{1-k_y^2}{1-K_y^2}\right)^{\frac{1}{2}}\right] A_M = 0.$$

So there is no A_M component in γ. Considering A_L,

$$\begin{aligned}&-2F A_L\left\{\frac{k_y k_z K_x K_y}{k_x}\left(\frac{1-k_y^2}{1-K_y^2}\right)^{\frac{1}{2}} + \right. \\ &\left. k_z(1-k_y^2)^{\frac{1}{2}}(1-K_y^2)^{\frac{1}{2}} + k_y^2 k_z\left(\frac{1-K_y^2}{1-k_y^2}\right)^{\frac{1}{2}} - \frac{k_y k_z K_x K_y}{k_x}\left(\frac{1-k_y^2}{1-K_y^2}\right)^{\frac{1}{2}}\right\} \\ &= -2F A_L\left[k_z(1-k_y^2)^{\frac{1}{2}}(1-K_y^2)^{\frac{1}{2}} + k_y^2 k_z\left(\frac{1-K_y^2}{1-k_y^2}\right)^{\frac{1}{2}}\right] \\ &= -2F A_L k_z(1-K_y^2)^{\frac{1}{2}}\left[(1-k_y^2)^{\frac{1}{2}} + \frac{k_y^2}{(1-k_y^2)^{\frac{1}{2}}}\right] \\ &= -2F A_L k_z(1-K_y^2)^{\frac{1}{2}}\left[\frac{1-k_y^2+k_y^2}{(1-k_y^2)^{\frac{1}{2}}}\right] \\ &\therefore \gamma = -2F A_L k_z\left(\frac{1-K_y^2}{1-k_y^2}\right)^{\frac{1}{2}}\end{aligned} \tag{D.21}$$

It is possible to convert from the e and m theories to a more complete *(e,m)-theory* through the following formulae:

$$\begin{aligned}\mathbf{E}^{(e,m)} &= \frac{1}{2}[\mathbf{E}^{(m)} + \mathbf{E}^{(e)}], \\ \mathbf{H}^{(e,m)} &= \frac{1}{2}[\mathbf{H}^{(m)} + \mathbf{H}^{(e)}].\end{aligned} \tag{D.22}$$

From Equations D.14 and D.15 we have the components on the electric field according the *m-theory*. That is, $E_l^{(m)} = \alpha$ and $E_m^{(m)} = \beta$. Similarly, we have the same field components found through the *e-theory* from Equations D.20 and D.21; $E_l^{(e)} = \gamma$ and $E_m^{(e)} = \delta$. For ease, the equations are repeated below:

$$E_l^{(m)} = 2F\left\{-K_z\left(\frac{1-k_y^2}{1-K_y^2}\right)^{\frac{1}{2}}A_L + A_M\left[k_xk_y\left(\frac{1-K_y^2}{1-k_y^2}\right)^{\frac{1}{2}} - K_xK_y\left(\frac{1-k_y^2}{1-K_y^2}\right)^{\frac{1}{2}}\right]\right\},$$

$$E_m^{(m)} = -2Fk_z\left(\frac{1-K_y^2}{1-k_y^2}\right)^{\frac{1}{2}}A_M,$$

$$E_l^{(e)} = -2Fk_z\left(\frac{1-K_y^2}{1-k_y^2}\right)^{\frac{1}{2}}A_L,$$

$$E_m^{(e)} = 2F\left\{\left[K_z\left(\frac{1-k_y^2}{1-K_y^2}\right)^{\frac{1}{2}}\right]A_M + \left[k_xk_y\left(\frac{1-K_y^2}{1-k_y^2}\right)^{\frac{1}{2}} - K_xK_y\left(\frac{1-k_y^2}{1-K_y^2}\right)^{\frac{1}{2}}\right]A_L\right\}.$$

Introducing some new variables to allow us to write the above in shorthand, let:

$$\begin{aligned} a_1^{(m)} &= -K_z\left(\frac{1-k_y^2}{1-K_y^2}\right)^{\frac{1}{2}}, \\ b_1^{(m)} &= K_xK_y\left(\frac{1-k_y^2}{1-K_y^2}\right)^{\frac{1}{2}} - k_xk_y\left(\frac{1-K_y^2}{1-k_y^2}\right)^{\frac{1}{2}}, \\ b_2^{(m)} &= -k_z\left(\frac{1-K_y^2}{1-k_y^2}\right)^{\frac{1}{2}}, \end{aligned} \tag{D.23}$$

and

$$\begin{aligned} a_1^{(e)} &= -k_z\left(\frac{1-K_y^2}{1-k_y^2}\right)^{\frac{1}{2}}, \\ a_2^{(e)} &= k_xk_y\left(\frac{1-K_y^2}{1-k_y^2}\right)^{\frac{1}{2}} - K_xK_y\left(\frac{1-k_y^2}{1-K_y^2}\right)^{\frac{1}{2}}, \\ b_2^{(e)} &= -K_z\left(\frac{1-k_y^2}{1-K_y^2}\right)^{\frac{1}{2}}, \end{aligned} \tag{D.24}$$

Using Equations D.23 and D.24 we have:

$$\begin{aligned} E_l^{(m)} &= 2F(a_1^{(m)}A_L + b_1^{(m)}A_M) \\ E_m^{(m)} &= 2Fb_2^{(m)}A_M \end{aligned} \tag{D.25}$$

$$\begin{aligned} E_l^{(e)} &= 2Fa_1^{(e)}A_L, \\ E_m^{(e)} &= 2F(a_2^{(e)}A_L + b_2^{(e)}A_M). \end{aligned} \tag{D.26}$$

Using Equations D.25 and D.26 along with equation D.22 we get,

$$E_l^{(e,m)} = \frac{2F}{2}(a_1^{(m)}A_L + b_1^{(m)}A_M + a_1^{(e)}A_L),$$

$$= 2F\left(\frac{(a_1^{(m)} + a_1^{(e)})A_L}{2} + \frac{b_1^{(m)}A_M}{2}\right).$$

Similarly we have for the component with respect to $\hat{\mathbf{m}}$

$$\begin{aligned} E_m^{(e,m)} &= \frac{2F}{2}(b_2^{(m)}A_M + a_2^{(e)}A_L + b_2^{(e)}A_M), \\ &= 2F\left(\frac{a_2^{(e)}A_L}{2} + \frac{(b_2^{(m)} + b_2^{(e)})A_M}{2}\right). \end{aligned}$$

These two results can be written as:

$$\begin{aligned} E_l^{(e,m)} &= 2F(a_1^{(e,m)}A_L + b_1^{(e,m)}A_M), \\ E_m^{(e,m)} &= 2F(a_2^{(e,m)}A_L + b_2^{(e,m)}A_M), \end{aligned} \tag{D.27}$$

where

$$\begin{aligned} a_1^{(e,m)} &= \frac{1}{2}(a_1^{(m)} + a_1^{(e)}) & a_2^{(e,m)} &= \frac{1}{2}a_2^{(e)} \\ b_1^{(e,m)} &= \frac{1}{2}b_1^{(m)} & b_2^{(e.m)} &= \frac{1}{2}(b_2^{(m)} + b_2^{(e)}) \end{aligned}$$

which is equation 5.16 in the paper [110].

Appendix E

Scattering Angle Bins

The scattering angle bins used in the Beam Tracing and ADDA models are given in Table E.1 along with the corresponding $\Delta\theta$ used in normalising the data, both in degrees. For azimuthal angles, angular bins of 1° were given leading to $\Delta\phi = 1°$.

i	θ	$\Delta\theta$	i	θ	$\Delta\theta$	i	θ	$\Delta\theta$	i	θ	$\Delta\theta$	i	θ	$\Delta\theta$
1	0.05	0.1	42	25	1	83	66	1	124	107	1	165	148	1
2	0.2	0.2	43	26	1	84	67	1	125	108	1	166	149	1
3	0.4	0.2	44	27	1	85	68	1	126	109	1	167	150	1
4	0.6	0.2	45	28	1	86	69	1	127	110	1	168	151	1
5	0.8	0.2	46	29	1	87	70	1	128	111	1	169	152	1
6	1	0.2	47	30	1	88	71	1	129	112	1	170	153	1
7	1.2	0.2	48	31	1	89	72	1	130	113	1	171	154	1
8	1.4	0.2	49	32	1	90	73	1	131	114	1	172	155	1
9	1.6	0.2	50	33	1	91	74	1	132	115	1	173	156	1
10	1.8	0.2	51	34	1	92	75	1	133	116	1	174	157	1
11	2	0.2	52	35	1	93	76	1	134	117	1	175	158	1
12	2.2	0.2	53	36	1	94	77	1	135	118	1	176	159	1
13	2.4	0.2	54	37	1	95	78	1	136	119	1	177	160	1
14	2.6	0.2	55	38	1	96	79	1	137	120	1	178	161	1
15	2.8	0.2	56	39	1	97	80	1	138	121	1	179	162	1
16	3	0.2	57	40	1	98	81	1	139	122	1	180	163	1
17	3.2	0.2	58	41	1	99	82	1	140	123	1	181	164	1
18	3.4	0.2	59	42	1	100	83	1	141	124	1	182	165	1
19	3.6	0.2	60	43	1	101	84	1	142	125	1	183	166	1
20	3.8	0.2	61	44	1	102	85	1	143	126	1	184	167	1
21	4	0.6	62	45	1	103	86	1	144	127	1	185	168	1
22	5	1	63	46	1	104	87	1	145	128	1	186	169	1
23	6	1	64	47	1	105	88	1	146	129	1	187	170	1
24	7	1	65	48	1	106	89	1	147	130	1	188	171	1
25	8	1	66	49	1	107	90	1	148	131	1	189	172	1
26	9	1	67	50	1	108	91	1	149	132	1	190	173	1
27	10	1	68	51	1	109	92	1	150	133	1	191	174	1
28	11	1	69	52	1	110	93	1	151	134	1	192	175	0.75
29	12	1	70	53	1	111	94	1	152	135	1	193	175.5	0.5
30	13	1	71	54	1	112	95	1	153	136	1	194	176	0.5
31	14	1	72	55	1	113	96	1	154	137	1	195	176.5	0.5
32	15	1	73	56	1	114	97	1	155	138	1	196	177	0.5
33	16	1	74	57	1	115	98	1	156	139	1	197	177.5	0.5
34	17	1	75	58	1	116	99	1	157	140	1	198	178	0.5
35	18	1	76	59	1	117	100	1	158	141	1	199	178.5	0.5
36	19	1	77	60	1	118	101	1	159	142	1	200	179	0.35
37	20	1	78	61	1	119	102	1	160	143	1	201	179.2	0.2
38	21	1	79	62	1	120	103	1	161	144	1	202	179.4	0.2
39	22	1	80	63	1	121	104	1	162	145	1	203	179.6	0.2
40	23	1	81	64	1	122	105	1	163	146	1	204	179.8	0.2
41	24	1	82	65	1	123	106	1	164	147	1	205	179.95	0.1

Table E.1: Scattering angles used in computations

Appendix F

Example Bash Code for Generating a Scattering Database

The following BASH code is an example of how a scattering database can be created using the Beam Tracing model. In this example hexagonal prisms are made of varying size, the smallest of which is $x = 50$. The code works by taking the node ID and multiplying it by 10. This is then incremented from 1-9 before being added to the base size of 50. For example, if the code was on node 2, it would lead to the creation of hexagonal prisms of size parameter $50 + (2 \times 10 + (i = 1, ..., 10))$. The corresponding radius and length of the prism are then found and saved in a text file called "column_details.txt".

Creation of crystal files for the given size parameters:

For a given size parameter a directory is made. The script copies in Fortran code (Makehex) and the required data files "allcolumns.points" and "column_details.txt". The crystal file is then made by running Makehex. Other files are copied into the directory including the file "eulerangles.txt" containing the Euler angles used for the prism, the executable of the Beam Tracer itself and a file called "prehexagon" which has default parameters stored in it. The input file 'hexagon' for the Beam Tracer is updated with the new crystal input file name, wavelength and real and imaginary part of the refractive index and the Beam Tracing code is executed. Once done, the script moves back into the former directory and the loop continues.

In this way a particle scattering database can be created and used.

```
#===============CREATE SCATTERING DATABASE==============
#!/bin/sh
#PBS -e test.err
#PBS -o test.out
#PBS -q cair_l
#PBS -l walltime=02:00:00
#PBS -k oe
#PBS -j oe
#PBS -e test.err
ulimit -s unlimited export
LD_LIBRARY_PATH=$LD_LIBRARY_PATH:/soft/intel-compilers \
```

```
/composerxe-2011.3.174/compiler/lib/intel64:/soft \
/intel-compilers/composerxe-2011.3.174/ipp/../compiler \
/lib/intel64:/soft/intel-compilers/composerxe-2011.3.174 \
/ipp/lib/intel64:/soft/intel-compilers/composerxe-2011.3.174\
/compiler/lib/intel64:/soft/intel-compilers\
/composerxe-2011.3.174/mkl/lib/intel64:\
/soft/intel-compilers/composerxe-2011.3.174\
/tbb/lib/intel64//cc4.1.0_libc2.4_kernel2.6.16.21:/usr \
/lib64/mpich2/lib:/soft/intel-compilers\
/composerxe-2011.3.174/mpirt/lib/intel64
executable=Beam_Tracer_ClusterRun
Makehex=hexgen
#Move to directory
cd /cair-scratch/ltaylor/ClusterRun/SizeParam
# size parameter is to be incremented in step sizes of 1
for i in `seq 1 9`; do
#Take node number and multiply by 10
        cur_pos1=$((PBS_ARRAYID*10))
#Then increment
        cur_pos=$((cur_pos1+i))
# Add this to 50
        size_param=$((50+cur_pos))
# calculate radius and length, wavelength is set as 532nm
        wavenumber=11.81
#radius=$((size_param/wavenumber)) |bc
        radius=$(echo "$size_param  / $wavenumber" | bc -l )
#length=$((2*radius))
        length=$(echo "$radius*2.0" | bc -l)
# make a directory for this size
        DirName="size_parameter$size_param"
        mkdir $DirName
#Move into the directory for this size
        cd $DirName
#test_file
        echo $wavenumber > test_file.txt
        echo $radius >> test_file.txt
        echo $length >> test_file.txt
        # Copy various files
        cp ../allcolumns.points .
        cp ../$Makehex .
# Generate crystal, put column length and width in file
        echo $length >  column_details.txt
        echo $radius >> column_details.txt
#Makehex creates the corresponding prism crystal file
        ./$Makehex
# rename the crystal file
        NewName="Smooth_size$size_param"
        mv test.crystal $NewName.crystal
```

```
# copy some more files
        cp ../prehexagon .
        cp ../eulerangles.txt .
        cp ../$executable .
# Make hexagon file
# (this is the file properties such as wavelength
#, refractive index etc)
#Insert crystal geomtry name
        echo $NewName.crystal > hexagon
# default wavelength and refractive index
        echo 0.532 1.31 0.0 >> hexagon
# remaining details for the file
        cat prehexagon >> hexagon
# run file and make log file
        ./$executable &> log.txt
        cd ..
done
```

Appendix G

Co-authored Paper: "Effects of Surface Roughness with Two Scales on Light Scattering by Hexagonal Ice Crystals Large Compared to the Wavelength: DDA Results"

The following paper was published in the Journal of Quantative Spectroscopy and Radiative Transfer (JQRST) in June 2016. The paper discusses the formation of a a rough hexagonal ice crystal geometry whose roughness parameters were derived from analysis of the surface of a sand grain. I contributed in the structure of the paper, especially in the earlier sections. I also helped create many of the plots shown throughout. The Beam Tracing model was applied to smooth crystal geometries to identify various geometric optics peaks, and the beam paths that create them. In addition, the model was used to determine how much of the incident energy is carried away by certain beams.

Journal of Quantitative Spectroscopy & Radiative Transfer 182 (2016) 225–239

Contents lists available at ScienceDirect

Journal of Quantitative Spectroscopy & Radiative Transfer

journal homepage: www.elsevier.com/locate/jqsrt

Effects of surface roughness with two scales on light scattering by hexagonal ice crystals large compared to the wavelength: DDA results

C.T. Collier [a,*], E. Hesse [a], L. Taylor [a], Z. Ulanowski [a], A. Penttilä [b], T. Nousiainen [c]

[a] University of Hertfordshire, Centre for Atmospheric and Instrumentation Research, Hatfield, Hertfordshire AL10 9AB, UK
[b] Department of Physics, University of Helsinki, P.O. Box 64, FI-00014, Finland
[c] Finnish Meteorological Institute, FI-00101 Helsinki, Finland

ARTICLE INFO

Article history:
Received 10 February 2016
Received in revised form
5 June 2016
Accepted 6 June 2016
Available online 9 June 2016

Keywords:
Light scattering
Rough ice crystals
Cirrus
DDA

ABSTRACT

The effect of ice crystal surface roughness on light scattering by ice crystals which are large compared to the wavelength was studied, in particular changes to the 2D scattering patterns, azimuthally averaged phase functions, degree of linear polarisation patterns and asymmetry parameters for a range of orientations and roughness scales. It was found that roughness has an effect on light scattering by hexagonal prisms, particularly when the roughness features are of comparable size to the wavelength. The roughness model that has the most effect on light scattering takes account of more than one roughness scale.

Rough geometry was implemented by a Gaussian roughness method that took roughness parameters derived from sand grains, which have been reported to be suitable proxies for rough ice crystals. Light scattering data for these geometries was computed using the ADDA discrete dipole approximation method.

1. Introduction

A hospitable climate is vital to our long-term survival, and so the study of it is very important. The conclusion that the climate is being changed rapidly by human activity [1] makes this study even more urgent. Future climate behaviour can be predicted by the use of climate models, which work well for predicting the global climate decades into the future; however, there are necessarily assumptions and simplifications involved that limit the accuracy of these methods. One of the largest sources of error within these models is the interaction of clouds with radiation [2]. It is known that clouds have a large effect [3–5], but their interaction with climate is complex; their overall effect depends on the balance between reflected, absorbed and transmitted shortwave (from the sun) and longwave (from the surface and lower clouds) radiation [6].

Although cirrus clouds typically allow most incident sunlight to pass through them, their extent makes them a major factor for the climate; cirrus coverage is typically 30% [7]; over the tropics it is typically 70% [8]. It has been shown that smooth hexagonal prisms with size parameter $X = 2\pi r/\lambda$ (where r is the characteristic length of the particle and λ is the wavelength of the incident light) of at least 100 exhibit the 22° halo [9]. This minimum size is a consequence of diffraction – if the ice crystals are too small then diffraction effects become stronger and the halo peak is spread out. The halo is quite rarely seen with real cirrus clouds [9] potentially due to the constituent ice crystals in cirrus having complex geometries [10] and/or displaying

* Corresponding author.
E-mail addresses: ctcollier@gmail.com (C.T. Collier), e.hesse@herts.ac.uk (E. Hesse), l.taylor3@herts.ac.uk (L. Taylor), z.ulanowski@herts.ac.uk (Z. Ulanowski), antti.i.penttila@helsinki.fi (A. Penttilä), timo.nousiainen@fmi.fi (T. Nousiainen).

http://dx.doi.org/10.1016/j.jqsrt.2016.06.007

surface roughness [11,12]; it is the latter which is the focus of this work. Note that it has also been reported in the literature [13] that irregularities in the geometry of hexagonal ice crystals can give rise to scattering properties indicative of surface roughness, such as the smoothing out of the phase function. Roughness of ice crystal surfaces has a large effect on the radiative properties – experimental results [14] show that surface roughness causes more light to be scattered in the backward hemisphere, lowering the asymmetry parameter. Understanding the extent to which roughness causes this effect is important for better characterising ice crystals in clouds.

Since direct imaging of particles in clouds is not accurate enough to characterise particle roughness [15], previous work on characterising ice crystal roughness has been done in the laboratory. Examples include using ice crystal analogues [14], studying ice growth under a scanning electron microscope [16–18], ice crystal creation using cloud chambers [19] and retrieval of roughness parameters from observations of dust [20]. Geometric optics has been used to simulate light scattering by particles with large-scale irregularity [21], in which deviations from perfect crystal geometry are modelled by randomly tilted facets. This method has also been applied to model surface roughness. However, as tilted facets are not usable within exact light scattering models, the simulation is not exactly repeatable and it does not account for more complex ray paths, as the tilting only occurs when the ray hits (i.e. there are no closed surfaces). Also, geometric optics is an invalid approximation at smaller size parameters and for wavelength-scale surface roughness features on larger size parameter objects. Improved roughness modelling has already been done, using the Improved Geometric Optics (for large size parameters) and Pseudospectral Time-Domain (for small size parameters) methods; however the parameters used there were not derived from physical

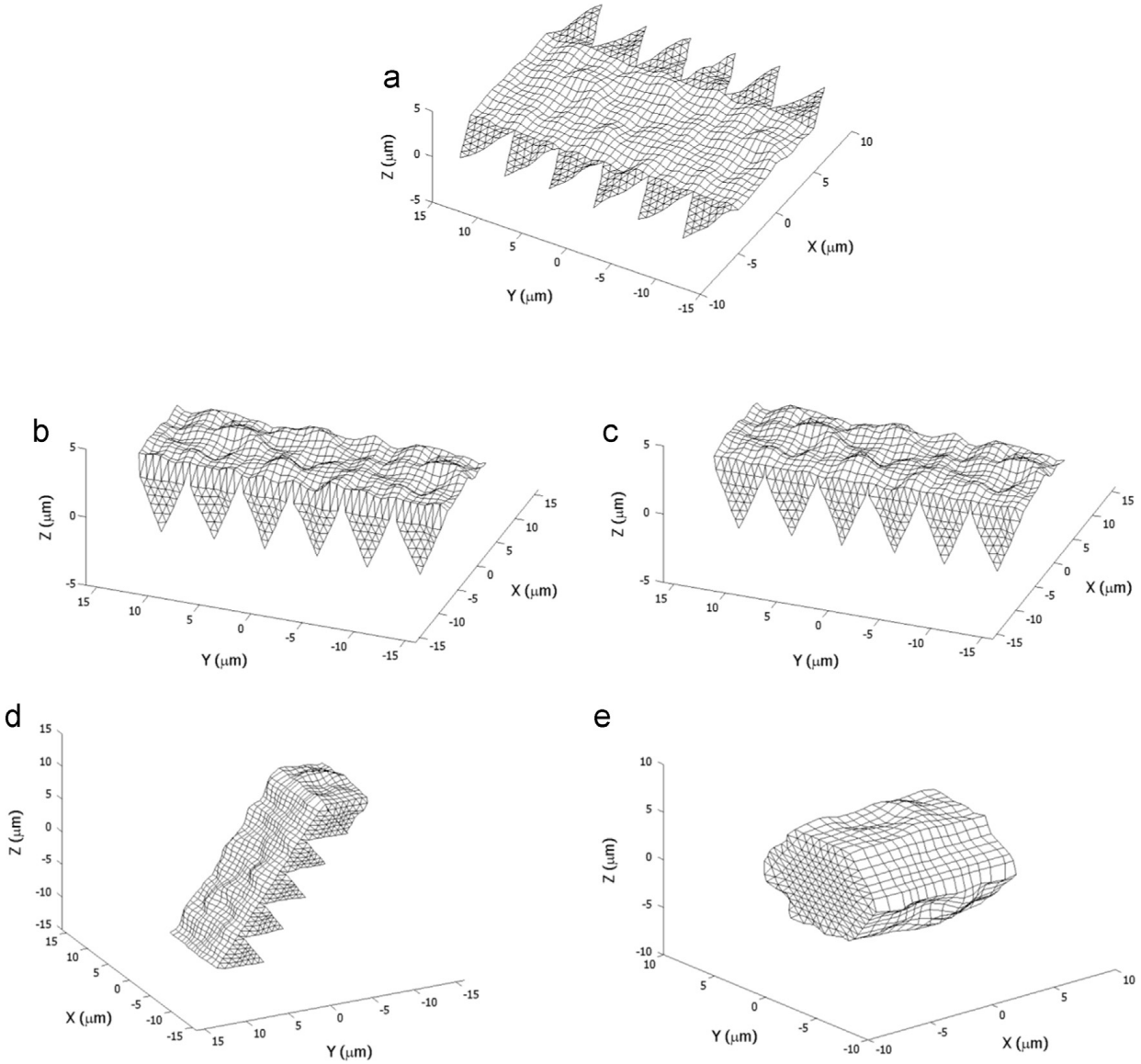

Fig. 1. (a) The crystal in its unfolded state. The triangles will be folded down, and then the rectangle will be folded to create the prism facets. (b) The crystal with its triangular parent facets folded down. Subfacet stretching can be seen at the edge where the rotation has taken place. (c) The crystal with its triangular parent facets folded down and corrected edge subfacets. (d) The crystal after one subfacet rotation is complete. (e) The crystal with all the sections folded into position and the unconnected edges joined together. (a)–(e) All have a correlation length of 1 μm and a standard deviation of 0.3 μm.

measurements and do not account for the possibility of multiple roughness scales [22].

In this work, Gaussian rough ice crystal models are created using parameters taken from analysis of sand grain surfaces, which have been found to have a similar effect on light scattering as ice crystal roughness [23]. Simulations were run using these roughened crystals on the Discrete Dipole Approximation (DDA) light scattering software ADDA [24].

2. Gaussian rough ice crystals

A Gaussian random crystal (Fig. 1e) is constructed from a Gaussian random surface (Fig. 1a). This is a surface for which the height varies as a function of the lateral x and y dimension; the height of each point is calculated as a Fourier series given in Eq. (1). Gaussian roughness has previously been used to describe roughness for cylinders [25], spheres [26], spheroids [27] and surfaces [28]. The fundamental parameters in Gaussian roughness are a correlation length, which describes the dominant spatial frequencies, and a standard deviation, which describes the variation in height.

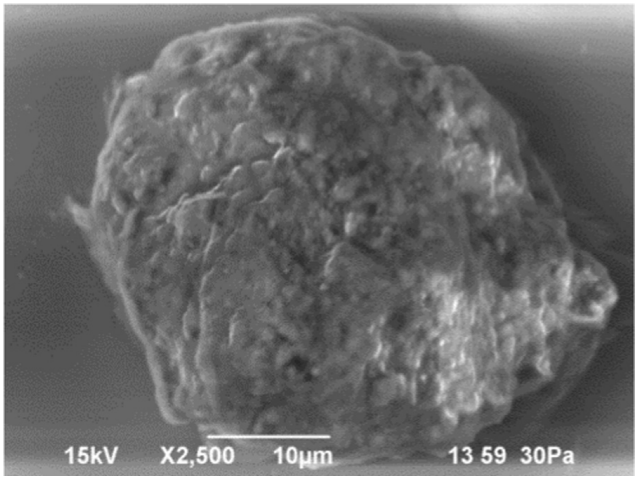

Fig. 2. An SEM scan of one of the analysed sand grains from Mitribah, Kuwait. It has a diameter of approximately 40 μm.

2.1. Gaussian random surface

A method was devised for creating input files describing the geometry of roughened hexagonal prisms for use with computational light scattering models.

The implementation of this involved the application of a Gaussian random surface creation method, adapted from previous work by Muinonen and Saarinen [25], which uses a 2D Fourier series technique, taking as its parameters the correlation length (l) and standard deviation of the height (σ) to create roughness across a previously flat surface. These two parameters can be chosen by the user; in this work they are determined from analysis of a sand grain. Theoretically, the height z of a point with coordinates (x,y) on a rough surface is given by the following:

$$z(x,y)=\sum_{p=-\infty}^{\infty}\sum_{q=-\infty}^{\infty} z_{pq}\, e^{i(pKx+qKy)} \tag{1}$$

Where $K=\pi/L$ is the wavenumber; L is half a period in x and y, and must be chosen to be large compared to the correlation length. z_{pq} are independent Gaussian random complex numbers, with zero means and variances:

$$Var(Re(z_{pq}))=\frac{1}{8}(1+\delta_{p0}+\delta_{q0}+5\delta_{p0}\delta_{q0})c_{pq}\sigma^2 \tag{2a}$$

$$Var(Im(z_{pq}))=\frac{1}{8}(1+\delta_{p0}+\delta_{q0}-3\delta_{p0}\delta_{q0})c_{pq}\sigma^2 \tag{2b}$$

The same z_{pq} values are used for all x,y. The c_{pq} are cosine series coefficients:

$$c_{pq}=\left[(2-\delta_{p0})\sqrt{\frac{\pi}{2}}\frac{l}{L}e^{-\left(\frac{1}{2}p^2\pi^2\frac{l^2}{L^2}\right)}\right]\left[(2-\delta_{q0})\sqrt{\frac{\pi}{2}}\frac{l}{L}e^{-\left(\frac{1}{2}q^2\pi^2\frac{l^2}{L^2}\right)}\right] \tag{3}$$

Practicality requires that the summations in Eq. (1) must be performed over finite ranges. As such, the correlation statistics of the surface must be taken into account to calculate suitable limits for p and q. To do this, we consider the correlation function representing a Gaussian random surface:

$$C(\zeta,\eta)=e^{-\left(\frac{\zeta^2+\eta^2}{2l^2}\right)} \tag{4}$$

Where ζ is the difference between the x positions of two points and η is the difference between the y positions of the same two points. The two dimensional Fourier

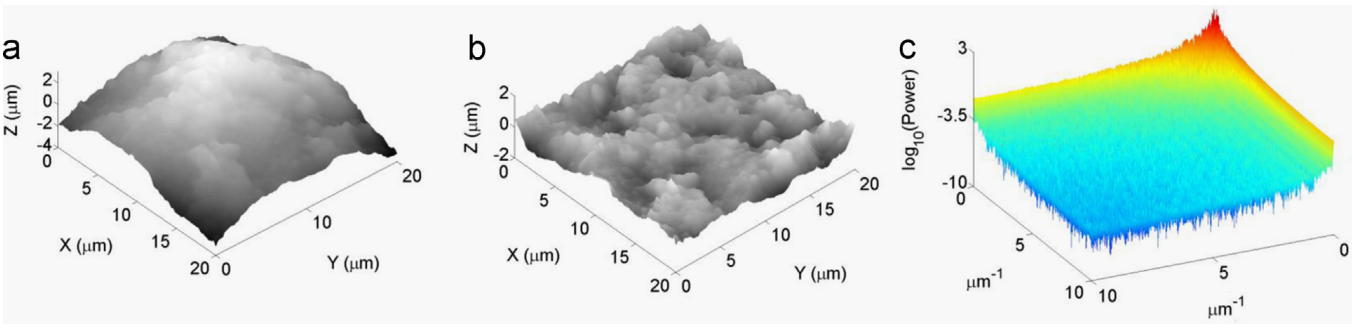

Fig. 3. (a) The surface before it has had the overall profile removed. (b) The surface after the overall profile has been removed. (c) Power spectrum of the surface in (b).

expansion of the surface correlation function is:

$$C(\zeta,\eta) = \sum_{p=-0}^{\infty}\sum_{q=-0}^{\infty} c_{pq}\cos pK\zeta\cos qK\eta \quad (5)$$

Evaluating Eqs. (4) and (5) for $\zeta=0$, $\eta=0$, we find the limits of the summations by seeking the p and q such that the difference between the two equations is less than 10^{-6}, that is:

$$1-\sum_{p=-p_0}^{p_{max}}\sum_{q=-q_0}^{q_{max}} c_{pq} < 1\times 10^{-6} \quad (6)$$

Where q_{max} must be less than or equal to p_{max}. Once p_{max} and q_{max} have been found, they can be substituted for the infinities in Eq. (1), which can be used to create the Gaussian random surface.

2.2. Crystal geometry creation

The process of creating a Gaussian random surface is shown in Fig. 1. The Gaussian random hexagonal prism is created by generating a roughened surface that can be folded to form a crystal. This is made up of six adjacent rectangular parent facets which form the prismatic facets and twelve equilateral triangular parent facets – two per prism facet – which eventually form the basal facets (Fig. 1a). After the roughening has been completed quadrilateral subfacets are generated.

Each triangular parent facet is folded along the edge between it and its adjoining prism facet, leaving them pointing down (Fig. 1b). It can be seen that subfacet stretching occurs where the triangular parents join the prism facets because the edge itself has not been rotated; to correct for this, the edge is rotated around its position in the unroughened state by 45° (Fig. 1c). Afterwards, the individual prism facets are rotated in turn (Fig. 1d).

Once the rotations are complete, gaps left due to the roughening procedure are joined together. The first and last prism facets are connected using an interpolation method. Likewise, interpolation is used to join the triangles at either end of the prism facets together to create the basal facets (Fig. 1e).

2.3. Obtaining Gaussian random surface parameters from sand grain microscopy

To obtain suitable parameters for roughness generation, analysis of the surface of an ice crystal in a cirrus cloud would be ideal. However, in situ cloud imaging methods are not able to provide the required optical resolution, and so a suitable proxy is needed. A sensitivity study using arbitrarily chosen roughness parameters would be the best approach; however the computational demands are prohibitive. An alternative technique is to derive roughness parameters from a physical model that shows similar levels of roughness to that of ice crystals;

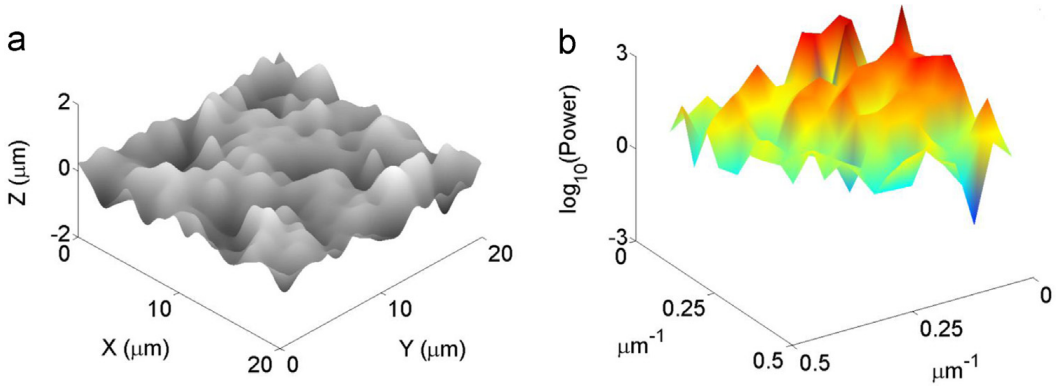

Fig. 4. (a) Simulated surface obtained after removing wavenumbers larger than 0.47 μm^{-1} from the Fourier transform of the surface in Fig. 3b and transforming back into spatial coordinates. (b) Power spectrum of the surface in (a).

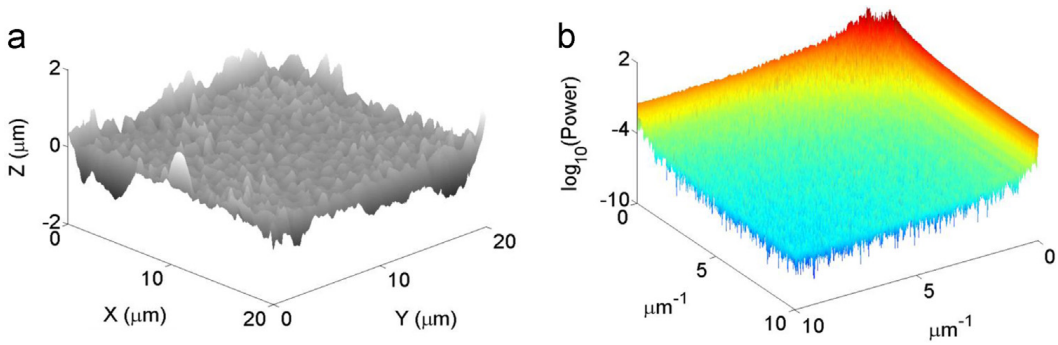

Fig. 5. (a) Simulated surface obtained after removing wavenumbers smaller than 0.47 μm^{-1} from the Fourier transform of the surface in Fig. 3b and transforming back into spatial coordinates. (b) Power spectrum of the surface in (a).

this is the method used in this study, which takes sand grains as the physical model. These were chosen because statistical measures of the texture of 2D scattering patterns taken by the SID-3 (Small Ice Detector) probe are consistent between sand grains and ice crystals from cirrus clouds [23].

Samples (e.g. Fig. 2) were prepared for detailed microscopy work using the Park Systems XE-100 Atomic Force Microscope (AFM) at Cardiff University. For this, suitably sized sand grains from a surface sample collected in Mitribah, Kuwait were selected using optical microscopy and mounted on a substrate. They needed to be less than approximately 50 μm in diameter, preferably close to this bound to get as large a scan area as possible (measured grains varied from 40 μm to 54 μm). Ulanowski et al. [23] showed that sand grains of diameter 41 μm and 47 μm display comparable scattering pattern-derived roughness to that of naturally occurring cirrus ice

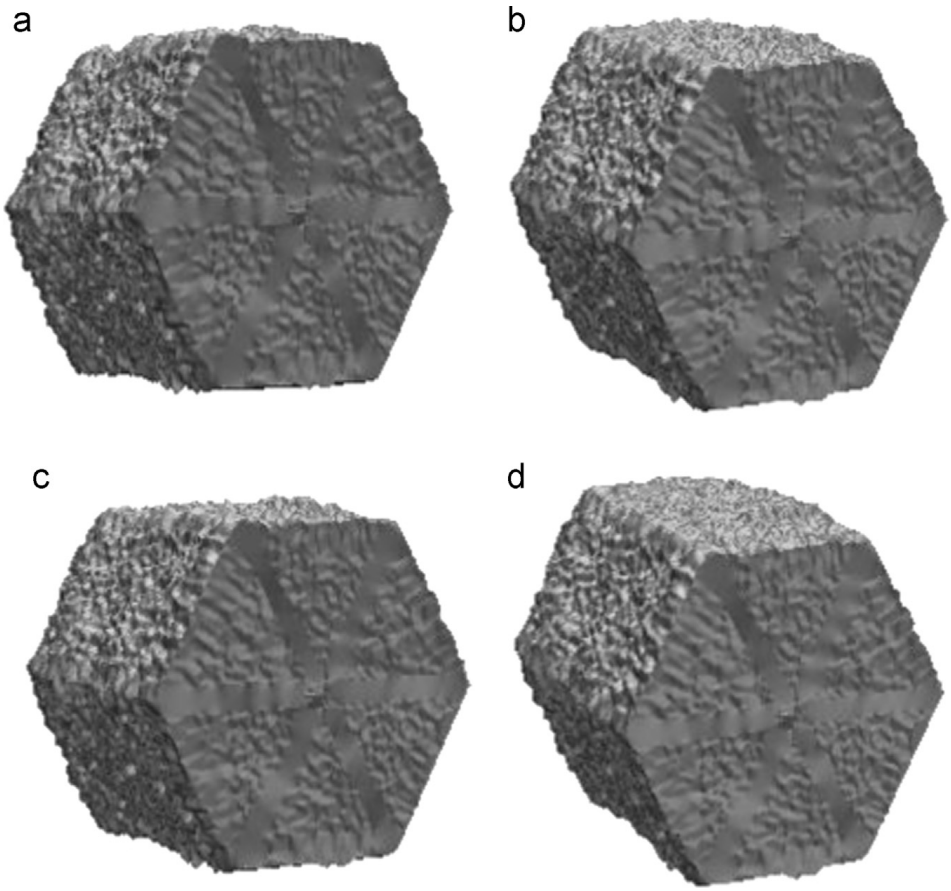

Fig. 6. The crystal orientations used in this work with the incident beam propagating out of the page, shown for a two-scale rough crystal. The stripes on the basal facets are a result of the interpolation used in the crystal creation procedure. All beam rotations are at 30° in the x–y plane; (a) has no other rotation, (b) is rotated 10° in the y–z plane, (c) is rotated 20° in the y–z plane and (d) is rotated 30° in the y–z plane. The coordinate system used can be seen in Fig. 7.

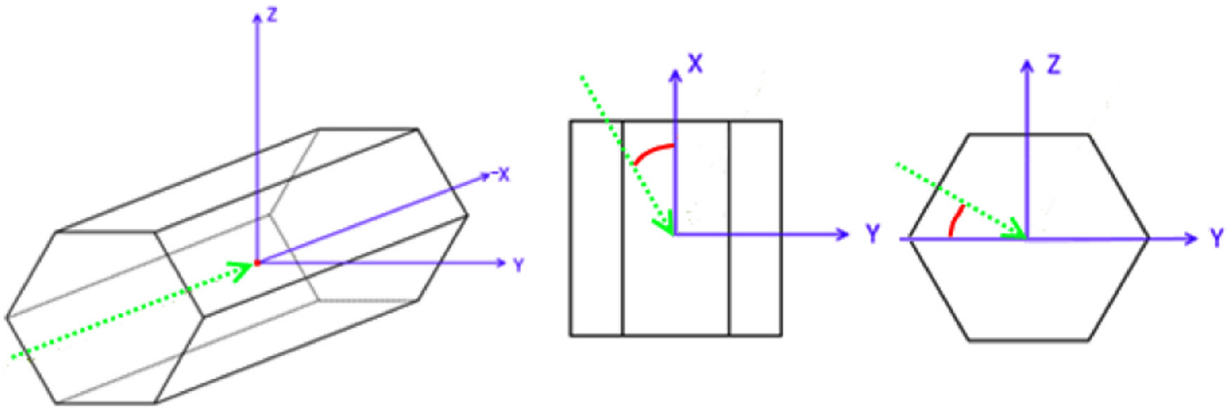

Fig. 7. Left: coordinate system of the incidence direction, which propagates in the negative x direction. Middle: the first rotation of the beam, which is around the z-axis. Right: the second rotation of the beam, which is around the x-axis.

crystals; similarly sized grains were chosen for this work because it is not known if this conclusion holds true at other sizes. This allowed for an effective scanning area of 20 μm × 20 μm, as the AFM probe is unable to scan areas that excessively deviate from being perpendicular to it.

To support the AFM work, images were taken of the topography of the sample grains using a Scanning Electron Microscope (SEM).

Data gained from the AFM work on sand grains was analysed to derive the correlation length and standard deviation values. Scanning artefacts were averaged out and the surface had a 2D polynomial subtracted from it to remove the grain's overall long-range profile and leave just the roughness (Fig. 3b). The 2D polynomial was calculated by performing a least square fit of the polynomial-generated surface to the measured surface; the order was increased until the roughness of the points of the resultant surface visually appeared to have no variation as a function of distance from the centre.

The resulting surface (Fig. 3b) was analysed to obtain correlation length and standard deviation values for the one-scale surface (as described in the next paragraph), before being Fourier transformed. A wavenumber cut-off was isotropically applied to split the power spectrum into two parts; one containing only the high spatial frequencies and one containing only the low spatial frequencies. Both of these were then transformed back into spatial coordinates to create two new surfaces. The one containing only low spatial frequencies was visually compared with the surface in Fig. 3b to check how it fit the latter's large scale features. The cut-off was varied until it satisfied this check. The resultant surfaces are shown in Figs. 4a and 5a with corresponding power spectra in Figs. 4b and 5b.

These surfaces were analysed to obtain values for the standard deviation and correlation length. Correlation lengths for both surfaces were retrieved by calculating autocorrelation and using a rearranged form of Eq. (4). The surface created using only large wavenumbers shows anomalously deviating z-values at the edges (a consequence of applying an isotropic cropping and therefore disregarding the effects of the finite sample size in the power spectrum), as can be seen in Fig. 5a. These were cropped out before the surface was used to derive these parameters. The same procedure was used to obtain correlation length and standard deviation for one-scale roughness by applying it to the surface containing all spatial frequencies (Fig. 3b). The correlation lengths and standard deviations derived from the surfaces in Fig. 3b, Figs. 4a and 5a were substituted into Eqs. (4) and (2), respectively. This allowed for the creation of a one-scale and a two-scale rough surface, both similar to that shown in Fig. 1a, to be created through using Eq. (1). By folding the resulting surface one is able to create a rough crystal; to obtain the two-scale rough crystal, the two rough surfaces are superimposed before folding. In effect, this method allows for the creation of rough particles with roughness properties derived from actual rough particles.

3. DDA results

Computations were carried out using the ADDA [24] implementation of the discrete dipole approximation light scattering method to find the light intensity and degree of linear polarisation (DLP, defined as $-P_{12}/P_{11}$, where these are both elements of the 4×4 scattering matrix) as a function of scattering angle and azimuthal angle for smooth, one-scale rough and two-scale rough hexagonal columns with an aspect ratio of 1 at a wavelength of 532 nm and refractive index $n=1.31+0.0\mathrm{i}$. This aspect ratio was chosen since our main interest is in the effect of roughness, we note that this is in line with other studies, e.g. [13,22,29]. Four different directions of the incident beam were considered (Fig. 6) for a fixed crystal orientation (Fig. 7).

Using this model, the incident beam originally propagates along the x-axis; Fig. 7 shows the rotations performed to achieve these beam orientations; all make an angle of 30° with the x axis in the x–y plane, and make a final rotation of 0°, 10°, 20° or 30° around the x axis in the y–z plane projection. Four crystal size parameters were considered; 20, 40, 60 and 100, with roughness being scaled proportionately with size.

The number of dipoles in the DDA presentation of the geometry was chosen so that it can present the particle roughness with reasonable accuracy, and that the dipole size compared to the wavelength is small enough. For the latter requirement, the 'rule-of-thumb' for ADDA [24] is used, requiring that $d\leq 10/(\lambda|n|)$, with d being the dipole size. We selected $d=0.0406107$ for the largest size, so that dipoles-per-wavelength is 13.3, while smaller sizes are achieved by decreasing the dipole size.

There are no analytical methods to estimate the accuracy of our DDA results, but we can check how well they satisfy the reciprocity relation. Following the method in Schmidt et al. [30], we report the 90° relative reciprocity error to be 0.037% and 0.045% for the largest smooth geometry with VV- and HH-polarizations, and 0.0017% and 0.093% for the largest geometry with two-scale roughness and VV- or HH-polarizations. The relative reciprocity errors for these largest geometries are very small, and are expected to stay as small or get smaller with smaller geometries.

Table 1
Ratios of correlation length and standard deviation to the wavelength of the incident beam for one-scale and two-scale roughness at size parameters: 20, 40, 60 and 100. For these sizes, the number of dipoles used per wavelength was 66.5, 33.25, 22.17 and 13.3 respectively. The wavelength is 532 nm.

	One-scale roughness		Two-scale roughness				
			1st roughness scale		2nd roughness scale		
X	l/λ	σ/λ	l/λ	σ/λ	l/λ	σ/λ	Total σ/λ
20	0.31	0.06	0.68	0.08	0.08	0.04	0.12
40	0.63	0.13	1.35	0.16	0.16	0.09	0.25
60	0.94	0.19	2.03	0.24	0.24	0.13	0.37
100	1.57	0.31	3.38	0.41	0.41	0.22	0.63

Crystals with the dust-derived standard deviation and correlation length are created at a size parameter of 32.5. For one-scale roughness, correlation length 0.5 μm and standard deviation 0.1 μm are used; for two-scale roughness, the Gaussian random surfaces from the large scale mode (correlation length 1.08 μm and standard deviation 0.13 μm) and from the small scale mode (correlation length 0.13 μm and standard deviation 0.07 μm) were superimposed. The coordinates that make up this crystal are then scaled linearly to derive the coordinates of crystals of size parameter 20, 40, 60 and 100.

Due to the scaling, the roughness parameter to wavelength ratios increase linearly with size parameter, as can be seen in Table 1. As these ratio values increase, the effect of the roughness on light scattering also increases, as can be seen for azimuthally averaged phase functions (which appear in Fig. 8 and which, for brevity, we will call phase functions from here on), asymmetry parameters (Table 2), 2D scattering patterns (Figs. 11a and 12a) and degree of linear polarisation (Figs. 11–13). The Fraunhofer criterion [38] for effectively smooth surfaces requires $\sigma/\lambda < 1/(32\cos(\alpha))$ (corresponding to a phase difference of $\pi/8$

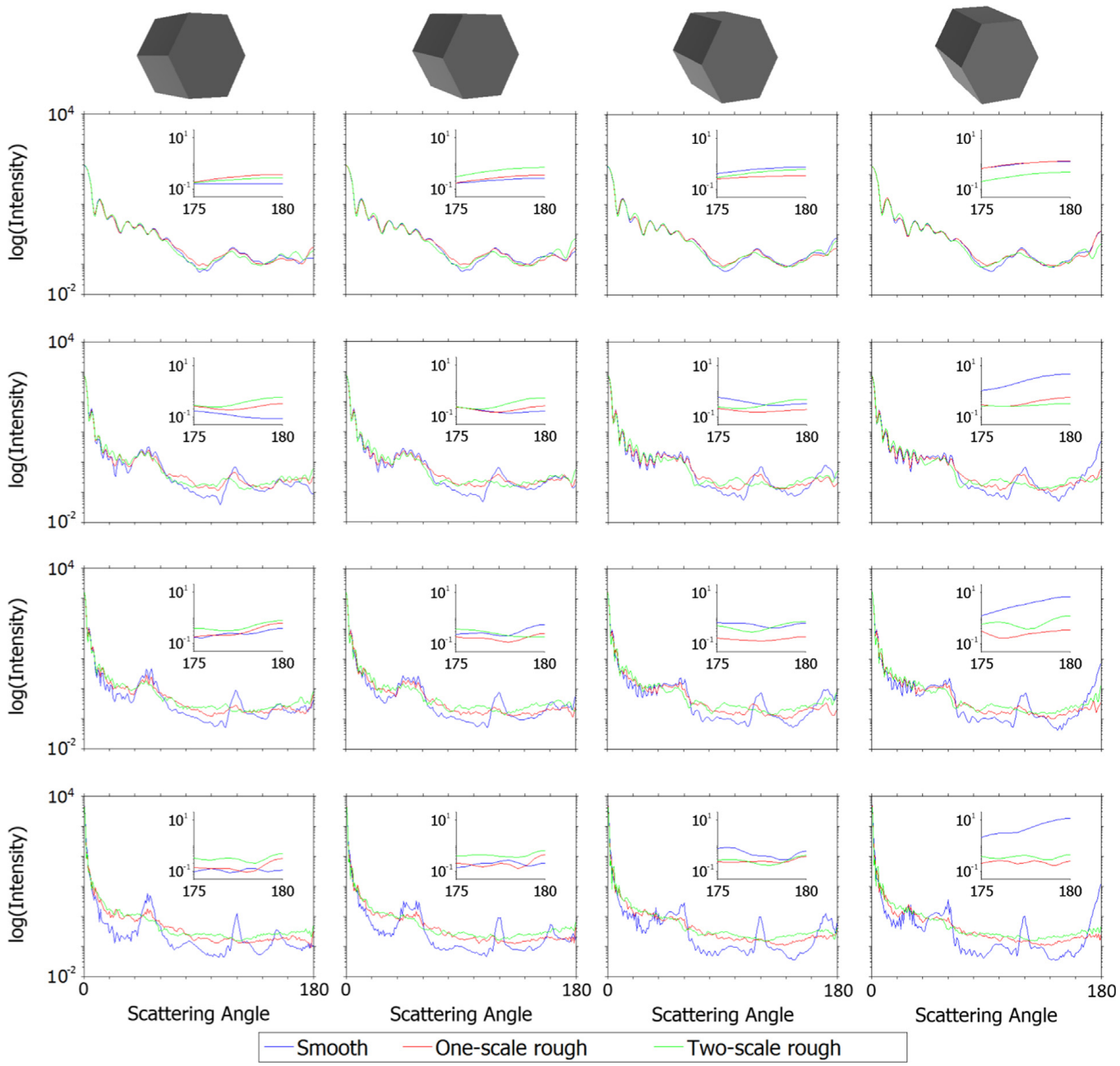

Fig. 8. Phase functions of smooth, one-scale rough and two-scale rough crystals. Different columns in the diagram represent different beam orientations – from left to right, the angle in the *y*–*z* plane increases from 0° to 30° in steps of 10°. Different rows represent different size parameters – from top to bottom, the size parameter is 20, 40, 60 and 100. Schematics above the top row show the crystal orientations where the incident beam propagates out of the page. Insets within the graphs show close-ups of the backscatter – from 175° to 180°. The same colours are used for the same roughness scales throughout the rest of this work. (For interpretation of the references to color in this figure legend, the reader is referred to the web version of this article.)

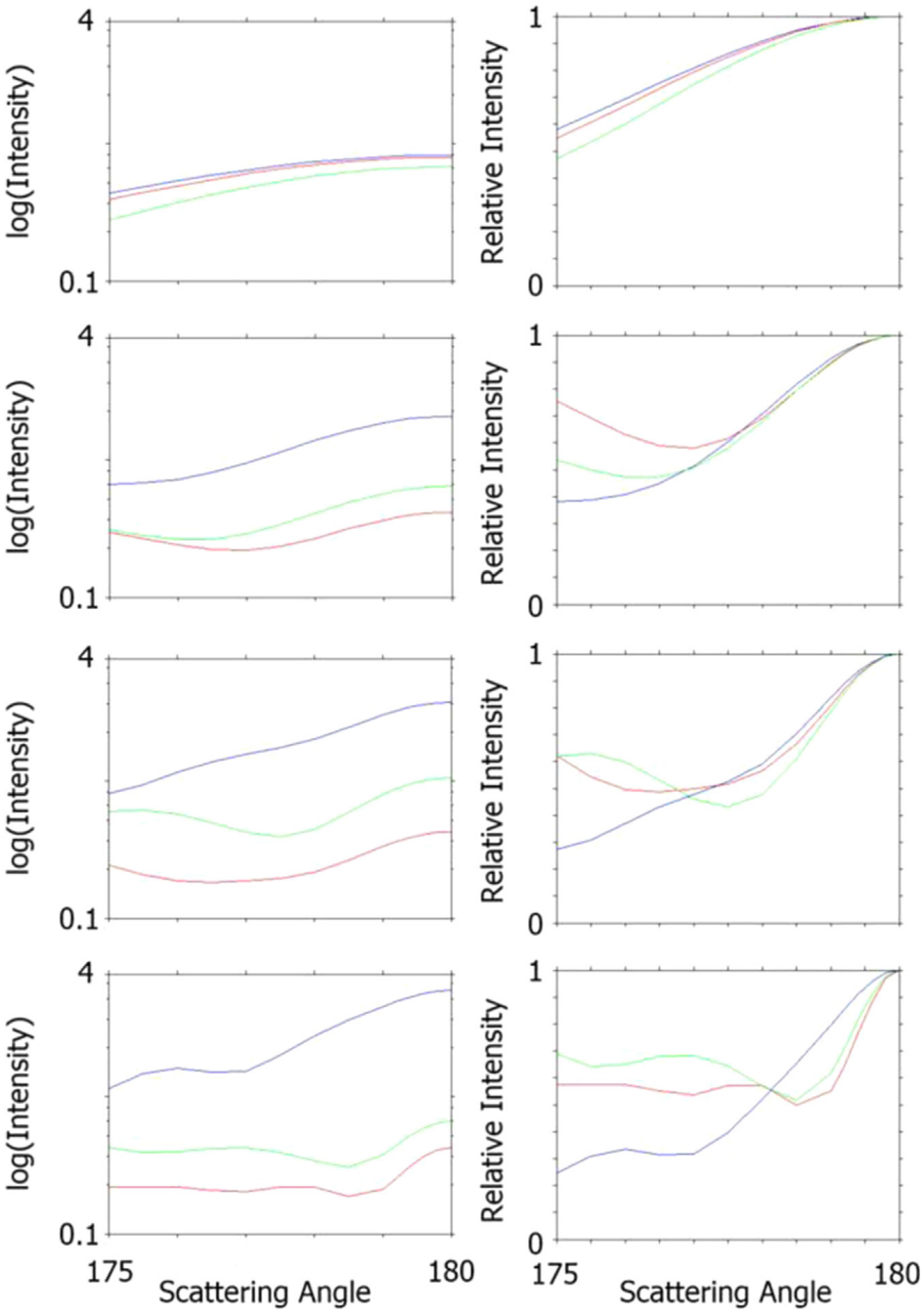

Fig. 9. 175°–180° phase functions for smooth (blue), one-scale rough (red) and two-scale rough (green) crystals averaged over all four orientations (left column) with corresponding "normalised-to-one" diagrams (right column). From top to bottom, the rows represent size parameters of 20, 40, 60 and 100. (For interpretation of the references to color in this figure legend, the reader is referred to the web version of this article.)

between two rays scattered at different points on the surface), where alpha is the angle between the incident wave vector and the surface normal of the corresponding smooth surface. For direct forward and backscattering the criterion has a value 0.031, which we note is about half the value for σ/λ for one scale roughness at size parameter 20, where the differences in scattering properties compared to the smooth crystal are found to be very small already.

Scattering from the largest size parameter smooth prism can be readily interpreted from a geometric/physical optics perspective, identifying peaks in the phase function as being caused by reflection/refraction events with local spreading caused by diffraction. We use the geometric optics terminology here as a means for interpreting the changes of scattering properties as the crystal is scaled. Light passing very close to the crystal is also scattered and so geometric optics (GO) ray tracing is usually combined with diffraction at the projected cross section (e.g. [21]), which we will refer to as external diffraction. If external diffraction is computed as diffraction at the incidence facing facets (a generalisation of Babinet's principle) and diffraction of rays or beams leaving the crystal is considered, scattering can be resolved azimuthally (e.g. [31,32]).

For the orientation with a rotation of 0° in the y–z plane, peaks can be seen for the smooth crystal at

scattering angles of 0° (transmission through the two parallel basal facets – known as δ-function transmission in GO [33] – superposed with the external diffraction peak), 51° (caused by reflection off the prism facets), 80° (due to light being transmitted through the two prism facets and passing through the two opposite them) and 120° (Figs. 11 and 12). This latter peak is mainly due to light reflecting off the basal facet and light passing through the basal facet facing the beam, internally reflecting off the other basal facet and exiting back through the first basal facet. There is also a peak at 151° due to at least two internal reflections either in one plane or including a rotation of reference plane (skew rays).

As the incident beam is rotated in the *x*–*y* plane, the prism reflection peak is split; at a rotation of 10°, peaks can be seen at scattering angles of 10°, 48°, 55°, 120° and 160°; at a rotation of 20°, peaks appear at scattering angles of 20°, 38°, 58°, 120° and 170°; finally, at a rotation of 30°, peaks are visible at scattering angles of 28°, 60°, 120° and 180° (see 4th row of Fig. 8, blue line). It is important to note that due to crystal symmetry more complex ray interactions can produce the same exit angle (e.g. external reflection and refraction into the crystal followed by internal reflection followed by refraction out of the crystal).

While such analysis is possible for smooth crystals, it becomes far more difficult when surface roughness is introduced due to the large number of sub-beams created at external incidence. Looking at the 2D scattering patterns in Figs. 11 and 12, we see that roughness reduces the prominent features seen for the smooth crystal into speckle. This blurring and spreading leads to the smoothing out of the peaks and troughs in the phase function (Fig. 8). For size parameter 100 the deviation in the phase function from the smooth case is substantial after a scattering angle of 10°. This can be seen also in the 2D scattering patterns by the external diffraction peak at the centre being the only remaining recognisable feature. Note that scattering in the direct forward direction is notably reduced due to roughness affecting the transmission peak, in particular for two-scale roughness (Table 3). Decreasing the size parameter reduces the influence roughness has on the 2D scattering patterns, with relatively little change occurring for the smallest size parameter (see Figs. 8 and 11). It can also be seen that two-scale roughness increases the number of speckle spots compared to one-scale, and that these spots decrease in size with increasing size parameter, as discussed in [34]. The scaling of roughness with size parameter means that smaller size parameters have roughness features which are much smaller than the wavelength (Table 1) which in turn means that light scattering is only weakly sensitive to it. If the roughness had not been scaled, it is possible that there would have existed surface roughness with size comparable to the wavelength. In such circumstances one would expect to observe a noticeable deviation from the smooth case in the associated scattering patterns and phase functions.

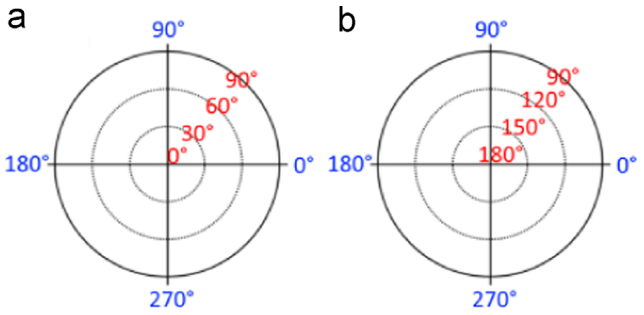

Fig. 10. Diagrams showing the azimuthal (blue) and scattering (red) angles for (a) forward 2D scattering patterns (Fig. 11) and backward 2D scattering patterns (Fig. 12). (For interpretation of the references to color in this figure legend, the reader is referred to the web version of this article.)

The 2D scattering patterns in Fig. 12 correspond to scattering in the backward hemisphere, where the effects of surface roughness are even more pronounced. For the largest size parameter, one can easily see that the bright spot at 120°, due to external reflection and some higher order events, is entirely removed as the reflection becomes diffuse and the transmission paths altered, leaving only speckle. Furthermore, we notice that surface roughness has less effect on the smallest size parameter, as for forward scattering.

In summary we see that deviations from the smooth case in the 2D scattering patterns and phase functions increase with size, and that forward scattering is less sensitive to

Table 2
Asymmetry parameters calculated for the crystals for which light scattering was modelled. The orientation angles refer to the rotations explained in Fig. 7.

Orientation	Smooth g_s	One-scale g_1	$\frac{(g_1-g_s)}{g_s}$[%]	Two-scale g_2	$\frac{(g_2-g_s)}{g_s}$[%]	Smooth g_s	One-scale g_1	$\frac{(g_1-g_s)}{g_s}$[%]	Two-scale g_2	$\frac{(g_2-g_s)}{g_s}$[%]
	Size parameter 20					Size parameter 40				
30°,0°	0.725	0.724	−0.207	0.744	2.607	0.710	0.694	−2.295	0.716	0.845
30°,10°	0.722	0.719	−0.471	0.740	2.535	0.700	0.689	−1.628	0.714	1.956
30°,20°	0.720	0.720	0.014	0.736	2.166	0.694	0.698	0.475	0.716	3.140
30°,30°	0.720	0.718	−0.292	0.734	2.043	0.698	0.705	1.046	0.723	3.583
Mean	0.722	0.720	−0.236	0.739	2.342	0.701	0.696	−0.628	0.717	2.354
	Size parameter 60					Size parameter 100				
30°,0°	0.711	0.722	1.434	0.702	−1.251	0.764	0.758	−0.785	0.726	−5.012
30°,10°	0.727	0.739	1.568	0.700	−3.713	0.761	0.758	−0.368	0.713	−6.280
30°,20°	0.725	0.738	1.779	0.710	−2.137	0.771	0.768	−0.389	0.724	−6.111
30°,30°	0.724	0.746	2.996	0.722	−0.373	0.766	0.767	0.170	0.729	−4.856
Mean	0.722	0.736	1.952	0.708	−1.883	0.766	0.763	−0.340	0.723	−5.577

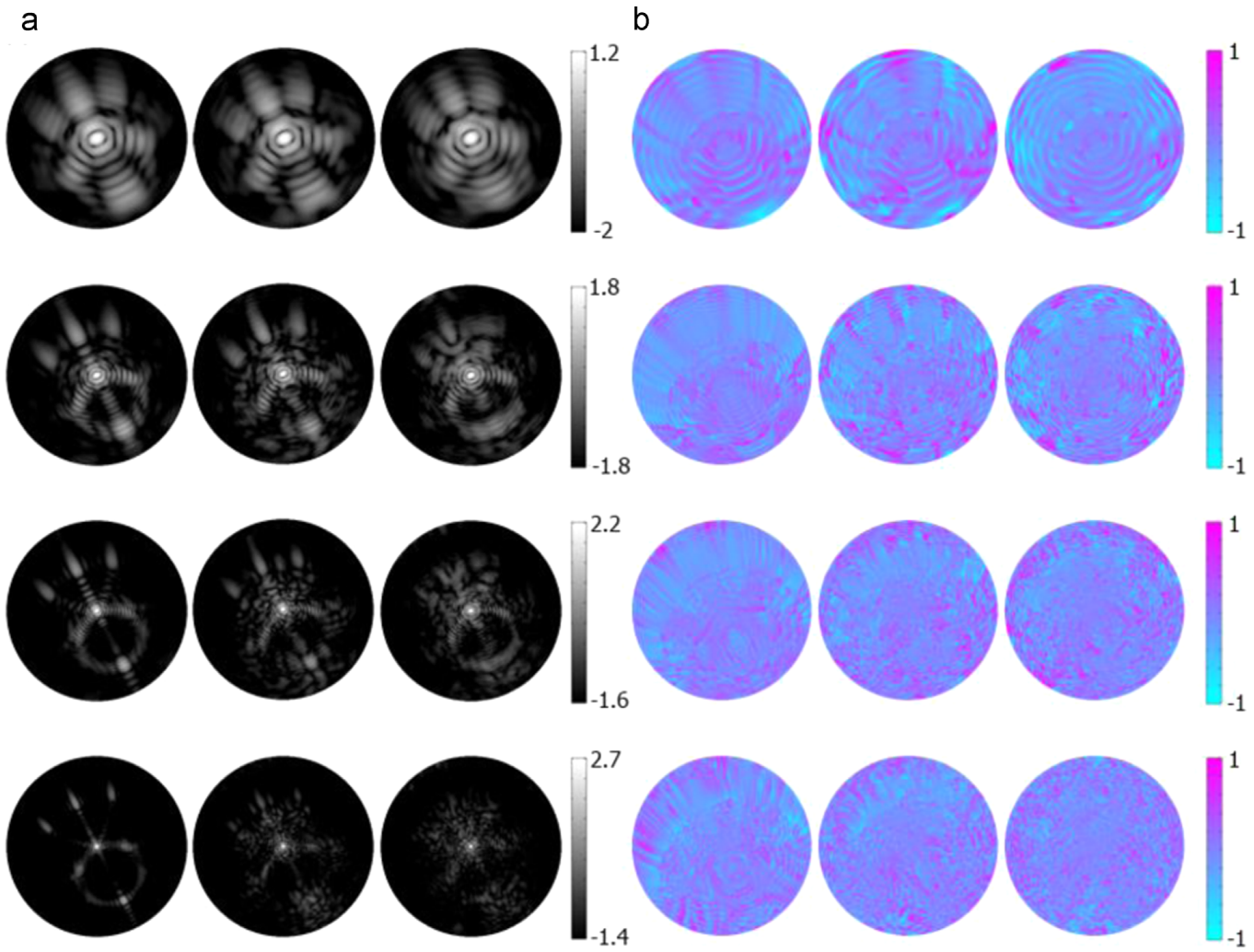

Fig. 11. Logarithmically scaled forward hemisphere 2D scattering patterns (a) and forward hemisphere degree of linear polarisation images (b) for the crystal shown in the inset of the 4th column of Fig. 8. Different rows represent different crystal size parameters; from top to bottom, they represent size parameters of 20, 40, 60 and 100. Different columns represent different roughnesses; from left to right they represent the smooth, one-scale rough and two-scale rough cases. The azimuthal (blue) and scattering (red) angles can be seen in Fig. 10(a). Since brightness increases with crystal size parameter, grey-scale ranges for the scattering patterns in (a) were varied to best show the features at each size parameter. (For interpretation of the references to color in this figure legend, the reader is referred to the web version of this article.)

surface roughness than back scattering. This is because external diffraction, which has low sensitivity to surface roughness as it depends on the crystal's 3-dimensional contour, strongly contributes to forward scattering. Furthermore, two-scale roughness results in more speckle than one-scale roughness because of the change in σ/λ which leads to considerable phase differences in the reflected light. Note that due to the scaling of roughness with size, σ/λ is greatest at larger size parameters, contributing to more pronounced speckle with increasing crystal size. However, the angular region enclosing the direct backscattering direction needs to be considered separately. For orientations where direct backscattering is strong for the smooth crystal due to retro-reflections at or close to 180° (4th column in Fig. 8) a reduction will be observed due to surface roughness, in a similar way as was discussed for other large angles. This effect is strongest for large size parameters and can be imagined as distortion of the GO ray paths. However, for orientations where direct backscattering is weak for the smooth crystal (first column in Fig. 8) a slight increase with surface roughness is seen, which would be predicted by GO due to suitable ray paths becoming available which could also contribute to coherent backscattering. Fig. 15 shows a 2D scattering pattern over the angular range $175^{\circ} \leq \theta \leq 180^{\circ}$ for the phase function for size parameter 100.

Surface roughness causes the scattered field to have a spatially wider distribution resulting in higher contributions into the direct backscattering direction. We expect there to be an 'optimum range' of roughness parameters which allows diffraction into the backscattering direction with sufficiently high electric field amplitude. The half-height width of the back scattering peak is about 0.6° for size parameter 100 and increases with decreasing crystal size. For size parameter 100 the phase functions between 175° and 180°of the two rough crystals look very similar for all four orientations. The absolute values for double scale roughness (see Figs. 8 and 15) are very slightly higher but the enhancement factor is slightly less than for single scale roughness. The latter is thought to be due to more spread out diffraction which results in smaller irradiance

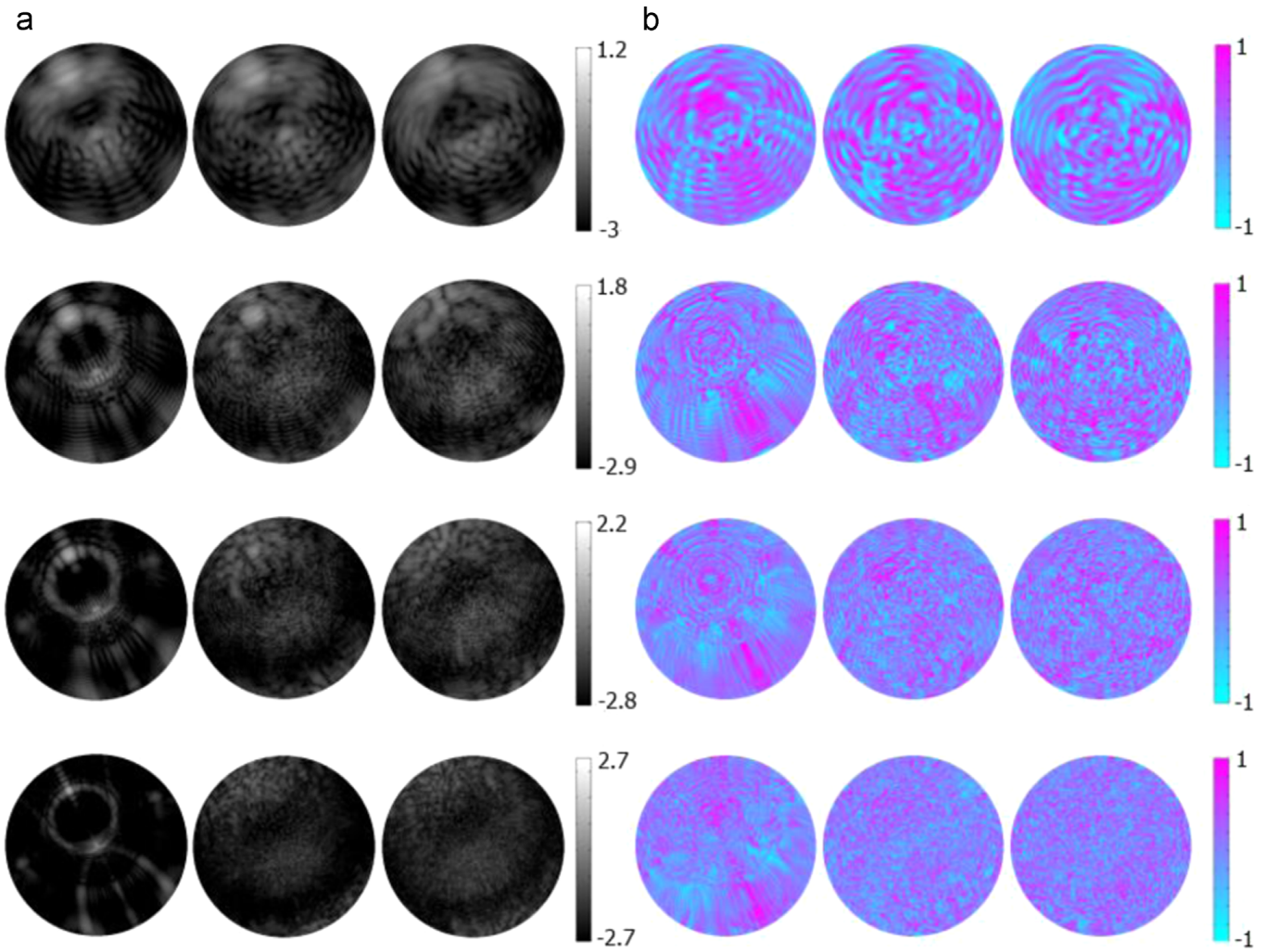

Fig. 12. Same as Fig. 11, but for the backward scattering hemisphere. The azimuthal (blue) and scattering (red) angles can be seen in Fig. 10(b). Notice that the size of the speckle in the 2D scattering patterns decreases with increasing size parameter. (For interpretation of the references to color in this figure legend, the reader is referred to the web version of this article.)

contributions to the backscattering peak. In this work the ratio of intensities at 180° and 175° is taken as a measure for backscattering amplification. For the roughened prisms, values averaged over the four orientations are 1.79 for the one-scale roughness and 1.45 for the two-scale. Note that the maximum possible enhancement factor due to interference is two. The observed peak height is fairly independent of particle size (see insets of Figs. 8 and 9). These observations are similar to results for roughened hexagonal crystals with random orientation in [29] and [35]. The effect of surface roughness on the polarisation of the scattered light for the cases investigated is best discussed through use of the right column of Fig. 13. These plots show clearly that the greatest deviation from the smooth crystal's polarisation occurs in the backscattering. This is no surprise since back-scattering is not only more sensitive to surface roughness, but also contains contributions from near spatial skew rays [36], which also change with surface roughness. For all but the smallest size parameter the magnitude of DLP stays broadly the same (away from backscattering), irrespective of roughness. Table 2 and Fig. 14 show the asymmetry parameters for several fixed orientations (which should not be considered to be representative of a cloud of randomly oriented ice crystals) derived from DDA, including percentages of deviation from the value for the smooth crystal. Crystal symmetry means that results for beam rotations of 0°, 10° and 20° around the *x*-axis apply to rotations around the same axis of 60°, 50° and 40°, respectively. Experimental results on ice analogues with submicron roughness (at size parameters of 395 and 493) [14] and modelling results using Improved Geometric Optics [37] have shown that the asymmetry parameter would be expected to be reduced for rough crystals compared to smooth ones. Modelling results from this study are in agreement with this, with the greatest reduction in the asymmetry parameter being seen at the largest size parameter with two-scale roughness, potentially indicating that the two-scale roughness is more representative of 'real' roughness.

4. Conclusions

2D scattering pattern, phase function, asymmetry parameter and degree of linear polarisation results were

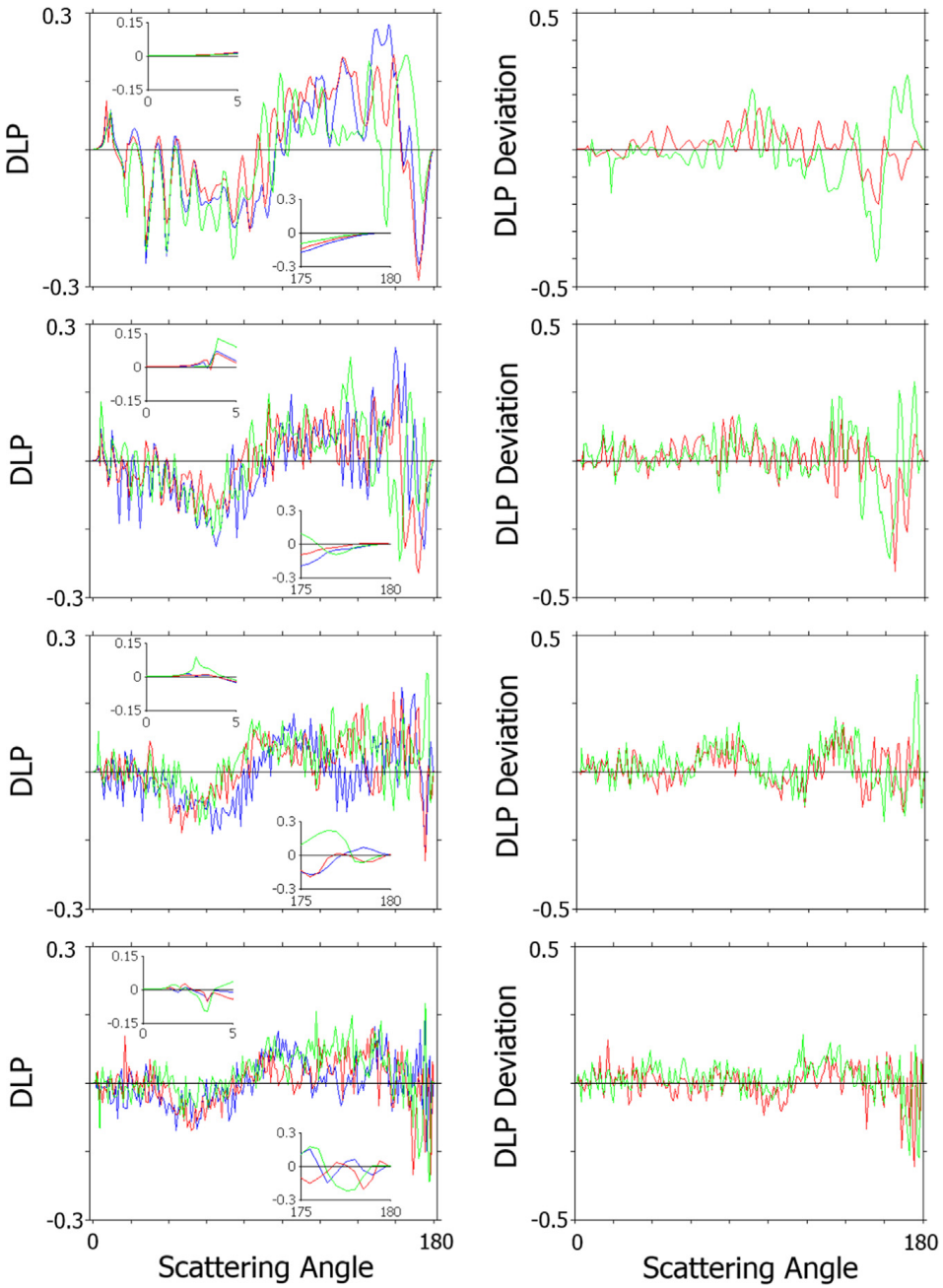

Fig. 13. Left column: azimuthally averaged degree of linear polarisation for smooth (blue), one-scale rough (red) and two-scale rough (green) crystals at the same orientation as in Figs. 11 and 12. The first and last 5 degrees can be seen in the insets. Right column: the difference between the DLP of the smooth crystal and the one-scale rough (red) and two-scale rough (green) crystals for each of the crystal sizes considered. The deviation graphs are intended to more clearly show where DLP for the rough crystals deviates from DLP for the smooth crystals. Different rows represent different crystal size parameters; from top to bottom, they represent size parameters of 20, 40, 60 and 100. (For interpretation of the references to color in this figure legend, the reader is referred to the web version of this article.)

computed using the ADDA code for smooth, one-scale and two-scale Gaussian rough crystals of various orientations and size parameters of 20, 40, 60 and 100. Fourier analysis of data obtained through atomic force microscopy of a grain of Kuwaiti desert sand returned correlation lengths and standard deviations which were used to create Gaussian rough surfaces. These rough surfaces were then folded to create rough crystals. The roughness was scaled linearly with crystal size.

2D scattering patterns for fixed orientation of known particle geometries are an important tool for interpreting SID-3 patterns. Our results show that roughness causes characteristic features related to smooth crystals to blur, fragment and disappear leaving behind speckle, when the scaling is large enough, for both forward and backward scattering hemispheres; the effect is strongest for the backscattering hemisphere. The roughness-induced deviations become more apparent as the crystal size parameter increases, and are more apparent for two-scale roughness than for one-scale roughness. With two-scale roughness at a size parameter of 100 considered, mainly the external diffraction peak with some speckle remains

Table 3
Percentage changes in direct forward transmission (i.e., a scattering angle of 0°) for one-scale and two-scale rough crystals, compared to the smooth crystal. The orientation angles refer to the rotations explained in Fig. 7.

Orientation	Size parameter 20		Size parameter 40		Size parameter 60		Size parameter 100	
	One-scale % change	Two-scale % change	One-scale % change	Two-scale % change	One-scale % change	Two-scale % change	One-scale % change	Two-scale % change
30°,0°	2.67	2.55	1.36	1.86	4.21	3.58	−2.36	−7.68
30°,10°	2.25	4.06	4.10	6.58	1.19	−0.39	−0.50	−5.36
30°,20°	2.20	3.28	4.52	9.45	0.95	−3.17	−2.64	−11.53
30°,30°	0.94	1.11	4.27	7.93	2.30	−2.14	−2.60	−12.80
Mean	2.02	2.76	3.53	6.37	2.12	−0.64	−2.05	−9.45

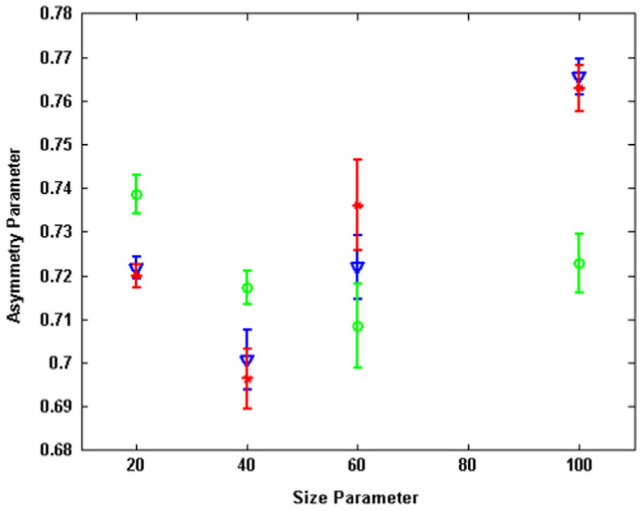

Fig. 14. Graphical representation of asymmetry parameter results of smooth (blue, triangle markers), one-scale rough (red, asterisk markers) and two-scale rough (green, circle markers) crystals. Markers show the position of the mean and bars show the standard deviation of the asymmetry parameter derived from the four computed orientations. Note that the orientations are not independent. (For interpretation of the references to color in this figure legend, the reader is referred to the web version of this article.)

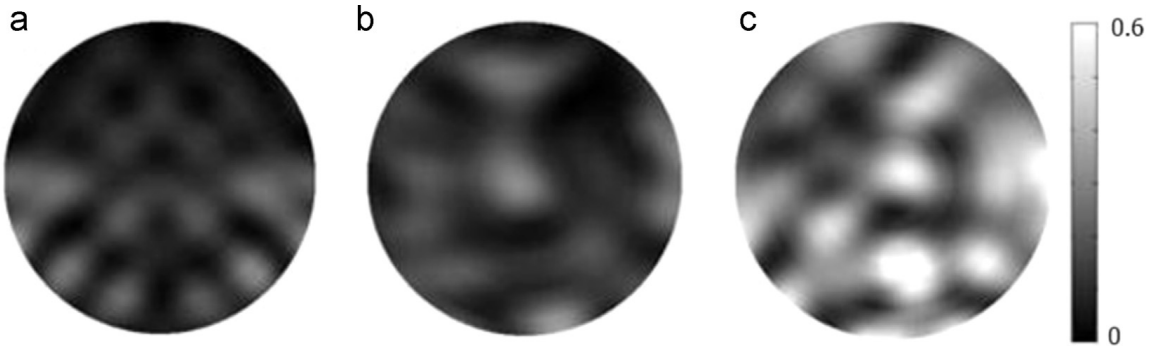

Fig. 15. Two-dimensional intensity patterns with linear scale for the size parameter 100 crystal in the orientation shown in the first column of Fig. 8 for the angular region $175^{\circ} \le \theta \le 180^{\circ}$. (a) corresponds to the smooth crystal, (b) the one-scale rough crystal and (c) the two-scale rough crystal. It can be seen that adding roughness increases the intensity of the backscattered light because of coherent backscattering.

for forward scattering. However, the angular region enclosing the direct backscattering direction needs to be considered separately. For orientations where direct backscattering is strong for the smooth crystal due to retro-reflections at or close to 180° it will be reduced by surface roughness in a similar way as discussed for other large scattering angles. Yet, for orientations where direct backscattering is weak for the smooth crystal it is slightly increased by surface roughness, which is thought to be partly due to coherent backscattering.

Phase functions show that the effects of roughness increase as the particle is scaled towards larger sizes with larger roughness features in the investigated range - little change is seen (compared to the smooth crystal case) for rough crystals scaled to a size parameter of 20. It should be noted that (l/λ) and (σ/λ) are very small at size parameter

20; wavelength scale roughness features may well increase light scattering by a crystal of this size.

As the asymmetry parameter is easily affected by orientation we cannot draw firm conclusions on how roughness affects it since the orientation sample is small. Calculation of a sufficient number of random orientations for proper orientation averaging would be extremely computationally expensive. That said, we see that deviation from the smooth case is largest when the two-scale roughness is used in conjunction with the largest size parameter, which is qualitatively in agreement with previous experimental results [14].

Degree of linear polarisation 2D patterns show that, compared to results for smooth crystals, roughness disrupts patterns in scattering angle and azimuth for forward and backward scattered light. Backward scattering is affected more than forward scattering; the same effect as seen for intensity. These effects become more pronounced as the crystal is scaled up in size and for two-scale roughness.

Overall we have shown that for hexagonal prisms Gaussian roughness with the investigated parameters reduces features seen in the phase function compared with the smooth counterpart and reduces the asymmetry parameter, as long as the effective period and amplitude of the spectrum of spatial oscillations making up the roughness are of an approximately equal or greater size to the wavelength – this appears to begin happening noticeably at a size parameter of 40. Larger roughness features cause more deviation from scattering observed for smooth crystals, but the most effective roughness model for ice crystals investigated here takes account of both large features and features whose size is small compared to the wavelength.

Acknowledgements

Many thanks are due to Emmanuel Brousseau of the Institute of Mechanical and Manufacturing Engineering at Cardiff University for his AFM work with sand grains. E Hesse and Z. Ulanowski acknowledge support by the Natural Environment Research Council (NERC), United Kingdom, grant NE/I020067/1. C.T. Collier and L. Taylor acknowledge support from the NERC Doctoral Training Programme. T. Nousiainen acknowledges funding by the Academy of Finland Grant no. 255718 and the Finnish Funding Agency for Technology and Innovation (Tekes) Grant no. 3155/31/2009. A. Penttilä acknowledges funding by the Academy of Finland Grant no. 1257966. The DDA results have been computed using CSC's resources. CSC is the Finnish IT Centre for Science and is owned by the Ministry of Education, Finland.

The authors also gratefully acknowledge the helpful contributions from two anonymous reviewers.

References

[1] Contribution of working group I to the fifth assessment report of the Intergovernmental Panel on Climate Change; 2013.
[2] Colman RA. A comparison of climate feedbacks in general circulation models. Clim Dyn 2003;20:865–73.
[3] Liou KN, Takano Y, Yang P Y. In: Mishchenko MI, Hovenier JW, Travis LD, editors. Light scattering by nonspherical particles. New York: Academic Press; 1999. p. 417–49.
[4] Baran AJ. From the single-scattering properties of ice crystals to climate prediction: A way forward. Atmos Res 2012;112:45–69.
[5] Yang P, Liou KN, Bi L, Liu C, Yi BQ, Baum BA. On the radiative properties of ice clouds: Light scattering, remote sensing and radiation parameterization. Adv Atmos Sci 2015;32(1):32–63.
[6] Wendisch M, Yang P, Pilewskie P. Effects of ice crystal habit on thermal infrared radiative properties and forcing of cirrus. J Geophys Res 2007;112:D08201.
[7] Wylie DP, Menzel WP, Woolf HM, Strabala KI. Four years of global cirrus cloud statistics using HIRS. J Clim 1994;7:1972–86.
[8] Nazaryan H, McCormick MP, Menzel WP. Global characterization of cirrus clouds using CALIPSO data. J Geophys Res 2009;113:D16211.
[9] Mishchenko MI, Macke A. How big should hexagonal ice crystals be to produce halos? Appl Opt 1999;38:1626–9.
[10] Noel V, Winker DM, McGill M, Lawson P. Classification of particle shapes from lidar depolarization ratio in convective ice clouds compared to in situ observations during CRYSTAL-FACE. J Geophys Res 2004;109:2156–202.
[11] Ulanowski Z, Kaye PH, Hirst E, Greenaway R. Light scattering by ice particles in the Earth's atmosphere and related laboratory measurements. In: Proceedings of the electromagnetic light scattering conference XII; 2010.
[12] Cole BH, Yang P, Baum BA, Riedi J, Labonnote LC. Ice particle habit and surface roughness derived from PARASOL polarization measurements. Atmos Chem Phys 2014;14:3739–50.
[13] Liu C, Panetta RL, Yang P. The effective equivalence of geometric irregularity and surface roughness in determining particle single-scattering properties. Opt Soc Am 2014;22:23620–7.
[14] Ulanowski Z, Hesse E, Kaye PH, Baran AJ. Light scattering by complex ice-analogue crystals. J Quant Spect Rad Trans 2006;100:382–92.
[15] Connolly PJ, Flynn MJ, Ulanowski Z, Choularton TW, Gallagher MW, Bower KN. Calibration of the cloud particle imager probes using calibration beads and ice crystal analogs: the depth of field. J Atmos Ocean Tech 2007;24:1860–79.
[16] Pfalzgraff WC, Hulscher RM, Neshyba SP. Scanning electron microscopy and molecular dynamics of surfaces of growing and ablating hexagonal ice crystals. Atmos Chem Phys 2010;10:2927–35.
[17] Ritter G. The growth and morphology of small ice crystals in a diffusion chamber [PhD Thesis]. Hatfield, UK: University of Hertfordshire; 2015 Available at: http://uhra.herts.ac.uk/handle/2299/16329.
[18] Neshyba SP, Lower B, Benning M, Lawson A, Rowe PM. Roughness metrics of prismatic facets of ice. J Geophys Res Atmos 2013;118:3309–18.
[19] Wagner R, Linke C, Naumann K-H, Schnaiter M, Vragel M, Gangl M, Horvath H. A review of optical measurements at the aerosol and cloud chamber AIDA. J Quant Spect Rad Trans 2009;110:930–49.
[20] Kemppinen O, Nousiainen T, Lindqvist H. The impact of surface roughness on scattering by realistically shaped wavelength-scale dust particles. J Quant Spect Rad Trans 2015;150:55–67.
[21] Macke A, Mueller J, Raschke E. Single scattering properties of atmospheric ice crystals. J Atmos Sci 1996;53:2813–25.
[22] Liu C, Panetta RL, Yang P. The effects of surface roughness on the scattering properties of hexagonal columns with sizes from the Rayleigh to the geometric optics regimes. J Quant Spect Rad Trans 2013;129:169–85.
[23] Ulanowski Z, Kaye PH, Hirst E, Greenaway RS, Cotton RJ, Hesse E, Collier CT. Incidence of rough and irregular atmospheric ice particles from Small Ice Detector 3 measurements. Atmos Chem Phys 2014;14:1649–62.
[24] Yurkin MA, Hoekstra AG. The discrete-dipole-approximation code ADDA: capabilities and known limitations. J Quant Spect Rad Trans 2011;112:2234–47.
[25] Muinonen K, Saarinen K. Ray optics approximation for Gaussian random cylinders. J Quant Spect Rad Trans 2000;64:201–18.
[26] Muinonen K, Nousiainen T, Fast P, Lumme K, Peltoniemi JI. Light scattering by Gaussian random particles: ray optics approximation. J Quant Spect Rad Trans 1996;55:577–601.
[27] McCall DS. Measurement and modelling of light scattering by small to medium size parameter airborne particles.PhD thesis. Hatfield, UK: University of Hertfordshire; 2010 Available at: http://uhra.herts.ac.uk/handle/2299/6374.
[28] Jämsä S, Peltoniemi JI, Lumme K. Thermal emission from a rough surface: ray optics approach. Astron Astrophys 1993;271:319–25.
[29] Zhou C, Yang P. Backscattering peak of ice cloud particles. Opt Express 2015;23(9):11995–2003.

[30] Schmidt K, Yurkin MA, Kahnert M. A case study on the reciprocity in light scattering computations. Opt Express 2012;20:23253–74.
[31] Hesse E, Collier CT, Penttilä A, Nousiainen T, Ulanowski Z, Kaye PH. Modelling light scattering by absorbing smooth and slightly rough facetted particles. J Quant Spect Rad Trans 2015;157:71–80.
[32] Taylor L, Hesse E, Ulanowski Z, Kaye PH, Penttilä A, Nousiainen T. Beam tracing with diffraction. In: Proceedings of the 15th electromagnetic and light scattering conference: Leipzig, Germany; 21–26 June, 2015.
[33] Takano Y, Liou KN. Solar radiative transfer in cirrus clouds. Part 1: single scattering and optical properties of hexagonal ice crystals. J Atmos Sci 1989;46:3–19.
[34] Ulanowski Z, Hirst E, Kaye PH, Greenaway R. Retrieving the size of particles with rough and complex surfaces from two-dimensional scattering patterns. J Quant Spect Rad Trans 2012;113:2457–64.
[35] Borovoi A, Kustova N, Cole B. Interference phenomena at backscattering by ice crystals of cirrus clouds. Opt Express 2015;23:24557–71.
[36] Takano Y, Jayaweera K. Scattering phase matrix for hexagonal ice crystals computed from ray optics. Appl Opt 1985;24:3254–63.
[37] Yang P, Bi L, Baum BA, Liou KN, Kattawar GW, Mishchenko MI, Cole B. Spectrally consistent scattering, absorption, and polarization properties of atmospheric ice crystals at wavelengths from 0.2 to 100 μm. J Atmos Sci 2013;70:330–47.
[38] Ulaby FT, Moore RK, Fung AK. Microwave Remote Sensing: Active and Passive, Volume II. Mass., USA: Addison-Wesley Publ.; 1982.